Photonic Engineering of Near- and Far-field Radiative Heat Transfer

by

Jonathan Kien-Kwok Tong

Submitted to the Department of Mechanical Engineering
in partial fulfillment of the requirements for the degree of

Doctor of Philosophy

at the

MASSACHUSETTS INSTITUTE OF TECHNOLOGY

June 2016

© Massachusetts Institute of Technology 2016. All rights reserved.

Author……..
Department of Mechanical Engineering
May 18, 2016

Certified by…….
Gang Chen
Carl Richard Soderberg Professor of Power Engineering
Thesis Supervisor

Accepted by…….....
Rohan Abeyaratne
Chairman, Department Committee on Graduate Students

Photonic Engineering of Near- and Far-field Radiative Heat Transfer

by

Jonathan Kien-Kwok Tong

Submitted to the Department of Mechanical Engineering on May 18, 2016,

in partial fulfillment of the requirements for the degree of Doctor of Philosophy

Abstract

Radiative heat transfer is the process by which two objects exchange thermal energy through the emission and absorption of electromagnetic waves. It is one of nature's key fundamental processes and is ubiquitous in all facets of daily life from the light we receive from the Sun to the heat we feel when we place our hands near a fire. Fundamentally, radiative heat transfer is governed by the photonic dispersion, which describes all the electromagnetic states that can exist within a system. It can be modified by the material, the shape, and the environment. In this thesis, morphological effects are used to modify the photonic dispersion in order to explore alternative methods to spectrally shape, tune, and enhance radiative heat transfer from the near-field to the far-field regimes.

We start by investigating the application of thin-film morphologies to different types of materials in the near-field regime using a rigorous fluctuational electrodynamics formalism. For thin-film semiconductors, trapped waveguide modes are formed, which simultaneously enhance radiative transfer at high frequencies where these modes are resonant and suppress radiative transfer at low frequencies where no modes are supported. This spectrally selective behavior is applied to a theoretical thermophotovoltaics (TPV) system where it is predicted the energy conversion efficiency can be improved. In contrast, thin-films of metals supporting surface plasmon polariton (SPP) modes will exhibit the opposite effect where the hybridization of SPP modes on both sides of the film will lead to a spectrally broadened resonant mode that can enhance near-field radiative transfer by over an order of magnitude across the infrared wavelength range.

In order to observe these morphological spectral effects, suitable experimental techniques are needed that are capable of characterizing the spectral properties of near-field radiative heat transfer. To this end, we developed an experimental technique that consists of using a high index prism in an inverse Otto configuration to bridge the momentum mismatch between evanescent near-field radiative modes and propagation in free space in conjunction with a Fourier transform infrared (FTIR) spectrometer. Preliminary experimental results indicate that this method can be used to measure quantitative, gap-dependent near-field radiative heat transfer spectrally.

While utilizing near-field radiative transfer remains a technologically challenging regime for practical application, morphological effects can still be used to modify the optical properties of materials in the far-field regime. As an example, we use polyethylene fibers to design an infrared transparent, visibly opaque fabric (ITVOF), which can provide personal cooling by allowing thermal radiation emitted by the human body to directly transmit to the surrounding environments while remaining visible opaque to the human eye.

Thesis Supervisor: Gang Chen
Title: Carl Richard Soderberg Professor of Power Engineering

Acknowledgments

I was once told that to pursue a doctoral degree, the most important trait to have as a student is to be persistent. It is this undeniable stubbornness that can enable one to overcome the inevitable failures encountered when doing graduate level research. However, as I've come to learn from my own experience, persistence alone can only get you so far. There will often be times when despite considerable effort, samples continuously break, experiments won't yield a signal, or calculations don't converge and it may feel such research projects are simply insurmountable. It is in these moments that the people supporting you can enable you to push past these failures in order to ultimately find success. During my time at MIT, I was fortunate to have a number of people who did just that for me.

I'd like to thank my advisor Prof. Gang Chen who gave me my first opportunity to conduct research in his lab back in the summer of 2008. Without his generosity, I never would have had the opportunity to attend graduate school at MIT. I've learned more than I ever could have imagined under his tutelage. I am also grateful for his guidance as he showed me that I was capable of far more than I ever thought possible. I would also like to thank my thesis committee members, Prof. Nicholas Fang and Prof. Marin Soljačić for their support, advice, and words of encouragement throughout my Ph.D.

I also want to thank my colleagues in the NanoEngineering group. It was a real honor to be a member of such a talented, hardworking, and humble group of people. First, I'd like to thank my former colleagues Sheng Shen, Tony Feng, and Nitin Shukla who were not only true role models for me when I first started as a graduate student, but great friends as well. I would also like to specially thank my colleague Wei-Chun Hsu who has not only been an incredible colleague who I shared many wonderful discussions of ideas and concepts with over the years, but also a great friend who has always been there to pick me up whenever I was down. I also want to thank Svetlana Boriskina who has been a true mentor to me. She was not only the inspiration for much of my own work, but through her patience and encouragement I discovered the beauty of optics and all the possibilities it can lead to in research. I would also like to thank many of my other current and former colleagues who I shared many great memories with that would be far too many to list here. In no particular order, I'd like to thank Poetro Sambegoro, Anastassios Mavrokefalos, Brian Burg, Matthew Branham, Kimberlee Collins, Daniel Kraemer, Kenneth McEnaney, Maria Luckyanova,

Bo Qiu, Xiaopeng Huang, Jivtesh Garg, Selçuk Yerci, Yongjie Hu, Sang Eon Han, Amador Guzman, Kazuki Ihara, Bolin Liao, Lingping Zeng, Yi Huang, Yoichiro Tsuramaki, Te-Huan Liu, George Ni, Yanfei Xu, Lee Weinstein, David Bierman, Kuang-Han Chu, Rong Xiao, and Tom Cooper. I'm sure I missed more people, but I hope you know who you are.

I would also like to thank the support staff of the NanoEngineering group who have had the unenviable task of ensuring the administrative functions of the group are always properly maintained. I especially want to thank Ed Jacobson for his friendship and the many conversations we had about all manner of things in life from our favorite books to the best places to go grocery shopping. But most importantly, he was a constant source of encouragement to me especially as I became acclimated to life as a graduate student. I also want to thank Mai Hoang, Keke Xu, and Juliette Pickering for their support and for not batting an eye whenever I gave them a pile of receipts for purchases I made.

I also want to thank the technicians that manage the shared facilities at MIT and Boston College, who I believe are one of the most valuable resources an aspiring experimentalist could ever have with their breadth and depth of knowledge. In particular, I want to thank Kurt Broderick at EML for his advice and patience in answering many of my deposition-related questions. I also want to thank Tim McClure at CMSE for his advice and constant encouragement on my near-field thermal emission experiments.

I also want to thank my family for their enduring love and support over these many years. I will always cherish all the care packages sent to me, the many home-cooked meals, and most importantly the moments we all shared together as a family despite the fact we all live in different regions of the world. And last, but certainly not least, I want to thank my girlfriend, Sohae Kim, who has been an anchor for me in the truest sense of the word. I know for a fact I never would have it made this far if it wasn't for her support. All the adventures we had and the many happy memories we shared together gave me the fortitude to push past the struggles of graduate school. I will forever be grateful to her.

Table of Contents

1 Introduction **29**

1.1 Historical Development of Classical Radiative Heat Transfer 30

1.2 Engineering Radiative Heat Transfer 32

1.3 Organization of Thesis 33

2 Morphological Modification of Near-field Radiative Heat transfer **35**

2.1 Near-field Radiative Heat Transfer 35

2.2 Morphological Effects on the Photonic Dispersion 41

2.2.1 Thin-film Optical Waveguides 42

2.2.2 Surface Polariton Waveguides 43

2.3 Theoretical Model for Near-field Radiative Heat Transport 45

2.3.1 Fluctuational Electrodynamics Formalism 45

2.3.2 Formulation for Infinite 1D Multilayer Geometry 49

2.3.3 Solutions for a Single Thin-film Supported by a Semi-Infinite Substrate . . 51

2.4 Morphological Effects on Dielectrics 57

2.4.1 Overview of Thermophotovoltaic Systems 58

2.4.2 System Configuration 59

2.4.3 Shaping Radiative Heat Transfer with Thermal Wells 61

2.4.4 Generality of Thermal Well Effect on Thermal Radiation 66

2.5 Impact of Thermal Well Effect on TPV Performance 67

2.5.1 Electrical Model for TPV Performance 67

2.5.2 Shockley Queisser Limit 68

2.5.3 Electrical Model with Non-radiative Recombination Losses 69

2.5.4 Predictions of TPV Performance using Thermal Well Effect 71

2.6 Morphological Effects on Surface Polariton Mode Resonances 79

2.6.1 Thin-film Morphology Effects on Surface Polariton Modes 79

2.6.2 Combining SPP and SPhP Resonant Modes in a Multilayer Geometry . . 84

2.7 Summary 86

3 Near-field Thermal Emission Spectroscopy **89**
3.1 Empirical Investigations of Near-field Radiative Heat Transfer 89
3.1.1 Spectral Measurements of Near-field Radiative Heat Transfer 92
3.1.2 Optical Coupling Schemes for High Momentum Evanescent Modes . . . 93
3.1.3 Overview of Experimental Approach 94
3.2 Dependency of Near-field Coupling on Prism Refractive Index. 95
3.3 Experiment Apparatus 97
3.3.1 Measurement Methodology 100
3.3.2 Cantilever Design. 101
3.3.3 Thermal Emitter and Heater Design 103
3.3.4 Extraction Prism and Holder Design 105
3.3.5 Optics for Emission Collection 109
3.3.6 Modeling Curvature Effects 111
3.3.7 Temperature Variability and Analysis 112
3.4 Results & Analysis 116
3.4.1 Validation of the Far-field Reference 118
3.4.2 Near-field Enhancement in Direct Contact. 120
3.4.3 Gap-dependent Near-field Enhancement 122
3.4.3.1 Magnitude Offset Correction 123
3.4.3.2 Spectral Shape Correction 126
3.4.4 Estimation of Angular Coupling Efficiency 130
3.4.5 Evaluation of Parasitic Emission from Prism and Holder 132
3.5 Summary 138

4 Infrared-Transparent, Visible-Opaque Fabrics **141**
4.1 Rayleigh and Mie Scattering of Light 141
4.2 Energy Management in Building Infrastructure 145
4.3 Current State-of-the-Art Personal Cooling Technologies 145
4.4 Heat Transfer Analysis for Personal Thermal Comfort 147
4.4.1 Requirements for Radiative Cooling of Human Body 147

4.4.2 Model Formalism 148
4.4.3 Control Volume Analysis 151
4.4.4 Temperature Profile in Cloth 153
4.4.5 Results and Analysis 156
4.5 Spectral Properties of Common Textiles 158
4.6 Design Strategy for ITVOF 161
4.7 Numerical Electromagnetics Modeling 164
4.8 Results and Discussion 166
4.9 Summary 174

5 Summary & Future Outlook **177**
5.1 Summary of Thesis 177
5.2 Future Outlook 178

List of Figures

Figure 1.1: A comparison of the original empirical fitting functions developed by Wien and Rayleigh to the Planck's distribution. As shown, Wien's function correctly captures the spectral radiative heat flux in the short wavelength limit while the Rayleigh-Jeans function correctly models the long wavelength limit. 31

Figure 2.1: A schematic illustration of the various types of modes contributing to radiative heat transfer in the near-field regime when the gap separation is smaller than the wavelength of thermal radiation. 36

Figure 2.2: (a) The dispersion characteristics for a surface polariton mode and (b) the resulting local density of states at a distance of d = 10 nm from the interface. The particular dispersion shown corresponds to silicon carbide, which supports a SPhP mode. 37

Figure 2.3: The dispersion for a high index (n = 2) slab waveguide suspended in vacuum. (a) Schematic illustration of slab waveguide system. (b) The dispersion for a 150 nm thick high index thin-film. (c) The dispersion for a 1 μm thick high index thin-film. The first fundamental modes shown in (b) and (c) do not exhibit a cut-off frequency due to the symmetric nature of the waveguide. If asymmetry is introduced, e.g. the high index thin-film is placed onto a supporting substrate, this fundamental mode will exhibit a cut-off frequency. 43

Figure 2.4: The dispersion for a thin-film metal supporting SPP modes suspended in vacuum. (a) Schematic illustration of surface polariton waveguide. (b) The dispersion for a single metal-air interface (black) and thin films with progressively smaller thicknesses. The red and blue branches correspond to the even and odd coupled SPP modes, respectively. Illustrations of the field for each mode is shown in the inset. The Drude model parameters for the metal are $\lambda_p = 1.1\mu\text{m}$, $\gamma = 0$, $\varepsilon_\infty = 3$. 45

Figure 2.5: A schematic illustration for a general 1D multilayer geometry used to evaluate thin-film morphology effects in near-field radiative heat transfer. Films a and b are arbitrarily chosen to illustrate the general form of radiative heat transfer for this system. 48

Figure 2.6: A schematic illustration of the single thin-film, single substrate system considered for derivation of exact solutions to the formulation presented in Eqs. (2.12) and (2.13). . . . 51

Figure 2.7: The TPV system consists of a thin-film emitter and a thin-film PV cell. Both films are placed onto semi-infinite back reflectors. 58

Figure 2.8: The dielectric permittivity of: (a) germanium (Ge), (b) tungsten (W), (c) gallium antimonide (GaSb), and (d) silver (Ag). The optical constants for the perfect metal were taken in the long wavelength limit of silver and were assumed to be dispersionless for the wavelength range computed. 61

Figure 2.9: The normalized transmission function, G_{NT}, comparing a bulk system to a thin-film system for different emitter materials and a GaSb cell: (a) a bulk Ge emitter and bulk GaSb cell, (b) a thin-film Ge emitter and a thin-film GaSb cell. The thin-film thicknesses are t_H = 860 nm and t_C = 136 nm, (c) a bulk W emitter and a bulk GaSb cell, (d) a bulk W emitter and a thin-film GaSb cell. The thin-film thickness is t_C = 134 nm. This comparison clearly showcases the effect of morphology on the trapped optical modes available for radiative transfer. The gap distance is assumed to be g = 100 nm. The light line is also plotted to differentiate propagating modes (above the light line) and evanescent modes (below the light line). 62

Figure 2.10: The spectral heat flux as a function of the emitter and the PV cell thicknesses assuming an emitter temperature T_H = 1000 K and a gap distance g = 100 nm: (a) the spectral heat flux for a Ge emitter, (b) the spectral heat flux for a W emitter. By making the emitter and the PV cell thin, radiative energy transfer at wavelengths below the band gap is significantly suppressed.. . 64

Figure 2.11: At high temperatures, the optical properties of Ge will change due to a combination of thermal expansion which decreases the electronic band-gap and a significant increase in the

population of thermally excited free-carriers. These factors will both lead to emission at longer wavelengths. (a) To assess whether this will impact the spectral selectivity, the imaginary component of permittivity of germanium was artificially increased to simulate this effect. Each case was re-optimized to maximize efficiency. For $Im(\varepsilon_H \to \infty) = 1$: $t_H = 100$ nm, $t_C = 100$nm, $Im(\varepsilon_H \to \infty) = 10$: $t_H = 90$ nm, $t_C = 100$nm, $Im(\varepsilon_H \to \infty) = 20$: $t_H = 80$ nm, $t_C = 100$nm (b) The spectral radiative heat flux for a Ge thin-film emitter and a GaSb PV cell supported by a perfect metal still exhibits spectrally selective radiative transfer even for high material losses in the emitter. This can be explained by the inability of the GaSb thin-film to absorb long wavelength thermal radiation emitted by Ge due to the cutoff frequency of the lowest frequency mode. Although the spectral heat flux broadens and redshifts for higher material losses, the efficiency computed for each case is 39.8% for $Im(\varepsilon_H \to \infty) = 1$, 37.7% for $Im(\varepsilon_H \to \infty) = 10$, and 36% for $Im(\varepsilon_H \to \infty) = 20$.. . 65

Figure 2.12: To show the generality of the 'thermal well' effect in manipulating thermal radiative transfer, several alternative material combinations were calculated, including: (a) lead telluride (PbTe) emitter and absorber assuming an emitter temperature of $T_H = 600$ K and absorber temperature of $T_C = 300$ K at a separation distance of 100 nm, (b) indium arsenide (InAs) emitter and absorber assuming an emitter temperature of $T_H = 600$ K and absorber temperature of $T_C = 300$ K at a separation distance of 100 nm, and (c) indium antimonide (InSb) emitter and absorber assuming an emitter temperature of $T_H = 500$ K and absorber temperature of $T_C = 300$ K at a separation distance of 100 nm. In all cases, the back reflector is chosen to be a perfect metal. It should be noted that these materials were not intended for use in high-temperature TPV applications, but rather to assess the potential spectral selectivity of thermal emission that could be achieved using the thermal well concept with different materials. 66

Figure 2.13: A schematic illustration of the PV cell electrical model. The view of the PV cell is magnified detailing the structure assumed for the electrical analysis. The PV cell consists of a p-type quasi-neutral region, a n-type quasi-neutral region, and a space charge region. In this study, the thicknesses of the p-type and n-type quasi-neutral regions are assumed equal.. . . . 70

Figure 2.14: The energy conversion efficiency, η, from the emitter to the PV cell for several material combinations. (a) The efficiency as a function of temperature assuming a gap distance of g = 100 nm. (b) The predicted efficiencies from (a) normalized by efficiencies computed using the Shockley Queisser formulation for varying blackbody emitter temperatures. (c) The efficiency as a function of gap distance assuming an emitter temperature T_H = 1000 K. The legend is identical to (a). The optimal thicknesses for the case of a Ge emitter on a W substrate and a GaSb cell on a Ag substrate with a MgF_2 spacer is t_H = 119 nm, t_C = 100 nm, and t_S = 1.25 μm. The optimal thicknesses for a Ge emitter on a W substrate and a GaSb cell on a perfect metal are t_H = 58 nm and t_C = 94 nm. The optimal thicknesses for a bulk W emitter and a GaSb cell on a Ag substrate with a MgF_2 spacer is t_C = 59 nm and t_S = 750 nm. 72

Figure 2.15: The predicted efficiency, η, using the Shockley-Queisser formulation for the same radiative power density based on Fig. 2.10. (a) The efficiency as a function of the emitter temperature assuming a gap separation of g = 100 nm. (b) The efficiency as a function of the gap separation assuming an emitter temperature of T_H = 1000 K. 76

Figure 2.16: A preliminary design for a multilayer dielectric mirror was developed to show that it is possible to approach a near unity reflectance using real materials. This particular design is composed of silicon dioxide (SiO_2) and silicon (Si) supported by a silver (Ag) substrate with layer thicknesses from the top to the bottom of: 112 nm, 242 nm, 86 nm, 209 nm, and 308 nm. The dielectric mirror was specifically designed to improve the reflectance in the 2 to 3 μm wavelength range where parasitic absorption is more prevalent. Compared to a Ag mirror, which exhibits a reflectance of about 98.3%, the dielectric mirror can achieve a reflectance as high as 99.7%. This may not appear to be a significant improvement, but, as discussed in the main text, a perfect metal back reflector and a Ag back reflector can lead to significant differences in the energy conversion efficiency. These results thus show that a simple multilayer dielectric stack can readily approach the perfect metal limit, suggesting it is possible to achieve high TPV efficiencies for a real system. It should be noted that this calculation was performed at normal incidence. 77

Figure 2.17: The complex dielectric permittivity of a polar dielectric, SiC, and a metal, AZO. The solid and dashed lines correspond to the real and imaginary component of permittivity, respectively. 80

Figure 2.18: A comparison of the spectral near-field radiative heat flux for bulk and thin-film media supporting SPP and SPhP resonant modes. (a) The spectral radiative heat flux for bulk semi-infinite AZO and SiC emitters and absorbers. The hot and cold side temperatures are T_H = 1000 K and T_C = 300 K, respectively. The gap separation is g = 20 nm. (b) The spectral radiative heat flux for identical thin-film AZO and SiC emitters and absorbers suspended in vacuum. The film thicknesses for AZO and SiC are 2 nm and 20 nm, respectively, which were obtained by optimization to maximize the total radiative heat flux. The hot and cold side temperature and the gap separation are identical to (a). The blackbody distribution is also shown in (a) and (b) for comparison. (c) The total integrated radiative heat flux as a function of the hot side temperature for the case of a 2 nm thick AZO thin-film and a 20 nm thick SiC thin-film. The cold side temperature and gap separation are again 300 K and 20 nm, respectively. 81

Figure 2.19: The transmission function, which provides the radiative modes that contribute to heat transfer as a function of wavelength and in-plane wave vector, for the following: (a) Bulk SiC, (b) bulk AZO, (c) thin-film SiC, and (d) thin-film AZO. The gap separation is again assumed to be g = 20 nm.. 84

Figure 2.20: The complex dielectric permittivity for other common polar dielectrics, SiO_2 and MgF_2. The solid and dashed lines correspond to the real and imaginary component of permittivity, respectively. 85

Figure 2.21: The impact of combining films and substrates supporting both SPP and SPhP modes. (a) The spectral radiative heat flux between 2 nm thick AZO films suspended in vacuum (red line) and supported by a semi-infinite SiO_2 substrate (blue line). (b) The transmission function for the case of an AZO film supported by a SiO_2 substrate shown in (a). (c) The spectral radiative heat flux for a multilayer stack comprised of a 5 nm SiO_2 film, a 5 nm MgF_2 film, a 5 nm SiC film, and a 2 nm AZO film. (d) The transmission function for the multilayer geometry shown in (c). In all

cases, the hot and cold side temperatures are T_H = 1000 K and T_C = 300 K, respectively. The gap separation is also g = 20 nm. 86

Figure 3.1: Schematic illustrations detailing (a) the Otto and (b) the Kretschmann configurations, which were used to externally excite SPP modes supported at the metal-air interface. . . 94

Figure 3.2: Theoretical predictions of the spectral radiative heat flux on the refractive index, n, of prism. (a) A schematic illustration of the system simulated. A hot side temperature of T_H = 550 K and a gap separation of g = 100 nm is used. (b) The dielectric permittivity of SiO_2. (c) The spectral radiative heat flux for a varying prism refractive index. 96

Figure 3.3: (a) A schematic illustration detailing the method used to calibrate the contact point between the thermal emitter and the prism. The thermal emitter is mounted onto a cantilever, which will only bend when contact is made with the prism. This bending response is measured optically using a laser reflected off the tip of the cantilever onto a position sensitive detector (PSD). (b) A corresponding image of the actual experimental platform detailing how these components are used. 98

Figure 3.4: (a) The simulated temperature distribution along the cantilever beam made of Macor. As shown, the large temperature gradient indicates the cantilever is sufficiently thermally insulating. (b) An image of the cantilever and the heater mounted onto the piezo stag. (c) An example contact calibration where the heater was brought into contact with the prism, resulting in a linear bending response. 102

Figure 3.5: (a) A cross-section view of the heater and the thermal emitter with several retaining rings and washers for support. (b) Side and front view images of the thermal emitter mounted onto the cantilever with a N-BK7 thermal emitter.. 104

Figure 3.6: (a) Front and rear images of the ZnSe prism and the holder used to support the prism. (b) An image of the pinhole aperture fabricated to reduce the far-field contribution to the measured

thermal emission intensity. A schematic illustration is also included, showing a cross section image of the pinhole aperture. 106

Figure 3.7: Ray tracing analysis to evaluate angular extraction efficiency from ZnSe lens geometry. (a) Schematic illustration of the system modeled. A point source is used to emulate emission into the prism at different angles, Θ. (b) The resulting extraction efficiency for the particular ZnSe lens geometry used in this experiment. 108

Figure 3.8: An on-axis parabolic mirror can be used to collimate thermal emission extracted from the ZnSe prism. (a) A schematic illustration detailing the ray tracing analysis used to design an optimal on-axis parabolic mirror. (b) An image detailing the fabrication of the mirror, which consisted of overlaying metallized mylar segments onto a negative mold made of balsa wood. (c) A top-down image of the fabricated on-axis parabolic mirror placed around the ZnSe lens on the prism holder. 109

Figure 3.9: An off-axis parabolic (OAP) mirror is used to collect and guide thermal emission into the FTIR spectrometer. (a) An image of the OAP mirror used in the experiment. (b) A comparison of the measured spectral emission intensity when using a flat mirror and an OAP mirror. . 111

Figure 3.10: A heat transfer model is used to analyze the temperature variation along the thermal emitter caused by heat conduction losses through the air gap separating the emitter and the prism. (a) A schematic illustration of the heat transfer model detailing the various heat transfer mechanisms simulated. For visual clarity, the Al prism holder and supports are not shown, but are included in the heat transfer analysis. (b) The temperature profiles along the thermal emitter surface at various gap separations. The color gradient near the center represents the region where thermal emission is collected through the pinhole aperture. (c) The corresponding temperature profiles along the flat side of the ZnSe prism at various gap separations. In (b) and (c), the colored circles represent temperature measurements taken at the edge of the thermal emitter and ZnSe prism, respectively, at the corresponding gap separation. The measurement at contact yielded a peak-to-peak magnitude in the interferogram of 5.64, which was used as a reference to calibrate subsequent measurements at larger gap separations. 113

Figure 3.11: (a) The dielectric permittivity of ZnSe. (b) The ratio of the far-field spectral radiative heat flux at emitter temperatures of T_H = 115.9°C and T_H = 123.8°C, which correspond to the minimum and maximum averaged temperatures based on the heat transfer model. . . . 115

Figure 3.12: Validation of the far-field reference measurements. (a) The ratio of the background corrected emission intensities measured in the far-field regime at g = 50 μm and 100 μm, respectively. (b) The corresponding theoretical prediction assuming an emitter temperature of T_H = 110°C. The curvature of the thermal emitter is approximated using the PFA approximation. 119

Figure 3.13: (a) The measured near-field enhancement, β, when the thermal emitter is placed into contact with the ZnSe prism. The far-field measurement taken at g = 50 μm is used. The as measurement near-field enhancement (blue line) is spectrally averaged (red line) over $\Delta\eta \sim 58$ cm^{-1}. (b) The theoretically predicted near-field enhancement assuming an emitter temperature of T_H = 110°C. As an approximation to contact, the gap separation is chosen to be g = 3 nm.. . . 121

Figure 3.14: (a) The as-measured near-field enhancement, β, at variable gap separations before and after contact. The far-field measurement taken at g = 50 μm is used. The color of each line corresponds to specific gap position based on the color bar. (b) The corresponding near-field enhancement spectrally averaged over $\Delta\eta \sim 58$ cm^{-1}. 123

Figure 3.15: (a) The spectral emission intensities originally measured at various gap separation. The far-field measurement at g = 50 μm is also included (black dashed line). (b) The spectral emission intensities after the normalization correction is applied. 125

Figure 3.16: (a) The normalized near-field enhancement, β^N, for various gap separations. The far-field measurement taken at g = 50 μm is used for reference. (b) The normalized theoretical near-field enhancement, which was calculated assuming an emitter temperature of 110°C and spectrally averaged over $\Delta\eta \sim 58$ cm^{-1}. 126

Figure 3.17: (a) The ratio of Bose-Einstein distributions at temperatures of T_1 = 103ºC and T_2 = 110ºC, respectively. (b) The estimated temperature decrease of the thermal emitter as a function of the gap position using Eq. (3.7). 127

Figure 3.18: (a) The spectrally corrected, normalized near-field enhancement, $\beta^{N,C}$, for various gap separations. The far-field measurement taken at g = 50 μm is used for reference. The normalized near-field enhancement, β^{N}, is also plotted for the direct contact measurement (dashed black line). (b) The normalized theoretical near-field enhancement, which was calculated assuming an emitter temperature of 110ºC and spectrally averaged over $\Delta\eta \sim 58$ cm^{-1}. 129

Figure 3.19: (a) A schematic illustration of the ray tracing system used to evaluate the angular components collected by the OAP mirror. (b) The OAP extraction efficiency as a function of the emission angle, Θ. 131

Figure 3.20: (a) The spectrally corrected, normalized near-field enhancement, $\beta^{N,C}$, for various gap separations. The far-field measurement taken at g = 50 μm is used for reference. The normalized near-field enhancement, β^{N}, is also plotted for the direct contact measurement (dashed black line). (b) The normalized, angularly weighted theoretical near-field enhancement,$\beta^{N,A}$, which was calculated at various gap separations assuming an emitter temperature of 110ºC and spectrally averaged over $\Delta\eta \sim 58$ cm^{-1}. 132

Figure 3.21: To evaluate the effect of parasitic background thermal emission from the extraction apparatus (pinhole aperture, ZnSe prism, and prism holder), the apparatus is heated to similar temperatures observed in the near-field enhancement measurements. (a) Schematic illustration of heater placement and size. (b) An image showing the heater in relation to the pinhole aperture and thermocouple. (c) The theoretical temperature distribution along the ZnSe prism and holder when heated by an N-BK7 thermal emitter and by a small heater, corresponding to measurements with similar ZnSe prism temperatures of T_z = 77.7ºC and 77.3ºC, respectively. For the direct heating case, a small air gap 5 μm thick is assumed between the heater and prism. 134

Figure 3.22: (a) The spectral emission intensities from the extraction apparatus at various temperatures. (b) The measured spectral emission intensities in the near-field enhancement measurement at contact and g = 50 μm. (c) The subtraction of spectral emission intensities from (a) using T_{ZnSe} = 77.3°C and 59.2°C. (d) The subtraction of spectral emission intensities from (b). 136

Figure 3.23: The spectral emittance of the pinhole aperture and ZnSe prism were also measured to further validate the near-field enhancement results. (a) A schematic illustration of the experimental configuration used to measure the spectral emittance. (b) The measured spectral emittances for the aluminum reference, the pinhole aperture, and the pinhole aperture with the ZnSe prism. . 138

Figure 3.24: The predicted temperature profile along the thermal emitter surface for the configuration shown in Fig. 3.10 when placed in vacuum. 139

Figure 4.1: The variation in scattering efficiency, Q_{sca}, of a SiO_2 sphere as it transition from the Rayleigh scattering regime through the Mie scattering regime to the geometric ray optics regime. (a) Q_{sca} as a function of the particle radius at a wavelength of λ = 600 nm. (b) A color map of Q_{sca} as a function of both the particle radius and wavelength of incident light. As shown, several distinct bands can be observed, which is indicative of the appearance of WGM resonances in the sphere. 143

Figure 4.2: A heat transfer model was developed to analyze heat dissipation from a clothed human body to the ambient environment. Various heat transfer contributions that lead to dissipation of heat from the human body, such as radiation, heat conduction, and heat convection are included. To model loose fitting clothing, a finite air gap is assumed between the cloth and the skin.. 148

Figure 4.3: Illustrations depicting the control volume analysis and temperature profile formulation for the heat transfer model. (a) The control volumes chosen in this analysis consist of CV1 around the human body and CV2 around only the cloth. (b) A schematic illustrating the differential element and energy balance used to derive the temperature profile within the cloth. In addition to heat conduction, this analysis includes radiative absorption and emission. 153

Figure 4.4: Evaluation of ITVOF mid- to far-IR optical requirements to maintain personal thermal comfort at elevated ambient temperatures. (a) A temperature map was computed showing the maximum ambient temperature attainable without compromising thermal comfort as a function of the total reflectance and transmittance of the cloth. It is assumed the air gap is t_a = 1.05 mm and the convective heat transfer coefficient is h = 3 W/m^{2}K. (b) A corresponding temperature map assuming t_a = 2.36 mm and h = 5 W/m^{2}K. The range of h is typical for cooling via natural convection. (c) An additional cooling power curve showing quantitatively the effect of radiative cooling as a function of the total cloth transmittance and reflectance assuming t_a = 1.05 mm and h = 3 W/m^{2}K. (d) An additional cooling power curve assuming t_a = 2.36 mm and h = 5 W/m^{2}K. As shown, by decreasing the reflectance and increasing the transmittance, it is possible to achieve the necessary 23 W of cooling at an ambient temperature of 26.1 ^{o}C using only thermal radiation. 156

Figure 4.5: Optical properties of conventional clothing. SEM images of (a) undyed cotton cloth and (b) undyed polyester cloth which show the intrinsic fabric structure. The insets are optical images of the samples characterized. For both samples, the fiber diameter is on average 10 μm and the yarn diameter is greater than 200 μm. The scale bars both correspond to 100 μm. (c) Experimentally measured optical properties in the visible wavelength range. (d) Experimentally measured FTIR transmittance spectra of undyed cotton cloth (thickness, t = 400 μm) and undyed polyester cloth (t = 300 μm) showing the opaqueness of common fabrics in the IR. . . . 159

Figure 4.6: Intrinsic absorptive properties of various synthetic polymers. (a) The FTIR transmittance spectra for a single cotton yarn (diameter, d = 200 μm) and a polyester thin-film (thickness, t = 12.5 μm). The transmittance spectra is normalized to provide similar scaling due to the order of magnitude difference in sample size. (b) The FTIR transmittance spectra for two candidate materials for the ITVOF. These materials include thin-films of nylon 6 (t = 25.4 μm) and UHMWPE (t = 102 μm). 162

Figure 4.7: Simulation parameters. (a) A schematic of the numerical simulation model used to predict the optical properties of the ITVOF design. The parameters include: D_f – the fiber diameter,

D_y – the yarn diameter, D_s – the fiber separation distance, and D_p – the yarn separation distance. For all simulations, the yarns were staggered 30° relative to the horizontal plane. In addition, incident light was assumed to be at normal incidence and the optical properties for unpolarized light were calculated by average light polarized parallel and perpendicular to the fiber axis. (b) The optical constants of polyethylene (PE) taken from the literature. The refractive index, n, is extrapolated from shorter wavelength data. Based on the dispersion of the extinction coefficient, k, it is expected the refractive index will also exhibit some dispersion. However, this is assumed to be small and is thus neglected in this study. 165

Figure 4.8: Numerical simulation results for the IR optical properties of a polyethylene-based ITVOF illustrating the effect of reducing the fiber and yarn size. Upper row: The yarn diameter is varied (D_y = 30 μm, 50 μm, and 100 μm) assuming a fixed fiber diameter of D_f = 10 μm. Lower row: The fiber diameter is varied (D_f = 1 μm, 5 μm, and 10 μm) assuming a fixed yarn diameter of D_y = 30 μm. For all simulations, the fiber separation distance is D_s = 1 μm and the yarn separation distance is D_p = 5 μm. The spectrally integrated transmittance (τ_c) and reflectance (ρ_c) is shown in each plot weighted by the Planck's distribution assuming a body temperature of 33.9°C (93°F). For D_f = 10 μm, the material volume per unit depth for a single yarn is 4870 μm^2 for D_y = 100 μm, 1492 μm^2 for D_y = 50 μm, and 550 μm^2 for D_y = 30 μm. For D_y = 30 μm, the material volume is 373 μm^2 for D_f = 5 μm and 136 μm^2 for D_f = 1 μm. The optical properties of the ITVOF are calculated for the wavelength range from 5.5 to 24 μm, which will provide a conservative estimate of the total transmittance and the reflectance. 167

Figure 4.9: Theoretical results for the visible and IR wavelength range highlighting the contrast in optical properties needed for an ITVOF. These results correspond to the case of D_f = 1 μm, D_y = 30 μm, D_s = 1 μm, and D_p = 5 μm. For comparison, the experimentally measured reflectances and transmittances of cotton and polyester cloths are also shown. 169

Figure 4.10: The visible wavelength extinction, scattering, and absorption efficiency of a single polyethylene fiber. The efficiency factor, Q, is defined as the ratio of the effective cross section normalized to the geometric cross section. The diameter of the fiber is D = 1 μm and the incident light is assumed to be unpolarized. For computation, the standard Mie theory solutions for an

infinitely long cylinder were used. As shown, the absorption efficiency exhibits a similar trend to the total hemispherical absorptance shown in Fig. 6 in the main text. The oscillatory behavior is indicative of whispering gallery modes supported by the fiber which are broadened due to material loss ($n = 1.5$, $k = 5 \cdot 10^{-4}$). In addition, a broad Fabry-Perot resonance is also supported by the fiber as indicated by the scattering efficiency, which increases from 460 nm to 700 nm. 170

Figure 4.11: Numerical simulation results for the IR optical properties of a polyethylene-based ITVOF for the case of a varying fiber diameter ($D_f = 1$ μm, 5 μm, and 10 μm) assuming a fixed yarn diameter of $D_y = 50$ μm. As before, all simulations assume the fiber separation distance is $D_s = 1$ μm and the yarn separation distance is $D_p = 5$ μm. The spectrally integrated transmittance (τ_c) and reflectance (ρ_c) is shown in each plot weighted by the Planck's distribution assuming a body temperature of 33.9°C. Compared to the case where $D_y = 30$ μm, the overall transmittance is lower, as expected, due to the combination of a larger material volume that absorbs more incident IR radiation and a larger number of fibers available to scatter incident IR radiation thus increasing the reflectance. However, by reducing the size of the fiber to be $D_f = 1$ μm, which is far smaller than IR wavelengths, the total transmittance can again be significantly enhanced from 0.63 to 0.969 which is nearly equal to the case where $D_y = 30$ μm. Simultaneously, the reflectance of the ITVOF is reduced from 0.27 to 0.019 further improving radiative cooling. These results show that reducing the fiber size is far more important than reducing the yarn size. Therefore, this structuring methodology could potentially be applied to ITVOF that are comparable in size to conventional fabrics. The material volume per unit depth for a single yarn is 1492 μm^2 for $D_f = 10$ μm, 1217 μm^2 for $D_f = 5$ μm, and 445 μm^2 for $D_f = 1$ μm. The optical properties of the ITVOF are again calculated for the wavelength range from 5.5 to 24 μm, which will provide a conservative estimate of the total transmittance and the reflectance. 171

Figure 4.12: (a) Numerical simulation results for the IR optical properties of an ITVOF blend of polyethylene and polyester with varying volumetric concentrations. The PE and PET fibers were randomly distributed in the simulation. For all simulations it is assumed $D_f = 1$ μm, $D_y = 30$ μm, $D_s = 1$ μm, and $D_p = 5$ μm. Again, the spectrally integrated transmittance (τ_c) and reflectance (ρ_c) is shown in each plot weighted by the Planck's distribution assuming a body temperature of 33.9°C.

As shown, a progressive increase in the volumetric concentration of PET results in an increase in the spectral absorptance thus decreasing the total transmittance. However, it can also be observed that the spectral reflectance is ~0.04 for all cases and exhibits no significant variation spectrally further reinforcing the point that so long as the fiber is sufficiently small compared to IR wavelengths, scattering will be minimal. Based on these results, even the highest volumetric concentration of PET fibers (25%PE/75% PET) can provide sufficient cooling to raise the ambient temperature to 26.1^{o}C due to a combination of a high total transmittance of 0.728 and a low total reflectance of 0.038. The material volume per unit depth for a single yarn in all cases is equal to 135.9 μm^2. The optical properties of the ITVOF are again calculated for the wavelength range from 5.5 to 24 μm, which will provide a conservative estimate of the total transmittance and the reflectance. (b) The optical constants of polyethylene terephthalate (PET), more commonly known as polyester, taken from the literature. A Lorentzian model was used to fit experimental data from previous studies. 173

List of Tables

Table 3.1: Overview of measurements used to evaluate near-field spectral enhancement. . 117

Table 3.2: Measured temperatures at the edges of the N-BK7 thermal emitter and ZnSe prism. 118

Table 3.3: Measured temperatures of the heater and at the edge of the ZnSe prism. . . . 135

Table 4.1: Input Parameters 150

Chapter 1

Introduction

Radiative heat transfer is the process in which two objects exchange thermal energy by the emission and absorption of electromagnetic waves. It is one of nature's key fundamental processes and is ubiquitous in all facets of daily life from the sunlight we receive to the heat we feel when we place our hands near a fire. Fundamentally, radiative emission originates from thermally fluctuating charges in matter whose collective motion results in the emission of light. The nature of these fluctuations, and hence the electromagnetic energy emitted, are intrinsically tied to the medium's temperature. Absorption, by contrast, is the reciprocal response of charges to incoming light that results in the annihilation and subsequent conversion of electromagnetic energy to other forms of energy such as heat or electricity.

Thermal radiation can be seen in a myriad of processes from conventional incandescent lighting to the dull red glow of a heated stovetop. But perhaps the greatest impact of thermal radiation can be felt in its role in regulating Earth's climate. The greenhouse effect, the process in which thermal radiation emitted by the Earth's surface is trapped by absorption and reemission from atmospheric gases, is the process that keeps the surface of Earth sufficiently warm, thus enabling the development and sustaining of life. However, since the advent of industrialization, mankind has continued to add greenhouse gases, namely CO_2, to the atmosphere to such an extent that if left undeterred, will warm Earth's climate to levels that will irreparably damage ecosystems, lead to mass extinction of species, disrupt agriculture impacting our food supply, and increasing the number and severity of extreme weather events.[1–3]

In order to curb global climate change, the challenge now is to develop new technologies that can provide sustainable, clean energy and reduce the consumption of electricity. Thermal radiation has an important role to play in this endeavor from the development of renewable energy technologies such as solar photovoltaics or solar thermal power systems to green technologies such as smart roof or windows to regulate building temperatures. The choice of the material, geometry, and environment are all parameters that can affect thermal radiation. By improving the

understanding and use of each parameter, it may be possible to spectrally shape, tune, and enhance radiative heat transfer to an extent previously unattainable.

1.1 Historical Development of Classical Radiative Heat Transfer

The study of thermal radiation has appeared throughout history with the earliest known observations by John della Porta in 1698 where he felt variations in heat by a candle placed in a parabolic silver bowl.[4,5] Subsequent experiments in the late 18th century and early 19th century by Marc-Auguste Pictet, Horace-Benedict de Saussure, and Count Rumford established the notion that thermal radiation is emitted by all objects with an intensity that increases with temperature.[4,5] It wasn't until the mid-19th century that more systematic empirical investigations were conducted to further understand the nature of thermal radiation. Balfour Stewart and Gustav Kirchoff independently developed the concept of a blackbody, which is an ideal object that absorbs all incident thermal radiation.[6–8] If at thermal equilibrium with its surroundings, a blackbody will reciprocally emit the same energy back to the environment. In the late 19th century and early 20th century, work by Wilhelm Wien, who developed Wien's displacement law, and Lord Rayleigh led to approximate empirical fits to the blackbody spectrum in the short and long wavelength ranges, respectively as shown in Fig. 1.1.[9,10]

In 1900, Max Planck, who had earlier been intrigued by Wien's results, deduced a mathematical form based on the short and long wavelength limits that provided the first fitting to match experimental results at all wavelengths as shown in Fig. 1.1.[11,12] The empirical fit was expressed in the following form,

$$I_{BB}(\lambda) = \frac{C_1}{\lambda^5\left(e^{\frac{C_2}{\lambda T}}-1\right)} \tag{1.1}$$

where $I_{BB}(\lambda)$ is the radiative intensity with units of power per unit area, per unit solid angle, and per unit wavelength, λ is the wavelength, T is the emitter temperature, and C_1 and C_2 are empirical fitting constants. In an effort to provide a physical explanation for the fitting, Planck resorted to the use of statistical physics developed by Ludwig Boltzmann to provide an *ab initio* derivation of Eq. (1.1), which required the concept that thermal energy radiated in discrete quanta.[13,14] This led to formal definitions of the empirical fitting constants such that $C_1 = 2hc^2$ and $C_2 = hc/k_b$ where h became known as the Planck's constant, c is the speed of light, and k_b is the Boltzmann constant.

Unbeknownst to Planck at the time, the idea that energy was discrete rather than continuous was a revelation that would later be affirmed by Albert Einstein in 1905 with his work on the photoelectric effect and would prove to be pivotal in the development of quantum mechanics.[15] Equation (1.1) thus provided the first rigorous description of thermal radiation from a blackbody, from which a limit can be derived that states an object at a given temperature can maximally radiate a set amount of energy. This limit implicitly assumes the emitting and absorbing objects in the system are sufficiently far apart at distances much greater than the wavelength of thermal radiation.

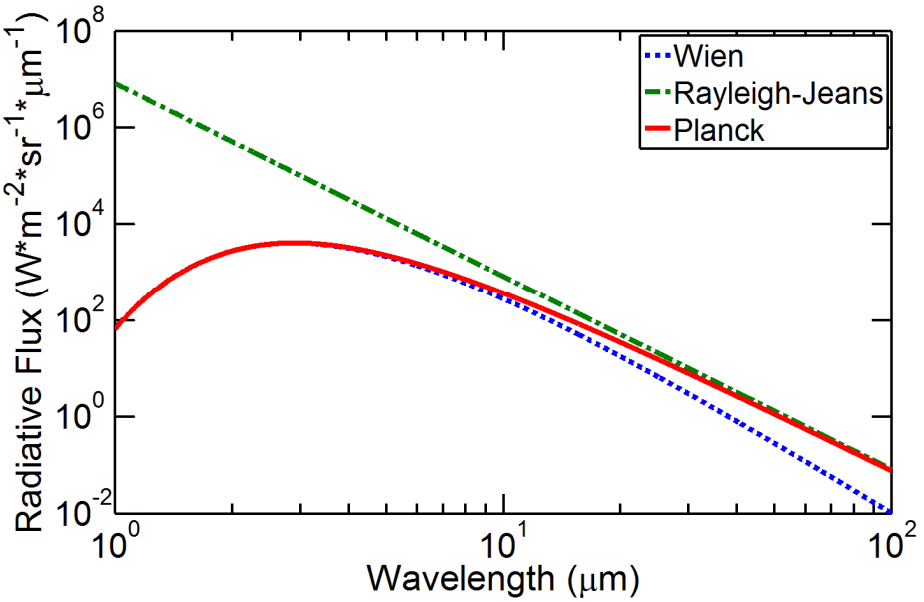

Figure 1.1: A comparison of the original empirical fitting functions developed by Wien and Rayleigh to the Planck's distribution. As shown, Wien's function correctly captures the spectral radiative heat flux in the short wavelength limit while the Rayleigh-Jeans function correctly models the long wavelength limit.

The development of Planck's distribution laid the theoretical and physical foundation for what is now considered the field of classical radiative heat transfer. In the following decades, physicists and engineers utilized Planck's law as a basis to evaluate the radiative properties for an entire catalogue of materials, to better understand radiative exchange in systems with participating and non-participating media, and to provide a series of simple formulations for view factors in systems that consist of multiple radiating surfaces.[16]

1.2 Engineering Radiative Heat Transfer

To provide a more physically intuitive understanding of the Planck's distribution, it is possible to rewrite Eq. (1.1) using more general terms that symbolize the fundamental contributions to radiative heat transfer from the perspective of photon transport.[17] For convenience, Eq. (1.1) is expressed using angular frequency, ω, instead of the wavelength, λ, as follows,

$$I_{BB}(\omega) = \frac{1}{4\pi} \cdot \underbrace{(c)}_{v_g} \cdot \underbrace{(\hbar\omega)}_{E} \cdot \underbrace{\left(e^{\hbar\omega/k_bT}-1\right)^{-1}}_{f(\omega,T)} \cdot \underbrace{\left(\omega^2\pi^{-2}c^{-3}\right)}_{D(\omega)} \tag{1.2}$$

where $\hbar = h/2\pi$ is the reduced Planck's constant. Although Eq. (1.2) corresponds to the particular case of a blackbody emitter, it is possible to more generally express radiative transport as a product of the following terms: (1) the energy of the photons, E, (2) the statistical distribution of photons, e.g. the Bose-Einstein distribution, that are thermally excited, f(ω,T), (3) the group velocity of the photons, v_g, participating in transport and (4) the number of available states photons can occupy at each frequency interval, D(ω), which is also known as the density of states (DOS). For this particular case, the factor of 4π corresponds to isotropic radiation.

The combination of the four terms identified in Eq. (1.2) thus provides a complete description of radiative heat transfer for any system. To evaluate possible paths to design and engineer radiative heat transfer, one simply needs to consider the degrees of freedom offered by each term. For instance, the energy of a photon is an intrinsic property and is determined solely by the frequency of the photon. The use of the Bose-Einstein distribution is also inherent since photons are fundamentally bosons. It is possible to alter the Bose-Einstein distribution through the introduction of a chemical potential in the exponential term such that it becomes $(\hbar\omega-\mu)/k_bT$ where μ is the chemical potential.[18] This term physically represents a deviation in the photon distribution from thermal equilibrium. For example, the luminescent emission of photons, which are typically generated electrically or optically, can be blue-shifted to higher energies when combined with heat.[18]

On the other hand, the group velocity and the density of states are dependent on the photonic dispersion, which is defined as the distribution of eigenstates that photons can occupy within a system as a function of the frequency and the wavevector, k. By definition, the group velocity is the slope of the dispersion and the photonic DOS is the number of states in the dispersion at a given frequency. Typically, the photon DOS is more sensitive to alterations in the photon dispersion than the group velocity. In general, the photon dispersion is dependent on

several properties including the material and the morphology of the emitter as well as coupling to the environment. Therefore, a number of possible approaches can be taken to design and manipulate radiative heat transfer through the photon dispersion. In the past, radiative heat transfer was designed primarily through the use of different materials and modifications to the surface roughness of these materials. However, it is also possible to change both the shape of an emitter as well as the coupling of thermal radiation to other media in the environment, which can lead to substantial changes in the photon dispersion and thus radiative heat transfer.

1.3 Organization of Thesis

Therefore, this thesis seeks to explore the modification of the photon dispersion through use of morphology and evaluate the impact on radiative heat transfer. Three topics will be presented that each focus on different regimes of radiative heat transfer including the near- and far-field regimes and the transition between both regimes. In Chapter 2, morphology effects in the form of ultra-thin films will be applied in the near-field regime to both semiconductors and optically metallic materials supporting surface polariton modes. It will be theoretically shown that depending on the nature of the material, at thin-film morphology can lead to either greater spectral selectivity, which can be useful in a thermophotovoltaics application, or greater broadband enhancement. In Chapter 3, the focus will shift towards developing an experimental technique to spectrally characterize gap-dependent variations in near-field radiative heat transfer. This is accomplished by using an inverse Otto configuration to bridge the momentum mismatch between evanescent near-field radiative modes and propagation in free space. Preliminary results will be shown that indicate this approach can be used to quantitatively evaluate near-field thermal emission spectrally. In Chapter 4, morphology effects will be used in the far-field regime in the design of a proposed infrared transparent, visibly opaque fabric (ITVOF). By leveraging both Mie and Rayleigh scattering, it will be theoretically shown that a proposed ITVOF can provide greater cooling to the human body by allowing thermal radiation emitted by the human body to directly transmit to the surrounding environments while remaining visibly opaque to the human eye. And finally, Chapter 5 will summarize the findings of this thesis and provide a future outlook on the role of morphology in radiative heat transfer.

Chapter 2

Morphological Modification of Near-field Radiative Heat Transfer

Near-field radiative heat transfer will occur when two objects are placed sufficiently close to one another such that trapped high-momentum radiative modes can evanescently tunnel from the emitter to the absorber. This tunneling provides additional channels for radiative heat exchange, which can enable radiative heat transfer in this regime to exceed the blackbody limit established by Planck's law. Due to the confined nature of these evanescent modes, near-field radiative heat transfer is especially sensitive to the photonic dispersion of the emitting and absorbing medium.
To show the impact of morphological modifications to the dispersion, this chapter will show two examples where a simple thin-film morphology is applied to evanescent modes originating from total internal reflection and surface polariton modes. First, the theoretical framework to evaluate near-field radiative heat transfer for a thin-film morphology will be discussed. This formulation then applied to thin-films of semiconductors where it will be shown that as the film dimensionality is reduced, trapped waveguide modes within the film will result in a morphologically tunable spectral selectivity. These effects are then applied to a theoretical thermophotovoltaic system to estimate the potential performance gains due to this morphological effect. A thin-film morphology will also be applied to materials supporting surface polariton modes where reductions in film thickness will lead to broadening of near-field radiative heat transfer as a result of modal splitting of the surface polariton modes supported on both sides of the film. It will be shown that this broadening can substantially enhance near-field radiative transfer for high frequency plasmonic materials even at low temperature where it is traditionally difficult to thermally excite these modes.

2.1 Near-field Radiative Heat Transfer

In classical radiative heat transfer, the exchange of thermal energy occurs via radiative emission and absorption of electromagnetic waves that propagate in free-space between objects. It is in this

far-field regime where Planck's law was developed and thus an upper bound to radiative heat transfer was established in the form of the blackbody limit.[11–14] However, this limit is not absolute as Planck himself noted that this formulation is only valid when all characteristic length in the system, including the separation distance between objects, are much larger than the wavelength of thermal radiation. When two objects are separated by distances comparable to the wavelength of thermal radiation, radiative exchange can also occur by evanescent tunneling of radiative modes confined within or near the boundaries of the emitting medium. In this so-called near-field regime, radiative heat transfer can greatly exceed the far-field blackbody limit as evanescent tunneling enables a greater number of radiative modes to participate in energy exchange.[19]

Generally, there are two primary sources of evanescent modes for near-field radiative heat transfer: total internal reflection and surface polariton modes. A conceptual illustration of each mode is shown in Fig. 2.1. Total internal reflection is perhaps the most common source, which occurs when thermal radiation emitted within a high index medium suspended in vacuum approaches the boundaries of the medium at angles larger than the critical angle. Under these conditions, thermal radiation will be reflected entirely back to the bulk of the medium. However, an evanescent field will form that exponentially decays into vacuum. If a cold medium is placed in proximity to the emitting medium, the evanescent field can couple to the cold medium, resulting in frustrated total internal reflection that enables transport of thermal energy. Nearly all materials can exhibit some degree of evanescent coupling via total internal reflection provided the material has a refractive index larger than vacuum.

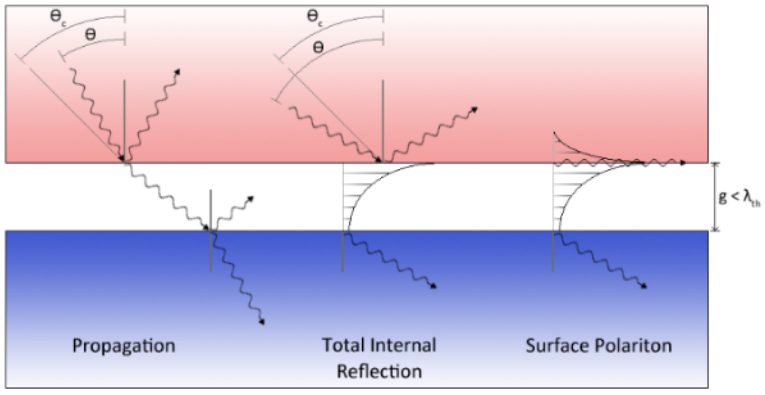

Figure 2.1: A schematic illustration of the various types of modes contributing to radiative heat transfer in the near-field regime when the gap separation is smaller than the wavelength of thermal radiation.

Surface polariton modes are electromagnetic modes that exist only at the interface of the emitting medium and vacuum. These modes are a manifestation of the coupling between photons and matter and consist of a family of modes that are distinguished by the type of quasiparticles coupled to light. Perhaps the most common types of surface polaritons encountered are surface plasmon polariton (SPP) modes, where photons are coupled to free electrons in electrically conducting materials, and surface phonon polariton (SPhP) modes, where photons are coupled to resonant vibrational modes supported in the crystal lattice of a material.[20–23] The confined nature of these modes results in a dispersion that yields a large number of radiative modes within a narrow wavelength range, as shown in Fig. 2.2. The local density of states (LDOS), which is the spatially variant form of the DOS defined in Sect. 1.2, will exhibit substantial enhancement, especially at distances close to the interface where the surface polariton mode is confined. As a result, near-field radiative heat transfer can also be dramatically enhanced.

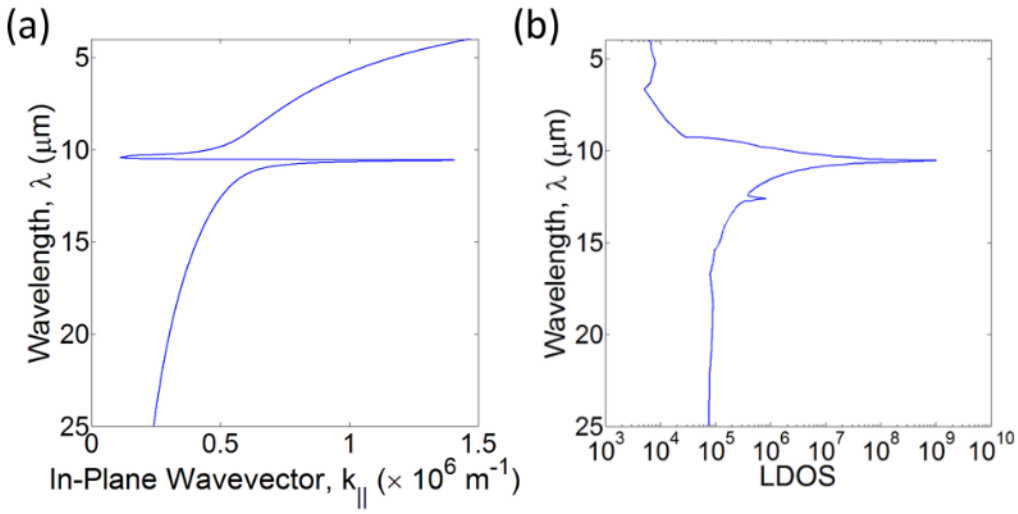

Figure 2.2: (a) The dispersion characteristics for a surface polariton mode and (b) the resulting local density of states at a distance of d = 10 nm from the interface. The particular dispersion shown corresponds to silicon carbide, which supports a SPhP mode.

The potential to exceed the bounds established by Planck's law has led to the field of near-field radiative heat transfer garnering immense fundamental interest over the past several decades with a myriad of empirical and theoretical studies to better elucidate the nature of radiative transport in this regime. Historically, the theoretical framework to model radiative heat transfer in

the near-field regime began with the development of fluctuational electrodynamics by Sergei Rytov in the 1950's, where he applied thermally fluctuating electromagnetic fields to study radiative transport between two closely spaced semi-infinite media composed of a lossy medium at finite temperature and a cold, nearly perfect mirror.[24] While the work by Rytov laid the foundation for future studies of radiative transport in this regime, it wasn't until the 1960's that there was renewed interest with the analysis of radiative heat transfer between closely spaced metal foils for thermal insulation in cryogenic fuels.[22] It was during this period of time that the first empirical studies were performed for two parallel-plate type systems and the first evidence of radiative transfer exceeding Planck's law was observed.[25–27] In 1971, Dirk Polder and Michel Van Hove developed a more generalized application of this method, which utilized fluctuating current sources based on the fluctuation dissipation theorem, in order to analyze near-field radiative heat transfer between two semi-infinite media with arbitrary dispersion.[28]

While the original theoretical description for near-field radiative heat transfer has been known since the 1970's, progress in the field was limited by the experimental and computational tools available at the time. It wasn't until the turn of the century, that the field of near-field radiative heat transfer experienced a renewed interest with advancements in nanopositioning, lithography, and computational facilities enabling more sophisticated theoretical and experimental studies. Perhaps one of the most important studies in this field occurred in 2002 by Mulet *et al.*, where it was first shown that materials supporting resonant surface waves can lead to orders of magnitude enhancement in radiative heat transfer at sub-micron gap separations.[23] In particular, polar dielectrics, such as silicon dioxide or silicon carbide, were shown to support SPhP modes in the infrared wavelength range, which not only exhibit a substantially enhanced DOS, as discussed earlier, but more crucially are readily excited thermally at room temperature.

This study was a distinct departure from earlier works that focused on metals at cryogenic temperatures and provided the catalyst to further explore the limits of radiative heat transfer in this regime. As a result, much of the advances in this field occurred only within the past decade. In lieu of the plethora of studies since this seminal work, a brief review of the theoretical methods developed to investigate more complex systems and their application to a variety of material systems will now be provided. A thorough review of experimental efforts to measure near-field radiative transfer will be provided in Ch. 3.

One of the most prevalent analytical methods to theoretically model near-field radiative transfer is still fundamentally based on the original fluctuational electrodynamics approach developed by Polder and Van Hove. However, one key modification to this formulation that came in more recent studies was the incorporation of the dyadic Green's functions, which is an operator used in field theory to determine field solutions at an arbitrary location in space relative to a point source.[23,29,30] This provided an elegant approach to simplify the formulation and expand it to other geometries where analytical solutions to the Green's functions can be found. These geometries include multilayer-1D films, spheres, cylinders, and dipoles.[23,29–43]

A variety of numerical methods have also been developed to evaluate near-field radiative heat transfer in systems with even greater geometrical complexity. The finite difference time domain (FDTD) method is perhaps the most intuitive approach where the Maxwell equations are discretized spatially and temporally, enabling simulation of arbitrary geometries based on the time evolution of emitted fields within the system. FDTD methods have primarily been used to study near-field radiative heat transfer in photonic crystals.[44–47] For systems composed of an arbitrary number of emitting and absorbing objects, a scattering matrix approach was developed, which utilizes a partial wave expansion to define a basis that fully describes the emission and subsequent scattering of electromagnetic waves by a particular object. This approach has been used to study a variety of geometrical configurations including cylinders, sphere-plate systems, and cone-plate systems.[48–55] Alternatively, a fluctuating surface current (FSC) method was also developed, which utilizes the surface-integral-equation formalism for electromagnetics in conjunction with well-established boundary element method models to model arbitrarily shaped radiating objects. The FSC method has been applied to more exotic geometrical configurations including interwoven toroids, cones, and circular plates.[51,56,57] Yet another method recently developed is the thermal discrete dipole approximation (T-DDA), where emitting objects are discretized into smaller volumes that behave as electrical dipoles. This method also enables modeling of arbitrarily shaped 3D objects and has been applied to spherical and cubic emitters.[58,59]

Based on the plethora of analytical and numerical methods developed within the past decade, a variety of material systems have since been investigated. From the seminal work by Mulet *et al*. in 2002, many studies have focused on exploring the fundamental limits and gap-dependence of near-field radiative transfer with materials supporting SPhP modes often used as a baseline reference.[23,29,30,32,35,36,38,40–42,45,58–60] Recently, the extreme near-field, where an emitter

and absorber are separated by distances less than a 1 to 2 nanometers, has been of particular interest as the fluctuational electrodynamics formalism leads to a non-physical divergence in radiative heat transfer due to non-local effects associated with this regime. Several studies have proposed corrections as well as more rigorous mechanical models to account for these non-local effects.[61–65] However, it's important to emphasize this is an exceptional case and that the fluctuational electrodynamics formalism remains valid for gap separations greater than a few nanometers.

As a natural extension to SPhP modes, SPP modes have also been studied for their use in near-field radiative heat transfer. Early works focused on noble metals, but the high frequencies where SPP resonances occur limited near-field enhancement since prohibitively high temperatures are needed to thermally excite these modes.[66–68] However, alternative plasmonic materials have been identified with lower SPP resonant frequencies that are more amenable to practically realizable temperatures. Refractory metals, such as tungsten, exhibit SPP modes in the near-infrared wavelength range, and an intrinsically high melting temperature, which have led to their proposed use in high temperature applications such as near-field enhanced thermophotovoltaics and thermoelectrics.[43,69–77] Low-loss plasmonic materials, such as transition metal nitrides and conducting oxides, have also been a focus of recent studies, especially in application to heat-assisted magnetic recording where a high near-field enhancement combined with minimal self-heating is desired.[78–80] Graphene and doped semiconductors exhibit even lower frequency SPP resonances within the mid-IR wavelength range, which can be tuned electrically or through variation in doping concentration.[81–83] These materials, along with phase change materials, such as vanadium dioxide, can potentially be used for active and passive modulation of near-field radiative heat transfer, enabling thermal rectification and thus the creation of a thermal diode.[84–88]

The application of micro- and nano-structuring to emitting and absorbing media in the near-field regime has also been investigated with structures including gratings, photonic crystals, metamaterials, and metasurfaces.[20,44–47,49,56,89–95] Gratings have been used to provide direct coupling of near-field thermal radiation to the far-field regime via momentum matching based on the grating periodicity.[90,92] Photonic crystal structures have yielded frequency selective structures based on the Bloch modes supported within the structure.[44–47,56] Anisotropic metamaterials, such as hyperbolic metamaterials have also been an area of recent focus with these structures providing broadband enhancement to radiative heat transfer in the near-field regime based on its unique hyperbolic dispersion.[20,43,89,91,93,94]

In all these studies of near-field radiative heat transfer, the underlying key that enables enhancement to radiative transfer is the dispersion of high momentum radiative modes that contribute to evanescent tunneling. As introduced in Ch. 1, this dispersion directly affects radiative heat transfer based on the group velocity and density of states. While the core focus of near-field enhancement has been based on surface polariton modes in bulk materials, several studies have shown that modifications to the morphology of the emitting and absorbing medium can yield profound effects on near-field radiative transport.[36,38,96] In an effort to better elucidate the connection between morphology, dispersion, and radiative transfer, this chapter will focus on the application of a simple thin-film morphology to materials supporting evanescent modes originating from either total internal reflection or surface polariton modes to show that even simple geometries can dramatically affect near-field radiative heat transfer.

2.2 Morphological Effects on the Photonic Dispersion

In the fields of optics and photonics, a morphologically-modified photonic dispersion has been used in a myriad of optical resonator designs to manipulate the propagation of light. For instance, Bragg mirrors, optical fibers, and Whispering Gallery mode resonators are all common examples that utilize morphological confinement across various levels of dimensionality to internally confine and shape light.[97–99] Morphological effects are also commonly used in the field of plasmonics to spectrally shape and tune the surface plasmon polariton resonance such as in the use of metallic nanorods, nanoparticles, and core-shell designs.[21] Depending on the shape and the material, changes in the morphology will typically result in the formation of discrete modes, which restrict the coupling of light to specific combinations of frequency and wavevector. Therefore, for a given material, the photon dispersion can be dramatically changed just by simply altering its shape.

To distinguish materials that support evanescent modes that originate from either total internal reflection or surface polariton resonances, one simply need to evaluate the sign of the real part of the dielectric permittivity. With this criteria in mind, a thin-film morphology is applied to semiconductors ($\mathrm{Re}(\varepsilon) > 0$) and optically metallic materials that supports surface polariton modes (($\mathrm{Re}(\varepsilon) < 0$). Despite the inherent simplicity of this morphology, the following sections will show that the dispersion characteristics can profoundly change just by simply reducing the dimensionality along one dimension.

2.2.1 Thin-film Optical Waveguides

Perhaps the simplest waveguide available is a slab waveguide, which can consist of either a high index film that is sandwiched between two low index materials to provide total internal reflection or a transparent dielectric sandwiched between two metals. In either case, three media are required to form a slab waveguide, as shown in Fig. 2.3a. The slab waveguide is a well-studied problem with a dispersion that fundamentally consists of four types of modes based on the polarization and symmetry of the modes (even or odd). If we take the case of a high index thin-film suspended in vacuum, the dispersion relation for each mode can be expressed as follows,[99]

$$\text{TM: } \sqrt{\left(\frac{\omega}{c}\right)^2\left(n_1^2-1\right) - k_z^2} = \begin{cases} \frac{k_z}{n_1^2}\tan\left(k_z d\right) & ; \text{Even} \\ -\frac{k_z}{n_1^2}\cot\left(k_z d\right) & ; \text{Odd} \end{cases} \tag{2.1}$$

$$\text{TE: } \sqrt{\left(\frac{\omega}{c}\right)^2\left(n_1^2-1\right) - k_z^2} = \begin{cases} k_z\tan\left(k_z d\right) & ; \text{Even} \\ -k_z\cot\left(k_z d\right) & ; \text{Odd} \end{cases} \tag{2.2}$$

where ω is the angular frequency, c is the vacuum speed of light, n is the refractive index, k_z is the cross-plane wave vector, and 2d is the thickness of the film. Since Eqs. (2.1) and (2.2) are transcendental equations, acquiring a solution to the dispersion requires solving Eqs. (2.1) and (2.2) using a numerical or graphical scheme.

To show the general dispersion characteristics for this type of waveguide, Eqs. (2.1) and (2.2) are solved for a film thickness of L = 100 nm, assuming the film is a lossless dielectric with a refractive index of $n_1 = 2$. The resulting dispersion in Fig. 2.3b shows the fundamental even and odd modes that are supported in the waveguide, which are bounded by the light lines for vacuum and the high index film. Based on this dispersion, a few key observations can be made on the nature of these trapped waveguide modes. First, the higher order modes exhibit a distinct cut-off frequency below which light cannot couple and thus cannot be guided using these modes. It should be noted that the first fundamental TE even mode does not exhibit a cut-off frequency, which is due to the symmetric nature of the waveguide. If the high index film is placed onto a substrate and the other medium is still vacuum, the asymmetry in this case will ensure a cut-off exists. Second, all frequencies above the cut-off frequency can be guided. Based on the shape of the dispersion for each mode, the photon DOS will increases at higher frequencies. The dispersion of each mode can also be tuned based on the thickness of the film.

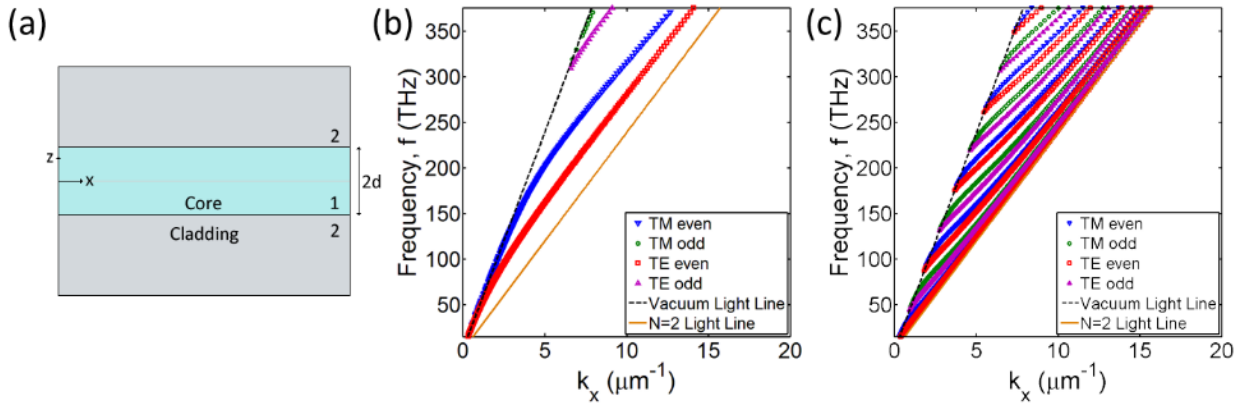

Figure 2.3: The dispersion for a high index (n = 2) slab waveguide suspended in vacuum. (a) Schematic illustration of slab waveguide system. (b) The dispersion for a 150 nm thick high index thin-film. (c) The dispersion for a 1 μm thick high index thin-film. The first fundamental modes shown in (b) and (c) do not exhibit a cut-off frequency due to the symmetric nature of the waveguide. If asymmetry is introduced, e.g. the high index thin-film is placed onto a supporting substrate, this fundamental mode will exhibit a cut-off frequency.

Generally, variations in the thickness will change the number of available modes at a given frequency as well as the cut-off frequencies for these modes. For comparison, Fig. 2.3c shows the dispersion for a film thickness of L = 1 μm. Compared to the case where L = 100 nm, a substantially greater number of modes are now supported within the waveguide. Additionally, the cut-off frequencies for these higher order modes are redshifted to lower frequencies. If the thickness of the waveguide were to increase to infinity, the dispersion will ultimately converge to the bulk limit as the number of modes at given frequency continues to increase. Based on these properties, the slab waveguide will exhibit a photon DOS that has a distinct spectral selectivity due to the combination of the resonant enhancement of the waveguide and their corresponding cut-off frequency. By simply changing the thickness, this spectral selectivity can be tuned to different frequencies. For near-field radiative heat transfer, this type of morphological manipulation can be used to spectrally shape and tune thermal and absorption.

2.2.2 Surface Polariton Waveguides

Similar to the slab waveguide discussed in Sect. 2.2.1, it is also possible to apply a thin-film morphology to materials supporting surface polariton modes, such as metals or polar dielectrics,

in order to shape their dispersion. The key difference in this case is the dispersion is shaped by the interference of the surface polariton modes supported on both interfaces of the film rather than interference of light as in the dielectric slab waveguide. The geometry of the waveguide will again consist of a thin-film suspended in vacuum. This type of geometry is also a well-studied problem with a well-defined dispersion relation that is based on two fundamental TM modes as follows,[21]

$$\text{Odd: } \tanh\left(k_{x,1}d\right) = -\frac{k_{x,2}\varepsilon_1}{k_{x,1}\varepsilon_2} \tag{2.3}$$

$$\text{Even: } \tanh\left(k_{x,1}d\right) = -\frac{k_{x,1}\varepsilon_2}{k_{x,2}\varepsilon_1} \tag{2.4}$$

where $k_{x,1}$ is the in-plane wavevector in the film, $k_{x,2}$ is the in-plane wavevector in vacuum, L is again the thickness of the film, and ε is the dielectric permittivity of each medium. Eqs. (2.3) and (2.4) are also transcendental equations, which can again be solved numerically or graphically.

To show the effect of varying the film thickness, Eqs. (2.3) and (2.4) are solved assuming the film to be a Drude metal with the following dielectric function,[21]

$$\varepsilon = \varepsilon_\infty - \frac{\omega_p^2}{\omega\left(\omega+i\gamma\right)} \tag{2.5}$$

where ω is the angular frequency, ω_p is the plasma frequency, γ is a damping coefficient, and ε_∞ is the permittivity in the high frequency limit. The following model parameters are used: $\lambda_p = 2\pi c/\omega_p = 1.1$ μm, $\gamma = 0$, and $\varepsilon_\infty = 3$. As shown in Fig. 2.4, the dispersion of the SPP mode in the bulk limit exhibits a distinct resonance characterized by the flat dispersion at approximately $\lambda = 2.25$ μm, which leads to a high photon DOS. Once the film thickness decreases to within the penetration depth of the metal, the resonant SPP mode will split due to coupling between the SPP modes on both sides of the film resulting in the creation of a high frequency odd mode and a low frequency even mode. As the film thickness decreases further, the effect of this modal splitting becomes more pronounced. The impact of this thin-film morphology is to dramatically broaden the SPP mode, especially at lower frequencies, which results in a photon DOS with a much broader enhancement compared to the narrowband enhancement in the bulk limit.

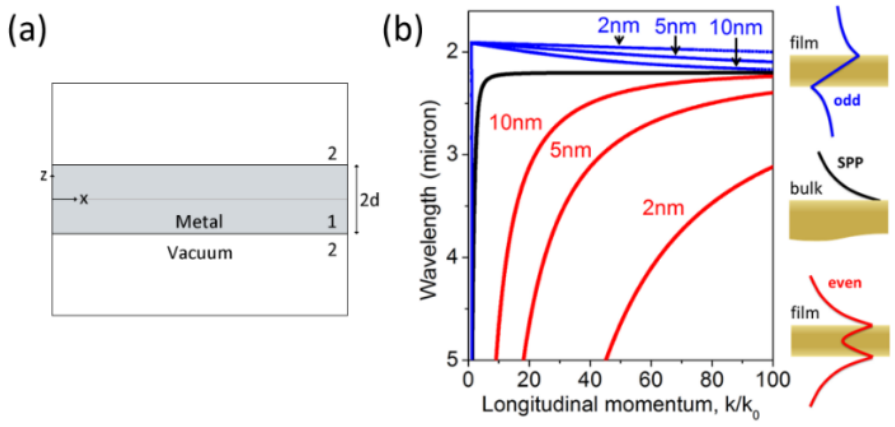

Figure 2.4: The dispersion for a thin-film metal supporting SPP modes suspended in vacuum. (a) Schematic illustration of surface polariton waveguide. (b) The dispersion for a single metal-air interface (black) and thin films with progressively smaller thicknesses. The red and blue branches correspond to the even and odd coupled SPP modes, respectively. Illustrations of the field for each mode is shown in the inset. The Drude model parameters for the metal are $\lambda_p = 1.1\mu\text{m}$, $\gamma = 0$, $\varepsilon_\infty = 3$.

Despite the same morphology, this behavior is entirely opposite to the dielectric slab waveguide, illustrating the choice of the materials, and thus the underlying physics, can lead to dramatically different morphological effects on the dispersion of the system. In this case, thin-film morphological effects applied to surface polariton modes can dramatically increase near-field radiative transfer by virtue of this broadening.

2.3 Theoretical Model for Near-field Radiative Heat Transport

In this section, a theoretical formulation is developed to investigate thin-film morphological effects on near-field radiative heat transfer. To rigorously model radiative heat transfer, a fluctuational electrodynamics formalism combined with Dyadic Green's functions will be used in application to a system comprised of a 1D multilayer stack of thin-films. In the following sections, an overview of the derivation will be provided.

2.3.1 Fluctuational Electrodynamics Formalism

In the fluctuational electrodynamics formalism, the source for thermal emission is modelled as randomly fluctuating currents to emulate the random thermal motion of charged particles, such as

electrons and ions, within the emitting medium.[23,24,37,100,101] By incorporating these fluctuating current sources into the Maxwell's equations, the resulting electromagnetic fields emitted by these sources can be found. From these field solutions, it is then possible to determine the energy flux density, or the Poynting vector, which is in essence the thermal radiation emitted by the medium. In this manner, radiative heat transfer is modelled rigorously and is applicable in both the near- and far-field regimes. For the sake of brevity, an overview of the model will be provided in this section. For a full derivation, readers can refer to earlier studies.[37,38]

The key challenge in this model is determining the field solutions resulting from a volume of fluctuating current sources. Conceptually, this can be accomplished by obtaining the field solution for each current source and utilizing the linearity of the Maxwell's equations to superimpose the fields from all sources to determine the total field emitted by the entire medium. The formulation of this approach requires use of Dyadic Green's functions, which mathematically are linear operators applied to a system described by an inhomogeneous differential equation to relate the response of the system to a source. In the case of thermal radiation, it is applied to the electromagnetic vector wave equation to determine the electric and magnetic fields due to the fluctuating current sources. Using the Dyadic Green's functions, the electric and magnetic fields can be generally expressed as follows,

$$\begin{aligned}\overline{E}\left(\overline{r},\omega\right) &= i\omega\mu_0\mu_r\int dV' \cdot \overline{\overline{G}}_e\left(\overline{r},\overline{r}',\omega\right)\cdot \overline{J}\left(\overline{r}',\omega\right)\\ \overline{H}\left(\overline{r},\omega\right) &= \int dV' \cdot \overline{\overline{G}}_h\left(\overline{r},\overline{r}',\omega\right)\cdot \overline{J}\left(\overline{r}',\omega\right)\end{aligned} \tag{2.6}$$

where $\overline{E}\left(\overline{r},\omega\right)$ and $\overline{H}\left(\overline{r},\omega\right)$ are the electric and magnetic fields, respectively, at a spatial coordinate $\overline{r}$ and angular frequency ω, $\overline{J}\left(\overline{r}',\omega\right)$ is the current at a spatial coordinate $\overline{r}'$, ω is the μ_0 is the vacuum magnetic permeability, μ_r is the relative permeability, V' is the emitter volume, $\overline{\overline{G}}_e\left(\overline{r},\overline{r}',\omega\right)$ and $\overline{\overline{G}}_h\left(\overline{r},\overline{r}',\omega\right)$ are tensors corresponding to the electric and magnetic Dyadic Green's functions, respectively, and are related by $\overline{\overline{G}}_h\left(\overline{r},\overline{r}',\omega\right)=\nabla\times\overline{\overline{G}}_e\left(\overline{r},\overline{r}',\omega\right)$. In Eq. (2.6), it is assumed the spatial coordinate r is outside the emitting volume. Given these general expressions for the electric and magnetic fields, the time-averaged Poynting vector in the z coordinate, corresponding to transport between the films, can be found as follows,

$$\left\langle \bar{S}_z\left(\bar{r},\omega\right)\right\rangle = \frac{1}{2}\cdot \mathrm{Re}\left\{ i\omega\mu_0\mu_r \int dV' \int dV'' \left[G_{e,xn}\left(\bar{r},\bar{r}',\omega\right) G^*_{h,yj}\left(\bar{r},\bar{r}'',\omega\right) - \ldots \right.\right. \tag{2.7}$$

$$\left.\left. \ldots - G_{e,yn}\left(\bar{r},\bar{r}',\omega\right) G^*_{h,xj}\left(\bar{r},\bar{r}'',\omega\right) \right] \cdot \left\langle J_n\left(\bar{r}',\omega\right)\cdot J^*_j\left(\bar{r}'',\omega\right)\right\rangle \right\}$$

where $\left\langle \bar{S}_z\left(\bar{r},\omega\right)\right\rangle$ is the time-averaged Poynting vector in the z-direction, subscripts *n* and *j* refer to a summation over the spatial coordinates at the emitter position $\bar{r}'$ and $\bar{r}''$. For example, the x-component of the Dyadic Green's function is $G_{e,xn}J_n = G_{e,xx}J_x + G_{e,xy}J_y + G_{e,xz}J_z$. The Poynting vector is equivalent to the spectral radiative heat flux $q_\omega\left(\bar{r},\omega\right)$ and will now be referred to as such for the remainder of the chapter. It can also be observed in Eq. (2.7) that the radiative heat flux is dependent on the autocorrelation of the current sources in the emitter medium. The fluctuation dissipation theorem can be used to evaluate the correlation function assuming each thermally emitting layer is at a local thermal equilibrium with a uniform temperature T, each layer is non-magnetic, and the dielectric permittivity of each layer is isotropic and local in space. Under these assumptions, the correlation function can be expressed as follows,

$$\left\langle J_i\left(r',\omega'\right) J^*_j\left(r'',\omega''\right)\right\rangle = \frac{\omega\varepsilon_0\varepsilon''_r\left(\omega\right)}{\pi}\Theta\left(\omega,T\right)\cdot\delta\left(\omega'-\omega''\right)\delta\left(r'-r''\right)\delta_{ij} \tag{2.8}$$

where ε''_r is the imaginary component of the relative permittivity for the emitting medium, ε_0 is the vacuum permittivity, $\Theta\left(\omega,T\right)$ is the mean energy of a Planck oscillator, $\delta\left(\omega'-\omega''\right)$ indicates the sources are temporally uncorrelated, $\delta\left(r'-r''\right)$ indicates the sources are spatially uncorrelated or local in the materials' optical response, and δ_{ij} implies the material is isotropic. The Planck oscillator term, $\Theta\left(\omega,T\right)$, determines the thermal distribution of modes contribution to radiative heat transfer and in its most general form includes the Bose-Einstein distribution and a zero-point energy term as follows,

$$\Theta\left(\omega,T\right) = \frac{\hbar\omega}{2} + \frac{\hbar\omega}{e^{\frac{\hbar\omega}{k_B T}} - 1} \tag{2.9}$$

where ħ is the reduced Planck constant and k_B is the Boltzmann constant. For transport calculations, the zero-point energy term is negated by emission from both the hot and cold media. Upon substituting Eqs. (2.8) into (2.7), the spectral radiative heat transfer between two media can be expressed as follows,

$$q_\omega\left(\bar{r},\omega,T\right)=\frac{\theta\left(\omega,T\right)}{\pi^2}\cdot\ldots \tag{2.10}$$

$$\ldots\cdot\underbrace{2\pi k_v^2\cdot\mathrm{Re}\left\{i\varepsilon''\int dV'\left[G_{E,xn}\left(\bar{r},\bar{r}',\omega\right)G_{H,yn}^{*}\left(\bar{r},\bar{r}',\omega\right)-G_{E,yn}\left(\bar{r},\bar{r}',\omega\right)G_{H,xn}^{*}\left(\bar{r},\bar{r}',\omega\right)\right]\right\}}_{G_T}$$

where k_v is the vacuum wave vector. Equation (2.10) represents the most general expression of radiative heat flux emitted by a medium at temperature T in this model. The term G_T is defined as the transmission function and is generally dependent on both frequency and the in-plane wavevector, k_r, of photons participating in the radiative heat exchange. This dependency on k_r will be explicitly shown in the following section. The transmission function represents the available radiative channels for energy transport between two media. Therefore, any modification of the photon dispersion imposed on the system by changing the geometry and/or material, such as thin-film morphological effects, will manifest itself directly in the transmission function.

To apply Eq. (2.10) to a 1D multilayer stack of thin-films, as illustrated in Fig. 2.5, requires determining an exact form for the Dyadic Green's functions. In the following sections, a general formulation for the 1D multilayer geometry will be shown followed by a specific solution for the case of a thin-film supported by a semi-infinite substrate.

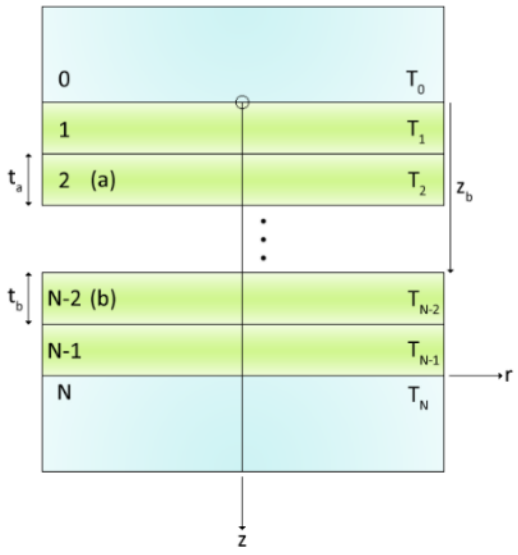

Figure 2.5: A schematic illustration for a general 1D multilayer geometry used to evaluate thin-film morphology effects in near-field radiative heat transfer. Films a and b are arbitrarily chosen to illustrate the general form of radiative heat transfer for this system.

2.3.2 Formulation for Infinite 1D Multilayer Geometry

Analytical solutions to the dyadic Green's functions for a 1D multilayer geometry have been obtained in past studies.[37,38] For this geometry, it is more convenient to express the spectral radiative heat flux in Eq. (2.10) using a cylindrical coordinate system, which allows the fundamental TE and TM polarizations to be explicitly separated in the formulation. Additionally, the volume integral can also be simplified via explicit integration of the polar angle coordinate, which under the earlier assumption of isotropy, will result in a factor of 2π. Based on these changes, the spectral radiative heat flux can be expressed as follow,

$$q_{\omega}^{ab}\left(z,\omega,T_a\right)=\frac{k_v^2\cdot\Theta\left(\omega,T_a\right)}{\pi^2}\cdot\mathrm{Re}\left\{i\varepsilon''\int dz'\int_0^{\infty}k_r dk_r\cdot\left[\underbrace{-G_{e,\theta\theta}^{ab}\left(k_r,z,z',\omega\right)G_{h,r\theta}^{ab*}\left(k_r,z,z',\omega\right)}_{TE}+\ldots\right.\right. \quad (2.11)$$

$$\left.\left.\ldots\underbrace{G_{e,rr}^{ab}\left(k_r,z,z',\omega\right)G_{h,\theta r}^{ab*}\left(k_r,z,z',\omega\right)+G_{e,rz}^{ab}\left(k_r,z,z',\omega\right)G_{h,\theta z}^{ab*}\left(k_r,z,z',\omega\right)}_{TM}\right]\right\}$$

where $q_{\omega}^{ab}\left(z,\omega,T_a\right)$ is the radiative heat flux from layer *a* to layer *b*, k_r is the in-plane wavevector, z is a position in film *b*, and z' is the source position in film *a*. Explicit expressions for the product of Dyadic Green's functions can be found by observing that in this 1D multilayer geometry, four types of waves can exist based on the direction of propagation in film *b* (+/- z) and the direction of emission in film *a* (+/- z'). In a similar manner to the formulation of the transfer matrix method, these four waves form a basis with amplitudes that are dependent on the reflection and transmission of thermal radiation at interfaces separating the two layers. The electric and magnetic Dyadic Green's functions can thus be written in terms of these four waves. The subsequent products of the Dyadic Green's functions shown in Eq. (2.11) for the TM polarization will be as follows,

$$
\begin{aligned}
&G_{e,rr}^{ab}G_{h,\theta r}^{ab*}\left(k_r,z=z_b,\omega\right)+G_{e,rz}^{ab}G_{h,\theta z}^{ab*}\left(k_r,z=z_b,\omega\right)=\ldots\\
&\quad\ldots=\frac{ik_{z,b}k_b^*}{8\mathrm{Re}\left(k_{z,a}\right)\mathrm{Im}\left(k_{z,a}\right)k_b\left|k_a\right|^2\left|k_{z,a}\right|^2}\cdot\ldots\\
&\quad\ldots\cdot\Big[\mathrm{Re}\left(k_{z,a}\right)\left(e^{2\mathrm{Im}\left(k_{z,a}\right)t_a}-1\right)\left(\left|k_{z,a}\right|^2+k_r^2\right)\cdot\left(-\left|A_b^{TM}\right|^2-A_b^{TM}B_b^{TM*}+A_b^{TM*}B_b^{TM}+\left|B_b^{TM}\right|^2\right)\cdot\ldots\\
&\quad\ldots\cdot i\cdot\mathrm{Im}\left(k_{z,a}\right)\left(e^{-i\cdot2\mathrm{Re}\left(k_{z,a}\right)t_a}-1\right)\left(\left|k_{z,a}\right|^2-k_r^2\right)\cdot\left(A_b^{TM}C_b^{TM*}+A_b^{TM}D_b^{TM*}-B_b^{TM}C_b^{TM*}-B_b^{TM}D_b^{TM*}\right)\cdot\ldots\\
&\quad\ldots\cdot i\cdot\mathrm{Im}\left(k_{z,a}\right)\left(1-e^{i\cdot2\mathrm{Re}\left(k_{z,a}\right)t_a}\right)\left(\left|k_{z,a}\right|^2-k_r^2\right)\cdot\left(A_b^{TM*}C_b^{TM}+B_b^{TM*}C_b^{TM}-A_b^{TM*}D_b^{TM}-B_b^{TM*}D_b^{TM}\right)\cdot\ldots\\
&\quad\ldots\cdot\mathrm{Re}\left(k_{z,a}\right)\left(1-e^{-2\mathrm{Im}\left(k_{z,a}\right)t_a}\right)\left(\left|k_{z,a}\right|^2+k_r^2\right)\cdot\left(-\left|C_b^{TM}\right|^2-C_b^{TM}D_b^{TM*}+C_b^{TM*}D_b^{TM}+\left|D_b^{TM}\right|^2\right)\Big]
\end{aligned}
\tag{2.12}
$$

where t_a is the thickness of film *a* and $k_{z,a}$ and $k_{z,b}$ are the cross-plane wave vectors. Coefficients A and B correspond to emission in film *a* in the +z' direction resulting in +z and –z propagation in film *b*, respectively. Likewise, coefficients C and D correspond to emission in film *a* in the –z' direction resulting in +z and –z propagation into film *b*, respectively. Note that Eq. (2.12) was obtained by integrating over the z' coordinate, assuming a finite thickness t_a. Also, the position z = z_b refers to the first interface of film *b* before propagation through the film. A similar expression can be found for the TE polarization as follows,

$$
\begin{aligned}
&G_{e,\theta\theta}^{ab}G_{h,r\theta}^{ab*}\left(k_r,z=z_b,\omega\right)=\ldots\\
&\quad\ldots=\frac{ik_{z,b}^*}{8\mathrm{Re}\left(k_{z,a}\right)\mathrm{Im}\left(k_{z,a}\right)\left|k_{z,a}\right|^2}\cdot\ldots\\
&\quad\ldots\cdot\Big[\mathrm{Re}\left(k_{z,a}\right)\left(e^{2\mathrm{Im}\left(k_{z,a}\right)t_a}-1\right)\cdot\left(\left|A_b^{TE}\right|^2-A_b^{TE}B_b^{TE*}+A_b^{TE*}B_b^{TE}-\left|B_b^{TE}\right|^2\right)\cdot\ldots\\
&\quad\ldots\cdot i\cdot\mathrm{Im}\left(k_{z,a}\right)\left(e^{-i\cdot2\mathrm{Re}\left(k_{z,a}\right)t_a}-1\right)\cdot\left(A_b^{TE}C_b^{TE*}-A_b^{TE}D_b^{TE*}+B_b^{TE}C_b^{TE*}-B_b^{TE}D_b^{TE*}\right)\cdot\ldots\\
&\quad\ldots\cdot i\cdot\mathrm{Im}\left(k_{z,a}\right)\left(1-e^{i\cdot2\mathrm{Re}\left(k_{z,a}\right)t_a}\right)\cdot\left(A_b^{TE*}C_b^{TE}-B_b^{TE*}C_b^{TE}+A_b^{TE*}D_b^{TE}-B_b^{TE*}D_b^{TE}\right)\cdot\ldots\\
&\quad\ldots\cdot\mathrm{Re}\left(k_{z,a}\right)\left(1-e^{-2\mathrm{Im}\left(k_{z,a}\right)t_a}\right)\cdot\left(\left|C_b^{TE}\right|^2-C_b^{TE}D_b^{TE*}+C_b^{TE*}D_b^{TE}-\left|D_b^{TE}\right|^2\right)\Big]
\end{aligned}
\tag{2.13}
$$

The evaluation of coefficients A, B, C, and D involves a combination of the transfer matrix method and the scattering matrix method. These two approaches are used in an effort to minimize potential numerical instabilities that arise from terms with exponential growth. By combining these two approaches, a recursive formulation is developed that enables the derivation of analytical expressions for the amplitude coefficients. It should also be mentioned that in this geometry, the view factor is assumed equal to 1.

2.3.3 Solutions for a Single Thin-film Supported by a Semi-Infinite Substrate

The combination of Eqs. (2.12) and (2.13) thus provides a general formulation to evaluate radiative heat transfer for an arbitrary number of layers within the system. In order to facilitate the investigation of thin-film morphological effects on near-field radiative heat transfer, a simpler system is adopted, which consists of a single thin-film supported by a semi-infinite substrate on both the hot and cold sides separated by a finite gap in vacuum, as shown in Fig. 2.6. The choice to use a single thin-film on both sides of the system enables modification of not only thermal emission, but absorption as well by varying the respective thicknesses of each film. In this section, exact solutions for this particular system will be determined by using the recursive formulation described in the previous section to derive explicit expressions for the A, B, C, and D coefficients.

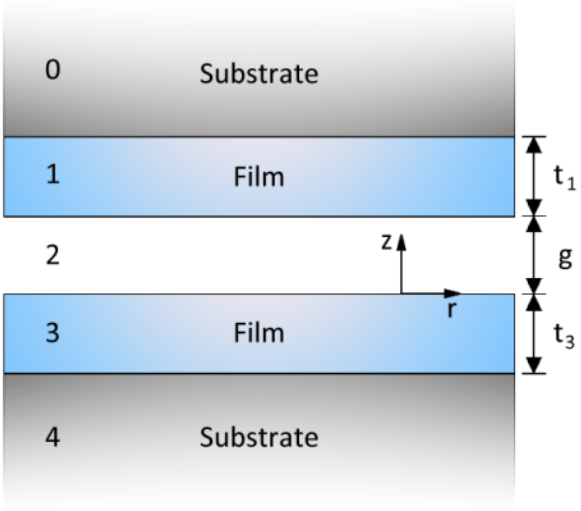

Figure 2.6: A schematic illustration of the single thin-film, single substrate system considered for derivation of exact solutions to the formulation presented in Eqs. (2.12) and (2.13).

To maintain generality in this formulation, the supporting substrates can also emit and absorb. As a result, it would be useful to keep track of where emission and absorption occurs within the system, e.g. emission or absorption by the film or substrate. The following derivations will thus consist of developing a complete set of equations to isolate emission and absorption for each component in the system. We start by considering the radiative heat flux from film 1 transferred to the first interface of film 3. The coefficients will consist of the following,

$$
\begin{aligned}
A_3^{TM,TE} &= \frac{e^{ik_{z,1}t_1}e^{ik_{z,2}g}t_{21}^{TM,TE}t_{23}^{TM,TE}}{\left(1+r_{21}^{TM,TE}r_{10}^{TM,TE}e^{2ik_{z,1}t_1}\right)\left(1+r_{23}^{TM,TE}r_{34}^{TM,TE}e^{2ik_{z,3}t_3}\right)\left(1-r_{20}^{TM,TE}r_{24}^{TM,TE}e^{2ik_{z,2}g}\right)} \\
B_3^{TM,TE} &= r_{34}^{TM,TE}e^{2ik_{z,3}t_3}\cdot A_3^{TM,TE} \\
C_3^{TM,TE} &= r_{34}^{TM,TE}\cdot A_3^{TM,TE} \\
D_3^{TM,TE} &= \left(r_{34}^{TM,TE}\right)^2 e^{2ik_{z,3}t_3}\cdot A_3^{TM,TE}
\end{aligned}
\tag{2.14}
$$

where g is the gap separation between the hot and cold media, t_1 and t_3 are the thickness of layers 1 and 3, respectively, and r_{ij} and t_{ij} are the Fresnel reflection and transmission coefficients for either an interface ($|i-j| = 1$) or a slab ($|i-j| = 2$). For TM and TE polarizations, respectively, the Fresnel coefficients for an interface are,

$$
\begin{aligned}
r_{ij}^{TM} &= \frac{\varepsilon_j k_{z,i}-\varepsilon_i k_{z,j}}{\varepsilon_j k_{z,i}+\varepsilon_i k_{z,j}} \\
t_{ij}^{TM} &= \frac{2k_{z,i}\sqrt{\varepsilon_i}\sqrt{\varepsilon_j}}{\varepsilon_j k_{z,i}+\varepsilon_i k_{z,j}}
\end{aligned}
\tag{2.15}
$$

$$
\begin{aligned}
r_{ij}^{TE} &= \frac{k_{z,i}-k_{z,j}}{k_{z,i}+k_{z,j}} \\
t_{ij}^{TE} &= \frac{2k_{z,i}}{k_{z,i}+k_{z,j}}
\end{aligned}
\tag{2.16}
$$

where ε_i and ε_j is the complex dielectric permittivity for layers i and j, respectively. Likewise, for a thin slab with index j, the reflection and transmission coefficients are,

$$
\begin{aligned}
r_{ik}^{TM,TE} &= \frac{r_{ij}^{TM,TE}+r_{jk}^{TM,TE}e^{2ik_{z,j}t_j}}{1+r_{ij}^{TM,TE}r_{jk}^{TM,TE}e^{2ik_{z,j}t_j}} \\
t_{ik}^{TM,TE} &= \frac{t_{ij}^{TM,TE}t_{jk}^{TM,TE}e^{ik_{z,j}t_j}}{1+r_{ij}^{TM,TE}r_{jk}^{TM,TE}e^{2ik_{z,j}t_j}}
\end{aligned}
\tag{2.17}
$$

Substituting Eqs. (2.14)-(2.17) into Eqs. (2.11)-(2.13) combined with extensive mathematical manipulation will yield the following simplified expression for the spectral radiative heat flux from film 1 entering film 3 split in terms of free space propagation modes and evanescent modes in accordance to the value of the in-plane wave vector relative to the vacuum wavevector,

$$q^{1\to34}_{\omega,prop}\left(\omega,T_1\right)=\frac{\theta\left(\omega,T_1\right)}{\pi^2}\int_0^{k_v}k_r dk_r\left\{\frac{\left[\left[1-\left|r^{TE}_{20}\right|^2-\left|t^{TE}_{20}\right|^2\cdot Re\left(\frac{k^{*}_{z,0}k^{'}_{z,2}}{\left|k_{z,2}\right|^2}\right)\right]\cdot\left[1-\left|r^{TE}_{24}\right|^2\right]\right]}{4\left|1-r^{TE}_{20}r^{TE}_{24}e^{2ik^{'}_{z,2}g}\right|^2}+\ldots\right.$$

$$\left.\ldots+\frac{\left[\left[1-\left|r^{TM}_{20}\right|^2-\left|t^{TM}_{20}\right|^2\cdot Re\left(\frac{k_{z,0}k^{*}_{0}k^{'}_{z,2}}{k_0\left|k_{z,2}\right|^2}\right)\right]\cdot\left[1-\left|r^{TM}_{24}\right|^2\right]\right]}{4\left|1-r^{TM}_{20}r^{TM}_{24}e^{2ik^{'}_{z,2}g}\right|^2}\right\} \tag{2.18}$$

$$q^{1\to34}_{\omega,eva}\left(\omega,T_1\right)=\frac{\theta\left(\omega,T_1\right)}{\pi^2}\int_{k_v}^{\infty}k_r dk_r e^{-2k^{''}_{z,2}g}\left\{\frac{\left[\left[Im\left(r^{TE}_{20}\right)-\frac{\left|t^{TE}_{20}\right|^2}{2}\cdot Re\left(\frac{k^{*}_{z,0}k^{''}_{z,2}}{\left|k_{z,2}\right|^2}\right)\right]\cdot\left[Im\left(r^{TE}_{24}\right)\right]\right]}{\left|1-r^{TE}_{20}r^{TE}_{24}e^{-2k^{''}_{z,2}g}\right|^2}+\ldots\right.$$

$$\left.\ldots+\frac{\left[\left[Im\left(r^{TM}_{20}\right)-\frac{\left|t^{TM}_{20}\right|^2}{2}\cdot Re\left(\frac{k_{z,0}k^{*}_{0}k^{''}_{z,2}}{k_0\left|k_{z,2}\right|^2}\right)\right]\cdot\left[Im\left(r^{TM}_{24}\right)\right]\right]}{\left|1-r^{TM}_{20}r^{TM}_{24}e^{-2k^{''}_{z,2}g}\right|^2}\right\} \tag{2.19}$$

where the superscripts ‘ and ‘’ correspond to the real and imaginary components of the wavevector, respectively. The factors of k_z in the transmittance terms for film 1 are due to the generality of the system where an arbitrary substrate is assumed to support the thin-films. If the thin-films are suspended in vacuum, these factors will cancel to equal unity in correspondence to earlier studies.[36,38]

It is important to observe that Eqs. (2.18) and (2.19) actually provides the heat from film 1 that is coupled to film 3 and substrate 4. It does not consider the portion of energy that leaves film 3 due to transmission. To account for this loss, the A, B, C, and D coefficients must be re-derived for the case of heat flux originating from film 1 entering substrate 4. Following the same procedure as before, these coefficients will be as follows,

$$
\begin{aligned}
A_4^{TM,TE} &= \frac{e^{ik_{z,1}t_1}e^{ik_{z,2}g}e^{ik_{z,3}t_3}t_{21}^{TM,TE}t_{23}^{TM,TE}t_{34}^{TM,TE}}{\left(1+r_{21}^{TM,TE}r_{10}^{TM,TE}e^{2ik_{z,1}t_1}\right)\left(1+r_{23}^{TM,TE}r_{34}^{TM,TE}e^{2ik_{z,3}t_3}\right)\left(1-r_{20}^{TM,TE}r_{24}^{TM,TE}e^{2ik_{z,2}g}\right)} \\
B_4^{TM,TE} &= 0 \\
C_4^{TM,TE} &= r_{34}^{TM,TE}\cdot A_4^{TM,TE} \\
D_4^{TM,TE} &= 0
\end{aligned}
\tag{2.20}
$$

where $B_4 = D_4 = 0$ since there will be no backwards traveling waves in substrate 4 by virtue of being semi-infinite. Upon substituting Eq. (2.20) into Eqs. (2.11)-(2.13) as before, the resulting spectral radiative heat flux for free space propagating modes and evanescent modes will be,

$$
\begin{aligned}
q_{\omega,prop}^{1\to4}\left(\omega,T_1\right) = \frac{\theta\left(\omega,T_1\right)}{\pi^2}\int_0^{k_v} k_r dk_r \Bigg\{ & \frac{\left[1-\left|r_{20}^{TE}\right|^2-\left|t_{20}^{TE}\right|^2\cdot\mathrm{Re}\left(\frac{k_{z,0}^{*}k_{z,2}^{'}}{\left|k_{z,2}\right|^2}\right)\right]\cdot\left[\left|t_{24}^{TE}\right|^2\cdot\mathrm{Re}\left(\frac{k_{z,4}^{*}k_{z,2}^{'}}{\left|k_{z,4}\right|^2}\right)\right]}{4\left|1-r_{20}^{TE}r_{24}^{TE}e^{2ik_{z,2}^{'}g}\right|^2}+\ldots \\
\ldots+ & \frac{\left[1-\left|r_{20}^{TM}\right|^2-\left|t_{20}^{TM}\right|^2\cdot\mathrm{Re}\left(\frac{k_{z,0}k_0^{*}k_{z,2}^{'}}{k_0\left|k_{z,2}\right|^2}\right)\right]\cdot\left[\left|t_{24}^{TM}\right|^2\cdot\mathrm{Re}\left(\frac{k_{z,4}k_4^{*}k_{z,2}^{'}}{k_4\left|k_{z,2}\right|^2}\right)\right]}{4\left|1-r_{20}^{TM}r_{24}^{TM}e^{2ik_{z,2}^{'}g}\right|^2}\Bigg\}
\end{aligned}
\tag{2.21}
$$

$$
\begin{aligned}
q_{\omega,eva}^{1\to4}\left(\omega,T_1\right) = \frac{\theta\left(\omega,T_1\right)}{\pi^2}\int_{k_v}^{\infty} k_r dk_r e^{-2k_{z,2}^{''}g} \Bigg\{ & \frac{\left[\mathrm{Im}\left(r_{20}^{TE}\right)-\frac{\left|t_{20}^{TE}\right|^2}{2}\cdot\mathrm{Re}\left(\frac{k_{z,0}^{*}k_{z,2}^{''}}{\left|k_{z,2}\right|^2}\right)\right]\cdot\left[\frac{\left|t_{24}^{TE}\right|^2}{2}\cdot\mathrm{Re}\left(\frac{k_{z,4}^{*}k_{z,2}^{''}}{\left|k_{z,2}\right|^2}\right)\right]}{\left|1-r_{20}^{TE}r_{24}^{TE}e^{-2k_{z,2}^{''}g}\right|^2}+\ldots \\
\ldots+ & \frac{\left[\mathrm{Im}\left(r_{20}^{TM}\right)-\frac{\left|t_{20}^{TM}\right|^2}{2}\cdot\mathrm{Re}\left(\frac{k_{z,0}k_0^{*}k_{z,2}^{''}}{k_0\left|k_{z,2}\right|^2}\right)\right]\cdot\left[\frac{\left|t_{24}^{TM}\right|^2}{2}\cdot\mathrm{Re}\left(\frac{k_{z,4}k_4^{*}k_{z,2}^{''}}{k_4\left|k_{z,2}\right|^2}\right)\right]}{\left|1-r_{20}^{TM}r_{24}^{TM}e^{-2k_{z,2}^{''}g}\right|^2}\Bigg\}
\end{aligned}
\tag{2.22}
$$

To isolate the radiative heat flux from film 1 to film 3, a simple subtraction is needed using Eqs. (2.18)-(2.19) and Eqs. (2.21)-(2.22) as follows,

$$q_{\omega,prop}^{1\to3}\left(\omega,T_1\right)=\frac{\theta\left(\omega,T_1\right)}{\pi^2}\int_0^{k_v}k_r dk_r\left\{\frac{\left[1-\left|r_{20}^{TE}\right|^2-\left|t_{20}^{TE}\right|^2\cdot\mathrm{Re}\left(\frac{k_{z,0}^{*}k_{z,2}^{'}}{\left|k_{z,2}\right|^2}\right)\right]\cdot\left[1-\left|r_{24}^{TE}\right|^2-\left|t_{24}^{TE}\right|^2\cdot\mathrm{Re}\left(\frac{k_{z,4}^{*}k_{z,2}^{'}}{\left|k_{z,4}\right|^2}\right)\right]}{4\left|1-r_{20}^{TE}r_{24}^{TE}e^{2ik_{z,2}^{'}g}\right|^2}+\ldots\right.$$

$$\left.\ldots+\frac{\left[1-\left|r_{20}^{TM}\right|^2-\left|t_{20}^{TM}\right|^2\cdot\mathrm{Re}\left(\frac{k_{z,0}k_0^{*}k_{z,2}^{'}}{k_0\left|k_{z,2}\right|^2}\right)\right]\cdot\left[1-\left|r_{24}^{TM}\right|^2-\left|t_{24}^{TM}\right|^2\cdot\mathrm{Re}\left(\frac{k_{z,4}k_4^{*}k_{z,2}^{'}}{k_4\left|k_{z,2}\right|^2}\right)\right]}{4\left|1-r_{20}^{TM}r_{24}^{TM}e^{2ik_{z,2}^{'}g}\right|^2}\right\} \tag{2.23}$$

$$q_{\omega,eva}^{1\to3}\left(\omega,T_1\right)=\frac{\theta\left(\omega,T_1\right)}{\pi^2}\int_{k_v}^{\infty}k_r dk_r e^{-2k_{z,2}^{''}g}\left\{\frac{\left[\mathrm{Im}\left(r_{20}^{TE}\right)-\frac{\left|t_{20}^{TE}\right|^2}{2}\cdot\mathrm{Re}\left(\frac{k_{z,0}^{*}k_{z,2}^{''}}{\left|k_{z,2}\right|^2}\right)\right]\cdot\left[\mathrm{Im}\left(r_{24}^{TE}\right)-\frac{\left|t_{24}^{TE}\right|^2}{2}\cdot\mathrm{Re}\left(\frac{k_{z,4}^{*}k_{z,2}^{''}}{\left|k_{z,2}\right|^2}\right)\right]}{\left|1-r_{20}^{TE}r_{24}^{TE}e^{-2k_{z,2}^{''}g}\right|^2}+\ldots\right.$$

$$\left.\ldots+\frac{\left[\mathrm{Im}\left(r_{20}^{TM}\right)-\frac{\left|t_{20}^{TM}\right|^2}{2}\cdot\mathrm{Re}\left(\frac{k_{z,0}k_0^{*}k_{z,2}^{''}}{k_0\left|k_{z,2}\right|^2}\right)\right]\cdot\left[\mathrm{Im}\left(r_{24}^{TM}\right)-\frac{\left|t_{24}^{TM}\right|^2}{2}\cdot\mathrm{Re}\left(\frac{k_{z,4}k_4^{*}k_{z,2}^{''}}{k_4\left|k_{z,2}\right|^2}\right)\right]}{\left|1-r_{20}^{TM}r_{24}^{TM}e^{-2k_{z,2}^{''}g}\right|^2}\right\} \tag{2.24}$$

The combination of Eqs. (2.21)-(2.24) thus provides a set of equations to describe thermal emission from a hot thin-film, which is absorbed by a cold thin-film and a supporting substrate. However, to completely describe the system in Fig. 2.6, it is also necessary to consider thermal emission from the supporting substrate of the hot emitter.

In order to isolate this contribution, it is possible to make use of the formulation for radiative heat transfer between two semi-infinite media. Despite the presence of thin-films, previous studies have proven that the formulation for two semi-infinite media can still be used to calculate the total radiative heat transfer for a hot emitter and cold absorber composed of an arbitrary number of layers assuming the hot and cold side temperatures are uniform across their respective layers. The spectral radiative heat flux in this case will consist of the following,

$$q_{\omega,prop}^{01\to34}\left(\omega,T_1\right)=\frac{\theta\left(\omega,T_1\right)}{\pi^2}\int_0^{k_v}k_r dk_r\left\{\frac{\left[1-\left|r_{20}^{TE}\right|^2\right]\cdot\left[1-\left|r_{24}^{TE}\right|^2\right]}{4\left|1-r_{20}^{TE}r_{24}^{TE}e^{2ik_{z,2}'g}\right|^2}+\frac{\left[1-\left|r_{20}^{TM}\right|^2\right]\cdot\left[1-\left|r_{24}^{TM}\right|^2\right]}{4\left|1-r_{20}^{TM}r_{24}^{TM}e^{2ik_{z,2}'g}\right|^2}\right\} \tag{2.25}$$

$$q_{\omega,eva}^{01\to34}\left(\omega,T_1\right)=\frac{\theta\left(\omega,T_1\right)}{\pi^2}\int_{k_v}^{\infty}k_r dk_r e^{-2k_{z,2}''g}\left\{\frac{\left[\mathrm{Im}\left(r_{20}^{TE}\right)\right]\cdot\left[\mathrm{Im}\left(r_{24}^{TE}\right)\right]}{\left|1-r_{20}^{TE}r_{24}^{TE}e^{-2k_{z,2}''g}\right|^2}+\frac{\left[\mathrm{Im}\left(r_{20}^{TM}\right)\right]\cdot\left[\mathrm{Im}\left(r_{24}^{TM}\right)\right]}{\left|1-r_{20}^{TM}r_{24}^{TM}e^{-2k_{z,2}''g}\right|^2}\right\} \tag{2.26}$$

where it is assumed the temperature of substrate 0 is equal to the temperature of film 1. The reflection coefficients represent the total reflectance of the thin-film and substrate for the hot and cold sides. By combining Eqs. (2.25)-(2.26) with Eqs. (2.21)-(2.24), it is possible to obtain the absorption in thin-film 3 and substrate 4 due to thermal emission from substrate 0. With Eqs. (2.21)-(2.26), we now have a complete set of equations to describe radiative heat transport for a system composed of a single thin-film supported by a substrate on both the hot and cold sides. This formulation will serve as the foundation in the following sections to explore thin-film morphological effects on near-field radiative heat transfer using dielectrics and metals.

As will become evident in the following sections, the evaluation of radiative heat transfer between the hot and cold sides will require determining the net radiative heat flux transferred into a particular layer. Generally, this will be calculated as the difference between the incoming and outgoing Poynting vectors for that layer. For example, the net heat flux into film 3 is determined as follows,

$$q_{\omega,net}^{01\to3}=q_{\omega}^{01\to3}-q_{\omega}^{3\to01}=q_{\omega}^{0\to3}+q_{\omega}^{1\to3}-q_{\omega}^{3\to1}-q_{\omega}^{3\to0} \tag{2.27}$$

where each heat flux term is calculated using the derived formulation.

2.4 Morphological Effects on Dielectrics[†]

Based on the system configuration shown in Fig. 2.6, morphologically induced effects on radiative heat transfer will occur via thermal emission and absorption from the thin-films on the hot and cold sides, respectively. As discussed in Sect. 2.2, depending on the materials chosen for the thin-films, such as a dielectric or metal, these morphological effects on the photon dispersion can differ substantially resulting in either greater spectral selectivity or greater spectral broadening, respectively.

In this section, thin-film dielectrics will be the primary focus. As discussed in Sect. 2.2.1, support discrete waveguide modes that will modify the intrinsic photon dispersion depending on the thickness and refractive index of the films. The modified dispersion will result in the spectral shaping of thermal emission and absorption in analog to the use of electronic quantum confinement effects in quantum wells.[102,103] In lieu of the electronic comparison, we define this photonic approach henceforth as the 'thermal well' effect. To investigate the thermal well effect, thin-film semiconductors are used, which optically behave like dielectrics with different levels of loss depending on the photon energy relative to its electronic band gap. This intrinsic variation in optical losses between super-band gap and sub-band gap photons can lead to much greater spectral selectivity when combined with optical morphological effects. However, it should be emphasized that these morphological effects are general and can also be applied to wide-band gap insulting materials for the purposes of modifying sub-band gap thermal emission and absorption as well.

As an example to illustrate the utility of the thermal well effect, the system defined in Fig. 2.7 is used in a theoretical thermophotovoltaic (TPV) system, which consist of a thin-film emitter and a thin-film PV cell as the absorber. To provide context on the choice of materials used to evaluate the thermal well effect, a brief overview on TPV systems will be provided in the following section.

[†]Adapted from J. K. Tong, W.-C. Hsu, Y. Huang, S. V. Boriskina, and G. Chen, "Thin-film 'Thermal Well' Emitters and Absorbers for High-Efficiency Thermophotovoltaics," Scientific Reports, Vol. 5, 10661 (2015). Copyright 2015 Nature Publishing Group.

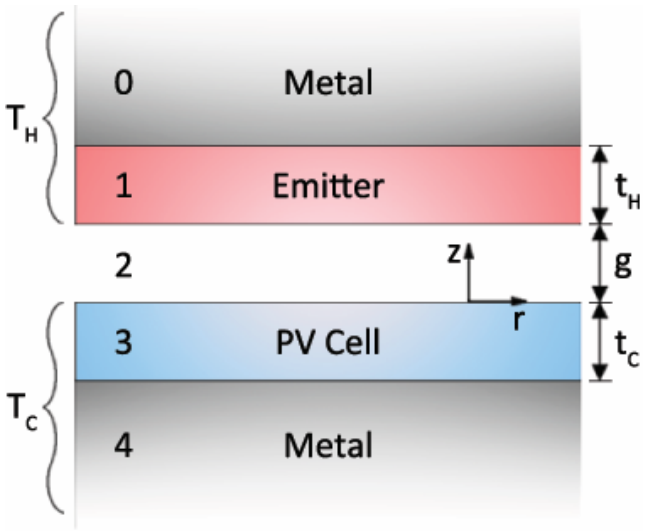

Figure 2.7: The TPV system consists of a thin-film emitter and a thin-film PV cell. Both films are placed onto semi-infinite back reflectors.

2.4.1 Overview of Thermophotovoltaic Systems

A TPV system is a unique type of heat engine that directly converts thermal energy to electricity.[104–107] Typical TPV systems consist of a thermal emitter and a photovoltaic cell in which there are no moving parts allowing for a compact power generation platform. In theory, TPV systems can convert radiative energy from the thermal emitter to electricity at an efficiency approaching the Carnot limit for monochromatic radiation and can be used for both waste heat and solar energy harvesting.[108–116] However, the efficiency achieved in practical TPV systems has been limited by the mismatch between the thermal emission spectra and the PV cell absorption, thermalization of high energy charge carriers, and non-radiative recombination losses which are typically high in narrow band gap PV cells used for TPV.

To improve the efficiency, past studies have generally followed two approaches: (1) using intermediate frequency filters, such as rugate filters, photonic crystal filters, and plasma reflectors, which recycle low energy photons by returning them back to the thermal emitter and (2) engineering the emitter using rare-earth dopants, plasmonic metamaterials, and photonic crystals to achieve spectrally selective emission and angular selectivity.[31,117–126] By utilizing these approaches and minimizing system losses, several recent studies have demonstrated significant improvement to overall system efficiency for combustion and solar-based TPV systems.[127–130] In addition, previous studies have also exhibited TPV efficiencies, defined as the electrical power

output divided by the net radiative heat input from the emitter to the PV cell, of nearly 24% by utilizing ternary, quaternary, and multi-quantum well cells at emitter temperatures of 1300-1500 K.[131–134] In parallel, other theoretical studies proposed utilizing the strong near-field coupling of electromagnetic fields between the emitter and PV cell separated by nanometer gaps to improve the efficiency and power density of TPV systems.[74,81,135–140] However, the proposed designs for high-efficiency near-field TPV systems required extremely narrow gap separations between the emitter and the PV cell, ultra-low band gap PV cells, and high emitter temperatures limiting practical realization.

While these approaches have certainly led to significant advances in the development of TPV systems, there is still a need for further improvements to the spectral selectivity. It is in this realm that the thermal well effect can provide a conceptually new approach towards improving the spectral selectivity of a TPV system by morphologically manipulating the optical properties of the emitter and the absorber.

2.4.2 System Configuration

To apply the thermal well effect to a potential TPV system, thin-film semiconductors were chosen with an electronic band gap that will spectrally overlap with the Planck oscillator term in Eqs. (2.21)-(2.26) at a maximum emitter temperature of T_H = 1000 K. Both of the thin-films are supported by semi-infinite metallic back reflectors. Back reflectors made of an ideal perfect metal and a real metal are considered. The use of a perfect metal eliminates emission and absorption in the substrate thus providing a way to evaluate the morphological effects on thermal emission and absorption due to only the thermal well effect. These results can then be directly compared to the case of a bulk emitter and absorber to highlight the benefits of morphological structuring.

Several configurations are evaluated to assess the potential of using thin-film emitters and absorbers to improve the performance of a TPV system. For all cases, a GaSb PV cell with a band gap of 0.726 eV is used, which is conventional in many TPV platforms.[141–144] To demonstrate the thermal well concept, we chose a thin-film of Ge as the thermal emitter. Ge is a high refractive index semiconductor with a band gap of 0.7 eV. The material absorption in Ge at wavelengths above the band gap naturally provides strong emission channels by virtue of Kirchoff's law.

A bulk W emitter was also considered in order to compare thermal emission spectra of waveguide modes confined in Ge thermal wells with previously studied emission of surface

plasmon polariton (SPP) modes thermally excited on the W surface.[74] W is a refractory metal that is thermally stable at high temperatures and supports SPP modes in the near infrared wavelength range. As discussed in Sect. 2.1, these modes can exhibit significant enhancement in the photon DOS and hence radiative transfer when in close proximity to the surface.[20,74] However, due to the highly confined nature of SPP modes, this enhancement in DOS decreases rapidly away from the surface. Nevertheless, W emitters are still used in more conventional TPV systems because of its low plasma frequency.[145] It is important to note that for this reference case, no morphological effects are imposed on the W emitter. However, in Sect. 2.6, the impact of imposing thin-film morphological effects on thermal emission from materials supporting SPP modes will be discussed.

The backside metal supporting the emitter and the absorber is chosen to be either a perfect metal (PM), silver (Ag) on the PV cell side, or tungsten (W) on the emitter side. When both W and Ag are used, a magnesium fluoride (MgF_2) spacer is placed between the GaSb cell and the Ag mirror in order to minimize coupling of SPP modes in W and Ag in the near-field regime. This modification is implemented in Eqs. (2.21)-(2.26) by replacing the reflection coefficient for the interface between film 3 and substrate 4 with an effective reflection coefficient that includes the MgF_2 layer in addition to the substrate. The optical constants of GaSb, Ge, MgF_2, Ag and W were all obtained from literature and are plotted in Fig 2.8.[146] The infrared optical properties of Ag were extrapolated using a Drude model.

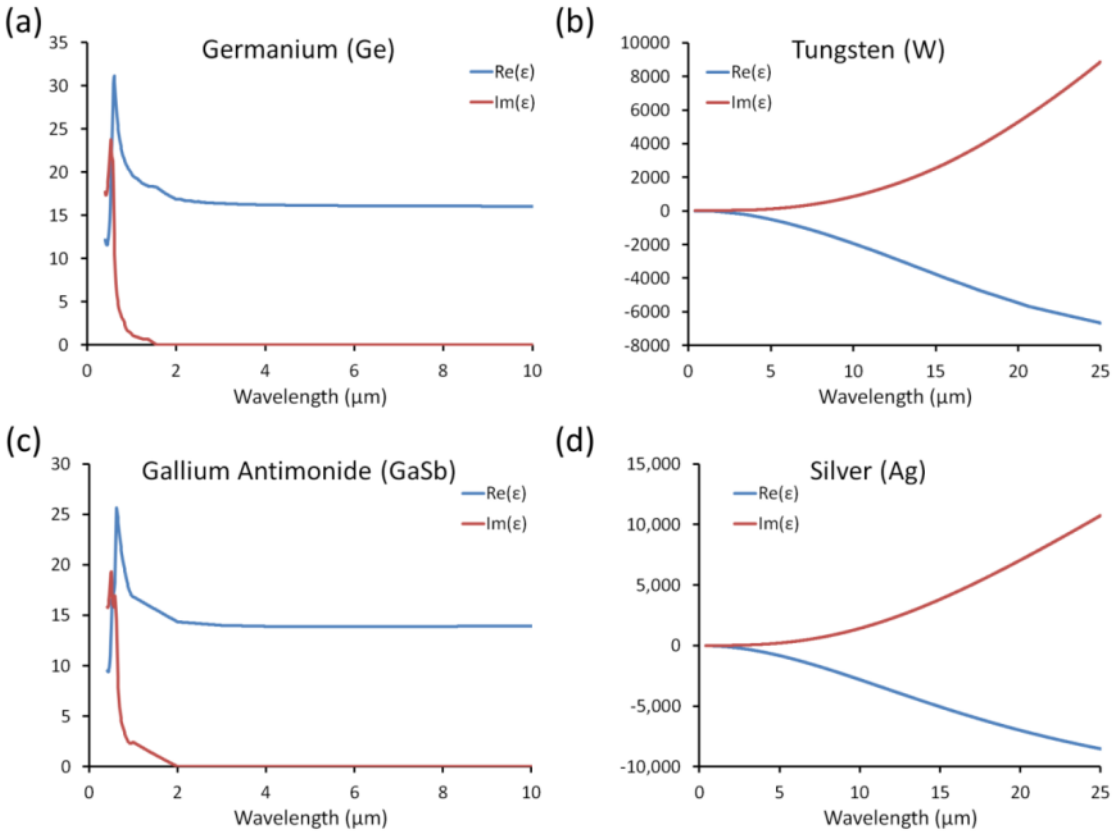

Figure 2.8: The dielectric permittivity of: (a) germanium (Ge), (b) tungsten (W), (c) gallium antimonide (GaSb), and (d) silver (Ag). The optical constants for the perfect metal were taken in the long wavelength limit of silver and were assumed to be dispersionless for the wavelength range computed. The optical constants of all materials were taken from literature.[146]

2.4.3 Shaping Radiative Heat Transfer with Thermal Wells

To demonstrate the effect of reducing a bulk system to a thin-film structure, Figs. 2.9a and 2.9b shows the normalized transmission function, G_{NT}, for a bulk Ge emitter and a bulk GaSb absorber and their corresponding thin-film counterparts, respectively. For the thin-film thermal well structure, a perfect metal was assumed to be on the backside of both the emitter and the absorber. Optimum film thicknesses were obtained that maximizes the TPV efficiency, which will be defined in Sect. 2.5, assuming an emitter temperature of 1000 K, an absorber temperature of 300 K, and a gap separation of 100 nm. The emitter temperature was chosen to be below the melting temperature of Ge which is nearly 1200 K. As shown in Fig. 2.9, the transmission function for the bulk system indicates that radiative modes are supported over a broad frequency range. This

corresponds to the n^3 enhancement in the bulk photon DOS of high refractive index media.[20] In contrast, the transmission function for the thin-film structure changes dramatically and is now comprised of several distinct bands which indicate the presence of trapped waveguide modes in both the Ge emitter and GaSb absorber. These waveguide modes intrinsically provide resonant enhancement, which can lead to greater thermal emission and absorption especially in the near field.[20,147] More importantly, these waveguide modes also exhibit cut-off frequencies beyond which thermal radiation is suppressed since no mode is available for emission and absorption.[148,149]

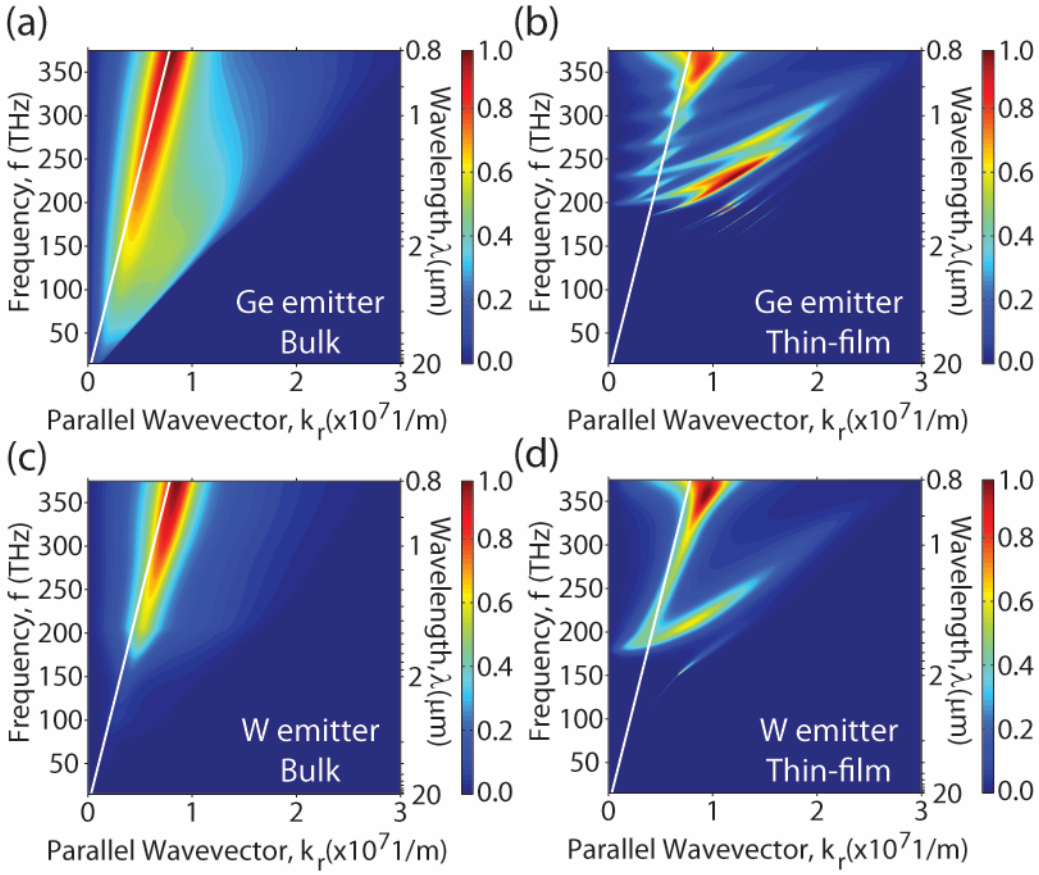

Figure 2.9: The normalized transmission function, G_{NT}, comparing a bulk system to a thin-film system for different emitter materials and a GaSb cell: (a) a bulk Ge emitter and bulk GaSb cell, (b) a thin-film Ge emitter and a thin-film GaSb cell. The thin-film thicknesses are t_H = 860 nm and t_C = 136 nm, (c) a bulk W emitter and a bulk GaSb cell, (d) a bulk W emitter and a thin-film GaSb cell. The thin-film thickness is t_C = 134 nm. This comparison clearly showcases the effect of morphology on the trapped optical modes available for radiative transfer. The gap distance is

assumed to be g = 100 nm. The light line is also plotted to differentiate propagating modes (above the light line) and evanescent modes (below the light line).

Depending on the coupling strength between these waveguide modes, radiative transfer can either be enhanced or suppressed. Stronger coupling occurs when the waveguide modes supported in the emitter and the absorber overlap in both frequency and in-plane wavevector and vice-versa for weaker coupling. Therefore, by choosing appropriate thicknesses for the thin-film emitter and absorber, it is possible to simultaneously enhance thermal radiation at wavelengths above the GaSb band gap and suppress thermal radiation at wavelengths below the band gap as shown in Fig. 2.9b. Between wavelengths of 1.1 μm and 1.6 μm, a strong band exists which indicates similar waveguide modes are supported in both the emitter and absorber resulting in strong coupling and thus large heat flux. However, at wavelengths shorter than 1.1 μm and wavelengths longer than 1.6 μm several weaker bands can be observed. This is due to the difference in thicknesses between the emitter and absorber where the more numerous waveguide modes supported in the emitter can only weakly couple to the few modes that are above the cut-off frequencies supported by the absorber in this wavelength range.

Although this mismatch in waveguide modes reduces the relative coupling strength for super-band gap modes, the suppression of sub-band gap radiative transfer is more crucial in the context of improving TPV performance for a Ge emitter and GaSb cell combination. Furthermore, since GaSb and Ge are both semiconductors with similar band gaps, both materials exhibit an increase in the imaginary component of the permittivity at wavelengths above the band gap. This results in the broadening of the waveguide modes which allows the increased radiative energy transfer from the emitter to the absorber. Although the mechanism of tailoring spectral thermal emission from low-dimensional structures is general and applicable to any material combination of the emitter and the absorber, the optimum thermal well thicknesses are specific to a particular combination of materials and operating temperatures.

For comparison with previously proposed near-field TPV designs, a bulk W emitter was also calculated. Figure 2.9c and 2.9d show the corresponding transmission functions for a bulk and a thin-film GaSb cell, respectively. Once again, the transmission function for the bulk system has a broad spectrum similar to Fig. 2.9a. In the thin-film case, we can still observe the formation of distinct bands. When compared to Fig. 2.9b, fewer bands are observed which indicates that these

bands are solely due to the waveguide modes in the PV cell. Similar to Fig. 2.9b, a distinct band can once again be observed from 1.1 μm to 1.6 μm. The peak at 950 nm is due to the surface plasmon polariton modes supported in the W emitter.

Figures 2.10a and 2.10b show the spectral heat flux for a Ge emitter and W emitter, respectively, again for the case that the back reflector is a perfect metal. For both cases, the emitter temperature was assumed to be 1000 K and the gap separation assumed to be 100 nm. In Fig. 2.10a, a progressive decrease in the thickness of the emitter and the absorber results in strong spectral shaping of the heat flux where long wavelength thermal radiation is significantly suppressed and short wavelength thermal radiation is enhanced resulting in thermal radiation higher than the blackbody limit at the same temperature. This behavior is expected as photonic confinement effects only occur when the thickness of the thin-films are comparable to or smaller than the wavelength of IR radiation. In this regime, the cut-off frequencies of the waveguides modes will blue shift as the thickness decreases. Therefore, long wavelength radiation is inherently more sensitive to variations in thickness. By comparison, the short wavelength range is relatively insensitive to variations in thickness and from Fig. 2.10a it can be observed in that even for thicknesses of 5 μm, the spectral heat flux overlaps with the bulk structure at wavelengths shorter than 1.5 μm.

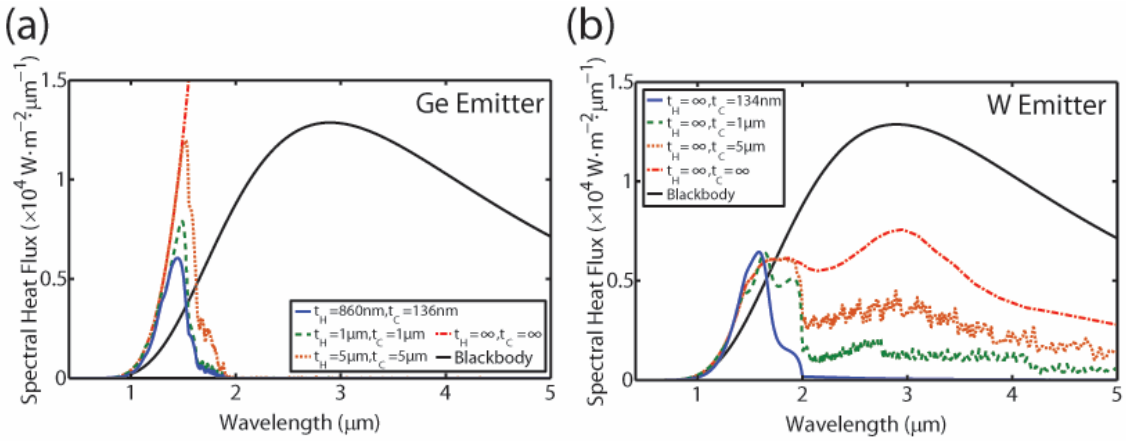

Figure 2.10: The spectral heat flux as a function of the emitter and the PV cell thicknesses assuming an emitter temperature T_H = 1000 K and a gap distance g = 100 nm: (a) the spectral heat flux for a Ge emitter, (b) the spectral heat flux for a W emitter. By making the emitter and the PV cell thin, radiative energy transfer at wavelengths below the band gap is significantly suppressed.

For the case of a bulk W emitter, Fig. 2.10b shows that as the thickness of the GaSb absorber decreases, long wavelength thermal radiation is still suppressed while short wavelength thermal radiation is again enhanced beyond the blackbody limit. This suggests that despite the broad emission of SPP modes, the thermal well effect can still be utilized to dramatically improve the spectral selectivity by simply making the absorber thin in order to suppress absorption at longer wavelengths.

It is also worth mentioning that Ge at high temperatures will also exhibit a broader emission spectrum due to a combination of band gap shrinkage and free carrier emission. For the sake of demonstrating the thermal well concept, this effect was not included in the results plotted in Figs. 2.9 and 2.10. Although neglecting this effect may appear to be an oversimplification, the results for the bulk W emitter indicate that despite the presence of long wavelength emission, the inability of the GaSb absorber to absorb thermal radiation in this wavelength range will ensure that the spectral selectivity is maintained. To confirm this assumption, additional calculations were performed, as shown in Fig. 2.11, in which the extinction coefficient of Ge was artificially raised to emulate the effects of high temperature and the results show that the spectral selectivity was still improved via the thermal well effect.

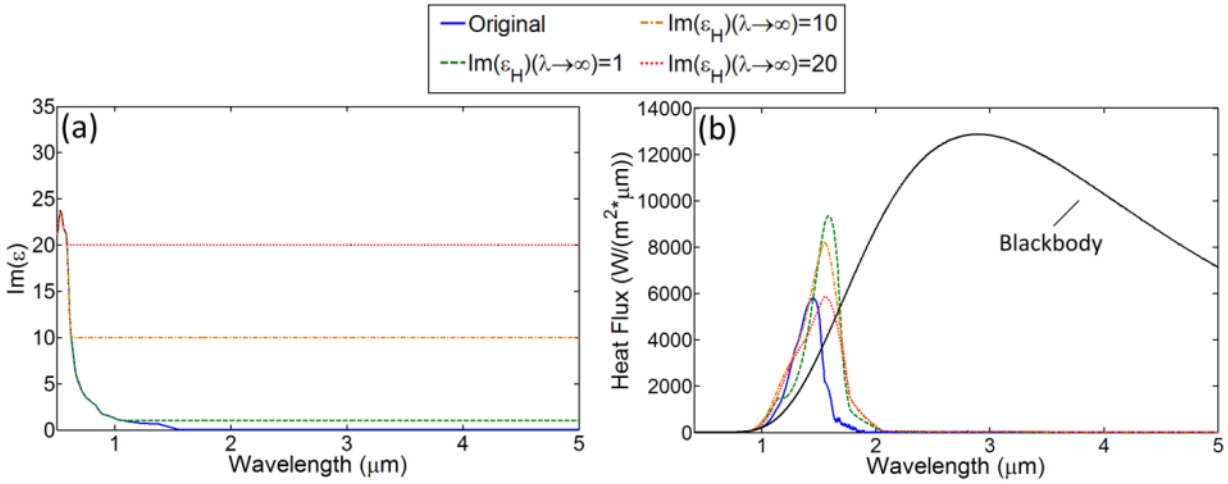

Figure 2.11: At high temperatures, the optical properties of Ge will change due to a combination of thermal expansion which decreases the electronic band-gap and a significant increase in the population of thermally excited free-carriers. These factors will both lead to emission at longer wavelengths. (a) To assess whether this will impact the spectral selectivity, the imaginary component of permittivity of germanium was artificially increased to simulate this effect. Each

case was re-optimized to maximize efficiency. For $Im(\varepsilon_H \to \infty) = 1$: $t_H = 100$ nm, $t_C = 100$nm, $Im(\varepsilon_H \to \infty) = 10$: $t_H = 90$ nm, $t_C = 100$nm, $Im(\varepsilon_H \to \infty) = 20$: $t_H = 80$ nm, $t_C = 100$nm (b) The spectral radiative heat flux for a Ge thin-film emitter and a GaSb PV cell supported by a perfect metal still exhibits spectrally selective radiative transfer even for high material losses in the emitter. This can be explained by the inability of the GaSb thin-film to absorb long wavelength thermal radiation emitted by Ge due to the cutoff frequency of the lowest frequency mode. Although the spectral heat flux broadens and redshifts for higher material losses, the efficiency computed for each case is 39.8% for $Im(\varepsilon_H \to \infty) = 1$, 37.7% for $Im(\varepsilon_H \to \infty) = 10$, and 36% for $Im(\varepsilon_H \to \infty) = 20$.

2.4.4 Generality of Thermal Well Effect on Thermal Radiation

At this point, the results presented thus far have been intended for use in a TPV system. However, it is important to emphasize that the thermal well effect is general and can be applied using a myriad of different materials to spectrally shape thermal emission and absorption. To convey the generality of this effect, several additional calculations were performed for different materials, as shown in Fig. 2.12. The thickness for the emitter and the absorber were chosen to be $t_H = t_C = 1000$ nm for all cases and the gap was set to g = 100 nm. These thicknesses were not optimized for a particular application, but nevertheless show that by simply reducing the dimensionality of an emitter and absorber, it is possible to dramatically shape thermal emission and absorption.

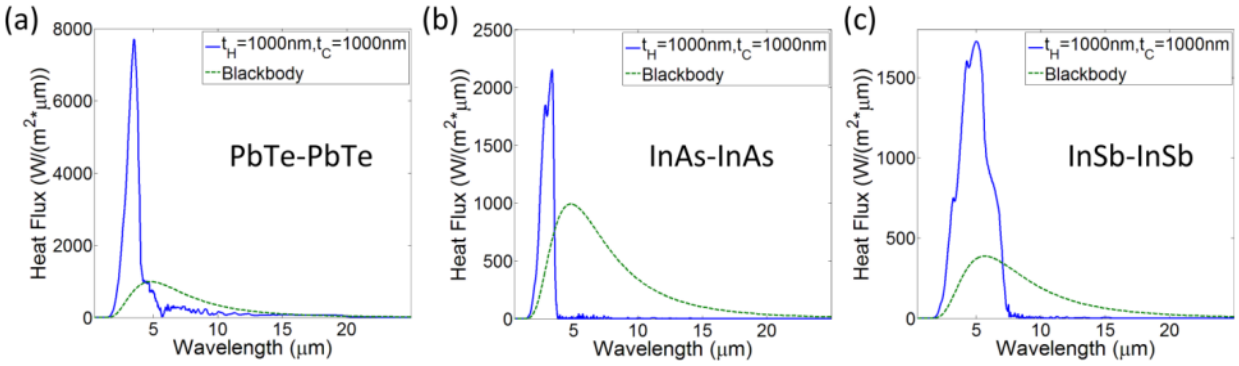

Figure 2.12: To show the generality of the 'thermal well' effect in manipulating thermal radiative transfer, several alternative material combinations were calculated, including: (a) lead telluride (PbTe) emitter and absorber assuming an emitter temperature of $T_H = 600$ K and absorber temperature of $T_C = 300$ K at a separation distance of 100 nm, (b) indium arsenide (InAs) emitter and absorber assuming an emitter temperature of $T_H = 600$ K and absorber temperature of $T_C =$

300 K at a separation distance of 100 nm, and (c) indium antimonide (InSb) emitter and absorber assuming an emitter temperature of T_H = 500 K and absorber temperature of T_C = 300 K at a separation distance of 100 nm. In all cases, the back reflector is chosen to be a perfect metal. It should be noted that these materials were not intended for use in high-temperature TPV applications, but rather to assess the potential spectral selectivity of thermal emission that could be achieved using the thermal well concept with different materials.

2.5 Impact of Thermal Well Effect on TPV Performance

In order to evaluate the impact of the thermal well effect on TPV system performance, an electrical model was developed to determine the energy conversion efficiency of the PV cell. In this section, a general overview of the electrical model is provided followed by specific solutions in accordance to the Shockley-Queisser limit and a more realistic model that takes into consideration radiative and non-radiative recombination for a single p-n junction device. With these models, predictions on the system performance will be shown using the results presented in Sect. 2.4 for a Ge or W emitter and a GaSb PV cell.

2.5.1 Electrical Model for TPV Performance

The electrical model follows the conventional analysis of solar PV cells, in which the cell is formulaically treated as an electrical diode. The current-voltage, or IV, curve of a PV cell is thus modeled based on the general diode equation as follows,

$$I = I_{PH} + I_0\left(1 - e^{\frac{qV}{k_B T_C}}\right) \tag{2.28}$$

where I is the output current from the PV cell, I_{PH} is the photogenerated current, I_0 is the dark saturation current, V is the voltage, k_B is the Boltzmann constant, T_C is the cell temperature, and q is the charge of an electron. The term $(k_B T_c/q)$ is also referred to as the thermally induced potential V_C. In Eq. (2.28), it is assumed the diode behaves as an ideal diode with an ideality factor of 1 and parasitic resistances, such as series or shunt resistances, are negligible.

From Eq. (2.28), the maximum electrical power density, P_E, of the PV cell, can be defined as the product of the short-circuit current, I_{SC}, the open-circuit voltage, V_{OC}, and the fill factor of the PV cell, FF, as follows,[74,150]

$$P_E = I_{SC} \cdot V_{OC} \cdot FF \tag{2.29}$$

The short-circuit current is generally dependent on the photogeneration rate, I_{PH}, and the diffusion length for minority electron and holes generated in the cell. The open-circuit voltage is determined by taking the limit of zero current in Eq. (2.28) and can be expressed as follows,

$$V_{OC} = V_C \cdot \ln\left(\frac{I_{SC}}{I_0} + 1\right) \tag{2.30}$$

The fill factor is defined as the maximum electrical power output from the PV cell normalized by the product of the short-circuit current and open-circuit voltage,

$$FF = \frac{\max(I \cdot V)}{I_{SC} \cdot V_{OC}} \tag{2.31}$$

Finally, following the conventional definition for the photovoltaic energy conversion efficiency, we can thus define the efficiency of our TPV system to be,[74,76,77,150–152]

$$\eta = \frac{P_E}{P_R} \tag{2.32}$$

where P_R is the radiative power density. The radiative power density is the net radiative heat transfer between the emitter and the PV cell integrated over all frequencies,

$$P_R = \int_0^\infty \left(q_{03} + q_{04} + q_{13} + q_{14} - q_{31} - q_{30} - q_{41} - q_{40}\right) d\omega \tag{2.33}$$

where q_{04} is the heat flux from emitter back reflector to the PV cell back reflector, q_{14} is the heat flux from the thin-film emitter to the PV cell back reflector, q_{41} is the heat flux from the PV cell back reflector to the thin-film emitter, and q_{40} is the heat flux from the PV cell back reflector to the emitter back reflector.

Equations (2.29)-(2.33) thus provide a general framework to estimate the electrical device performance of a PV cell. However, it is still necessary to define the specific methodology used to evaluate the photogeneration current and the dark saturation current as this will determine how ideal or how realistic the estimated energy conversion efficiency is. In fact, this formalism conveniently can be used to directly determine an ideal baseline limit in order to compare the impact of using morphological effects on both the emitter and PV cell.

2.5.2 Shockley Queisser Limit

An ideal limit can be formulated based on the well-known Shockley-Quiesser formulation, which has conventionally been used as a benchmark in solar photovoltaics.[150] In this limit, the PV cell is

assumed to behave as an ideal diode with an internal quantum efficiency of 100%, no non-radiative recombination processes, and only far-field radiative transfer between a hot emitter and a PV cell. Thus, the short-circuit current is equivalent to the photogeneration current, which is formulated assuming each absorbed photon with an energy larger than the electronic band gap produces one electron as follows,

$$I_{SC} \approx I_{PH} = \int_{\frac{E_g}{\hbar}}^{\infty} \frac{q}{\hbar\omega} \cdot Q_{\omega,a} d\omega \tag{2.34}$$

where $Q_{\omega,a}$ is the absorbed power spectra from the emitter. Similarly, the dark saturation current, I_o, is formulated in this ideal limit as simply the blackbody emission from the PV cell again for photon energies larger than the band gap as follows,

$$I_0 = \int_{\frac{E_g}{\hbar}}^{\infty} \frac{q}{\hbar\omega} \cdot Q_{\omega,e} d\omega \tag{2.35}$$

where $Q_{\omega,e}$ is the emitted power spectra from the PV cell. It should be noted that in the Shockley-Queisser formalism, the only material property considered is the electronic band gap. Thus the only radiative recombination loss is the blackbody emission from the PV cell itself.

2.5.3 Electrical Model with Non-radiative Recombination Losses

In order to provide a more realistic estimation of the TPV system performance compared to the more idealized Shockley Queisser formulation, specific material recombination lifetimes for both bulk radiative recombination, bulk non-radiative recombination, and surface recombination losses can be incorporated into the formalism. This is accomplished by treating the PV cell more rigorously by modeling it to have a p-type quasi-neutral region, n-type quasi-neutral region, and a space charge region as shown in Fig. 2.13.[74,76,77,152]

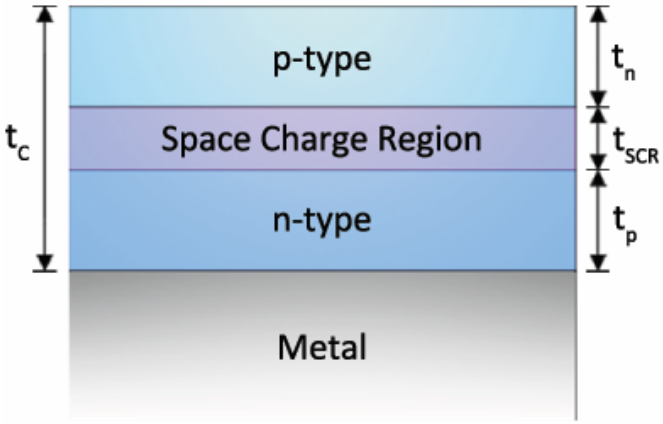

Figure 2.13: A schematic illustration of the PV cell electrical model. The view of the PV cell is magnified detailing the structure assumed for the electrical analysis. The PV cell consists of a p-type quasi-neutral region, a n-type quasi-neutral region, and a space charge region. In this study, the thicknesses of the p-type and n-type quasi-neutral regions are assumed equal.

In this analysis, it is again assumed the internal quantum efficiency (IQE) is 100%, thus the short-circuit current is approximately equal to the photogeneration current as defined in Eq. (2.34). Normally this will lead to an overestimation of PV performance. However, in the limit of ultra-thin PV cells, this assumption is a reasonable approximation since bulk recombination losses for minority carriers are significantly reduced if the p-type and n-type regions are negligibly thin. Subsequent surface recombination losses can also be significantly reduced using a good passivation layer.

To determine the saturation current, an analytical expression can be obtained by considering the diffusion of carriers in the PN junction under zero external bias. For a finite size PN junction, this expression is as follows,[151]

$$I_0 = \frac{eD_n n_i^2}{L_n N_p} \cdot F_n + \frac{eD_p n_i^2}{L_p N_n} \cdot F_p \; ; \; F_x = \frac{S_x \cdot \cosh\left(t_x/L_x\right) + D_x/L_x \cdot \sinh\left(t_x/L_x\right)}{D_x/L_x \cdot \cosh\left(t_x/L_x\right) + S_x \cdot \sinh\left(t_x/L_x\right)} \tag{2.36}$$

where is n_i the intrinsic carrier concentration, N_n is the n-type dopant concentration, N_p is the p-type dopant concentration, D_x is the carrier diffusivity, S_x is the surface recombination velocity, t_x is the thickness of the quasi-neutral regions, and L_x is the diffusion length. The subscripts n and p denote electrons and holes, respectively. The diffusion length can be defined in terms of a total recombination lifetime, $L = \sqrt{D \cdot \tau}$. The recombination lifetime is an inverse summation over all

recombination mechanisms including radiative recombination, Shockley-Read-Hall recombination, and Auger recombination.[151] The thickness of the p-type and n-type quasi-neutral regions are assumed equal and are obtained by taking the difference between the total thickness of the PV cell and the thickness of the space charge region which is expressed as,[153]

$$t_{SCR} = \sqrt{\frac{2k_b T_C \varepsilon}{e^2} \cdot \ln\left(\frac{N_n N_p}{n_i^2}\right) \cdot \left(\frac{1}{N_n} + \frac{1}{N_p}\right)} \tag{2.37}$$

where ε is the permittivity of the PV cell taken in the long wavelength limit. Since the PV cell thickness is chosen independently in the radiative heat transfer model, if the thickness of the PV cell is smaller than the space charge region, the thicknesses of the p-type and n-type quasi-neutral regions are assumed to be negligible so that the PV cell consists entirely of a fully depleted region. In this limit, surface recombination becomes the dominant loss mechanism.

The electrical properties of the GaSb cell were obtained from literature.[154] It is assumed the GaSb cell is at a uniform temperature of 300K. The intrinsic carrier concentration, n_i, is assumed to be $4.3 \cdot 10^{12}$ cm^{-3}. The electron and hole carrier concentrations are equal to $N_n = N_p = 10^{17}$ cm^{-3}. The recombination lifetimes are τ_R = 40 ns, τ_{SHR} = 10 ns, and τ_{Au} = 20 μs for radiative recombination, Shockley-Read-Hall recombination, and Auger recombination, respectively. The carrier diffusivities are D_n = 129 cm^2/s and D_p = 39 cm^2/s for electrons and holes, respectively. The surface recombination velocity is chosen to be $S_n = S_p$ = 100 cm/s in accordance to previous studies.[144]

2.5.4 Predictions of TPV Performance using Thermal Well Effect

To evaluate improvements to TPV performance using the thermal well effect, a Shockley Queisser limit is first established as a baseline reference for further comparison. If the emitter and the PV cell are assumed to be blackbodies at a temperature of T_H = 1000 K and T_C = 300 K, respectively, this formulation predicts the maximum efficiency achievable for a GaSb cell, which has an electronic band gap of 0.726 eV, is 1.5%. For an emitter temperature of T_H = 2000 K, the efficiency increases to 20.7%. The reason for such low efficiencies, particularly at T_H = 1000 K is due to the emission of photons at sub-band gap energies, which cannot be used by the PV cell for energy conversion. While a hotter emitter temperature can improve the efficiency by blueshifting the thermal emission spectra, these efficiencies are ultimately limited by the lack of spectral selectivity in the emission and absorption of photons.

Using the calculated radiative power spectra and Eqs. (2.29)-(2.33), (2.34), (2.36) and (2.37), the predicted efficiencies for the thin-film structure, which again includes non-radiative bulk and surface recombination losses, are shown in Fig. 2.14a as a function of temperature assuming a gap separation of 100 nm. At an emitter temperature of T_H = 1000 K, the predicted efficiencies in the bulk limit is 0.38% for a Ge emitter and 1.9% for a W emitter due to the broad spectrum of radiative heat transfer shown in Fig. 2.10. By applying the thermal well effect and reducing the dimensionality of the emitter and PV cell, the energy conversion efficiency can be improved dramatically. For the case where perfect metals are used for both back reflectors, the efficiency reaches 38.7% for a thin-film Ge emitter and 28.7% for a bulk W emitter, which is more than an order of magnitude higher than the bulk limit. These predicted efficiencies also exceed past TPV efficiency records of 22% for GaSb cells while using a substantially lower emitter temperature of 1000 K compared to temperatures higher than 1500 K.[112,155]

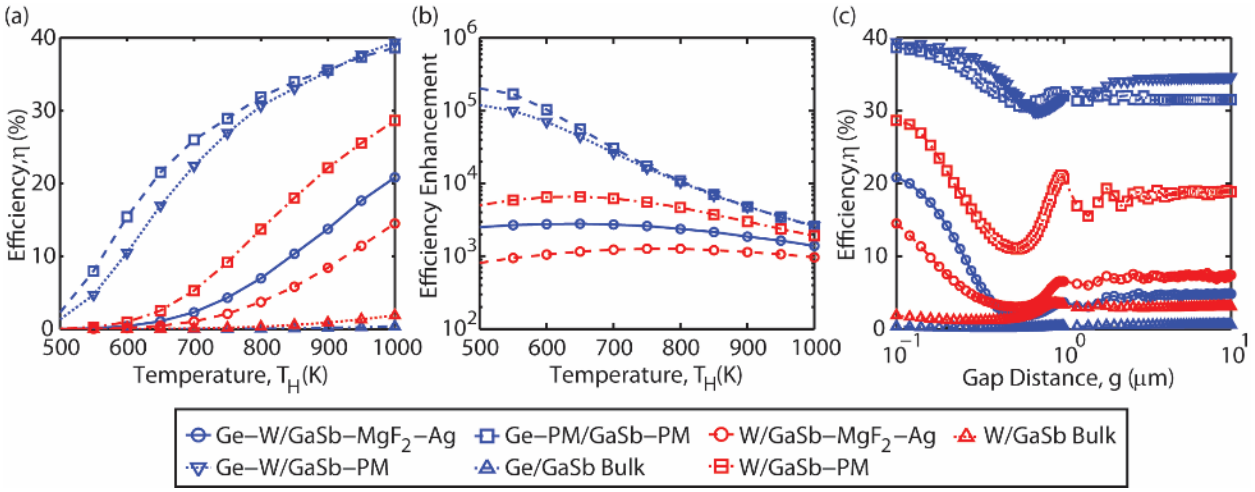

Figure 2.14: The energy conversion efficiency, η, from the emitter to the PV cell for several material combinations. (a) The efficiency as a function of temperature assuming a gap distance of g = 100 nm. (b) The predicted efficiencies from (a) normalized by efficiencies computed using the Shockley Queisser formulation for varying blackbody emitter temperatures. (c) The efficiency as a function of gap distance assuming an emitter temperature T_H = 1000 K. The legend is identical to (a). The optimal thicknesses for the case of a Ge emitter on a W substrate and a GaSb cell on a Ag substrate with a MgF_2 spacer is t_H = 119 nm, t_C = 100 nm, and t_S = 1.25 μm. The optimal thicknesses for a Ge emitter on a W substrate and a GaSb cell on a perfect metal are t_H = 58 nm

and t_C = 94 nm. The optimal thicknesses for a bulk W emitter and a GaSb cell on a Ag substrate with a MgF_2 spacer is t_C = 59 nm and t_S = 750 nm.

To investigate this enhancement further, if the perfect metal back reflector on a thin-film Ge emitter is replaced with W, it can be observed that at low temperatures the efficiency is lower compared to the case of a perfect metal due to broadening of thermal emission at longer wavelengths. However, at higher temperatures, shorter wavelength modes are preferentially excited as the Planck energy oscillator function blue shifts. As a result, the short wavelength SPP mode supported in W contributes more to radiative transfer compensating for the long wavelength emission. In conjunction with thermal emission from the thin-film Ge emitter, this combination can actually lead to an even higher efficiency of 39.4% again at T_H = 1000 K.

For a more realistic TPV system, where the back reflector is replaced with a Ag substrate separated from the PV cell by a transparent MgF_2 spacer layer, the efficiency decreases to 20.8% for a thin-film Ge emitter supported by a W substrate and 14.5% for a bulk W emitter at T_H = 1000 K. This reduction in performance is due to the use of W and Ag, which not only support SPP modes that can couple in the near-field regime, but also exhibit intrinsic parasitic absorption and emission at longer wavelengths due to the imperfect nature of these materials as back reflectors. Although the MgF_2 spacer layer reduces SPP mode coupling by increasing the distance between the emitter and the PV cell back reflectors, long wavelength absorption and emission still inhibit the predicted performance. This suggests that bulk metallic mirrors are not suitable to fully harness the thermal well effect. Despite the reduction in performance, the predicted efficiency still exceeds the bulk limit. Thus, even for a suboptimal system, the thermal well effect can still provide dramatic improvements to TPV performance.

In fact, the predicted efficiencies for all cases not only exceed the bulk limit, but also the Shockley Queisser limit for a blackbody emitter by several orders of magnitude. Figure 2.14b shows the predicted efficiency normalized to the efficiency from the Shockley Queisser formulation assuming the emitter is a blackbody and the PV cell has a band gap of 0.726 eV. For certain cases, the enhancement reaches its maximum at intermediate temperatures. This is due to the more sensitive nature of thermal emission in the near-field regime compared to blackbody emission where lower temperatures will red shift the population of radiating modes resulting in a more rapid decrease in thermal emission at wavelengths where strong evanescent coupling occurs.

The data presented in Figs. 2.10a and 2.10b demonstrate that the use of the thermal well effect can enable operation of near-field TPV systems with efficiencies higher than 30% at moderate temperatures of about 800 K.

Due to the inherent practical difficulties associated with utilizing the near-field regime in a TPV system, the conversion efficiency was also calculated as a function of the gap separation assuming an emitter temperature of T_H = 1000 K as shown in Fig. 2.14c. For all cases, the efficiency saturates at gap separations larger than 5 μm which corresponds to the far-field limit. In this limit, for the case where both back reflectors are perfect metals, the efficiency decreases to 31.5% for a thin-film Ge emitter and 18.9% for a bulk W emitter. For the case of a thin-film Ge emitter and a W back reflector, the efficiency decreases to 34.6%. This reduction in performance is expected as the enhancement by near-field coupling is no longer utilized. However, despite this reduction, the predicted efficiencies still clearly exceed the Shockley Queisser limit for a blackbody emitter. The oscillatory behavior of efficiency at intermediate gap separations is due to the vacuum gap behaving like a waveguide.

In the case where a Ag back reflector and a MgF_2 spacer on the PV cell are used, the efficiency decreases more significantly to 4.9% for a thin-film Ge emitter supported by a W substrate and 7.4% for a bulk W emitter. Again this can be attributed to parasitic emission and absorption in W and Ag which lead to significant radiative transfer at longer wavelengths which cannot be used for power generation.

The enhancement in TPV system efficiency, as demonstrated in Fig. 2.14, can be attributed to improvements to both the spectral selectivity of radiative transport via the thermal well effect, as was shown in Fig. 2.10, and a reduction in bulk recombination losses for a thin-film PV cell which results in a lower saturation current. It should be emphasized that although the thermal well effect was proposed as a way to manipulate the photon dispersion in the near-field regime, it can also be used to improve the spectral selectivity in the far-field limit as evidenced by the high efficiencies predicted for the cases that use a perfect metal as a back reflector in Fig. 2.14c. Again this can be attributed to the creation of quantized waveguide modes in the emitter and the PV cell. Although resonant enhancement for high photon energies larger than the band gap of the PV cell will be weaker due to the lack of near-field coupling, the suppression of emission and absorption below the cut-off frequency of these waveguide modes still ensures strong spectral selectivity in the far-field regime.

In regards to the electrical performance of the GaSb cell, the thickness of the space charge region formed is estimated to be t_{SCR} = 135 nm based on Eq. (2.37) and the properties of a typical GaSb cell. For the various cases presented, the PV thin-film thicknesses are either comparable to or smaller than the predicted size of the space charge region. This implies that the p-type and n-type quasi-neutral regions in the PV cell are so thin that bulk recombination losses are negligible. Surface recombination losses can also be dramatically reduced if the PV cell is well passivated. By significantly reducing these loss mechanisms, ultra-thin PV cells can exhibit an IQE that approaches 100% thus justifying our earlier assumption.[76,152] Furthermore, the saturation current will also decrease resulting in a higher open-circuit voltage. Both of these effects contribute to improve the energy conversion efficiency.

To show the impact of reducing bulk recombination losses on the PV performance, the predicted efficiency was also calculated using the Shockley-Queisser formulation assuming the same radiative power density for each case, as shown in Fig. 2.15. When both back reflectors are perfect metals, the predicted efficiencies at an emitter temperature of T_H = 1000 K and a gap separation of g = 100 nm are 46.4% and 34.5% for a thin-film Ge emitter and a bulk W emitter, respectively. For a thin-film Ge emitter supported by a W back reflector, the efficiency is 46.7%. And finally, for the PV cell back reflector composed of a Ag mirror and a MgF_2 spacer, the efficiency is 25.2% and 17.4% for a thin-film Ge emitter and a bulk W emitter, respectively. In all cases, the efficiencies calculated using the more realistic electrical model approach the performance predicted by the ideal Shockley Queisser formulation. Therefore it is clear that by using thin-film PV cells, the corresponding reduction in bulk recombination losses can dramatically improve the electrical performance of the device.

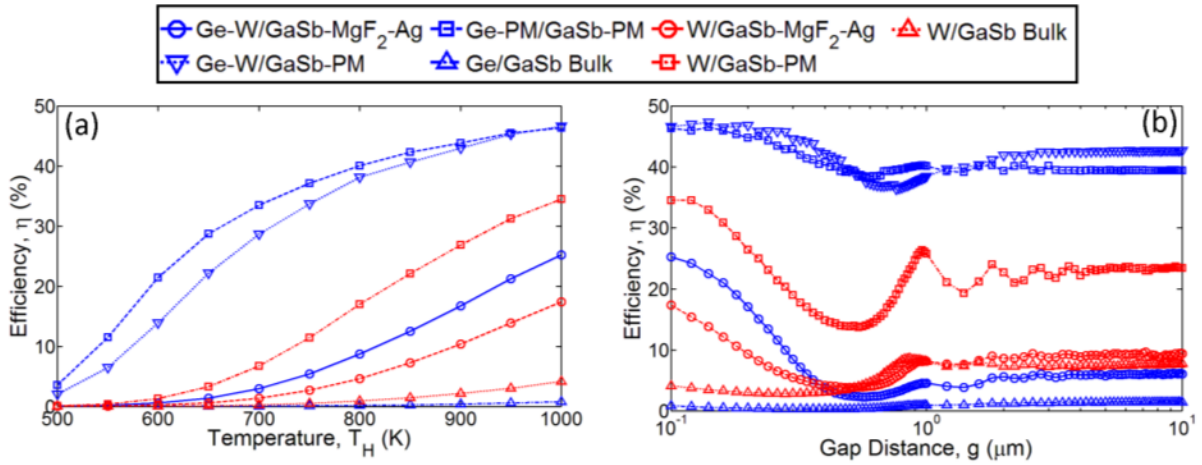

Figure 2.15: The predicted efficiency, η, using the Shockley-Queisser formulation for the same radiative power density based on Fig. 2.10. (a) The efficiency as a function of the emitter temperature assuming a gap separation of g = 100 nm. (b) The efficiency as a function of the gap separation assuming an emitter temperature of T_H = 1000 K.

It was also observed that by combining different emitting mechanisms, namely thin-film waveguide modes in Ge and SPP modes in W, it is possible at high temperatures to exceed the efficiency predicted using a perfect metal as the back reflector on the emitter. This suggests that there exists some flexibility in the design of the emitter and with an optimal material combination for the thin-film and substrate, even higher energy conversion efficiencies can be obtained compared to the predictions in this study. However, to achieve high energy conversion efficiencies the back reflector of the PV cell must exhibit a near unity reflectance to eliminate parasitic absorption and emission at photon energies smaller than the band gap of the PV cell. By replacing the perfect metal with a Ag substrate and a MgF_2 spacer, the performance was observed to decrease significantly, which indicates that bulk metallic mirrors are insufficient in this design approach. In general, no natural materials behave like a perfect metal; however, it is possible to design artificial photonic structures that can emulate the behavior of a perfect metal within a certain wavelength range. For example, a distributed Bragg reflector, which is commonly used as a high quality mirror, supports a photonic band gap, which can be positioned at photon energies just below the electronic band gap of the PV cell.[156,157] In fact, the concept of incorporating a Bragg reflector in a PV module is not new and has been used in the past as a way to recycle photons in various PV cells.[75,158–162] Although it is impossible to completely eliminate metal, since electrical contacts are needed to

extract charge carriers, a recent study has shown that it is ideal to minimize the contact area between the PV cell and the metal contacts to reduce recombination losses.[163] Therefore, the inclusion of a Bragg mirror could provide a path towards realistically achieving TPV performance that approaches the perfect reflector case presented in this work. To showcase the potential of using a dielectric mirror, a preliminary design was developed which exhibits a reflectance near unity at photon energies just below the band gap of the GaSb cell, as shown in Fig. 2.16.

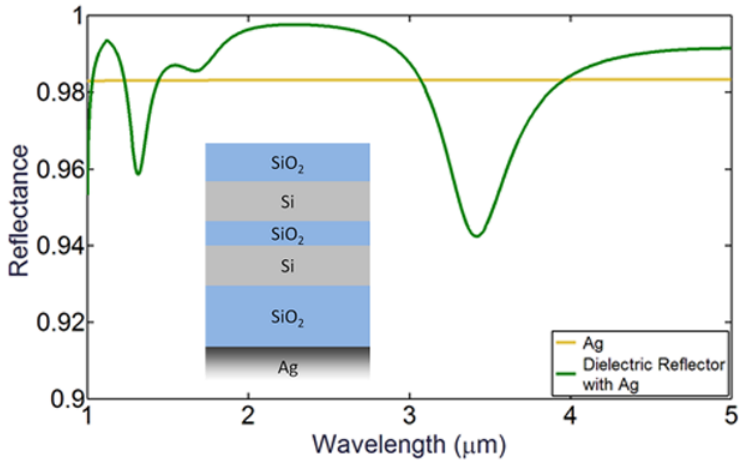

Figure 2.16: A preliminary design for a multilayer dielectric mirror was developed to show that it is possible to approach a near unity reflectance using real materials. This particular design is composed of silicon dioxide (SiO_2) and silicon (Si) supported by a silver (Ag) substrate with layer thicknesses from the top to the bottom of: 112 nm, 242 nm, 86 nm, 209 nm, and 308 nm. The dielectric mirror was specifically designed to improve the reflectance in the 2 to 3 μm wavelength range where parasitic absorption is more prevalent. Compared to a Ag mirror, which exhibits a reflectance of about 98.3%, the dielectric mirror can achieve a reflectance as high as 99.7%. This may not appear to be a significant improvement, but, as discussed in the main text, a perfect metal back reflector and a Ag back reflector can lead to significant differences in the energy conversion efficiency. These results thus show that a simple multilayer dielectric stack can readily approach the perfect metal limit, suggesting it is possible to achieve high TPV efficiencies for a real system. It should be noted that this calculation was performed at normal incidence.

To improve the performance of the TPV system even further, it should be stressed that the choice of the materials in this study are not the most optimal. For example, the band gap of the

GaSb cell is relatively large compared to the low emitter temperatures thus inhibiting the portion of thermal radiation that can be used for power generation. Smaller band gap ternary and quaternary PV cells, such as InGaAsSb or InGaSb devices, can extend the range of useful photons for power generation to longer wavelengths resulting in both a higher efficiency and a higher electrical power density at lower emitter temperatures. In fact, given that the optimal PV cell thickness in this study is significantly thinner than typical epitaxially grown ternary and quaternary devices, it is likely that TPV systems utilizing these materials will benefit from the thermal well effect.[117,164–166] Furthermore, the inherent simplicity of reducing the dimensionality of the emitter and the PV cell allows conventional components such as filters or antireflection coatings to be easily incorporated which can improve the spectral selectivity even further. For practical realization, additional studies are needed to evaluate the thermal well effect for a more realistic PV device architecture that includes passivation, electrical contacts, as well as 2D and 3D carrier transport. Thermal effects on TPV performance due to thermalization losses and parasitic heating should also be evaluated; though, it should be noted that by using the thermal well effect in conjunction with a PV cell with an optimal band gap, it may be possible reduce heating compared to conventional PV cells.[77]

By improving the spectral selectivity and reducing the saturation current, the studied thermal well effect is theoretically predicted to enhance the energy conversion efficiency of TPV systems by more than an order of magnitude compared to both the bulk limit and the Shockley Queisser limit for a blackbody emitter at the same temperature. For a thin-film Ge emitter and a thin-film GaSb PV cell supported by perfect metals, the TPV energy conversion efficiency was predicted to be as high as 38.7% at an emitter temperature of 1000 K and gap separation of 100 nm due to only the thermal well effect. In the far-field limit, this efficiency decreases to 31.5%; however, this is still significantly higher than the Shockley Queisser limit even for a blackbody emitter at a temperature of 2000 K. This is in stark contrast to past studies that utilized SPP modes to improve TPV systems as the efficiency enhancement is limited to the near-field regime which is challenging to realize in a practical system.

Overall, thermal well TPV systems can provide higher TPV efficiency at lower emitter temperatures much like quantum well lasers which feature lower pumping thresholds than conventional diode lasers while being exceedingly more efficient or quantum well thermoelectric generators, which have thermoelectric figures of merit that are much higher than bulk systems.[167]

By introducing morphological effects into a TPV system, not only can greater flexibility in engineering radiative heat transfer between the emitter and the PV cell be achieved, but also even simple, easily fabricated structures can have a profound effect on the overall performance of the TPV system.

2.6 Morphological Effects on Surface Polariton Mode Resonances‡

In the previous sections, it was demonstrated that thin-film morphological effects can be used to spectrally tailor near-field thermal radiation for optimum spectral selectivity in a theorteical TPV system by virtue of the waveguide modes the films supported. As mentioned in Sect. 2.2.2, it is also possible to apply a thin-film morphology to materials that support surface polariton modes. As will be shown in this section, this can also yield profound effects on near-field thermal radiation.

2.6.1 Thin-film Morphology Effects on Surface Polariton Modes

Surface polariton modes, as discussed in Sect. 2.1, intrinsically exhibit a large enhancement to the local photon DOS due to the confined nature of these modes. In Sect. 2.2.2, it was discussed that despite the lossy nature of these modes, it is still possible to apply morphological effects to alter the optical behavior. As an example to showcase the impact morphologically-modified surface polariton modes can have on near-field radiative heat transfer, ultra-thin films of conducting oxides supporting surface plasmon polariton (SPP) modes will be evaluated in comparison to thin-films of polar dielectrics supporting surface phonon polariton (SPhP) modes. Materials supporting SPP modes have conventionally exhibited limited enhancement to near-field radiative heat transfer due to the high frequencies of these modes, which require prohibitively large temperatures to thermally excite.[66–68] However, it will be shown that through morphology, the total spectrally integrated radiative heat flux for conducting oxides can exceed that of the polar dielectrics even at low temperatures where surface phonon polaritons spectrally overlap greater with the Planck oscillator distribution.

---

‡Adapted from S. V. Boriskina, J. K. Tong, Y. Huang, J. Zhou, V. Chiloyan, and G. Chen, "Enhancement and Tunability of Near-field Radiative Heat Transfer Mediated by Surface Plasmon Polaritons in Thin Plasmonic Films," Photonics, Vol.2 (2), 659-683 (2015).

Several configurations are again used to evaluate thin-film morphological effects on surface polariton modes. The optically metallic material is chosen to be aluminum zinc oxide (AZO), which is a conducting oxide that supports a near-infrared SPP mode. For comparison to a SPhP mode, silicon carbide (SiC), which is a common polar dielectric, is used. The dielectric constants for AZO were obtained by fitting to a Drude model using parameters from previous studies.[168] For SiC, the dielectric permittivity was taken directly from literature.[146] The dielectric permittivity for both materials is shown in Fig. 2.17.

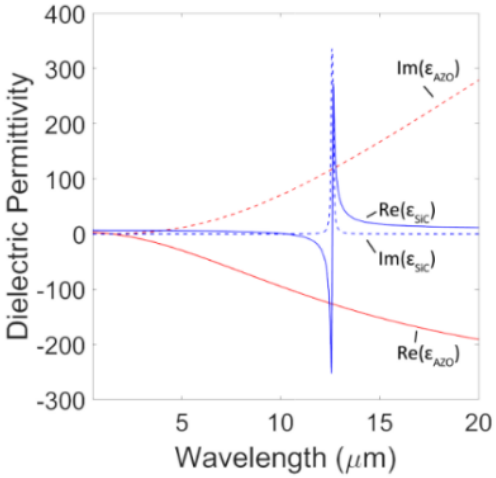

Figure 2.17: The complex dielectric permittivity of a polar dielectric, SiC, and a metal, AZO. The solid and dashed lines correspond to the real and imaginary component of permittivity, respectively.

It can be observed that for SiC, the spectral window where Re(ε) is negative exhibits a lower Im(ε) compared to AZO. The lower dissipative losses, which are typical when comparing SPhP modes in polar dielectrics to SPP modes in metals, enable the SPhP mode of SiC to extend to further in-plane wavevectors, resulting in a higher photon DOS and high near-field radiative heat transfer. For the sake of conceptual demonstration, the temperature-dependence of the dielectric permittivity is neglected. In all calculated cases, the thermal emitter and absorber were chosen to be the same material, e.g. either AZO or SiC. The hot side temperature is T_H = 1000 K and the cold side temperature is T_C = 360 K. The gap separation is g = 20 nm.

Using the formulation derived in Sect. 2.3, the near-field radiative transfer between bulk semi-infinite media is first calculated to serve as a benchmark for comparison to the thin-film

configurations. The spectral radiative heat flux for this case is shown in Fig. 2.18a. The spectral radiative heat flux for AZO peaks at a wavelength of ~1.5 μm corresponding to the resonant SPP mode and decreases at longer wavelengths as the non-resonant tail of the SPP mode is suppressed as the drude-like metal behaves progressively more like an ideal perfect metal. In comparison, the spectral radiative heat flux for SiC exhibits two peaks at ~10.6 μm and ~12.6 μm corresponding to the low-loss resonant SPhP mode and a high-loss resonant SPhP mode, respectively. Unlike AZO, the resonant SPhP mode for SiC is spectrally confined to a narrow window between 10 μm and 12.6 μm where the dielectric permittivity is negative. However, the lower dissipative losses of SiC, when compared to AZO, yield a much stronger enhancement as evidenced by the resonant peak at 10.6 μm of SiC, which is over an order of magnitude higher than the SPP resonant peak of AZO. This is especially remarkable given that the Planck oscillator distribution, which is represented in the far-field limit as the blackbody Planck's distribution in Fig. 2.18a, peaks closer to the SPP mode of AZO. Despite the narrowband enhancement for the resonant SPhP mode of SiC, the spectrally integrated radiative heat flux for SiC (4.61 MW/m^2) also exceeds AZO (2.06 MW/m^2). These results clearly illustrate a strongly enhanced local photon DOS can dramatically enhance near-field radiative transfer.

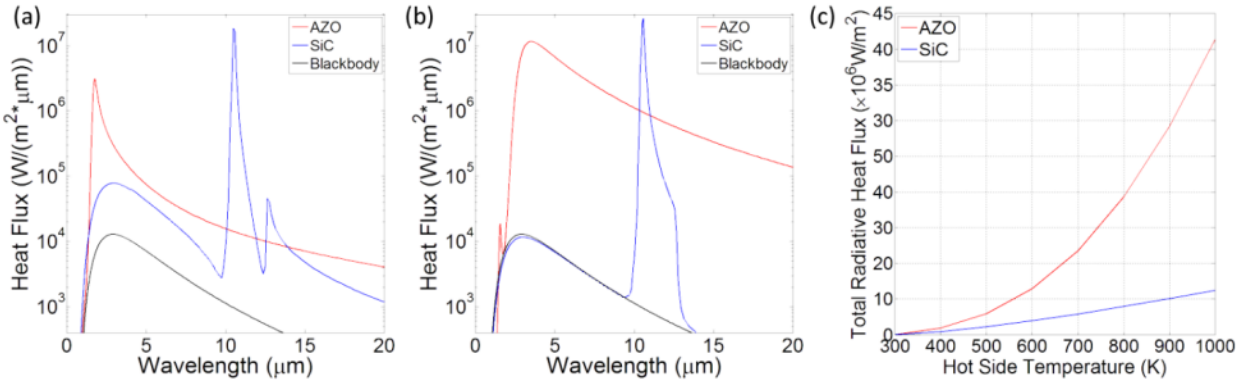

Figure 2.18: A comparison of the spectral near-field radiative heat flux for bulk and thin-film media supporting SPP and SPhP resonant modes. (a) The spectral radiative heat flux for bulk semi-infinite AZO and SiC emitters and absorbers. The hot and cold side temperatures are T_H = 1000 K and T_C = 300 K, respectively. The gap separation is g = 20 nm. (b) The spectral radiative heat flux for identical thin-film AZO and SiC emitters and absorbers suspended in vacuum. The film thicknesses for AZO and SiC are 2 nm and 20 nm, respectively, which were obtained by

optimization to maximize the total radiative heat flux. The hot and cold side temperature and the gap separation are identical to (a). The blackbody distribution is also shown in (a) and (b) for comparison. (c) The total integrated radiative heat flux as a function of the hot side temperature for the case of a 2 nm thick AZO thin-film and a 20 nm thick SiC thin-film. The cold side temperature and gap separation are again 300 K and 20 nm, respectively.

As discussed in Sect. 2.2.2, thin-film morphological effects applied to materials supporting surface polariton modes can lead to modal splitting due to coupling of the surface polariton modes on both sides of thin-film assuming both sides are in contact with either a dielectric or vacuum. This splitting will result in the formation of resonant odd and even modes, which can dramatically increase the local photon DOS over a broader wavelength range. Due to the lossy nature of these materials, modal splitting will only be observable when the films are thinner than the optical penetration depth, which for infrared wavelengths is typically on the order of tens of nanometers. In order to investigate the effects of thin-film morphology in comparison to the bulk reference case, the configuration simulated consists of two thin-films with identical thicknesses suspended in vacuum. Based on the optimization of the total radiative heat flux, it was observed progressively thinner AZO films results in a higher radiative heat flux. To avoid the non-local regime, the thickness was chosen to be 2 nm. For SiC, an optimal thickness of 20 nm was used. The spectral radiative heat flux for both cases is shown in Fig. 2.18b. For SiC, the resonant SPhP mode at 10.6 μm is enhanced compared to the bulk case, but more crucially broadens only within the spectral window where the real part of the dielectric permittivity is negative. This is an intrinsic limitation characteristic of SPhP modes which only exhibit significant near-field enhancement within a narrowband wavelength range. By comparison, the spectral radiative heat flux for AZO thin-films exhibits both substantial enhancement and broadening across the entirety of the simulated wavelength range. The SPP resonant mode at 1.5 μm is still lower in magnitude in comparison to the SPhP resonant peak of SiC at 10.6 μm; however, the overall spectral enhancement results in a spectrally integrated heat flux that now greatly exceeds SiC. While SiC exhibited a modest enhancement to the total radiative heat flux from 4.61 MW/m^2 to 6.27 MW/m^2, AZO exhibited a substantial enhancement from 2.06 MW/m^2 to 41.4 MW/m^2. Even at lower emitter temperatures, the total radiative heat flux for AZO still exceeds SiC as shown in Fig. 2.18c. This enhancement is also on par with more sophisticated structures based on hyperbolic metamaterials.[89,91,93,96]

To better understand the impact thin-film morphology has on near-field radiative transfer, Fig. 2.19 shows the transmission function, which again represents the radiative modes that contribute to radiative transfer between the emitter and the absorber, for all simulated cases. For bulk SiC and bulk AZO, it can be observed the SPhP resonant mode of SiC extends to a much greater in-plane wavevector compared to the SPP resonant mode of AZO, which is indicative of greater enhancement to the local photon DOS hence the higher spectral radiative heat flux. However, the SPP resonant mode of AZO is much broader compared to SiC, exhibiting an off-resonant tail that extends from the near-IR to the far-IR, which enables some near-field enhancement through the infrared wavelength range despite the lower photon DOS. For SiC, the thin-film morphology clearly leads to a broadening of the SPhP mode as evidenced in Fig. 2.19c; however, the enhancement due to this morphological effect is limited to a narrow wavelength range. In comparison, for AZO, the thin-film morphology has a much greater impact as the modal splitting results in a transmission function that exhibits substantial enhancement to the photon DOS over a much broader infrared wavelength range while simultaneously extending farther into the in-plane wavevector space.

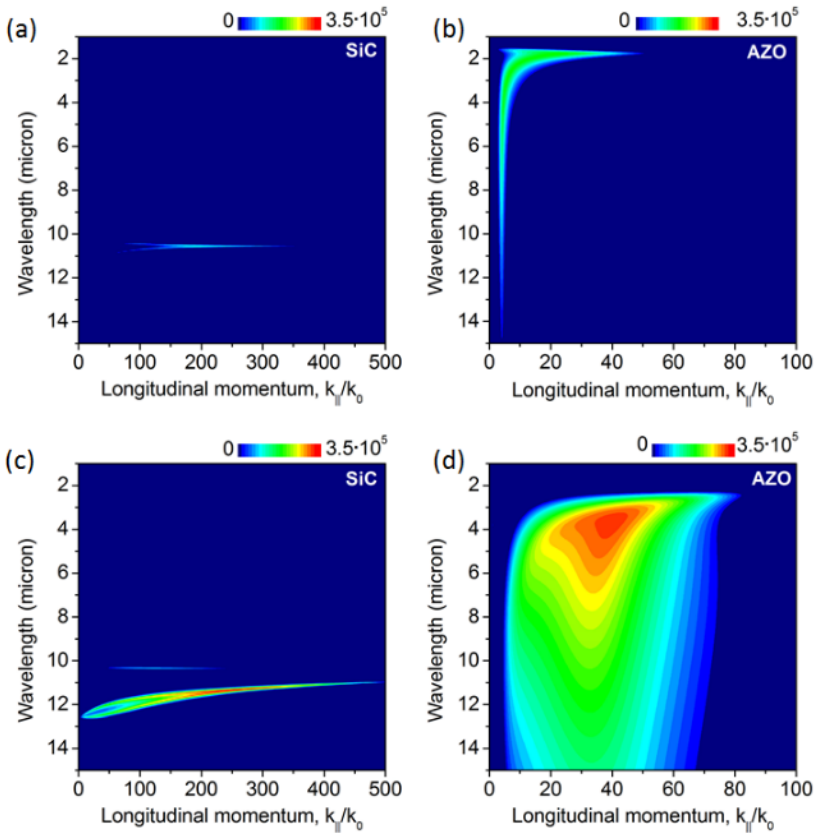

Figure 2.19: The transmission function, which provides the radiative modes that contribute to heat transfer as a function of wavelength and in-plane wave vector, for the following: (a) Bulk SiC, (b) bulk AZO, (c) thin-film SiC, and (d) thin-film AZO. The gap separation is again assumed to be g = 20 nm.

2.6.2 Combining SPP and SPhP Resonant Modes in a Multilayer Geometry

While these results show that a simple thin-film morphology can dramatically affect near-field radiative transfer, the cases calculated thus far are idealized in the sense that the films are suspended entirely in vacuum. For practical application, it would be useful to evaluate the effect of a substrate on this morphological enhancement. Ideally, to utilize the broadband enhancement of SPP modes in thin-films requires the substrate to be a transparent dielectric with a permittivity as close to 1. However, dielectric materials typically have a higher refractive index, and as evidenced by other polar dielectrics such as SiO_2 and MgF_2, can also support SPhP modes in the same wavelength range as the SPP mode, as shown in Fig. 2.20.

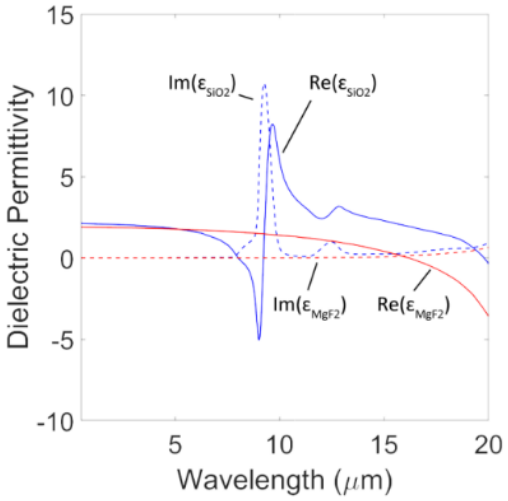

Figure 2.20: The complex dielectric permittivity for other common polar dielectrics, SiO_2 and MgF_2. The solid and dashed lines correspond to the real and imaginary component of permittivity, respectively.

For example, if the 2nm thick AZO films were placed onto SiO_2, it can be observed in Fig. 2.21a that the spectral radiative heat flux mostly matches the suspended thin-film case except in the spectral window where the SPhP resonant mode of SiC exists. Because the dielectric permittivity of SiC is negative in this window, near-field enhancement via modal splitting in the AZO film does not occur since there is no longer a SPP resonant mode at the AZO and SiC interface.

It is apparent from these results that to utilize thin-film morphological enhancement, surface polariton modes in the film cannot spectrally overlap with surface polariton modes in neighboring films or substrates. Given this observation combined with the fact that SPhP modes inherently exhibit a higher photon DOS compared to SPP modes, one can imagine that with a clever arrangement it is possible to effectively combine the high photon DOS SPhP modes of polar dielectrics with the broadband SPP modes of metals. For example, Fig. 2.21c shows the spectral radiative heat flux corresponding to a structure comprised of several thin-films of SiC, SiO2, and MgF_2, which are all polar dielectrics that support SPhP modes in different wavelength ranges. To provide near-field enhancement at wavelengths where no SPhP modes are supported, an AZO film is placed on the bottom. There is still spectral overlap between AZO and SiC, which results in a dip in the spectral radiative heat flux at 12.5 μm, but overall, this structure yields multiple peaks corresponding to the SPP and SPhP modes of all the films used. These results show that by using

a thin-film morphology, it is possible to construct a thermal emitter and absorber that can support multiple surface polariton modes, far greater than any single material available in nature.

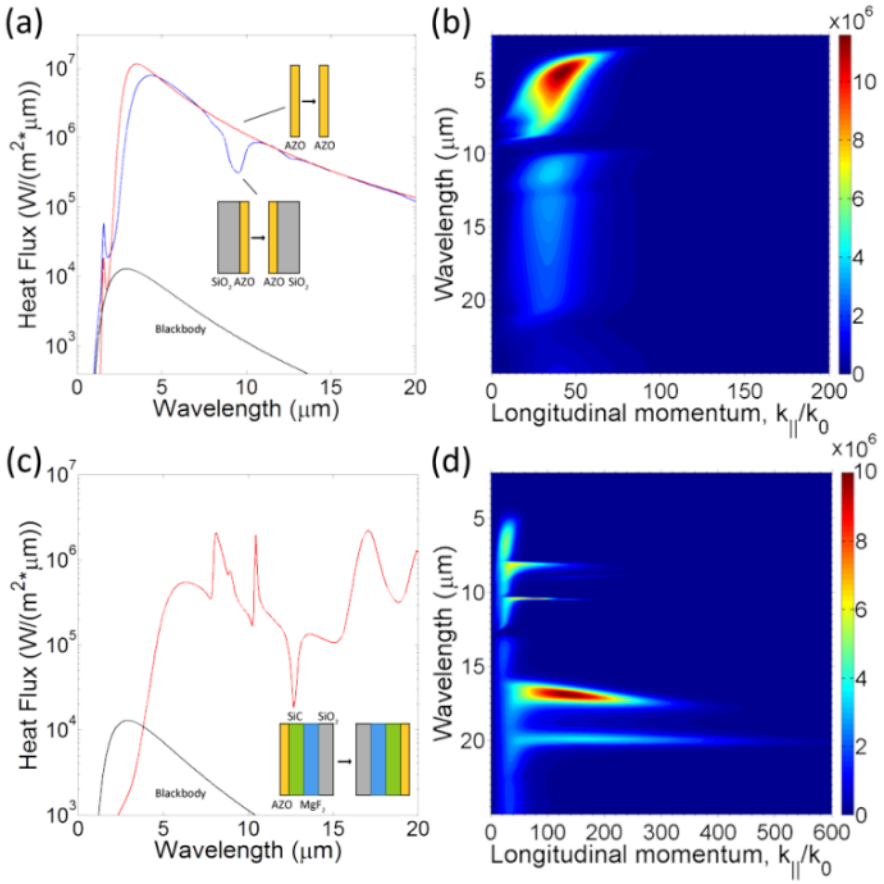

Figure 2.21: The impact of combining films and substrates supporting both SPP and SPhP modes. (a) The spectral radiative heat flux between 2 nm thick AZO films suspended in vacuum (red line) and supported by a semi-infinite SiO_2 substrate (blue line). (b) The transmission function for the case of an AZO film supported by a SiO_2 substrate shown in (a). (c) The spectral radiative heat flux for a multilayer stack comprised of a 5 nm SiO_2 film, a 5 nm MgF_2 film, a 5 nm SiC film, and a 2 nm AZO film. (d) The transmission function for the multilayer geometry shown in (c). In all cases, the hot and cold side temperatures are T_H = 1000 K and T_C = 300 K, respectively. The gap separation is also g = 20 nm.

2.7 Summary

It is well known that the morphology of an optical resonator can have a profound impact on the photon dispersion due to quantization effects that manifest by the interference of electromagnetic

waves within the resonator. When applied in the context of near-field radiative heat transfer, such morphology-driven effects can provide a degree of freedom to manipulate and tune the spectral emissive and absorptive properties beyond what is achievable using the intrinsic optical properties of the material alone. As shown in this chapter, even simple morphologies, such as a thin-film, can dramatically affect radiative heat transfer.

For semiconductors, which optically behave as lossy dielectrics, a thin-film morphology, denoted as the 'thermal well' effect, was shown to provide greater spectral selectivity in emission and absorption due to resonant enhancement from the trapped waveguide modes within the film and the cut-off frequencies these modes exhibit. As an example application that could benefit from this spectral selectivity, a theoretical TPV system was studied that consisted of a thin-film emitter and a thin-film PV cell. It was shown using a simple, yet realistic electrical model that the thermal well effect can dramatically improve the energy conversion efficiency of such a TPV system even at relatively low emitter temperatures. As an additional benefit, the use of a thin PV cell also reduces bulk non-radiative recombination losses, further improving the PV cell performance.

In contrast, a thin-film morphology applied to materials supporting surface polariton modes will result in a broadening of near-field radiative heat transfer due to modal splitting caused by the coupling of surface polariton modes on both sides of the film. Conventionally, near-field radiative transfer is most strongly enhanced for polar dielectrics supporting highly resonant SPhP modes at far-infrared wavelengths, where there is greater overlap with the Planck's distribution at modest temperatures, compared to metals, which support broad SPP modes at much shorter wavelengths. However, by applying a thin-film morphology, it was shown that the SPP mode of AZO will extend substantially further into the infrared wavelength range, enabling over an order of magnitude enhancement in radiative heat flux compared to the case of a bulk emitter and absorber. In fact, this enhancement in total radiative transfer for thin-films of AZO was shown to exceed SiC even at low temperatures. This is due to the Lorentzian dispersion of SiC, which limits broadening to a narrow spectral window. Given the inherent differences between SPP and SPhP modes, it was then shown that with clever arrangement, it is possible to stack thin-films of polar dielectrics and metals to create a composite material that supports multiple surface polariton modes that all contribute to near-field radiative heat transfer.

Chapter 3

Near-field Thermal Emission Spectroscopy

Empirical measurements of near-field radiative heat transfer have experienced significant progress in recent years due to advances in nanopositioning, microfabrication, and control. However, nearly all these studies utilize calorimetric methods, which can only provide measurements of the total, spectrally integrated radiative heat flux. Since near-field radiative heat transfer is an inherently spectrally dependent phenomena, it would be valuable to have experimental methods capable of resolving this spectral dependency both quantitatively and as a function of the gap separation. To this end, a measurement technique is developed in this chapter that can enable both quantitative and gap-dependent spectral measurements of near-field radiative heat transfer. The proposed method uses a high index prism, which can couple to evanescent near-field radiative modes due to its higher photon DOS, in an inverse Otto-configuration in combination with a Fourier-transform infrared (FTIR) spectrometer. In this chapter, a brief theoretical analysis will be provided to evaluate the limits of this approach. This will be followed by an overview of the experimental configuration and procedures used to evaluate near-field radiative heat transfer spectrally. And finally, preliminary experimental results will be presented that show this proposed method can indeed be used to quantitatively measure gap-dependent near-field thermal radiation spectrally.

3.1 Empirical Investigations of Near-field Radiative Heat Transfer

As introduced in Ch. 2, theoretical studies of near-field radiative heat transfer historically span several decades where much of the theoretical formulation was developed by the 1970's. This was followed by a more recent resurgence in the 2000's where more sophisticated methods were created to model increasingly complex geometries.[22] In parallel with these developments, empirical studies of near-field radiative heat transfer have followed a similar evolution over the years.

The earliest experiments date back to the late 1960's where calorimetric-based measurements of radiative heat transfer were performed between metallic disks in a parallel-plate

configuration.[25–27] Cravalho *et al.* and Domoto *et al.* were amongst the first to observe empirical evidence of near-field enhancement in 1968 and 1970, respectively, by measuring the radiative heat transfer between two cryogenically cooled copper disks at various gap separations.[25,26] In these measurements, the total radiative heat flux was measured by heating one disk to an elevated temperature and measuring the temperature rise of the other disk relative to the vacuum chamber wall. A similar study was performed by Hargeaves in 1969 where near-field enhancement was observed between two chromium-coated disks at room temperature separated by a gap as small as 10 μm.[27] In this work, the radiative heat flux was measured by heating one disk to an elevated temperature and measuring the heating power needed to maintain the other disk at a constant temperature for different gap separations. Although these early studies provided the first evidence of enhanced radiative transfer in the near-field regime, further efforts to measure near-field enhancement at smaller gap separations were hampered by technological limitations of the time associated with aligning two parallel plates with sub-micron precision.

Subsequent studies of near-field radiative heat transfer would not occur until a couple decades later with the inadvertent observation of anomalous heat transfer during operation of a scanning thermal profiler (STP), which was invented in the mid-1980's.[169] The STP consists of a scanning probe, similar to an atomic force microscope (AFM) or scanning tunneling microscope (STM) probe, with a small thermocouple integrated at the end of the tip. The purpose of the STP probe was to provide a material-independent and non-contact method for profilometry by measuring the heat flux between the heated probe and the sample substrate as it is moved along the surface. However, in these studies the heat transfer between the probe tip and the sample was found to be distance dependent, which could not be explained only by variations in ballistic heat conduction through air.[170] Subsequent studies in vacuum determined this variation to be due to near-field enhanced radiative heat transfer.[171–173] This tip-plate configuration was crucial to the progress of near-field radiative heat transfer, as it bypassed the difficulties of alignment in the parallel-plate configuration, thus enabling empirical measurements down to the extreme near-field with gap separations on the order of 10 nm and less. Although the measured near-field radiative heat flux is inherently small due to the tip geometry, initial studies with this configuration already utilized systems with heat flux sensitivities as low as 10 nW.[171] Since the inception of this configuration, further studies have been conducted with improvements to the reliability and

sensitivity of the system, enabling measurements for a wide variety of materials with gap separations as small as 2 nm.[174–177]

In the late 2000's, a sphere-plate configuration also became prominent, which enabled measurements of near-field enhancement between macroscopic media without the alignment difficulties associated with the parallel-plate configuration.[60,68,83,178–182] This led to some of the first near-field measurements with sub-micron gap separations. Measurements utilizing this configuration have primarily relied on an AFM-based method to measure near-field radiative heat transfer. In this approach, an AFM bilayer cantilever is used to detect radiative heat fluxes as small as several nanowatts by measuring a thermally-induced bending response caused by the thermal expansion of the two layers when a temperature change occurs across the cantilever.[60,68,83,178,179,181,182] A large microsphere is attached to the tip of the cantilever and heated using a laser. As the microsphere is brought close to a room temperature substrate, radiative heat transfer to the substrate will cool the microsphere, resulting in a bending response that is correlated to the near-field radiative heat flux. This method has led to observations of near-field enhancement several orders of magnitude higher than the far-field blackbody limit at gap separations as small as 30 nm for a variety of material systems. Recently, a more sophisticated calorimetric approach based on suspended microfabricated platforms with resistive heating and thermometry was used to measure the radiative heat flux between a heated polar dielectric microsphere and thin-films down to gap separations of 20 nm.[180]

Coinciding with the introduction of the sphere-plate configuration, a return to the parallel-plate configuration also occurred during this time, in which more sophisticated methods to control the gap separation were used. One study utilized polystyrene microsphere spacers to separate a hot glass plate emitter from a room temperature glass substrate where the radiative heat flux between the two plates was measured using a heat flux meter.[183] Although gap-dependent measurements were not possible with this configuration, the radiative heat flux was still shown to exceed the blackbody limit by 35% at a gap separation of 1 μm. Recent studies have also improved upon the experimental apparatuses used in the original studies from the 1960's and 1970's to measure near-field radiative transfer at smaller gap separations.[184–186] Specifically, the use of multiple piezoelectric actuators combined with capacitive sensing have enabled greater control of the alignment between two parallel plates enabling gap separations as small as 1 μm. Both cryogenic and room temperature studies have been performed using tungsten and sapphire plates,

respectively, showing radiative heat fluxes exceeding the blackbody limit by 1-2 orders of magnitude.[184–186] Microfabricated systems, similar to the sphere-plate configuration mentioned earlier, have also been used to study near-field radiative heat transfer between suspended plates and beams.[187–189] These systems again rely on calorimetric methods using resistive heating and thermometry to measure the radiative heat flux between a hot and cold planar medium. Using integrated piezoelectric actuation, near-field enhancement was observed for gap separations less than 100 nm.[189]

3.1.1 Spectral Measurements of Near-field Radiative Heat Transfer

The plethora of empirical studies conducted in the near-field regime over the years have led to substantial improvements for a variety of experimental techniques, which have enabled measurements of near-field radiative heat transfer at progressively smaller gap separations. However, in these studies the core methodology used to measure the radiative heat flux still rely upon calorimetric approaches, which can only provide measurements of the total, spectrally-integrated radiative heat flux. As discussed throughout Ch. 2, near-field radiative heat transfer can exhibit significant spectral variation, especially for materials supporting surface polariton modes. Despite the overall advances made to empirically measure near-field radiative heat transfer, there is still substantial room for the development of techniques that can measure the spectral properties of radiative transfer in this regime.

Since the mid-2000's, the development of methods to extract the spectral properties of radiative transfer in the near-field have focused primarily on using a scanning probe tip to scatter evanescent fields into the far-field regime.[190–197] The first demonstration utilized a STM probe to create high resolution images of an underlying sample by scattering evanescent fields thermally emitted by the sample into a photodetector.[190] This method became known as the thermal radiation scanning tunneling microscope (TRSTM). Subsequent studies modified this experiment by incorporating a Fourier-transform infrared (FTIR) spectrometer into the system, thus enabling spectral characterization of the scattered thermal radiation.[193] In this manner, direct measurements of the local density of states enhancement in the near-field regime became possible. Variants of this approach have also been developed in recent years including thermal infrared near-field spectroscopy (TINS)[192,196], which utilizes a heated AFM cantilever tip to locally heat a sample to

much greater temperatures than in TRSTM, as well as a scattering scanning near-field optical microscopy (s-SNOM), which uses an external infrared source to illuminate the sample.[191,194,195]

Although these scattering-based techniques enabled the first empirical spectral measurements of near-field radiative heat transfer, these techniques are limited as they are only able to provide qualitative measurements of near-field enhancement. Furthermore, the need to modulate the gap separation, which is used to improve the signal-to-noise ratio via lock-in detection, has limited systematic gap-dependent measurements of near-field enhancement as well. Therefore, there is a need for fundamentally new techniques that can provide quantitative spectral measurements of near-field radiative heat transfer at different gap separations. In an effort to satisfy these requirements, this chapter will introduce an alternative approach to spectrally measure near-field thermal radiation. This approach will utilize conventional techniques to externally couple light to high momentum evanescent modes in a reverse manner to extract evanescent thermal emission to the far-field regime.

3.1.2 Optical Coupling Schemes for High Momentum Evanescent Modes

The main challenge of measuring near-field radiative heat transfer spectrally is the need to extract thermally emitted evanescent modes to free space in order to perform spectral analysis. To devise a method that bridges the near- and far-field regimes while enabling quantitative and gap-dependent spectral measurements, inspiration can be drawn from the reciprocal problem of externally coupling light from free space to high momentum evanescent modes. This is an area that has been investigated since the 1960's in application to the excitation and probing of SPP modes at metal-air interfaces.[198,199]

In 1968, Andreas Otto devised a method to excite SPP modes with external illumination using an intermediate high index prism positioned at a small gap relative to the sample surface, as illustrated in Fig. 3.1a.[198] The high index prism provides additional momentum to the incoming light, which can be used to couple directly to high momentum SPP modes. This coupling occurs through frustrated total internal reflection, where evanescent fields at the prism-air interface created by the total internal reflection of light incident at angles larger than the critical angle can tunnel across the gap to excite SPP modes at the metal-air interface. Although this method provides a direct approach to couple light from the far-field regime to evanescent modes in the near-field

regime, its use in spectroscopy has been relatively limited due again to the practical difficulties associated with aligning the prism to the sample at sufficiently small gap separations.

To overcome these alignment difficulties, Erwin Kretschmann devised a modified approach in 1971 that also utilized a high index prism to excite SPP modes.[199] In this method, a thin-film of metal is deposited directly onto the prism, as shown in Fig. 3.1b. Evanescent fields are again formed via total internal reflection at the prism-metal interface, which can tunnel through the metal to excite SPP modes along the metal-air interface. In this manner, it became possible to excite SPP modes without requiring any alignment between the sample and the prism.

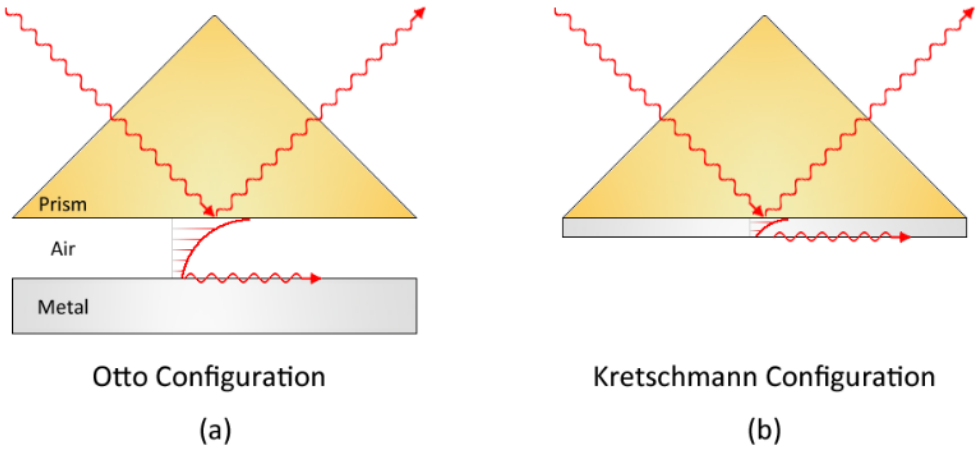

Figure 3.1: Schematic illustrations detailing (a) the Otto and (b) the Kretschmann configurations, which were used to externally excite SPP modes supported at the metal-air interface.

3.1.3 Overview of Experimental Approach

Based on these methods, an Otto configuration is chosen for spectral measurements of near-field radiative heat transfer as it enables gap-dependent variations of near-field coupling between the sample and the prism. The Kretschmann configuration, despite its experimental convenience, would only allow for direct contact measurements of near-field thermal radiation. By leveraging the photonic dispersion of the high index prism to match the high momentum evanescent modes of a thermal emitter, an inverse Otto configuration can enable the direct extraction of thermal emission from the near-field to the far-field regime.

In fact, as further justification for this approach, a recent study used a high index prism to enhance far-field radiative heat transfer based on a similar methodology.[200] In this study, a carbon

black emitter was placed in direct contact with a large zinc selenide (ZnSe) hemispherical prism. The n^3 enhancement in the photon DOS of the prism enabled thermal radiation that would otherwise be trapped via total internal reflection in the emitter to couple through the prism into the far-field regime. Although this study did not explore radiative heat transfer in the near-field regime, it nonetheless confirms the underlying mechanism of near-field extraction is valid.

In the remaining sections of this chapter, various aspects of the proposed method for near-field thermal emission spectroscopy will be discussed. First, a brief theoretical overview will be provided to evaluating the effect of the prism's refractive index on the spectral properties of the near-field thermal radiation measured. This will be followed by a detailed description of the experimental apparatus used in this work. And finally preliminary data will be presented that shows the first evidence that this method can indeed be used to quantitatively measure spectral radiative heat transfer in the near-field regime at various gap separations.

3.2 Dependency of Near-field Coupling on Prism Refractive Index

The key mechanism to measure near-field radiative heat transfer spectrally with the proposed inverse Otto configuration is the ability of the high index prism to sufficiently couple out high momentum near-field modes from the thermal emitter. This will depend greatly on the photonic dispersion of the prism, which is solely a function of its refractive index. In order to evaluate the impact of the refractive index on the spectral properties of the extracted near-field thermal emission, a theoretical calculation was performed using the formulations developed in Ch. 2 for two semi-infinite planar media. In reference to the experiment, the thermally emitting medium was chosen to be silicon dioxide with optical constants taken from literature as shown in Fig. 3.2b. The emitter temperature was set to a temperature of T_H = 550 K. To model the high index prism, a lossless dielectric with a variable refractive index was used. It should be noted that since the prism is transparent and thus will not emit, the temperature of the prism is not important in this analysis. The gap separation was fixed at g = 100 nm.

The theoretical predictions of the spectral radiative heat flux for this system are shown in Fig. 3.2c for various refractive indices. It can be observed that an optimal refractive index exists to maximize the spectral radiative heat flux at different wavelengths. Initially, an increase in the refractive index will lead to a corresponding increase in the spectral radiative heat flux as the prism couples to more high momentum near-field modes. However, as the refractive index continue to

increase further, this enhancement in the radiative heat flux will reach a maximum and subsequently decrease due to the growing impedance mismatch at the air-prism interface. As shown, the optimal refractive index will vary for different wavelengths depending on how far these near-field modes extend into momentum space.

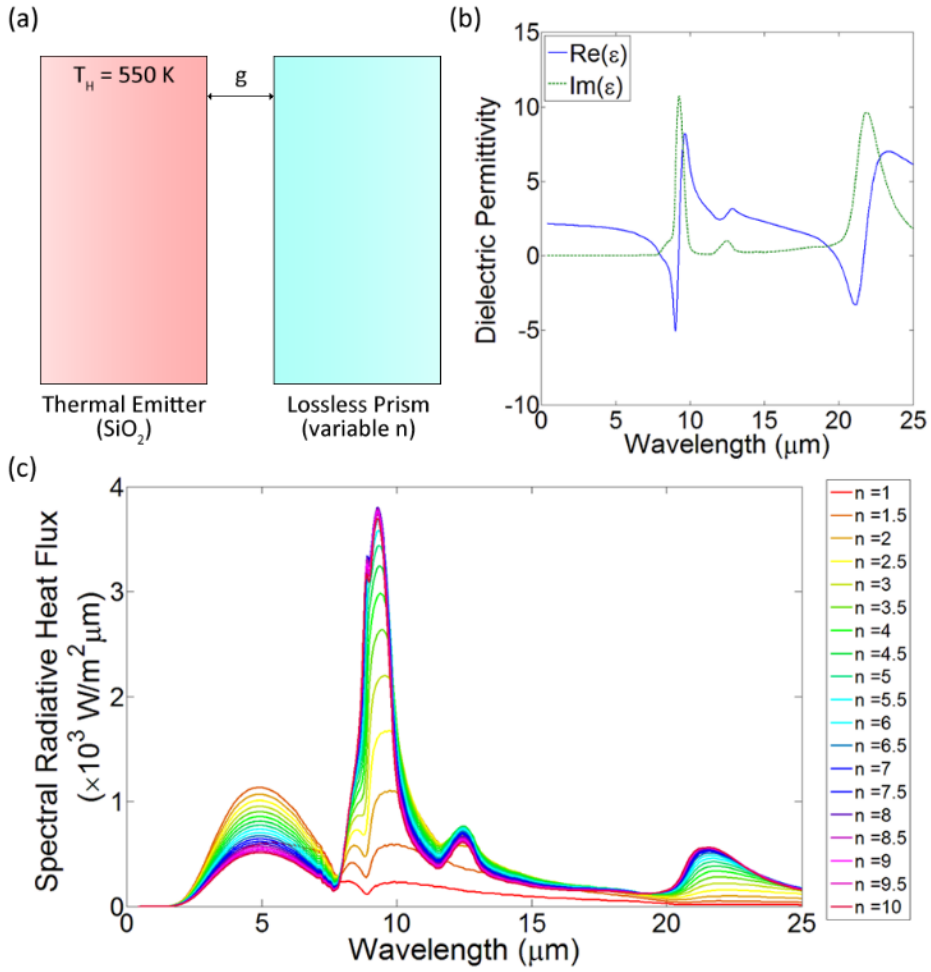

Figure 3.2: Theoretical predictions of the spectral radiative heat flux on the refractive index, n, of prism. (a) A schematic illustration of the system simulated. A hot side temperature of T_H = 550 K and a gap separation of g = 100 nm is used. (b) The dielectric permittivity of SiO_2. (c) The spectral radiative heat flux for a varying prism refractive index.

For example, bulk thermal emission from silicon dioxide, which primarily occurs at wavelengths shorter than 7.5 μm, reaches a maximum when the refractive index of the prism is 1.4, corresponding to the refractive index of silicon dioxide. At this optimum refractive index, the

prism can couple to all the radiative modes of silicon dioxide, including the evanescent modes trapped via total internal reflection. Further increases in the index of the prism do not provide any additional enhancement and with the increase in the Fresnel reflection coefficient at the prism-air interface, the radiative heat flux becomes suppressed. For comparison, the optimal refractive index at wavelengths between 7.5 μm and 11 μm is much larger with an index of ~8, corresponding to the SPhP mode of silicon dioxide. The SPhP mode extends much farther into momentum space compared to bulk thermal emission, hence the higher refractive index needed to fully extract this mode.

From these observations, it is clear the choice of the prism can affect the measured spectral properties of the near-field thermal radiation emitted by a sample. For a silicon dioxide thermal emitter, the optimal refractive index of the prism spans a rather large range from 1.4 to 8. It is important to note that prisms used in the infrared wavelength range tend to exhibit a much more limited range in the refractive index. Prisms made of ZnSe, silicon (Si), or germanium (Ge) are typically used, which exhibit refractive indices ranging from 2.3~4. Despite the limited range, a change in the refractive index from 2.3 to 4 can still yield a significant variation in the measured spectral radiative heat flux, as shown in Fig. 3.2c. Thus, the choice of the prism is still important and may vary depending on the nature of the evanescent modes supported in a sample.

3.3 Experiment Apparatus

A schematic illustration of the inverse Otto configuration used to spectrally measure near-field radiative heat transfer in this work is shown in Fig. 3.3. The primary challenge in applying this configuration for measurements in the near-field regime is the implementation of a method to control and calibrate the gap separation between a heated thermal emitter and a high index prism. As illustrated in Fig. 3.3, the approach used in this study consists of a heated thermal emitter mounted onto a cantilever beam, whose position is controlled by a piezoelectric motor. The calibration of the contact point between the emitter and the prism is achieved by measuring a change in the beam deflection as contact is made. The deflection of the cantilever is measured by reflecting a laser beam off a mirror mounted at the tip of the cantilever onto a position sensitive detector (PSD), which can spatially track the motion of the laser spot. This approach was inspired by previous studies that utilized atomic force microscope bilayer cantilevers as high sensitivity thermal sensors, in which measurements of deflection down to the sub-nanometer range were

achieved using this optical detection scheme.[201–204] With this approach, the position and contact of the thermal emitter and the prism can be controlled in the near-field regime with great precision.

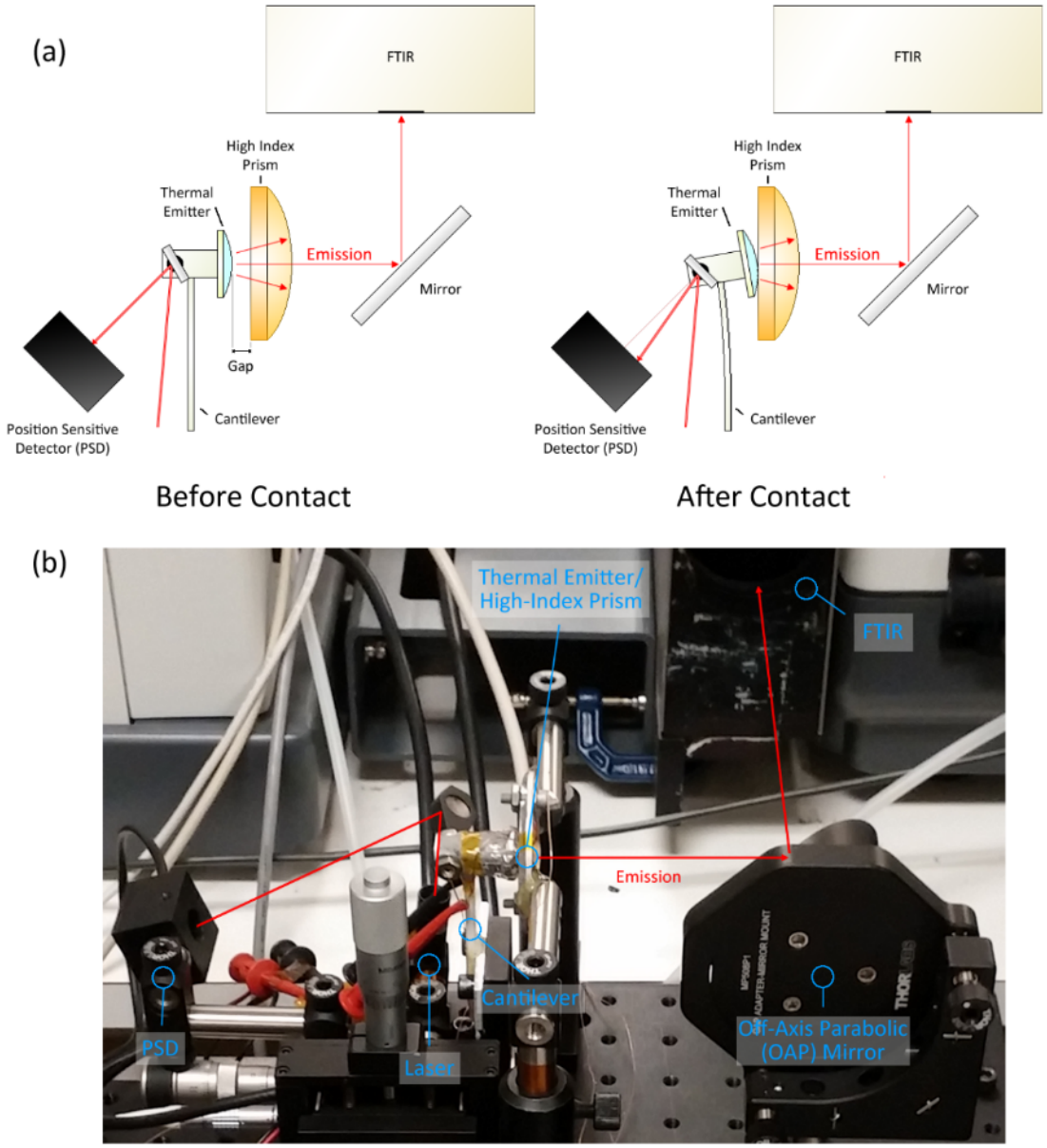

Figure 3.3: (a) A schematic illustration detailing the method used to calibrate the contact point between the thermal emitter and the prism. The thermal emitter is mounted onto a cantilever, which will only bend when contact is made with the prism. This bending response is measured optically using a laser reflected off the tip of the cantilever onto a position sensitive detector (PSD). (b) A corresponding image of the actual experimental platform detailing how these components are used.

For experimental convenience, the thermal emitter is chosen to have a spherically convex surface, similar to the sphere-plate configurations used in past studies. This eliminates the need to align two parallel surfaces with sub-micron precision. The tradeoff of this approach is that the measured thermal emission will include far-field thermal radiation, thus reducing the strength of the measured near-field contribution. However, by carefully choosing the appropriate curvature and restricting the measured emission area, it is possible to still observe near-field thermal enhancement.

Once the evanescent radiative modes in the near-field regime couple to the prism, it will propagate until it reaches the prism-air interface at which point a portion of this thermal radiation will transmit to the environment. This thermal emission is then optically guided into a Fourier-transform infrared (FTIR) spectrometer for spectral measurement. It should be stressed that the emission input into the FTIR is broadband. To acquire the spectral characteristics of the thermal emission, the FTIR (Thermofisher, Nicolet 6700) utilizes a Michelson interferometer to temporally transduce the spectral properties of the emission source, which are located in the high frequency THz range, to much lower frequencies that can be measured using conventional electronics. This process transforms the emission input, which was originally a continuous source as a function of time, into an interferogram that contains the spectral properties of the source at these lower frequencies. To measure the interferogram, a liquid nitrogen cooled mercury-cadmium telluride (MCT-A) photodetector is used. A Fourier transform is then applied to the interferogram to convert the measured emission from the time domain to the frequency domain resulting in a thermal emission spectrum. In this manner, near-field thermal emission extracted into the far-field regime can be spectrally characterized.

It should be mentioned that for the sake of conceptual demonstration, the experiment was conducted in open ambient air instead of in a vacuum chamber. This decision was made in the interest of significantly simplifying the experimental platform. However, the drawback is the added uncertainty of the emitter temperature due to conductive cooling. This uncertainty will require appropriate calibration and correction, which will be discussed in Sects. 3.3.7 and 3.4.3. In the following sections, further details will be provided on the design, construction, and operation of the various components used in the experiment.

3.3.1 Measurement Methodology

In this study, near-field thermal emission spectra extracted into the far-field regime is measured by taking a ratio of the thermal emission intensity in the near-field regime and dividing it by the intensity in the far-field regime. The near- and far-field regimes are determined by the position of the thermal emitter relative to the prism, which is controlled by the piezo stage. This ratio is defined as the near-field enhancement, β, and is formulaically expressed as follows,

$$\beta(\lambda) = \frac{I_{emi}^{NF}(\lambda)}{I_{emi}^{FF}(\lambda)} = \frac{I_{tot}^{NF}(\lambda) - I_{env}(\lambda)}{I_{tot}^{FF}(\lambda) - I_{env}(\lambda)} \tag{3.1}$$

where I_{emi}^{NF} and I_{emi}^{FF} are the thermal emission intensities in the near- and far-field regimes, respectively.

In the experiment, the measured intensities, I_{tot}^{NF} and I_{tot}^{FF}, will also include parasitic emission from the environment and the internal components in the FTIR. For the particular experimental configuration used, the dominant contribution of parasitic emission comes from the FTIR itself, which was observed by measuring a negligible change in the intensity when an external port to the FTIR is opened and closed. In addition, the internal optics of the FTIR will also parasitically absorb thermal emission as well. Thus the measured intensity is composed of the following terms,

$$I_{tot}(\lambda) = \alpha_{env}(\lambda) I_{emi}(\lambda) + I_{env}(\lambda) \tag{3.2}$$

where α_{env} is the parasitic absorptance of the FTIR and I_{env} is the environmental background emission intensity. To eliminate these sources of error, a background calibration is needed, which consists simply of a measurement where the extracted thermal emission from the prism is redirected away from the FTIR. The resulting background intensity can then be used to directly subtract out parasitic emission as shown in Eq. (3.1). Given that the parasitic absorptance remains the same for all measurements, taking the ratio of the background-corrected intensities will automatically compensate for this source of error. To maintain an accurate correction for these sources of error, a background calibration is performed before and after each near-field and far-field measurement. An average of both these measurements are used in Eq. (3.1).

3.3.2 Cantilever Design

The cantilever, which is used to calibrate the contact point between the thermal emitter and the prism, was designed to satisfy two main requirements: (1) the cantilever must be thermally insulating to prevent heating of the piezo stage and to reduce the heating power needed to maintain the thermal emitter at a high temperature and (2) the cantilever must be mechanically sensitive to enable contact calibration while exhibiting a resonance frequency that is high enough to avoid vibrational noise. To meet these requirements, the cantilever was fabricated from Macor (McMaster, 8489K54), which is a machinable glass-mica ceramic that exhibits mechanical properties similar to aluminum (E_{mac} ~ 66.9 GPa) and a thermal conductivity similar to glass.[205] The cantilever was machined with the following dimensions: the height, H, is 1/8" (3.175 mm), the width, W, is 3/8" (9.525 mm), and the length, L, is 1.3" (33 mm). These dimensions were chosen based on empirical tests of previous design iterations.

The thermal insulative performance of the cantilever was estimated using a simple heat transfer simulation where it was assumed the cantilever had a hot side temperature of T = 175^{o}C as well as both convective cooling (h_{conv} = 5 W/m^{2}K) and radiative cooling (ε_{mac} = 1). The thermal conductivity of Macor is k_{mac} ~ 1.4 W/mK. The temperature distribution, shown in Fig. 3.4a, suggest a rapid decrease along the length of the beam with a predicted base temperature of ~43^{o}C, which is only 20^{o}C higher than the ambient temperature. As shown in Fig. 3.4b, the cantilever was mounted on an aluminum plate using high strength epoxy, which was then screw mounted onto a bracket and placed on the piezo stage (Thorlabs, NFL5DP20S). Given the manner in which the Macor cantilever is mounted, it was empirically verified that at an emitter temperature of 175^{o}C, the piezo stage does not exhibit any appreciable heating.

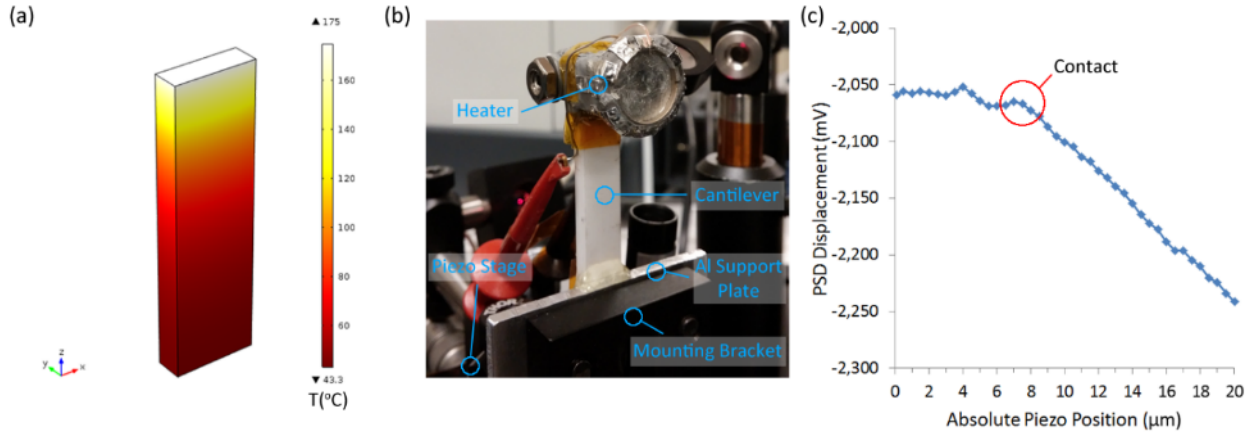

Figure 3.4: (a) The simulated temperature distribution along the cantilever beam made of Macor. As shown, the large temperature gradient indicates the cantilever is sufficiently thermally insulating. (b) An image of the cantilever and the heater mounted onto the piezo stag. (c) An example contact calibration where the heater was brought into contact with the prism, resulting in a linear bending response.

The resonant frequency of the cantilever beam can be estimated assuming the beam behaves as a simple harmonic oscillator such that $f = \sqrt{k/m}$, where k is the effective spring constant and m is the total mass at the end of the cantilever. To determine the effective spring constant, standard beam theory can be used for a beam constrained at one end and a point load applied at the free end. In this case, $k = 3EI/L^3$ where E is the Young's modulus and I is the moment of inertia. For a beam with a rectangular cross section, $I = WH^3/12$. The Young's modulus of Macor is $E_{mac} \sim 66.9$ GPa. The total mass is estimated to be m = 0.1 kg based on the weight of all the components used to construct the thermal emitter, which includes the mirror, the Macor supports, the heater, the sample emitter as well as several other components to secure the sample emitter as detailed in Sect. 3.3.3. Based on these parameters, the resonant frequency is predicted to be $f \sim 1.2$ kHz. This is substantially higher than common sources of vibrational noise, which typically occur at frequencies less than 100 Hz.

To evaluate the bending sensitivity of the cantilever, empirical tests were performed at room temperature to assess whether contact was observable by measuring the deflection of the cantilever optically as the piezo stage moves the thermal emitter into contact with the prism. To optically measure the bending of the cantilever, a 632 nm laser diode (Lasermate, LTG6354AH)

powered by a DC voltage supply and a 4 mm x 4 mm PSD (Ontrak Photonics, 2L4SP) are used, as shown in Fig. 3.3b. For these tests, the cantilever was initially placed several microns from contact using the micrometer on the piezo stage and incrementally moved in steps of 500 nm towards the prism past the point of contact. For each position, the data was averaged over a period of 5 seconds. An example set of contact calibration data is shown in Fig. 3.4c, which provides the beam spot position measured by the PSD as a function of the absolute position of the piezo stage. As shown, the position of the beam spot initially remains stationary, indicating that the cantilever is not bending, hence no contact between the thermal emitter and the prism. Once contact is made, the cantilever will begin to bend as indicated by the change in the beam spot position. Because this bending is small, the shift in the beam spot position is approximately linear. By applying linear fits to regions before and after contact is made, it is possible to estimate the piezo position where contact initially occurs. Based on the data shown in Fig. 3.4c, it was empirically verified the cantilever beam was sufficiently sensitive to calibrate the contact point.

To calibrate the contact position during the experiment, the micrometer is first used to coarsely position the thermal emitter to the contact point with the prism based on the PSD deflection signal. The piezo stage, which only has a range of 20 μm, is initially set to its midpoint during this coarse alignment in order to maximize the piezo range before and after contact. A similar procedure that produced the data in Fig. 3.4c, is then applied to precisely determine the contact point. This calibration is performed before and after the gap-dependent near-field measurement to verify there was no drift in the piezo stage during measurement.

3.3.3 Thermal Emitter and Heater Design

The heater was designed around a 0.5” diameter N-BK7 lens (Thorlabs, LA1213), which functions as the thermal emitter in this experiment. N-BK7 is a common borosilicate glass that supports a prominent surface phonon polariton mode in the 9 to 12 μm wavelength range. The thermal emitter was chosen to have a convex spherical curvature to eliminate the non-trivial requirement of aligning two parallel plates. The particular N-BK7 emitter used exhibits a radius of curvature of 25.8 mm, which was chosen to maximize the near-field contribution to thermal emission while avoiding premature contact with the pinhole aperture discussed in Sect. 3.3.4. To heat the thermal emitter, an aluminum nitride ceramic heater is used, which is covered by aluminum tape to avoid parasitic emission from the heater. The ceramic heater is embedded in several retaining rings,

which support the N-BK7 emitter, as shown in Fig. 3.5. This assembly was adhered together using a high temperature, low thermal expansion stainless steel adhesive (Cotronics Corp., Durabond 954).

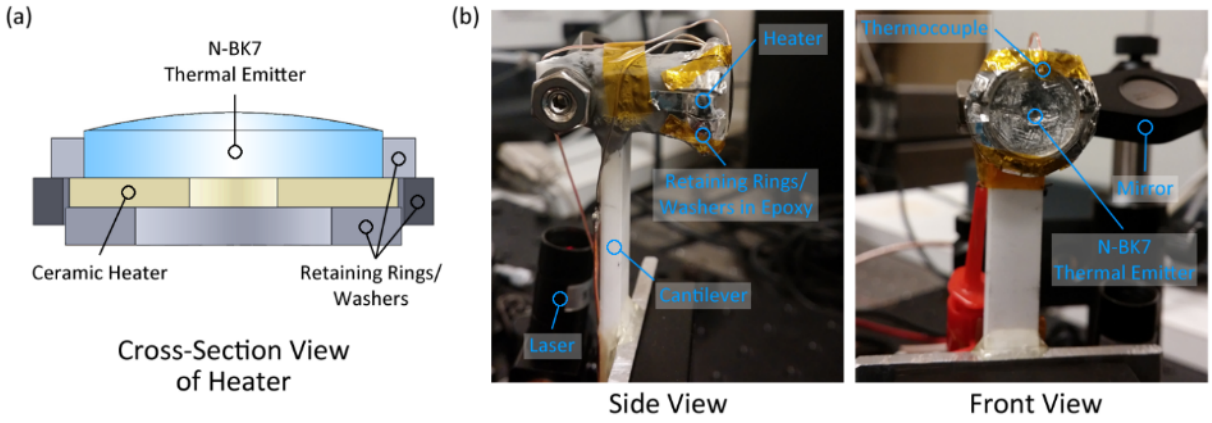

Figure 3.5: (a) A cross-section view of the heater and the thermal emitter with several retaining rings and washers for support. (b) Side and front view images of the thermal emitter mounted onto the cantilever with a N-BK7 thermal emitter.

Before the measurements were performed, the N-BK7 emitter was cleaned in a piranha solution to remove any organic contaminants. As shown in Fig. 3.5b, the N-BK7 emitter is press fit into the heater, taking care to avoid touching the center of the lens where emission is collected. Kapton tape is placed at the edge of the emitter to ensure the emitter remains in place since thermal expansion of the holder at elevated temperatures may cause the N-BK7 emitter to loosen. Although the Kapton tape may parasitically emit thermal radiation, the view factor between the edges of the thermal emitter and the pinhole aperture on the prism, which will be discussed in more detail in Sect. 3.3.4, is negligible. This ensures thermal emission is only measured from the center of the thermal emitter that is exposed by the pinhole aperture. To align the thermal emitter to the prism, alignment marks were incorporated on the heater and the prism holder as a visual reference.

A K-type thermocouple is also placed in direct contact with the thermal emitter 1 mm from its edge using Kapton tape. Temperature is measured using a handheld thermocouple reader (Omega, HH23A). While it is more ideal to place the thermocouple closer to the center, the thermocouple is intentionally placed near the edge to maintain sufficient clearance between the thermocouple and the prism in the near-field regime. As a result, the measured temperature will

overestimate the temperature of the near-field thermal emission collected by the FTIR, especially in the near-field regime where conducive heating losses are more dominant. As will be discussed in Sect. 3.3.7, this emitter edge temperature can nonetheless provide a reference point for an approximate calibration.

3.3.4 Extraction Prism and Holder Design

Similar to the design of the heater discussed in Sect. 3.3.3, the design of the prism holder was based around a 1" diameter zinc selenide (ZnSe) lens (Thorlabs, LA7542-UC-SP), which is used as the extraction prism in this study. Although ZnSe exhibits a relatively low refractive index of 2.3, which is not necessarily optimal for coupling to high momentum surface polariton modes as discussed in Sect. 3.2, it was chosen as it can be used over a large temperature range. Other widely available infrared optics made of silicon and germanium exhibit electronic band gaps of 1.1 eV and 0.67 eV, respectively. At elevated temperatures, the combination of band-gap shrinkage due to thermal expansion and the thermal excitation of free electrons from the valence band will render these materials opaque. By contrast, ZnSe exhibits a large electronic band gap of 2.7 eV, which exhibits a minimal decrease at temperature in excess of 300ºC.[206] Thus, ZnSe will remain transparent at the relevant temperatures used in the experiment.

By conducting the measurement in ambient conditions, the maximum temperature for ZnSe is approximately 300ºC, beyond which oxidation will damage the prism. A custom-made holder with screw-mounted clips was used to secure the ZnSe lens into place, as shown in Fig. 3.6a. A K-type thermocouple is also incorporated to monitor the temperature of the ZnSe lens during the experiment using the same handheld thermocouple reader mentioned in Sect. 3.3.3. Prior to using the ZnSe lens for the experiment, it was sonicated in a solution of acetone for 10 minutes and dried using lens paper to remove any organic contaminants.

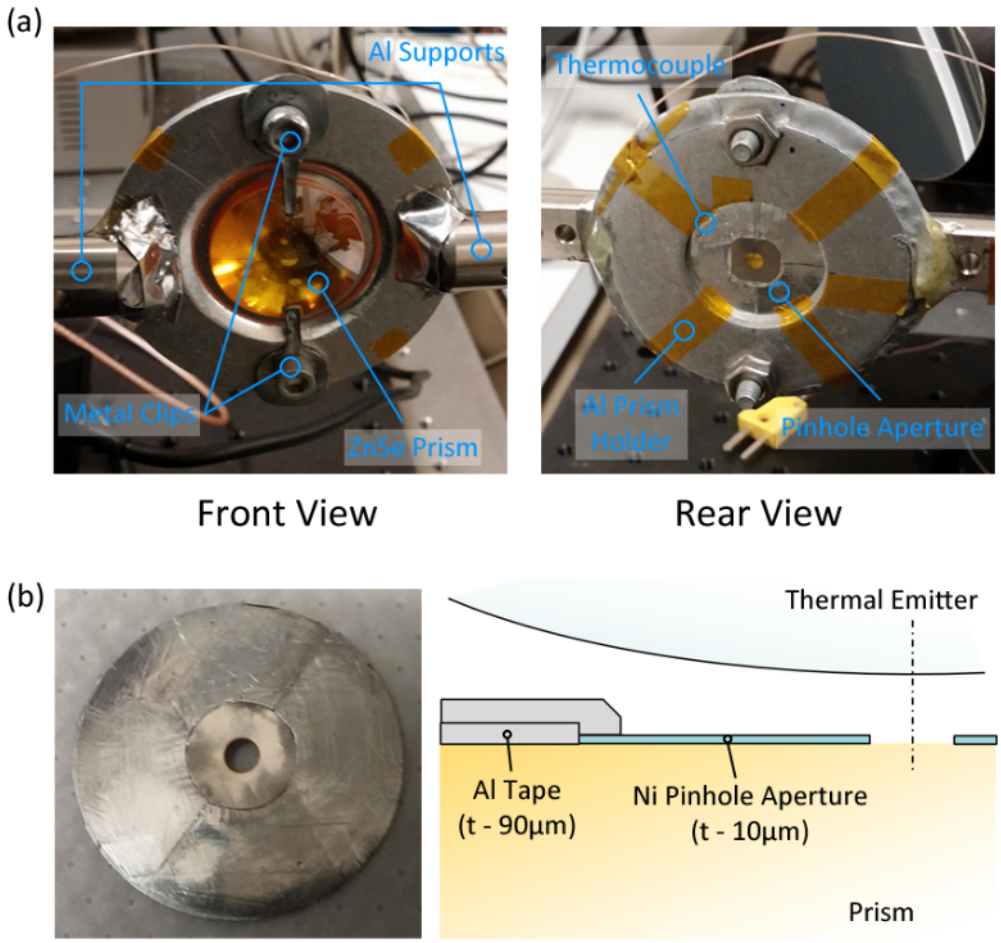

Figure 3.6: (a) Front and rear images of the ZnSe prism and the holder used to support the prism. (b) An image of the pinhole aperture fabricated to reduce the far-field contribution to the measured thermal emission intensity. A schematic illustration is also included, showing a cross section image of the pinhole aperture.

A pinhole aperture was also placed onto the planar side of the ZnSe lens to reduce the contributions of far-field thermal radiation from the periphery of the thermal emitter in order to more clearly observe the near-field thermal emission extracted from the prism. The specific pinhole aperture (National Aperture, Inc., 1-3000) used consists of a 9.525 mm diameter, 10 μm thick circular film of nickel with a 3 mm diameter aperture at its center. In order to fully cover the ZnSe prism, aluminum tape (3M, 1-5-433L) was used to extend the pinhole aperture to the edges of the ZnSe prism, as shown in Fig. 3.6b. Two pieces of aluminum tape, each 90 μm thick, were used to support the pinhole aperture at its edges without contaminating the ZnSe prism with

adhesive, as shown in the schematic drawing in Fig. 3.6b. Additionally, the placement of the tape supporting the pinhole aperture was carefully chosen to ensure the thermal emitter does not prematurely make contact with the pinhole aperture before contacting the ZnSe prism directly.

The decision to use a ZnSe lens is a departure from past studies, which used a more ideal hemisphere to eliminate total internal reflection of radiative modes coupled into the prism.[200] However, while total internal reflection may occur in a lens geometry, this does not necessarily mean near-field thermal radiation coupled to large angles will be trapped indefinitely. To prove this, a ray tracing analysis was applied to the ZnSe lens geometry to evaluate the extraction of thermal radiation at various angles. Schematically, the system is shown in Fig. 3.7a where a pinhole aperture was placed onto the ZnSe lens. A point source was positioned to be in direct contact with the ZnSe prism and emitted rays conically at a specific polar angle, Θ, and at all azimuthal angles. This configuration was chosen to emulate the coupling of near-field thermal emission to propagating modes within the prism at varying angles. The number of emitted rays was chosen to be N = 500,000 with a total input power of 1 W. The edge of the ZnSe lens is unpolished, which was assumed to behave as a lambertian scatterer.

To evaluate the extraction of thermal radiation for this geometry, an extraction efficiency is used defined as the ratio of the total power transmitted through the ZnSe prism divided by the total input power of 1 W. As a reference, the refractive index of ZnSe can be assumed to be n ~ 2.4, which yields a critical angle of approximately 25 degrees. Therefore, thermal emission emitted into the Znse lens at angles larger than 25 degrees will consist of near-field thermal emission. As shown in Fig. 3.7b, the extraction efficiency remains higher than 80% up to an emission angle of 65 degrees. Between 65 and 85 degrees, a noticeable decrease in the efficiency can be observed, which corresponds to emission hitting the corner of the ZnSe lens. Overall, it can be observed that despite multiple reflections within the lens, thermal radiation coupled to angles larger than 25 degrees can still couple out to free space. Thus, it is expected that using a ZnSe lens can still enable extraction of near-field thermal radiation. Given this observation, it is also important to consider the optics used to collect and guide the extracted thermal emission into the FTIR spectrometer. This aspect of the experiment will be discussed in Sects. 3.3.5 and 3.4.4.

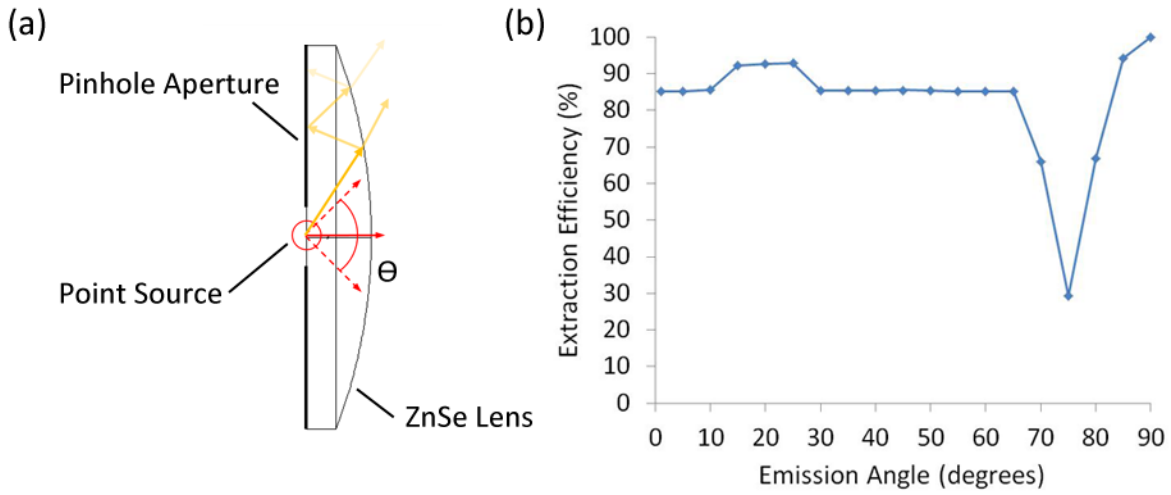

Figure 3.7: Ray tracing analysis to evaluate angular extraction efficiency from ZnSe lens geometry. (a) Schematic illustration of the system modeled. A point source is used to emulate emission into the prism at different angles, Θ. (b) The resulting extraction efficiency for the particular ZnSe lens geometry used in this experiment.

A similar ray tracing analysis was also applied to evaluate potential variations in the view factor as the gap separation between the thermal emitter and ZnSe prism is reduced. If the view factor does change, this will introduce systematic errors in the evaluation of the near-field enhancement as this will lead to a gap-dependent variation in the far-field regime. For this analysis, the system was modified by replacing the point source with the geometry of the N-BK7 thermal emitter. Thermal emission from this surface was assumed to be isotropic. Following the same methodology as before, the total power extracted through the pinhole aperture and the prism was compared for the cases where the thermal emitter was placed in contact with the ZnSe lens and when it was separated by a gap of 50 μm. From this simulation, it was observed the total power increased by 0.2% from 50 μm to contact. Based on Eq. (3.1), a 0.2% variation in the far-field contribution would result in a $\beta = \sim 1.002$ in the case where there is no near-field contribution. Therefore, if a spectral feature is experimentally observed that exceeds this baseline value, there is more confidence this can be attributed to near-field coupling rather than a variation in view factor.

3.3.5 Optics for Emission Collection

Another key component in this experiment are the optics used to collect and guide thermal emission into the FTIR spectrometer. In the interest of conceptually demonstrating measurement of near-field thermal emission spectra, the goal was to collect and direct as much of the thermal emission into the FTIR as possible. For the particular FTIR spectrometer used in this study, the emission input should ideally be collimated with a maximum beam spot diameter of 1.5" (38.1 mm). Given that the emitter area that is extracted into the far-field is defined by the pinhole aperture, which is 3 mm in diameter, it is safe to approximate the emitter area as a point source. Thus, to collimate a point source, ideally an on-axis parabolic mirror should be used.

A design for a parabolic mirror was developed using a ray tracing analysis. The mirror was designed to collimate the emission with a 2" beam spot, intentionally overfilling the required beam spot size for the FTIR. The design was optimized by minimizing the divergence of the rays reflected by the parabolic mirror. This resulted in an optimal focal length of 6.215 mm. With this design, an attempt was made to fabricate this mirror. A negative mold was made by adhering and sanding several layers of balsa wood, which were initially cut into circles with varying size approximating the parabolic profile, as shown in Fig. 3.8b. A series of aluminized mylar segments were cut from a sheet and then secured to the mold using Kapton tape, as shown in Fig. 3.8b. High strength epoxy was then overlaid onto the mylar segments and cured to hold the parabolic shape. The final trimmed mirror is shown in Fig. 3.8c.

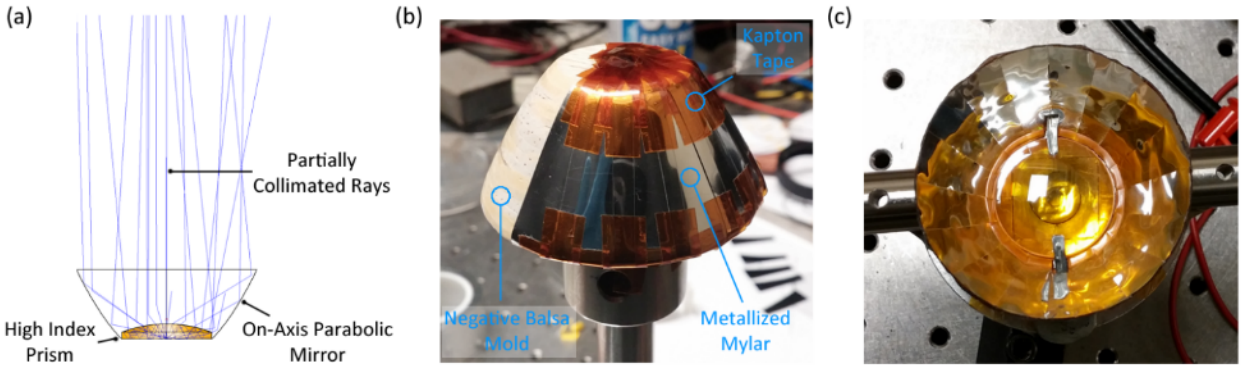

Figure 3.8: An on-axis parabolic mirror can be used to collimate thermal emission extracted from the ZnSe prism. (a) A schematic illustration detailing the ray tracing analysis used to design an optimal on-axis parabolic mirror. (b) An image detailing the fabrication of the mirror, which consisted of overlaying metallized mylar segments onto a negative mold made of balsa wood. (c)

A top-down image of the fabricated on-axis parabolic mirror placed around the ZnSe lens on the prism holder.

To evaluate the performance of the fabricated parabolic mirror, empirical tests were performed to assess improvements to the collection efficiency. These tests consist simply of measuring the peak-to-peak magnitude of the interferogram and the resulting intensity spectra with and without the parabolic mirror, when the thermal emitter was heated to an elevated edge temperature of ~ 175°C. To direct the thermal emission into an FTIR, a flat 2" square silver mirror was adjusted until the peak-to-peak magnitude was maximized. Based on these tests, minimal improvements to the signal strength were observed when using the parabolic mirror. It is likely that small deviations in the curvature of the mirror combined with the long optical path length required for the thermal emission to propagate through the FTIR spectrometer inherently make the mirror extremely sensitive to small imperfections. This suggests a more precise method of fabrication, such as CNC milling and polishing of an aluminum block, will be required to fabricate an on-axis parabolic reflector. As will be shown, this is one key area of improvement that is needed in future iterations of the experiment method.

As an alternative solution, an off-axis parabolic (OAP) mirror (Thorlabs, MPD249-P01) was used, which are more readily available compared to its on-axis counterpart. As depicted in Fig. 3.9a, the silver OAP mirror replaced the flat mirror in the experimental setup. This particular OAP mirror is designed with a 4" focal point that is 90 degrees rotated from the collimated beam. Therefore, the OAP mirror will only collimate thermal emission from a small solid angle, which will introduce some spectral variation in the measurement based on the angular distribution of thermal radiation collected. This angular dependence will be analyzed in Sect. 3.4.4. Empirical tests were again performed to compare the flat 2" square silver mirror with the OAP mirror. The OAP mirror was initially positioned approximately 4" from the prism and then rotated a few degrees until the peak-to-peak magnitude of the interferogram was maximized. Despite collimating only a fraction of the total thermal emission, the use of an OAP mirror increased the peak-to-peak magnitude by nearly one order of magnitude and dramatically improved the intensity spectra, as shown in Fig. 3.9b.

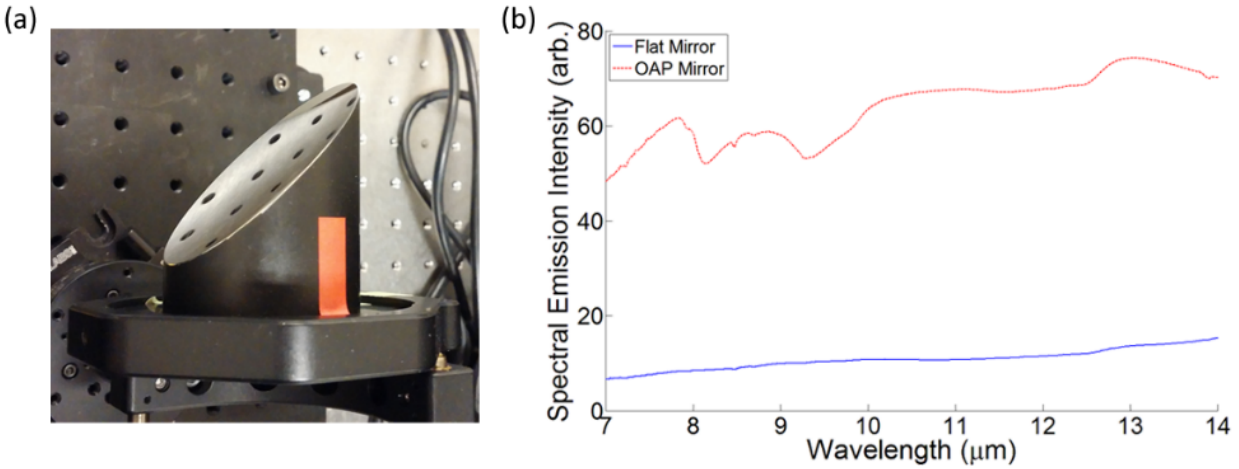

Figure 3.9: An off-axis parabolic (OAP) mirror is used to collect and guide thermal emission into the FTIR spectrometer. (a) An image of the OAP mirror used in the experiment. (b) A comparison of the measured spectral emission intensity when using a flat mirror and an OAP mirror.

3.3.6 Modeling Curvature Effects

Since the thermal emitter used in this experiment is spherically convex, accurate theoretical estimations of radiative heat transfer must account for the curvature introduced. This can be accomplished by using the proximity force approximation (PFA), which approximates a surface with curvature as a stack of semi-infinite parallel plates where each plate is positioned at a distance based on the curvature of the surface and weighted according to the projected area.[60,179,207] Utilizing the fluctuational electrodynamics formulation developed in Ch. 2 for two semi-infinite media, the modified near-field radiative heat flux with the PFA approximation is expressed as follows,

$$q_{\omega}^{PFA} = \int_{r=0}^{r=R} q_{\omega}^{H\rightarrow C}\left(\omega, T_H, g+d\left(r\right)\right)\cdot 2\pi r dr \tag{3.3}$$

where r is the radial coordinate of the convex surface, R is the cut-off radius corresponding in this case to the radius of the pinhole aperture, and d(r) is the additional separation distance based on the curvature of the surface at a given radial position r.

The PFA approximation will not rigorously account for the effect of curvature on evanescent radiative modes nor the interference of thermal radiation exchange between the convex thermal emitter and the prism. However, given the large radius of curvature and the relatively small aperture used in the experiment, this approximation can still provide a reasonable estimate

of radiative heat transfer between the thermal emitter and the prism, which includes both near- and far-field contributions.

3.3.7 Temperature Variability and Analysis

The decision to perform the experiment under ambient conditions instead of vacuum was made in the interest of simplifying the experimental approach. As a result, heat conduction through the air gap separating the thermal emitter and the prism will cause the temperature of the emitter to vary along its surface due to the curvature. Given that the evaluation of near-field enhancement, as defined in Eq. (3.1), relies on comparing thermal emission at different gap separations, this variation in temperature can potentially introduce errors in the measured near-field thermal emission spectra.

To partially compensate for variations in the emitter temperature, each thermal emission measurement is calibrated to have the same total emission intensity, I_{emi}, for all gap separations. This is achieved by adjusting the heating power in order to keep the peak-to-peak magnitude of the interferogram measured by the FTIR, which is proportional to the emission intensity, constant for all measurements. With this calibration, the temperature profile of the emitter may still vary at different gap separations, especially in the region where thermal emission is extracted through the pinhole aperture. However, by keeping the measured emission intensity constant, this ensures the average temperature at the center of the emitter remains similar for all measurements, thus compensating for the potentially large temperature gradients along the emitter surface as it is brought into contact with the prism. To evaluate the efficacy of this calibration, a combination of empirical measurements of temperature and a heat transfer model can be used to estimate the temperature profile along the surface of the emitter when this calibration procedure is applied.

The heat transfer model used to evaluate the calibration includes the N-BK7 thermal emitter with an aluminum retaining ring for support, the ZnSe lens, and the aluminum prism holder with external aluminum supports. A schematic illustration of the model is shown in Fig. 3.10a. The temperature at the base of the N-BK7 thermal emitter, which is in contact with the heater, is assumed to be constant. This temperature functions as the only adjustable input parameter in the simulation. Convective heat transfer is negligible between the thermal emitter and the prism as a gap separation of even 1 mm for a hot and cold side temperature of $T_H = 200^oC$ and $T_C = 22^oC$, respectively, will yield a Rayleigh number on the order of 1. This is well below the threshold of

Ra ~ 1700 for convection to be important.[208] Thus, it can be safely assumed that heat conduction is the primary heat transfer mechanism in the region of air separating the thermal emitter from the prism and the prism holder. For all remaining surfaces, a convective heat transfer boundary condition is assumed with a heat transfer coefficient of h = 5 $Wm^{-2}K^{-1}$. The thermal conductivities of the various materials used in this model were taken from literature and are as follows: k_{air} = 0.0331 $Wm^{-1}K^{-1}$, $k_{N\text{-}BK7}$ = 1.114 $Wm^{-1}K^{-1}$, k_{ZnSe} = 18 $Wm^{-1}K^{-1}$, k_{Al} = 167 $Wm^{-1}K^{-1}$.[208–210]

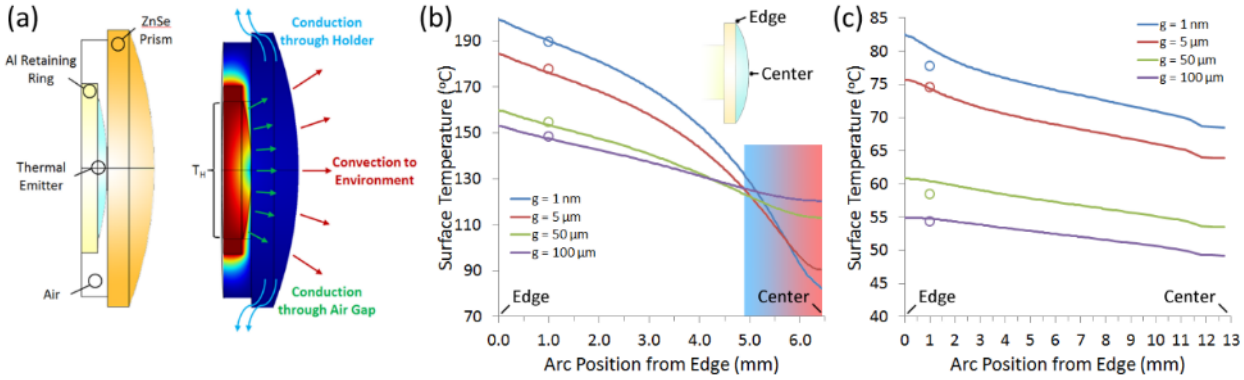

Figure 3.10: A heat transfer model is used to analyze the temperature variation along the thermal emitter caused by heat conduction losses through the air gap separating the emitter and the prism. (a) A schematic illustration of the heat transfer model detailing the various heat transfer mechanisms simulated. For visual clarity, the Al prism holder and supports are not shown, but are included in the heat transfer analysis. (b) The temperature profiles along the thermal emitter surface at various gap separations. The color gradient near the center represents the region where thermal emission is collected through the pinhole aperture. (c) The corresponding temperature profiles along the flat side of the ZnSe prism at various gap separations. In (b) and (c), the colored circles represent temperature measurements taken at the edge of the thermal emitter and ZnSe prism, respectively, at the corresponding gap separation. The measurement at contact yielded a peak-to-peak magnitude in the interferogram of 5.64, which was used as a reference to calibrate subsequent measurements at larger gap separations.

The temperature of the thermal emitter and the ZnSe lens was measured at various gap separations using the thermocouples attached near the edge of the N-BK7 lens and the ZnSe lens, respectively, as described in Sects. 3.3.3 and 3.3.4. These measurements were performed from contact to gap separations of 5 µm, 50 µm, and 100 µm, which were chosen based on the

measurements that will be used to evaluate near-field enhancement as discussed in Sect. 3.4. The calibration was applied for each measurement using the emission intensity measured at contact as a reference point. A theoretical fitting is performed on the temperature data by adjusting the base temperature of the thermal emitter in the heat transfer model until the predicted temperatures at the measured locations approximately match with the experimental data for each gap separation. To emulate contact, a gap separation of 1 nm is used in the simulation. From this fitting, the predicted temperatures profiles along the surface of the thermal emitter and the prism at various gap separations can be obtained. These profiles are shown in Figs. 3.10b and 3.10c for the thermal emitter and the prism, respectively.

As the gap separation decreases, it can be observed the temperature gradient of the thermal emitter from the edge to the center will become larger, which is expected due to the increase in heat conduction across the air gap as the thermal emitter moves closer to the prism. A similar trend can be observed along the surface of the ZnSe lens. Despite the temperature gradient, by calibrating each measurement to have the same total emission intensity, it can be seen that the overall magnitude in temperature at the center of thermal emitter is similar for all gap separations. In fact, when the temperature is averaged over the area that is exposed by the pinhole aperture, the average temperature ranges from T_{avg} = 114.6ºC at g = 1 nm to 123.3ºC at g = 100 μm. This variation is far smaller compared to the temperature difference predicted from the edge of the thermal emitter to its center, which ranges from ΔT = 116.5ºC at g = 1 nm to 32.5ºC at g = 100 μm. Therefore, this calibration appears to indeed provide a means to partially compensate for the temperature variation in the thermal emitter. However, it can also be observed in Fig. 3.10b that as a consequence of this calibration, the temperature at the center of the thermal emitter, where near-field coupling is dominant, will be underestimated at smaller gap separations. This will result in an underestimation of the measured near-field enhancement.

Additionally, by using a spherically convex thermal emitter, both near- and far-field components will be included in the measurement of thermal emission. As a result, the near-field enhancement defined by Eq. (3.1) will include a far-field component in both measurements where the emitter is positioned in the near- and far-field relative to the prism. Because of the temperature variations that may occur when the emitter is moved, it is also important to evaluate how this far-field component will change relative to the near-field thermal emission extracted in terms of both the magnitude and the spectral variation. To distinguish near- and far-field contributions, an

absolute gap separation of 10 μm is used as a threshold point. If the emitter is positioned 1 nm from the prism, the near-field contribution will include emission from the center of the emitter (r = 0) to a radial position where the gap is 10 μm (r~0.7 mm) based on the curvature of the N-BK7 lens. The far-field component thus includes emission from this position (r~0.7 mm) up the edge of the pinhole aperture (r = 1.5 mm). To evaluate the radiative heat flux from the near- and far-field regions of the thermal emitter, the modified fluctuational electrodynamics formalism introduced in Sect. 3.3.6 is used, which accounts for the variation in curvature of each region. The optical constants for ZnSe are taken from literature and are shown in Fig. 3.11a.[146]

Using the predicted temperature profiles, the area-averaged temperature for the near-field component (r < 0.7 mm) at a gap separation of 1 nm is 95°C. This results in a total radiative heat flux of 1.463 mW. Since the far-field contribution (0.7 mm < r < 1.5 mm) is independent of the gap separation, the change in the far-field component is calculated based on the minimum and maximum area-averaged temperatures amongst all gap separations modeled in Fig. 3.10b. The minimum and maximum averaged temperatures are 115.9°C and 123.8°C, respectively, which result in a total radiative heat flux of 4.456 mW and 4.857 mW. The difference in magnitude for the far-field contribution is thus estimated to be 0.401 mW, which is less than the near-field contribution, but is not negligible.

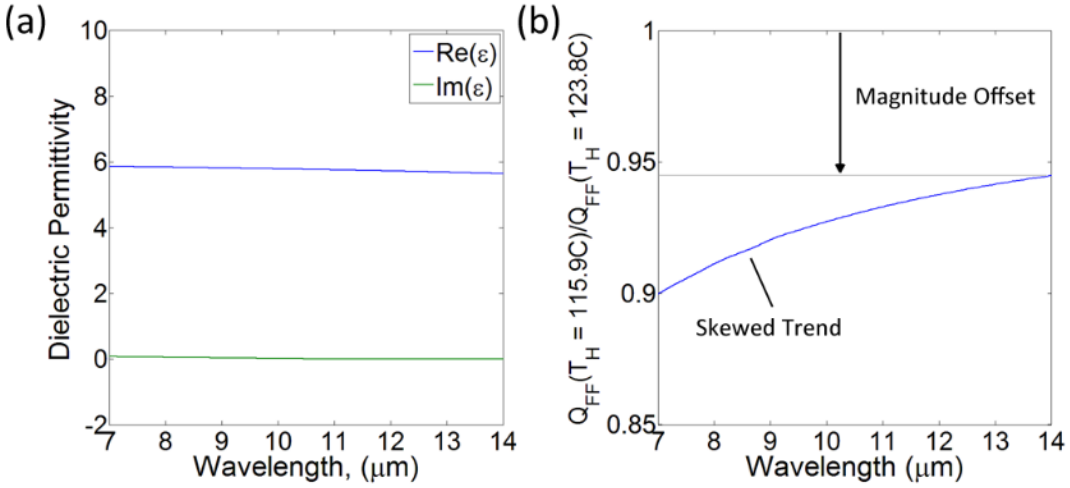

Figure 3.11: (a) The dielectric permittivity of ZnSe. (b) The ratio of the far-field spectral radiative heat flux at emitter temperatures of T_H = 115.9°C and T_H = 123.8°C, which correspond to the minimum and maximum averaged temperatures based on the heat transfer model.

To determine the impact variations in the far-field component will have on the measured near-field enhancement spectra, a simple ratio is taken of the far-field radiative heat flux spectra at 115.9^{o}C and 123.8^{o}C, as shown in Fig. 3.11b. It can be observed that this ratio shows no distinct spectral features, e.g. a peak, is expected to occur within the measured wavelength range. If such a feature is observed experimentally, this provides more confidence that it is indeed due to near-field enhancement. However, it can be observed in Fig. 3.11b that if the temperature in the far-field region of the emitter were to decrease as the emitter is moved closer to the prism, the near-field enhancement spectrum will be underestimated with a magnitude offset caused by the temperature difference. Additionally, a decrease in temperature will also underestimate contributions to thermal emission at shorter wavelengths, resulting in a spectrum that is skewed with an increasing magnitude at longer wavelengths. Both of these effects will require additional corrections, which will be discussed in Sects. 3.4.3.1 and 3.4.3.2.

3.4 Results & Analysis

To demonstrate that this experiment can provide quantitative and gap-dependent near-field enhancement spectra, a series of measurements were performed in the near- and far-field regimes. Two far-field measurements were performed at a gap separation of g = 50 μm and 100 μm, controlled by micrometer positioner on the piezo stage, in order to validate their use as a far-field reference. To demonstrate the measurement of near-field enhancement, a measurement was taken where the thermal emitter was pressed into contact with the prism in order to maximize evanescent coupling between the thermal emitter and the prism. To consistently apply the same pressure, the micrometer was set to a position that was 50 μm beyond the point of contact. For the final measurement, the thermal emitter was initially positioned several microns from contact and incrementally moved in steps of 100 nm towards the prism using the piezo stage. A summary of these measurements are provided in Table 3.1.

Table 3.1: Overview of measurements used to evaluate near-field spectral enhancement.

Measurement	Regime	Gap Position, g
1	Far-field	100 µm
2	Far-field	50 µm
3	Near-field	Contact (-50 µm)
4	Near-field	Variable (-2 µm to 5 µm)

The measurements outlined in Table 3.1 were performed using the experimental procedures described throughout Sect. 3.3. Each measured emission intensity spectrum was averaged over 64 scans. Furthermore, all background measurements as well as the far-field and near-field contact measurements (measurements 1-3) were take three times to verify consistency. As mentioned in Sect. 3.3.7, a calibration procedure is applied to each measurement to compensate for the temperature variation of the emitter as it is moved closer to the prism. The emission intensity for all measurements outlined in Table 3.1 are calibrated relative to the near-field contact measurement (measurement 3). For the gap-dependent near-field measurement (measurement 4), the emission intensity was calibrated at the initial piezo position. However, as the thermal emitter is moved closer to the prism the emission intensity will decrease due to conductive cooling.

For each emission measurement, the temperatures were measured at the edge of the thermal emitter, $T_{N\text{-}BK7}$, and the edge of the ZnSe prism, T_{ZnSe}, which are tabulated in Table 3.2. As shown, the emitter temperature varied from $T_{N\text{-}BK7}$ = 189.7ºC for the near-field contact measurement (measurement 3) to $T_{N\text{-}BK7}$ = 148.3ºC for the far-field measurement at a gap separations of 100 µm (measurement 1). Likewise, the temperature of the ZnSe prism ranged from T_{ZnSe} = 77.7ºC for measurement 3 to T_{ZnSe} = 54.3ºC for measurement 1. Based on the heat transfer modeling in Sect. 3.3.7, the effective temperature of thermal emission is taken to be T ~ 110ºC for all measurements. This temperature is used for all subsequent theoretical calculations.

Table 3.2: Measured temperatures at the edges of the N-BK7 thermal emitter and ZnSe prism.

#	Gap Position, g	N-BK7 Temperature, $T_{N\text{-}BK7}$	ZnSe Temperature, T_{ZnSe}
1	100 µm	148.3 ºC	54.3 ºC
2	50 µm	154.6 ºC	58.4 ºC
3	Contact (-50 µm)	189.7 ºC	77.7 ºC
4	Variable (5 µm start)	177.7 ºC	74.5 ºC

Due to the complexity of the experiment, the analyses of the measurements and the experiment are separated into several sections. First, the far-field measurements are validated as appropriate references to evaluate near-field enhancement spectra. This will be followed by the analysis of the near-field contact measurement, which will show that near-field enhancement was observed experimentally. Then, the gap-dependent near-field measurements will be analyzed. Because of the temperature variations in these results, two corrections are proposed and applied to the data at different gap positions. Additionally, the theoretical model is modified to account for angularly selective coupling of extracted thermal emission into the FTIR spectrometer using the OAP mirror. And finally, an evaluation of background thermal emission will be provided to validate the experimental measurements.

3.4.1 Validation of the Far-field Reference

In order to properly evaluate the near-field enhancement defined by Eq. (3.1), it is crucial for the far-field measurements to provide a correct representation of far-field thermal emission from the convex thermal emitter in order to compare with the near-field measurements. As mentioned in Sect. 3.3.4, any variations in the view factor or far-field lensing effects will introduce systematic errors that will lead to inaccuracies in the near-field enhancement ratio, which would prevent any meaningful quantitative assessment of near-field extraction.

To verify that the far-field measurements taken at gap separations of g = 50 µm and 100 µm do not include these effects, a simple ratio of the background corrected data can be taken using the definition of near-field enhancement shown in Eq. (3.1). In this case, the emission intensities used both correspond to the far-field measurements. As shown in Fig. 3.12a, the ratio of these measurements yields a spectrum that is near unity across the entire wavelength range. These results show that despite the change in gap separation, there is virtually no variation in the magnitude of

thermal emission measured in the far-field regime. This suggests that there is indeed no variation in the view factor in the experiment, which is in agreement with the theoretical ray tracing analysis performed in Sect. 3.3.4.

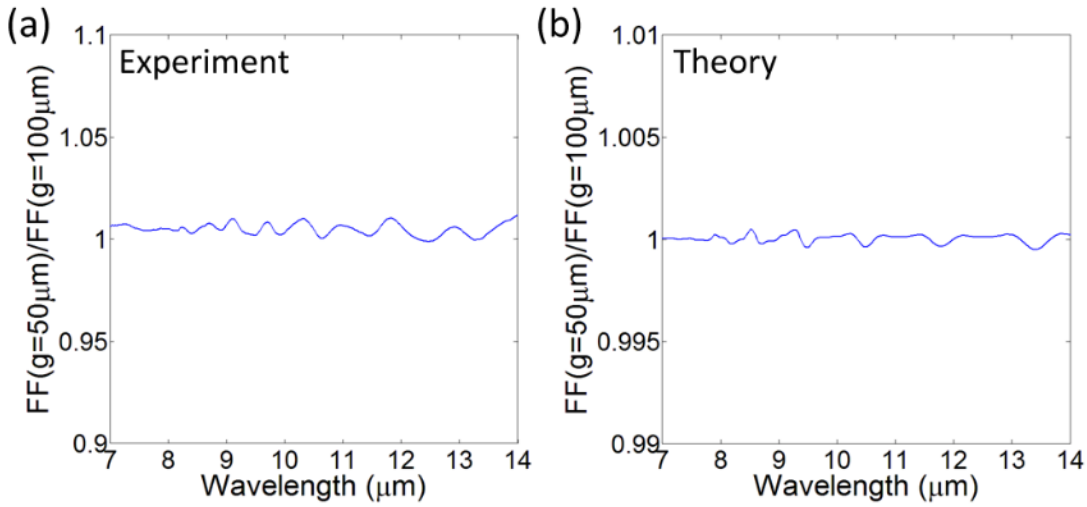

Figure 3.12: Validation of the far-field reference measurements. (a) The ratio of the background corrected emission intensities measured in the far-field regime at g = 50 μm and 100 μm, respectively. (b) The corresponding theoretical prediction assuming an emitter temperature of T_H = 110°C. The curvature of the thermal emitter is approximated using the PFA approximation.

However, from Fig. 3.12a, it can be observed that the ratio of these far-field measurements does lead to some oscillatory behavior at wavelengths longer than 8 μm. This oscillatory behavior is ultimately due to interference effects between the thermal emitter and the prism, which at a gap separation of 50 μm and 100 μm is still comparable to the wavelength of thermal radiation. The effect of this interference becomes amplified in the longer wavelength range where N-BK7 optically behaves as a metal where the real part of the dielectric permittivity is negative.

To verify this assertion, the oscillatory behavior was reproduced theoretically using Eq. (3.3), as shown in Fig. 3.12b. The difference in magnitude between experiment and theory is likely due to limitations associated with the PFA approximation used to model the convex surface of the thermal emitter where interference between the emitter and the prism, which effectively behaves as a tapered waveguide, is not properly captured in the model. Based on Eq. (3.1), this oscillatory behavior will also appear in the near-field enhancement spectra as well. In order to remove these

non-physical oscillations, a simple spectral averaging is applied to the near-field enhancement spectra to essentially smear out these oscillations.

3.4.2 Near-field Enhancement in Direct Contact

To evaluate whether the experimental apparatus has sufficient sensitivity to detect the extraction of near-field thermal emission, the near-field contact measurement (measurement 3) is used. By placing the thermal emitter in contact with the ZnSe prism, evanescent coupling is maximized, which would likewise maximize the near-field enhancement. The near-field enhancement spectra for this measurement is shown in Fig. 3.13a. Note that the far-field reference at g = 50 μm is used.

The resultant spectra, indicated by the red line, exhibits oscillations corresponding to interference in the far-field reference, as discussed in Sect. 3.4.1. To remove these oscillations, a spectral average is applied over a wavenumber interval of $\Delta\eta \sim 58$ cm^{-1}, as indicated by the blue line. This corresponds to a $\Delta\lambda \sim 0.28$ to 1.1 μm at wavelengths of 7 and 14 μm, respectively. As shown in Fig. 3.13a, a clear peak can be observed between 8 and 11 μm, which coincides with the wavelength range where the surface phonon polariton of N-BK7 is supported. The absolute magnitude of this peak also exceeds unity, which indicates more thermal emission was measured within this wavelength range in the near-field measurement compared to the far-field reference. Furthermore, the peak height is approximately ~0.02, which is larger than the predicted change in view factor of 0.002 in Sect. 3.3.4. Based on these observations, it is believed this a direct demonstration of a quantitative spectral measurement of near-field radiative heat transfer.

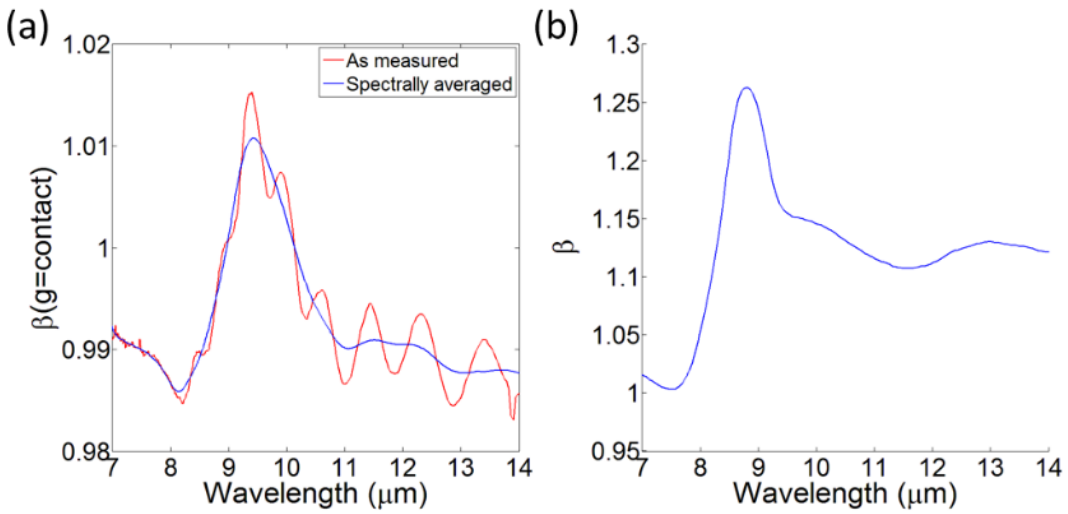

Figure 3.13: (a) The measured near-field enhancement, β, when the thermal emitter is placed into contact with the ZnSe prism. The far-field measurement taken at g = 50 μm is used. The as measurement near-field enhancement (blue line) is spectrally averaged (red line) over $\Delta\eta \sim 58$ cm^{-1}. (b) The theoretically predicted near-field enhancement assuming an emitter temperature of T_H = 110ºC. As an approximation to contact, the gap separation is chosen to be g = 3 nm.

For theoretical comparison, the near-field enhancement was calculated and spectrally averaged over the same wavenumber interval as the experiment assuming an emitter temperature of 110ºC, as shown in Fig. 3.13b. The gap separation for this calculation was chosen to be g = 3 nm to avoid the non-physical divergence in the fluctuational electrodynamics formalism. Although this may not accurately replicate the contact geometry in the experiment, the relative area where there the discrepancy in geometry occurs is expected to be small due to the curvature of the thermal emitter.

Upon comparing the experimental results with theory, qualitative agreement can be observed in the short wavelength range where a peak exists near 9 μm in both the experiment and theory. A distinct dip in the near-field enhancement can also be observed in both experiment and theory at 8.1 μm and 7.5 μm, respectively, which corresponds to the regime where the thermal emitter transitions from a dielectric (Re(ε) > 0) to a metal (Re(ε) < 0). However, at wavelengths longer than 10 μm, the experimental results qualitatively underestimate the enhancement compared with theory. And additionally, the magnitude of near-field enhancement across the entire wavelength range is significantly lower for the experiment.

There are several reasons for these discrepancies between experiment and theory. First, thermal emission is experimentally collected from a small solid angle by the off-axis parabolic mirror. By not collecting all of the high momentum evanescent modes coupled to the ZnSe prism, the near-field enhancement will inherently be underestimated. An estimate of the angular dependence collected by the OAP mirror will be discussed in Sect. 3.4.4 in an effort to provide a more appropriate theoretical comparison. Second, the calibration of the peak-to-peak magnitude of the interferogram will also inherently lead to an underestimation of near-field enhancement. Ideally, if the emitter surface temperature remains constant, it is expected that the extraction of near-field thermal emission will lead to a larger magnitude. This underestimation will be compensated in Sect. 3.4.3.1 when a normalization correction is applied to correct for variations in the emitter temperature. Third, the optical constants of N-BK7 and pure silicon dioxide are expected to differ since N-BK7 is typically composed of only 60-70% silicon dioxide with the remainder distributed between boron oxide, potassium oxide, barium oxide, and sodium oxide.[211] The inclusion of additional oxides can change the infrared optical properties of glasses quite substantially due to modifications to the molecular structure, which will affect the vibrational modes supported in the material.[211,212] As a result, near-field enhancement due to the SPhP modes supported in N-BK7 and pure silica are unlikely to be the same, which may be the reason for the differences in the spectral shape observed between experiment and theory in Fig. 3.13 in the long wavelength range.

3.4.3 Gap-dependent Near-field Enhancement

For the measurement of gap-dependent near-field enhancement, contact calibrations were performed before and after the experiment following the procedures discussed in Sect. 3.3.2 to ensure the contact point did not drift during measurement. The contact point for this measurement is estimated to be at the absolute piezo stage position of 7.5 μm. Based on this contact position, gap-dependent near-field enhancement spectra was then measured starting nearly 2 μm from contact and moving the thermal emitter in increments of 100 nm using the piezo stage.

The resulting gap-dependent near-field enhancement spectra is plotted in Fig. 3.14a before and after contact is made with the prism. It should be emphasized the color of each spectrum corresponds to a specific gap position. The measurement at g = 50 μm is again used as the far-field reference. As shown, the near-field enhancement spectra again exhibits oscillations due to the far-

field reference, which can be removed via spectral averaging over a wavenumber interval of $\Delta\eta \sim 58\ cm^{-1}$, as shown in Fig. 3.14b. Based on these results, no discernable gap-dependent variation in the spectra can be observed as the magnitude of the different gap-dependent spectra appears offset relative to one another. Additionally, the spectra also appears skewed with an increasing enhancement at longer wavelengths. As discussed in Sect. 3.3.7, these two features are a direct result of variations in the emitter temperature caused by varying heat conduction losses when the emitter is moved closer to the prism. To determine whether there is any gap-dependent variation in this data, corrections must be applied to compensate for these temperature variations. As will be shown, corrections will be used addressing the magnitude offset and the skewed spectral variation separately.

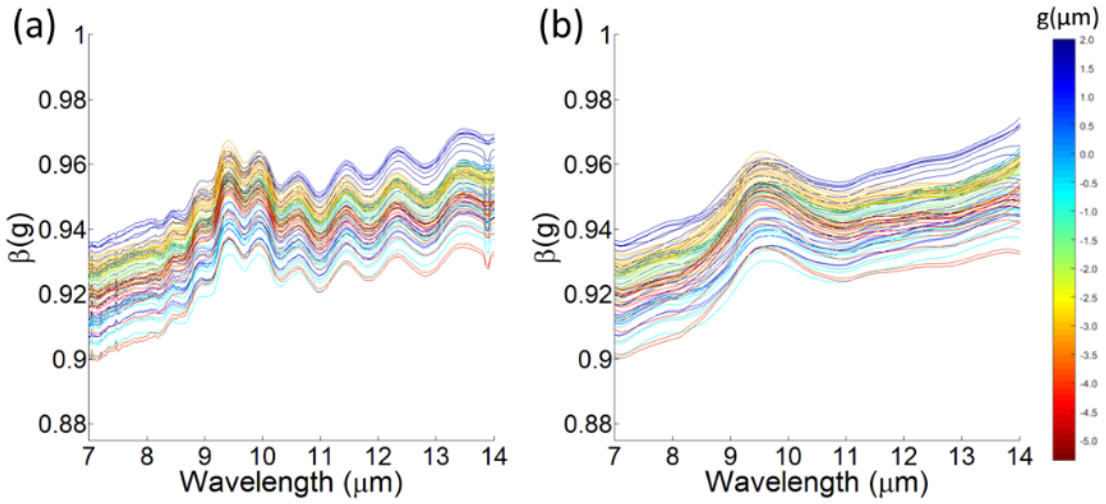

Figure 3.14: (a) The as-measured near-field enhancement, β, at variable gap separations before and after contact. The far-field measurement taken at g = 50 μm is used. The color of each line corresponds to specific gap position based on the color bar. (b) The corresponding near-field enhancement spectrally averaged over $\Delta\eta \sim 58\ cm^{-1}$.

3.4.3.1 Magnitude Offset Correction

The development of a rigorous correction to address the magnitude offset in the data requires precise knowledge of the temperature profile at the center of the emitter, which is expected to vary at different gap separations as discussed in Sect. 3.3.7. However, due to limitations in the experiment, this temperature profile cannot be measured experimentally. Instead, an approximate

correction is used to compensate the magnitude offset, which consists of normalizing each measured emission intensity by its spectrally integrated magnitude. This is applied to both the near- and far-field measurements, resulting in a modified expression for the near-field enhancement as follows,

$$\beta^{N}(\lambda) = \frac{\left(I_{emi}^{NF}(\lambda) \Big/ \int_{\lambda_1}^{\lambda_2} I_{emi}^{NF}(\lambda)\, d\lambda\right)}{\left(I_{emi}^{FF}(\lambda) \Big/ \int_{\lambda_1}^{\lambda_2} I_{emi}^{FF}(\lambda)\, d\lambda\right)} \tag{3.4}$$

where β^{N} is the normalized near-field enhancement spectrum and λ_1 and λ_2 is the spectral window used for normalization. Although this approach will not perfectly compensate for the magnitude offset in the data, it can nonetheless provide an accurate correction since the maximum offset in the data is ~0.04, which is small compared to the absolute magnitude of the near-field enhancement at ~0.94. It should be emphasized that by normalizing the emission intensity in this manner, a careful reinterpretation of the results is required. For example, a normalized near-field enhancement less than unity does not mean there is no coupling of near-field thermal radiation as this will depend on the magnitude of the near-field enhancement across the measured spectral range. In order to properly compare the normalized near-field enhancement spectra to theory, the same normalization procedure is applied to the theoretical calculations of the spectral radiative heat flux in the near- and far-field regimes.

In order to show the effect of this normalization correction, we begin first with the measured gap-dependent emission intensities and the far-field emission intensity at g = 50 μm, which are shown in Fig. 3.15a. Similar to the near-field enhancement spectra, the gap-dependent emission intensities exhibits a clear offset relative to one another. The far-field emission intensity is higher in magnitude compared with the gap-dependent emission intensities, which indicates the measurement was taken at a higher temperature. The results of applying the normalization correction to each emission intensity spectrum is shown in Fig. 3.15b. Compared to the original data, the normalized emission intensities exhibit significantly less spread, which indicates the correction does indeed compensate for the offset in the data. With these results, the normalized near-field enhancement, defined in Eq. (3.4), can thus be determined. It should be mentioned that since the normalization correction does not perfectly compensate for the magnitude offset, the ratio of normalized emission intensities can exhibit artificially enhanced or suppressed spectral features depending on whether the numerator or denominator was originally larger in magnitude,

respectively. For this data, the far-field emission intensity was originally larger in magnitude than the gap-dependent emission intensities, which lead to the suppression of near-field enhancement.

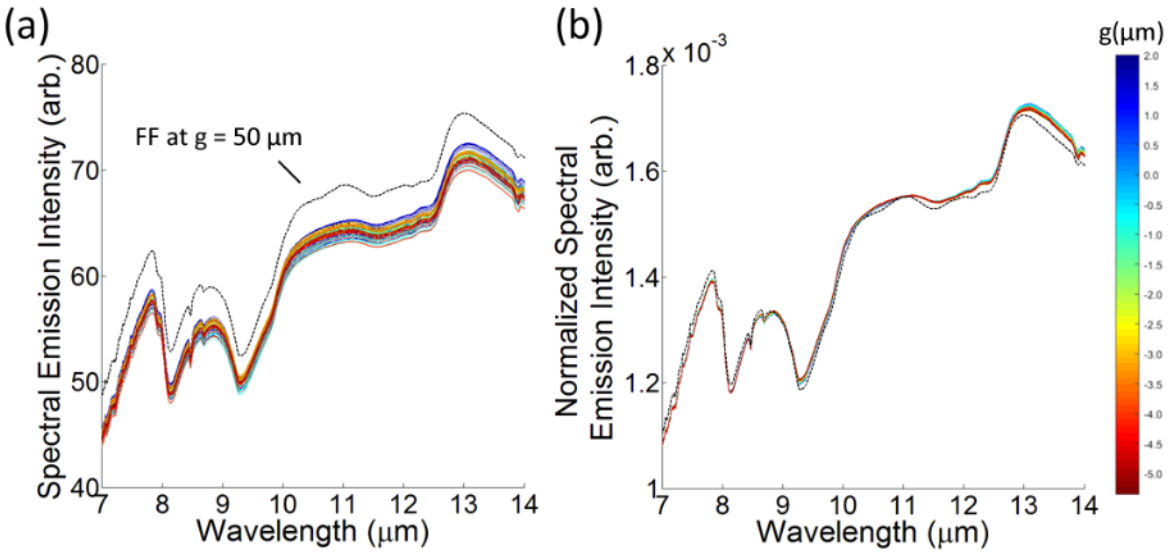

Figure 3.15: (a) The spectral emission intensities originally measured at various gap separation. The far-field measurement at g = 50 µm is also included (black dashed line). (b) The spectral emission intensities after the normalization correction is applied.

The results for the normalized gap-dependent near-field enhancement spectra are shown in Fig. 3.16a. By applying this correction, a clear gap-dependent variation can be observed where the peak from 8 to 11 µm, which again corresponds to the SPhP mode of N-BK7, progressively increases in magnitude as the thermal emitter is positioned closer to the ZnSe prism. In contrast, from 7 to 8 µm and 11 to 14 µm, the magnitude of the normalized near-field enhancement decreases at smaller gap separations. This is a consequence of the normalization correction, which will inherently underestimate the spectral range where near-filed coupling is weaker as the overall near-field contribution increases.

A theoretical comparison is also calculated using the same spectral averaging interval and normalization correction with an emitter temperature of 110ºC. As before with the contact measurement in Sect. 3.4.2, there is qualitative agreement where both experiment and theory exhibit a prominent peak within the same wavelength range. However, a few key differences can still be observed. First, there is still a distinct magnitude difference between experiment and theory. As before, this is believed to be due to the OAP mirror collecting only a fraction of the extracted

near-field thermal emission. This will be addressed in Sect. 3.4.4. Second, the near-field enhancement spectra is skewed with a clear increase in magnitude towards longer wavelengths. This will be addressed in the following section.

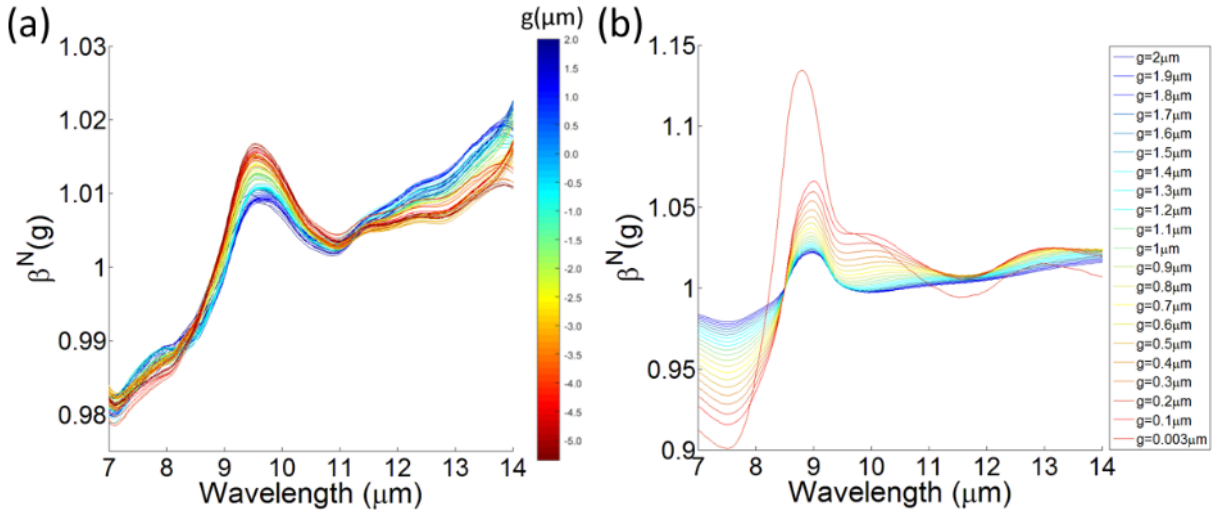

Figure 3.16: (a) The normalized near-field enhancement, β^N, for various gap separations. The far-field measurement taken at g = 50 μm is used for reference. (b) The normalized theoretical near-field enhancement, which was calculated assuming an emitter temperature of 110°C and spectrally averaged over $\Delta\eta \sim 58$ cm^{-1}.

3.4.3.2 Spectral Shape Correction

As shown in Sect. 3.4.3.1, a normalization correction can be used to compensate for the magnitude offset in the gap-dependent near-field enhancement spectra. However, upon applying this correction the spectra still exhibits a distinctly skewed behavior where the overall near-field enhancement increases at longer wavelengths. As discussed in Sect. 3.3.7, this can occur when the near- and far-field emission intensities are measured at different thermal emitter temperatures. With this assertion, a method to correct for the skewed spectra can be developed by theoretically evaluating the temperature dependency of the radiative heat flux.

Based on the formulation developed in Ch. 2, Eq. (2.10) shows the only temperature-dependent terms are the Planck oscillator distribution, which consists of the photon energy multiplied by the Bose-Einstein distribution, and the transmission function, which depends on the photon density of states of the system. Since the magnitude of the original gap-dependent near-

field enhancement spectra shown in Fig. 3.14a is close to unity, the thermal emitter temperature in the near- and far-field measurements is not expected to differ significantly. The optical properties of the thermal emitter are thus expected to remain the same between the near- and far-field measurements, which implies the photon density of states is constant. Therefore, the temperature dependency will be determined solely by the Bose-Einstein distribution, which is expressed as follows,

$$f(\omega,T) = \frac{1}{e^{\frac{\hbar\omega}{k_B T}} - 1} \tag{3.5}$$

where ω is the photon angular frequency, T is the temperature of the emitting medium, ħ is the Planck's constant, and k_B is the Boltzmann constant. To show how the Bose-Einstein distribution can cause a skewed spectra, Fig. 3.17a shows the ratio of Bose-Einstein distributions taken at temperatures of 103°C and 110°C. As expected, the shorter wavelength contributions to thermal emission will be underestimated resulting in a skewed trend that increases towards longer wavelengths.

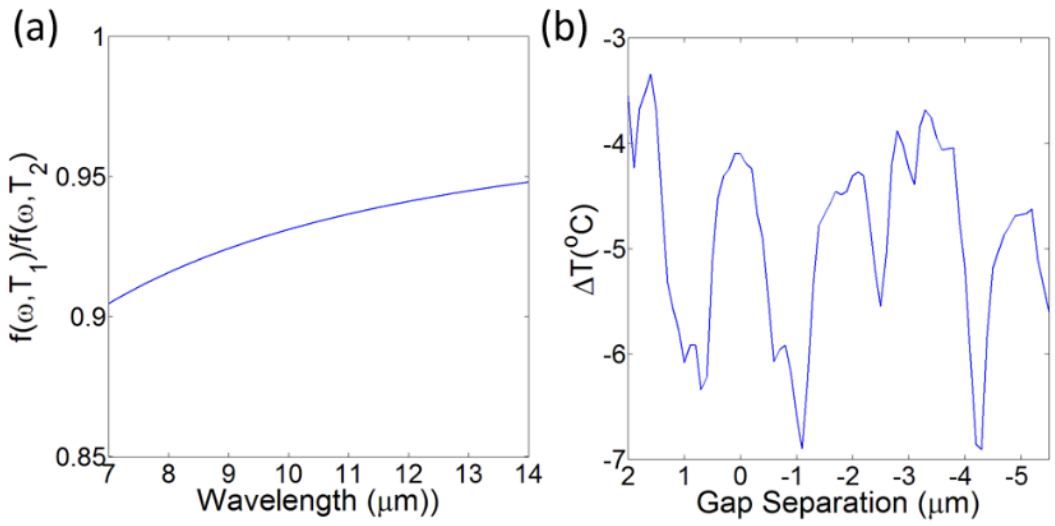

Figure 3.17: (a) The ratio of Bose-Einstein distributions at temperatures of T_1 = 103°C and T_2 = 110°C, respectively. (b) The estimated temperature decrease of the thermal emitter as a function of the gap position using Eq. (3.7).

From these observations, the skewed gap-dependent near-field enhancement spectra can be corrected by multiplying the near-field emission intensity with a ratio of Bose-Einstein factors

at thermal emitter temperatures corresponding to the near- and far-field measurements. This is formulaically expressed as follows,

$$\beta^{C}(\lambda) = \frac{1}{I_{emi}^{FF}(\lambda, T_{FF})} \cdot \left[I_{emi}^{NF}(\lambda, T_{NF}) \cdot \frac{f(\lambda, T_{FF})}{f(\lambda, T_{NF})} \right] \tag{3.6}$$

where β^{C} represents the spectrally corrected near-field enhancement. It is important to note that when this correction is applied in conjunction with the normalization correction described in Sect. 3.4.3.1, this Bose-Einstein correction is applied first. In this way, any magnitude offset introduced by this correction will be compensated by the normalization. The spectrally corrected, normalized gap-dependent near-field enhancement will be denoted by $\beta^{N,C}$.

In order to apply the Bose-Einstein correction expressed in Eq. (3.6), the thermal emitter temperature in the near-field at different gap separations must be known. As mentioned in Sect. 3.4.3.1, the temperature profile at the center of thermal emitter is not directly measured in the experiment. However, a rough estimate of the thermal emitter temperature can still be determined by using the peak-to-peak magnitude of the interferogram measured by the FTIR, which is proportional to the thermal emission intensity and thus the temperature. To determine a temperature from this data, a model to describe the collected thermal emission is needed to fit the emitter temperature as well as a reference measurement where the temperature of the emitter and the signal are both known. This is expressed as follows,

$$\frac{q_{BB}(\omega, T(g))}{q_{BB}(\omega, T = 110^{\circ}C)} = \frac{V_{pk\text{-}pk}(g)}{V_{pk\text{-}pk}(g = 50\mu m)} \tag{3.7}$$

For simplicity, thermal emission is modelled as a blackbody at a uniform temperature, which alleviates the need to know the spectral properties, the angular distribution, and the temperature distribution at the center of the thermal emitter. The far-field reference measurement at g = 50 μm is used as the reference with an emitter temperature of 110ºC. Based on Eq. (3.7), the estimated decrease in the thermal emitter temperature relative to the reference temperature of 110ºC is shown in Fig. 3.17b.

As shown in Fig. 3.17b, the thermal emitter temperature at different gap separations is estimated to be 4 to 7 degrees lower than the reference temperature of 110ºC. The non-monotonic nature of this decrease is attributed to instabilities in the heater during measurement. Although it may appear the assumptions used in this estimate are overly simplistic, the results shown in Fig. 3.17b are actually similar to the temperatures estimated by the heat transfer modeling in Sect. 3.3.7

where it was predicted the average temperature variation would be less than 10ºC. Furthermore, unlike the correction for the magnitude offset in Sect. 3.4.3.1, a precise thermal emitter temperature is not needed in this case as the spectral shape of the near-field enhancement spectra is less sensitive to the emitter temperature.

Upon applying Eq. (3.6) using the estimated emitter temperature in conjunction with the normalization correction from Sect. 3.4.3.1, the spectrally corrected, normalized gap-dependent near-field enhancement spectra is shown in Fig. 3.18a. For convenience, the theoretical results from Fig. 3.16b are again plotted in Fig. 3.18b. Compared to the data in Fig. 3.16a where only the normalization correction is applied, the inclusion of the Bose-Einstein correction removes the skewed behavior in the spectra, resulting in better qualitative agreement with theory. Additionally, the near-field enhancement for the contact measurement in Sect. 3.4.2 is also included in Fig. 3.18a where only the normalization correction is applied. As shown, the gap-dependent spectra is consistent with the contact spectra as well, providing further evidence to the validity of the Bose-Einstein correction. To account for the difference in magnitude between experiment and theory, the theoretical calculation will be modified in the following section to account for the angular distribution of emission collected by the OAP mirror.

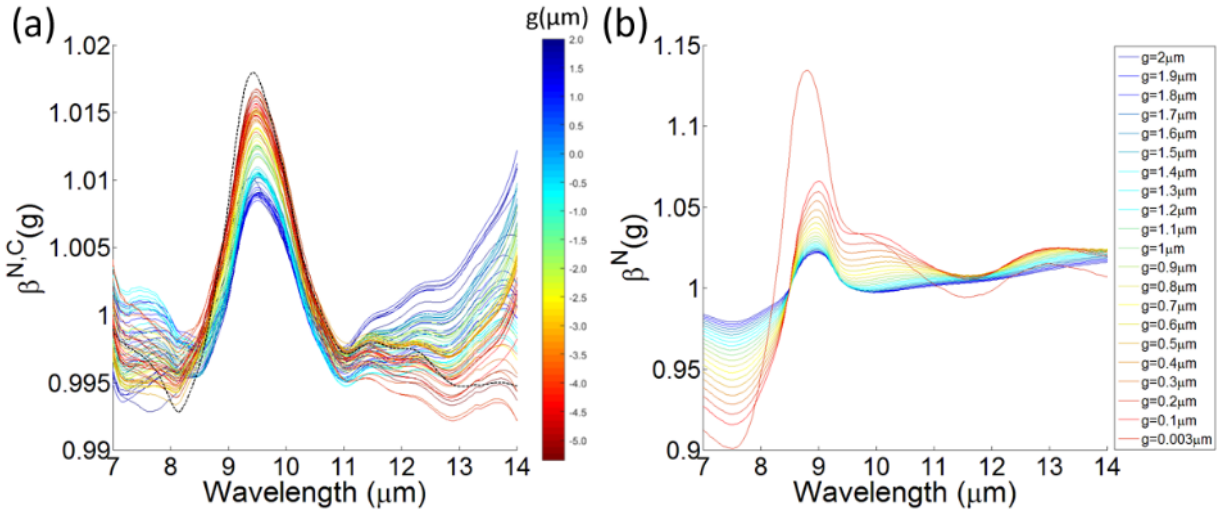

Figure 3.18: (a) The spectrally corrected, normalized near-field enhancement, $\beta^{N,C}$, for various gap separations. The far-field measurement taken at g = 50 μm is used for reference. The normalized near-field enhancement, β^{N}, is also plotted for the direct contact measurement (dashed black line).

(b) The normalized theoretical near-field enhancement, which was calculated assuming an emitter temperature of 110°C and spectrally averaged over $\Delta\eta \sim 58$ cm^{-1}.

3.4.4 Estimation of Angular Coupling Efficiency

In Sects. 3.4.3, it was shown the corrected experimental near-field enhancement spectra exhibits a discrepancy in magnitude when compared with theory. It is believed this discrepancy is due to the OAP mirror, which is used to collect and guide thermal emission extracted from the ZnSe lens into the FTIR. Because the high-momentum near-field radiative modes from the thermal emitter will couple to the prism at larger angles, the OAP mirror can only collect from a relatively small solid angle, thus resulting in the suppression of near-field enhancement.

In order to evaluate the extent of this suppression, a ray tracing analysis is used to determine the fraction of thermal emission collected by the FTIR at a particular emission angle. The system considered is based on the model used in Sect. 3.3.4 to evaluate the angular extraction efficiency and is schematically illustrated in Fig. 3.19a. Once again, a point source, which emits conically at a specified polar angle, Θ, is placed in contact with the ZnSe lens. A pinhole aperture is also included. The geometry of the OAP mirror is modelled rigorously based on the manufacturer specifications. The OAP mirror is initially positioned such that its focal point coincides with the point source. To match with experiment, it is then offset with $\Delta x = +5$ mm, and rotated 1 degree clockwise. To model the FTIR, the external emission input port and a collection mirror, which directs thermal emission into the Michelson interferometer, are both included. The external emission input port is modelled as an aperture with a diameter of 50.8 mm, which is positioned $\Delta y = 330.2$ mm (12”) from the OAP mirror. The collection mirror is modelled as a 38.1 x 38.1 mm square and is positioned $\Delta y = 635$ mm (25”) from the OAP mirror.

For this system, the OAP extraction efficiency is determined based on the emitted power that intersects the collection mirror divided by the input power of 1 W. The number of emitted rays was chosen to be N = 500,000. The calculated OAP extraction efficiency is shown in Fig. 3.19b as a function of the emission angle, Θ. As shown, the overall magnitude of the OAP extraction efficiency is below 10%, which indicates the OAP mirror collects only a small fraction of the thermal emission extracted from the ZnSe prism. It can also be seen that the efficiency is much smaller at emission angles larger than 25 degrees, which suggests near-field evanescent modes coupled to the prism at larger angles will be mostly lost. Combined with the large peak at emission

angles less than 10 degrees, where far-field thermal radiation is expected to strongly couple to the prism, the overall near-field enhancement is expected to be suppressed.

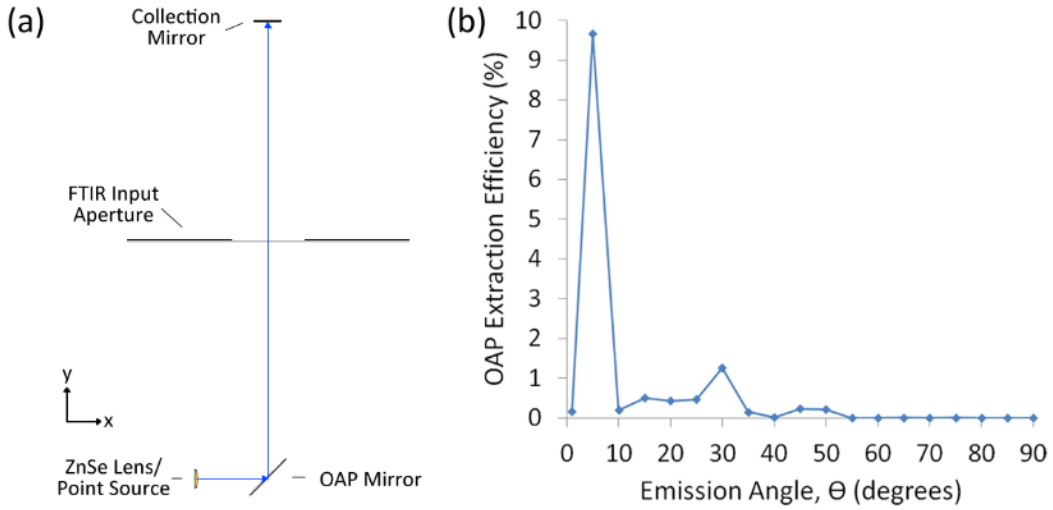

Figure 3.19: (a) A schematic illustration of the ray tracing system used to evaluate the angular components collected by the OAP mirror. (b) The OAP extraction efficiency as a function of the emission angle, Θ.

In order to incorporate the OAP extraction efficiency into the fluctuational electrodynamics formalism, the key is to recognize the emission angle is related to the in-plane wave vector by $k_x = n_{ZnSe} k_0 \sin\theta$, where n_{ZnSe} is the refractive index of ZnSe and k_0 is the vacuum wave vector. The OAP extraction efficiency can thus be used as a weighting function multiplied to the spectral, wave-vector dependent radiative heat flux. This will emulate the inability of the OAP mirror to collect all high-momentum radiative modes coupled into the ZnSe prism. For simplicity, the OAP extraction efficiency is assumed to be the same for all measured wavelengths.

For convenience, the spectrally corrected, normalized gap-dependent near-field enhancement spectra and the modified theoretical comparison are shown in Figs. 3.20a and 3.20b, respectively. The theoretical prediction in Fig. 3.20b with the angular weight leads to an overall suppression of near-field enhancement, resulting in a magnitude that is now similar to the experimental results. In terms of spectral agreement, both experiment and theory still exhibit a clear peak from 8 to 11 μm, which increases at smaller gap separations. There is, however, still some discrepancies particularly at wavelengths outside of the 8 to 11 μm window. Based on the

optical constants of silicon dioxide, thermal emission at these wavelengths is primarily due to bulk emission, which given the macroscopic size of the thermal emitter, will be quite sensitive to variations in the refractive index and extinction coefficient. Thus, the discrepancy is believed to be due to differences in the optical constants of N-BK7 and pure silicon dioxide. Despite, these discrepancies, overall the experiment still exhibits reasonable good agreement with theory. It thus believed these preliminary experimental results are the first observation of quantitative, gap-dependent spectral measurements of near-field enhancement.

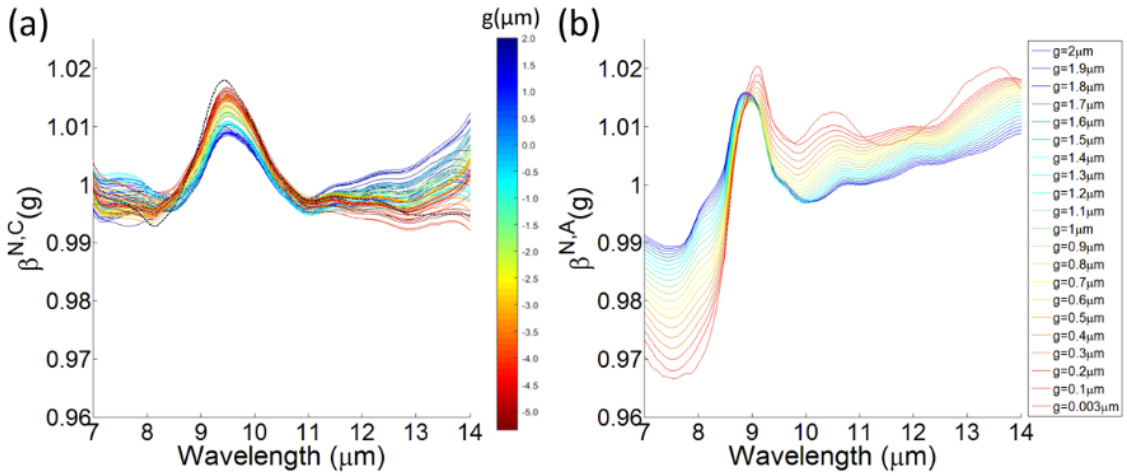

Figure 3.20: (a) The spectrally corrected, normalized near-field enhancement, $\beta^{N,C}$, for various gap separations. The far-field measurement taken at g = 50 μm is used for reference. The normalized near-field enhancement, β^{N}, is also plotted for the direct contact measurement (dashed black line). (b) The normalized, angularly weighted theoretical near-field enhancement,$\beta^{N,A}$, which was calculated at various gap separations assuming an emitter temperature of 110°C and spectrally averaged over $\Delta\eta \sim 58$ cm^{-1}.

3.4.5 Evaluation of Parasitic Emission from Prism and Holder

To further validate the results presented in Sects. 3.4.4, additional measurements were performed to assess the magnitude and spectral dependence of parasitic thermal emission originating from the extraction apparatus, which includes the pinhole aperture, the ZnSe prism, and the supporting aluminum prism holder. A small 5 x 7 mm ceramic heater is used to directly heat these components by pressing it into contact with the pinhole aperture, as shown in Fig. 3.21b. A small K-type thermocouple is embedded in the heater for temperature calibration. To ensure the thermal

emission measured in this experiment originates from only the extraction apparatus, the heater is intentionally positioned away from the center of the pinhole aperture. The OAP mirror is also left in its original position to ensure the angular collection efficiency is consistent with the near-field enhancement measurements. In this configuration, it is possible environmental thermal radiation can coupled into the prism through the exposed pinhole aperture. However, it was observed the emission intensity changed negligibly when the external emission port was opened and closed while the apparatus was at room temperature. Thus, any contribution to thermal emission from the environment is negligible in this measurement.

A K-type thermocouple is also used to measure the reference temperature at the edge of the ZnSe lens as before. To ensure thermal emission from the extraction apparatus is not underestimated, the heater is placed nearly opposite to the thermocouple, as shown in Fig. 3.21a. In the near-field enhancement experiments, the extraction apparatus was heated by the N-BK7 thermal emitter in a small region near the center of the prism, which resulted in a radially symmetric temperature distribution along the prism and the prism holder, as shown in Fig. 3.21c. In comparison, the use of a larger heater and its placement on the prism relative to the reference thermocouple will result in a much larger hot spot, as shown in Fig. 3.21d. As a result, it is expected this configuration will lead to an overestimation of measured thermal emission.

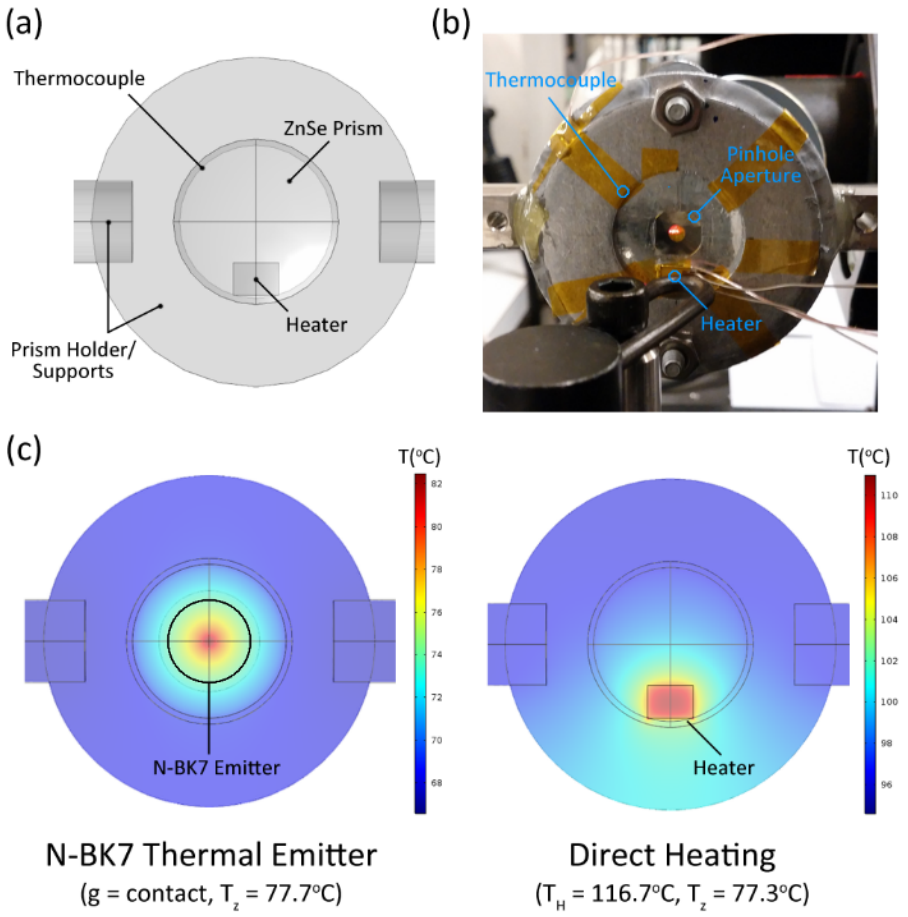

Figure 3.21: To evaluate the effect of parasitic background thermal emission from the extraction apparatus (pinhole aperture, ZnSe prism, and prism holder), the apparatus is heated to similar temperatures observed in the near-field enhancement measurements. (a) Schematic illustration of heater placement and size. (b) An image showing the heater in relation to the pinhole aperture and thermocouple. (c) The theoretical temperature distribution along the ZnSe prism and holder when heated by an N-BK7 thermal emitter and by a small heater, corresponding to measurements with similar ZnSe prism temperatures of T_z = 77.7°C and 77.3°C, respectively. For the direct heating case, a small air gap 5 µm thick is assumed between the heater and prism.

To evaluate the magnitude of thermal emission from the extraction apparatus, four measurements were performed where the heater temperature, T_H, was adjusted such that the temperatures measured at the edge of the ZnSe, T_{ZnSe}, lens matched the temperatures observed in the near-field enhancement measurements in Table 3.2. As before, a background calibration measurement is also performed. The measured heater and prism temperatures are shown in Table

3.3. The background corrected thermal emission intensity spectrum for each measurement is shown in Fig. 3.22a. For comparison, the emission intensity spectra from the near-field enhancement experiments are also shown in Fig. 3.22b corresponding to the near-field contact measurement and the far-field reference at a gap of 50 μm. It can be observed that the extraction apparatus does exhibit some parasitic thermal emission with an increase in magnitude at all wavelengths as the temperature is raised. However, the maximum magnitude is much smaller compared to the emission intensities measured in the near-field enhancement experiments. Therefore, it can be safely concluded the dominant thermal emission source originated from the N-BK7 thermal emitter.

Table 3.3: Measured temperatures of the heater and at the edge of the ZnSe prism.

#	Heater Temperature, T_H	ZnSe Temperature, T_{ZnSe}
1	72.1 ºC	53.2 ºC
2	85.1 ºC	59.2 ºC
3	103.7 ºC	69.1 ºC
4	116.7 ºC	77.3 ºC

Given that the thermal emission measured from the N-BK7 thermal emitter will include a far-field component, a comparison can also be made between just the near-field contribution and the parasitic emission from the extraction apparatus. To make this comparison, the emission intensities from the near-field enhancement experiments shown in Fig. 3.22a are subtracted from one another. This subtraction isolates the near-field contribution by removing the far-field components to the total emission intensity. However, it should be cautioned that unlike the formulation for the near-field enhancement in Eq. (3.1), this subtraction will still include parasitic absorption from the FTIR. A similar subtraction is applied to the thermal emission intensity data for the extraction apparatus at temperatures of T_{ZnSe} = 77.3ºC and 59.2ºC to match with the near-field enhancement data. This reflects the variations in the thermal emission from the extraction apparatus that occurs during experiment. The results of this subtraction are shown in Figs. 3.22c and 3.22d for the emission intensities from the extraction apparatus and the near-field enhancement experiments, respectively. The variation in emission intensity from the extraction apparatus exhibits no distinct spectral features. In contrast, a clear peak can be observed in the near-field

data, which matches the peaks observed in earlier results and corresponds to the wavelength range where a SPhP mode is expected to exist in N-BK7. However, the magnitude of the variation in emission intensity from the extraction apparatus is similar to the magnitude of the peak in the near-field data. As discussed earlier, the emission from the extraction apparatus is likely overestimated in these measurements, thus it can be concluded that the contribution of thermal emission from the extraction apparatus is at most comparable to the near-field contribution.

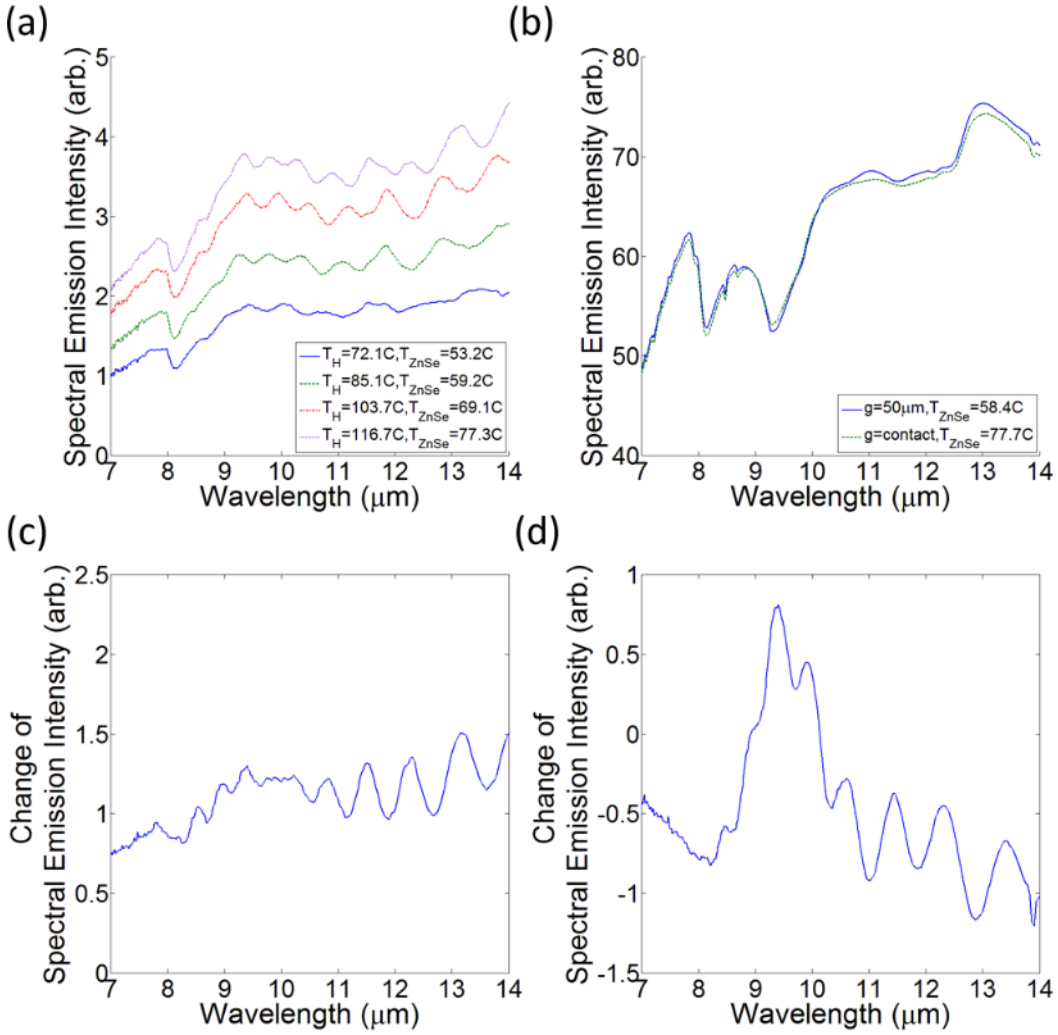

Figure 3.22: (a) The spectral emission intensities from the extraction apparatus at various temperatures. (b) The measured spectral emission intensities in the near-field enhancement measurement at contact and g = 50 μm. (c) The subtraction of spectral emission intensities from (a) using T_{ZnSe} = 77.3ºC and 59.2ºC. (d) The subtraction of spectral emission intensities from (b).

The spectral emissive properties of the extraction apparatus were also measured to verify the peak observed in the near-field enhancement data in Sects. 3.4.4 originates from only the N-BK7 thermal emitter. Specifically, the spectral emittance of the pinhole aperture and the ZnSe prism is measured by normalizing the background-corrected thermal emission from these components to a black reference (Acktar Advanced Coatings, Metal Velvet). A 50 x 50 mm heater is used to directly heat the components. A K-type thermocouple is embedded in the heater for temperature calibration. The heater is mounted onto the aluminum holder originally supporting the ZnSe prism. Since the heater in this case is larger than the sample, an iris combined with a large radiation shield made of aluminum foil is used to ensure thermal emission is only measured from the sample. An OAP mirror is again used to collect thermal emission into the FTIR spectrometer. To provide sufficient contrast to the background thermal emission, the temperature of all samples were measured at 100ºC. The setup is shown in Figs. 3.23a. To verify the experimental configuration yields accurate measurements of emittance, the spectral emittance of the bare heater, which is covered by aluminum, was measured as a reference, as shown in Fig. 3.23b. The spectral emittance of the aluminum reference is disperionless with no distinct spectral features and exhibits an average value of 0.04, consistent with literature data.[208]

The spectral emittances of the pinhole aperture with and without the ZnSe prism were then measured, as shown in Figs. 3.23b. The spectral emittance of the pinhole aperture without the ZnSe lens is approximately 0.1 within the measured wavelength range and exhibits no distinct spectral features. When the ZnSe prism is placed onto the pinhole aperture, the emittance becomes lower in the 10 μm to 14 μm wavelength range compared to shorter wavelengths. This may be due to both emission and absorption from the metal clips used to secure the ZnSe prism to the heater. However, in both measurements, there is crucially no observable peak between 8 and 11 μm that corresponds to the peak observed in the near-field enhancement data in Sect. 3.4.4. Therefore, based on these results, the observation of a peak in the near-field enhancement spectra in Sects. 3.4.4 can only originate from the N-BK7 thermal emitter. Therefore, this confirms a quantitative, gap-dependent near-field enhancement was indeed measured spectrally.

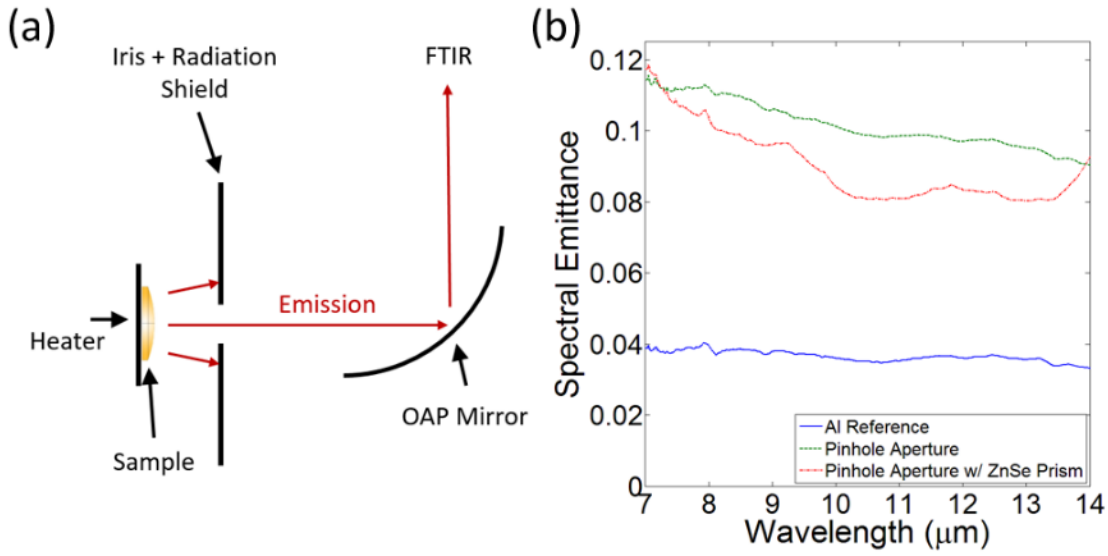

Figure 3.23: The spectral emittance of the pinhole aperture and ZnSe prism were also measured to further validate the near-field enhancement results. (a) A schematic illustration of the experimental configuration used to measure the spectral emittance. (b) The measured spectral emittances for the aluminum reference, the pinhole aperture, and the pinhole aperture with the ZnSe prism.

3.5 Summary

In summary, a measurement technique was developed to provide quantitative and gap-dependent spectral measurements of near-field thermal emission. The underlying approach consists of using a high index prism in an inverse Otto configuration in order to provide momentum to extract evanescent near-field modes. In an effort to conceptually demonstrate this method, a preliminary experimental configuration was developed, which consisted of using a heated spherically convex N-BK7 lens as a thermal emitter and a ZnSe lens as a prism in conjunction with a FTIR spectrometer to resolve the spectral components of the extracted near-field thermal emission. The thermal emitter was mounted onto a cantilever and a piezo stage, which provides contact calibration and gap control, respectively. Although the experiment was conducted in ambient conditions, which caused the temperature of the thermal emitter to vary, several corrections were developed to compensate for this systematic variation. As a result, preliminary measurements indicate that this measurement technique can resolve quantitative, gap-dependent near-field enhancement spectrally.

Given that this was a first-generation platform, a number of improvements can be made to further improve the accuracy of this method. First, a vacuum chamber should be incorporated in order to eliminate heat conduction losses between the emitter and the prism. As shown in Fig. 3.24, if the current experimental apparatus is placed into vacuum, it is predicted the temperature variation across the thermal emitter surface will be substantially minimized in comparison to the results previously shown in Fig. 3.10. If combined with a more sophisticated heating system with temperature feedback, it should be possible to minimize the temperature variation in the thermal emitter even further, thus eliminating the need to apply corrections to the near-field enhancement spectra. This will also enable higher temperature measurements, since the oxidation of ZnSe would no longer be a limitation. Second, a ZnSe hemisphere in conjunction with a precision-made on-axis parabolic mirror can be used to fully capture all extracted thermal emission. This will not only dramatically increase the emission intensity, and thus the signal strength, but will also ensure all thermal radiation coupled from the near-field regime is included in the resulting spectra. To better isolate the near-field thermal emission, a small optical mirror or trap can also be used to block thermal radiation coupled to small angles in the prism, where the far-field contribution to thermal emission predominantly exists.

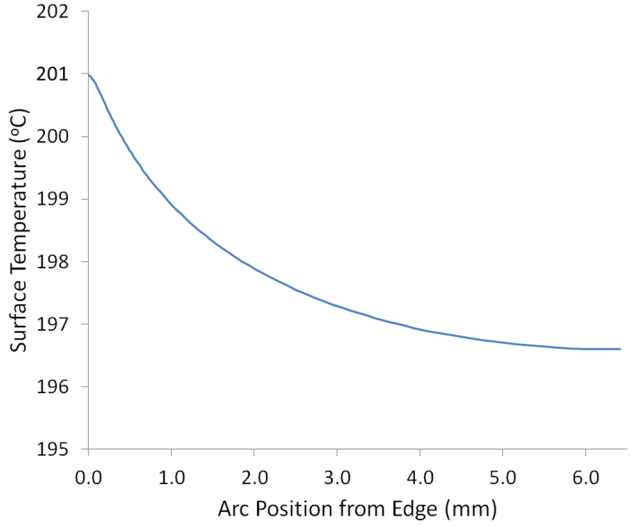

Figure 3.24: The predicted temperature profile along the thermal emitter surface for the configuration shown in Fig. 3.10 when placed in vacuum. The gap separation is 100 nm.

Third, a pinhole aperture should be directly fabricated onto either the thermal emitter the prism using an ultra-low emittance metal such as gold. This will provide suppression of far-field thermal radiation from the spherically convex thermal emitter while avoiding the unnecessary introduction of a parasitic source of thermal emission. And fourth, a step-scan FTIR spectrometer should be used with lock-in detection in order to maximize the signal-to-noise ratio. Furthermore, the Michelson interferometer should ideally be cooled with liquid nitrogen to minimize background thermal emission.

With these improvements, several additional modifications can also be incorporated to make this method more robust. If a hemispherical prism is used without the aid of a parabolic reflector, it should also be possible to measure near-field thermal emission coupled to the prism at different angles. By measuring near-field thermal emission spectrally at different angles, it should be possible to measure the photonic dispersion that governs near-field coupling between the emitter and the prism as a function of the wavelength and the wave vector. In addition, although a sphere-plate configuration is used for experimental convenience, this method is also applicable to the parallel-plate configuration, in which sophisticated systems developed in previous studies can be adapted for this approach.[184–186] This would enable spectral measurements of near-field radiative heat transfer without the inclusion of any far-field contribution.

Chapter 4

Infrared-Transparent Visible-Opaque Fabrics

Up to this point, the morphological modification of the photon dispersion has been applied to evanescent fields in an effort to manipulate near-field radiative heat transfer. However, it is also possible to apply morphological effects to change the optical properties of particulates in the far-field regime. In this chapter, an example application will be discussed that utilizes both Rayleigh and Mie scattering to create an infrared transparent, visibly opaque fabric (ITVOF) for use in personalized cooling. The ITVOF provides passive cooling by enabling thermal radiation emitted by the human body to directly transmit into the environment, while remaining opaque to the human eye. First, a brief overview of light scattering and personalized cooling will be provided. This will be followed by the development of a heat transfer model used to evaluate the required optical properties of the ITVOF for different environmental conditions. Then, an evaluation of common textiles is provided in an effort to develop a suitable design criteria for an ITVOF. And finally, theoretical predictions for a proposed ITVOF design will be presented.

4.1 Rayleigh and Mie Scattering of Light

The interaction of light with small particles is a well-studied phenomenon that traces its history back to the late 19th and early 20th centuries following the development of the Maxwell equations in 1861 with seminal studies by Lord Rayleigh, Ludwig Lorenz, Gustav Mie, Peter Debye, and many others.[213–218] In these works, the theoretical foundation to describe the interaction of light with particles comparable to or smaller than the wavelength of light was developed. For the sake of brevity, a brief overview of the historical development of light scattering theory will be provided here. For a more detailed account, readers are referred to several recent studies.[219–221]

In 1871, Rayleigh published the first of several studies on light scattering by particles, providing the first rigorous explanation for the origins of Earth's blue sky.[214,215] In this work, it was shown that particles, whose characteristic length scale are substantially smaller than the

wavelength of incident light, will exhibit a scattering efficiency, Q_{sca}, defined as the scattering cross section, C_{sca}, normalized to the geometric cross section of the particle, C_{geo}, as follows,

$$Q_{sca} = \frac{C_{sca}}{C_{geo}} = \frac{8}{3}x^4 \left|\frac{\varepsilon-1}{\varepsilon+2}\right|^2 \qquad ; x<<1 \tag{4.1}$$

where x is the size parameter of the particle defined as $x = 2\pi a/\lambda$, a is the particle radius, λ is the wavelength of light, and ε is the complex dielectric permittivity of the particle. As shown in Eq. (4.1), the scattering efficiency is extremely sensitive to the wavelength of light with a dependency of $Q_{sca} \sim \lambda^{-4}$, indicating that shorter wavelength light will scatter substantially more. It is for this reason Earth's sky is blue since air molecules in Earth's atmosphere will scatter more blue light as sunlight passes through the atmosphere. The results presented in this work formed the basis of what later became known as Rayleigh scattering, which is applicable to the regime where $x << 1$.

In 1908, Mie published a complete analytical solution to the scattering of light by spherical particles with a characteristic length scale comparable to the wavelength of light ($x \sim 1$).[216] This work was used to explain the variation in color of colloidal solutions composed of gold nanoparticles with varying size observed by Richard Zsigmondy during this period of time.[222] In this work, a spherical harmonic expansion was used to recast all electromagnetic waves into spherical form in order to analytically solve the electromagnetic wave equation for the case of a plane wave illuminating a spherical particle. Based on this solution, Mie was able to attribute the change in color to a resonance that shifts with the particle size. These results formed the basis of what is now known as Mie scattering. Unlike the results developed by Rayleigh in Eq. (4.1), this solution is general and can be applied to all size regimes from the geometric ray optics regime ($x >> 1$), to the Mie scattering regime ($x \sim 1$), and to the Rayleigh scattering regime ($x << 1$).

For the sake of historical accuracy, it would be prudent to mention that in 1909 Debye utilized the same methodology to analyze radiation pressure on spherical particles.[217] Predating both of these works, Lorenz also published identical solutions in 1890; however, the work was written in Danish and was thus virtually unknown to the scientific community.[218] For these reasons, these solutions are also referred to as the Mie-Lorenz theory and even Mie-Lorenz-Debye theory. Further details on the derivation and the particular solutions in the Mie regime can be found in earlier references.[223]

Naturally, the light scattering properties of a particle will depend upon the particles' material properties; however, as the particle transitions from the geometric ray optics regime to

the Rayleigh scattering regime, several general characteristic features can be observed to distinguish each light scattering regime. Fundamentally, the variation in optical properties between these different light scattering regimes is predicated on the same morphological modification of the photon dispersion discussed in previous chapters. As an example, the scattering efficiency of a SiO_2 sphere is plotted in Fig. 4.1 as a function of the sphere's radius. In the visible wavelength range, SiO_2 behaves as a nearly lossless, dispersionless dielectric.

As shown in Fig. 4.1, the scattering efficiency initially increases monotonically as the particle size increases, which is consistent with Eq. (4.1) in the Rayleigh regime. In this regime, incident light views the particle as a localized perturbation of refractive index in free space where light scattering occurs via absorption and subsequent isotropic re-radiation. As the material volume increases, this perturbation becomes stronger resulting in a larger scattering efficiency. Once the particle is sufficiently large, fundamental resonant modes in the form of whispering gallery mode (WGM) in the case of spheres will appear as indicated by the oscillations in the scattering efficiency.[97,224] The observation of resonant modes indicates a transition into the Mie regime. Like the trapped waveguide modes discussed in Chapter 2, the WGM resonances of a sphere increase in number and redshift as the particle size increases, as shown in Fig. 4.1.

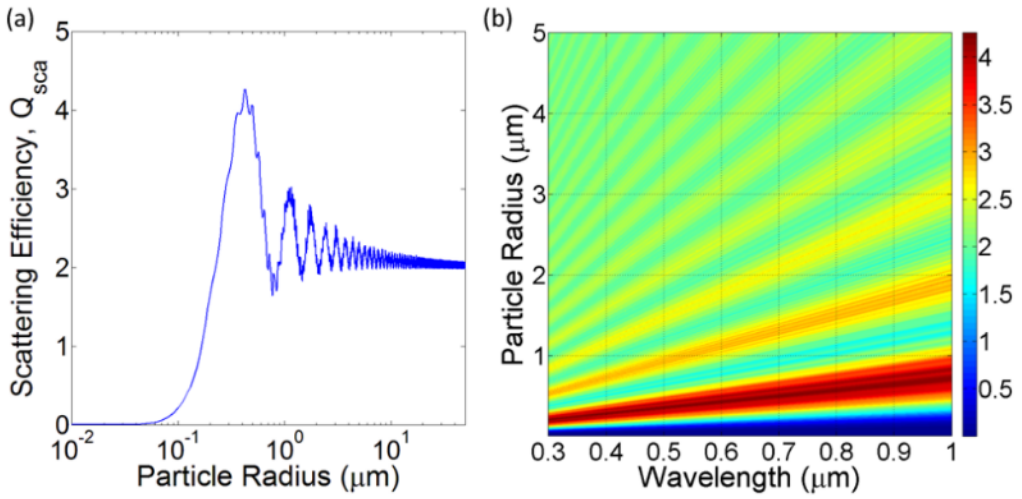

Figure 4.1: The variation in scattering efficiency, Q_{sca}, of a SiO_2 sphere as it transition from the Rayleigh scattering regime through the Mie scattering regime to the geometric ray optics regime. (a) Q_{sca} as a function of the particle radius at a wavelength of $\lambda = 600$ nm. (b) A color map of Q_{sca} as a function of both the particle radius and wavelength of incident light. As shown, several distinct bands can be observed, which is indicative of the appearance of WGM resonances in the sphere.

However, unlike the trapped waveguide modes, the confinement of a WGM resonance will vary with curvature.[97,224] When the first fundamental WGM resonance appears, the electromagnetic fields of the mode extend beyond the particle boundaries, rendering the mode leaky. This enables greater coupling with incident light, which results in a large scattering efficiency. As the particle size increases, the fields become more confined within the sphere, leading to a scattering efficiency that oscillates with a progressively smaller amplitude. As the particle size continues to increase, the scattering efficiency converges to a value of 2, which is a manifestation of the well-known extinction paradox in the geometric ray optics regime.[223] This example illustrates that morphological modification of the photon dispersion in the form of different sized spheres can dramatically affect far-field optical properties.

The theoretical formulations developed in this era have since been used in a variety of fields to design and analyze light scattering from small particles for a variety of applications. Perhaps one of the earliest applications of Mie theory is in the field of astronomy where in the 1950's this formulation was applied to analyze the scattering of light by interstellar dust to evaluate the composition, size, and distribution of particulates in different regions of our galaxy.[225–230] With the creation of the environmental protection agency in 1970 and the subsequent passing of the Clean Air Act, researchers also utilized light scattering theory to analyze the concentration of aerosol particulates in the atmosphere to evaluate the environmental damage that was being done due to air pollution and ozone depletion.[231–239] More recently, with the extensive developments in nanolithography and synthesis, the unique light scattering properties of sub-micron particulates have found use in even more fields of study including bio- and chemical sensing, imaging[240–248], photocatalysis, photodetection, light emitting diodes, photovoltaics[249–259], and many more applications.[260,261]

For radiative heat transfer, the same principles used to manipulate the optical properties of particulates can be applied to spectrally tune and shape not only the emissive and absorptive properties, but also the opaqueness of materials to thermal radiation. To show the impact of morphology in the far-field regime, the remainder of the chapter will focus on an example application that utilizes both Rayleigh and Mie scattering to create an infrared transparent, visibly opaque fabric. This fabric can enable passive personal cooling by transmitting thermal radiation emitted by the human body directly to the environment. The following sections are a direct reprint of an earlier publication shown in the following reference.

4.2 Energy Management in Building Infrastructure[Ψ]

In recent years, personal cooling technologies have been developed to provide local environmental control to ensure the user remains thermally comfortable when in extreme environmental conditions such as those faced by athletes, the military, or EMS personnel.[262] However, there remains a distinct lack of such technologies for everyday use by the average end user who spends the majority of the time in a sedentary state. This is especially important for indoor environments where incorporation of such technologies can offset energy consumed by HVAC systems for cooling while maintaining sufficient levels of thermal comfort. For instance, recent studies have shown that in the United States alone, residential and commercial buildings consume nearly 41% of total energy use each year with 37% of that energy devoted solely to heating and cooling.[262–264] To reduce energy usage, buildings have incorporated more renewable energy sources such as solar power, implemented advanced HVAC systems, utilized higher performing thermal insulation, and phase change materials for thermal storage all of which requires significant financial investment.[265–267] Instead, personal thermal comfort technologies offer a potentially low cost solution towards mitigating energy use by HVAC systems. Although these technologies can be used in a variety of indoor and outdoor environments, the focus of this work is to provide personal cooling in temperature regulated indoor environments.

4.3 Current State-of-the-Art Personal Cooling Technologies

At present, several technologies are commercially available which provide varying degrees of personal cooling. However, these technologies are typically tailored as high performance products, such as sportswear, body armor, and personal protection equipment, thus limiting functionality for everyday use. Arguably the most prevalent personal comfort technology used in industry today is moisture wicking where sensible perspiration is drawn away from the skin to the outer surface of the fabric and evaporated to ambient air thus cooling the wearer passively.[268–270]

[Ψ]Reprinted with permission from J. K. Tong, X. Huang, S. V. Boriskina, J. Loomis. Y. Xu, and G. Chen, "Infrared-Transparent Visible-Opaque Fabrics for Wearable Personal Thermal Management," ACS Photonics, Vol. 2, 6, 769-778 (2015). Copyright 2015 American Chemical Society.

The drawback of this technology is that it is activated only when the wearer is sufficiently perspiring so that moisture accumulates on skin; thus, moisture wicking is not suitable to provide cooling for sedentary individuals. Other technologies utilize phase change materials in the form of cold packs which can effectively draw heat from the human body due to the high latent heat of melting associated with water and other refrigerants.[271–274] However this technology tends to be bulky in size and requires frequent replacement of the cold packs over time rendering this technology inconvenient and expensive to the end user. And finally, several technologies provide active cooling through use portable air conditioning units or liquid cooling.[275–279] These systems not only consume power, but also tend to be prohibitively expensive.

To overcome these limitations, we introduce the concept of an infrared-transparent visible-opaque fabric (ITVOF) which utilizes the human body's innate ability to thermally radiate heat as a cooling mechanism during the summer season when environmental temperatures are high. A heat transfer model was developed in order to determine the required IR optical properties of the ITVOF to ensure thermal comfort is maintained for environmental temperatures exceeding the neutral band. From this analysis, it was experimentally observed that existing textiles fail to meet these requirements due to a combination of intrinsic material absorption and structural backscattering in the IR wavelength range. In lieu of these loss mechanisms, a design for an ITVOF was developed using a combination of optimal material composition and structural photonic engineering. Specifically, synthetic polymers which support few vibrational modes were identified as candidate materials to reduce intrinsic material absorption in the IR wavelength range. To reduce backscattering losses, individual fibers were designed to be comparable in size to visible wavelengths in order to minimize reflection in the IR by virtue of weak Rayleigh scattering while remaining optically opaque in the visible wavelength range due to strong Mie scattering. By additionally reducing the size of the yarn, which is defined as a collection of fibers, less material is used thus decreasing volumetric absorption in the IR wavelength range even further. The ITVOF design is numerically demonstrated to exhibit a high transmittance and a low reflectance in the IR wavelength range while remaining optically opaque in the visible wavelength range. Compared to conventional technologies, an ITVOF can be manufactured into simple form factors while providing a fully passive means to cool the human body regardless of the physical activity level of the user.

4.4 Heat Transfer Analysis for Personal Thermal Comfort

4.4.1 Requirements for Radiative Cooling of Human Body

In order to quantify the potential cooling power using thermal radiation, the maximum radiative heat transfer achievable between the human body and the surrounding environment can be computed using the Stefan-Boltzmann law. Past studies have shown that human skin behaves like a blackbody with an emittance near unity in the IR wavelength range.[280,281] Even if the skin is wet due to perspiration, the emittance is still 0.96 corresponding to water, which suggests human skin is an effective IR emitter for all levels of physical activity.[282] If it is assumed the surface area of an average adult human body is A = 1.8 m^2, the temperature of human skin is T_0 = 33.9°C (93°F), and the ambient temperature is T_3 = 23.9°C (75°F), which corresponds to the upper limit of a typical neutral temperature band for human thermal comfort in buildings, the radiative heat transfer coefficient between the skin and the environment is h_r = 6.25 W/m^2K.[283,284] Under these conditions, the cooling power predicted by the Stefan-Boltzmann law is 112 W.[208] Radiative heat loss from the human body is thus comparable to natural convection and the cooling power actually exceeds the total heat generation rate of q_{gen} = 105 W assuming a base metabolic rate at rest of 58.2 W/m^2.[285] From this estimation, it can be observed that thermal radiation clearly has the potential to provide significant cooling power.

To fully harness thermal radiation for cooling, clothing fabrics should be transparent to mid- and far-infrared radiation which is the spectral range where the human body primarily emits.[208,280] Although a total hemispherical transmittance of unity would be ideal, it would be useful to determine the transmittance required for the ITVOF to provide the necessary cooling power for an individual to feel comfortable at different indoor temperatures. This criterion is determined by assuming the cooling power should equal the total heat generation rate of q_{gen} = 105 W at a skin temperature of T_0 = 33.9°C (93°F) and a typical room temperature of T_3 = 23.9°C (75°F). Under these conditions, the effective heat transfer coefficient is equal to h_{ref} = 5.8 W/m^2K which is less than the maximum achievable using thermal radiation. If the ambient temperature increases, the additional cooling power, q_{cool}, needed is equal to the difference between the total heat generation rate, q_{gen}, and the heat loss due to h_{ref},

$$q_{cool} = q_{gen} - h_{ref}\left(T_0 - T_3\right) \tag{4.2}$$

For this study, the goal is to provide cooling at an elevated ambient temperature of T_3 = 26.1°C (79°F), which past studies have shown can lead to nearly 40% energy savings in indoor

environments for certain regions of the United States.[283] Using Eq. (4.2) at this temperature, the fabric must provide 23 W of additional cooling.

4.4.2 Model Formalism

Based on this criterion, a more detailed one-dimensional steady-state heat transfer model is used to determine the total mid- to far-IR transmittance and reflectance required for the ITVOF. This model, as illustrated in Fig. 4.2, includes a continuous cloth placed at a distance, t_a, from the human body to model the effect of a thermally insulating air gap when loose fitting clothing is worn. The model combines a control volume analysis and an analytical formulation of the temperature profile within the cloth in order to evaluate heat transfer between the human body, the cloth, and the ambient environment. Radiative heat transfer, heat conduction, and convection are all included in the analysis. For convenience, the following denotations are used in this model: 0 – surface of human skin, 1 – inner surface of the cloth, 2 – outer surface of the cloth, and 3 – the ambient environment.

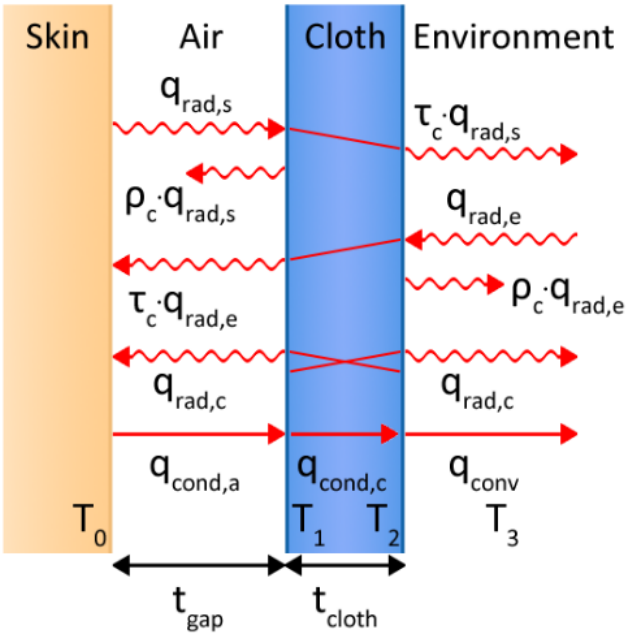

Figure 4.2: A heat transfer model was developed to analyze heat dissipation from a clothed human body to the ambient environment. Various heat transfer contributions that lead to dissipation of heat from the human body, such as radiation, heat conduction, and heat convection are included. To model loose fitting clothing, a finite air gap is assumed between the cloth and the skin.

To ensure this analysis remains mathematically tractable while still providing realistic estimates for radiative cooling based on the IR optical properties of the cloth, the following assumptions are used as follows,

(1) In general, the human body can be modelled as a cylinder with a 1 m diameter. In this analysis, the air gap thickness, t_a, and cloth thickness, t_c, are assumed to be much smaller compared to the diameter. Therefore, curvature effects are assumed to be negligible, thus heat transfer is modelled as 1D transport through parallel slabs. In this analysis, heat transfer is expressed as area-normalized heat fluxes.
(2) The human body is assumed to be in a sedentary state with a uniform skin temperature and heat generation.
(3) The cloth is assumed to cover 100% of the human body.
(4) The air between the skin and cloth is assumed to be stationary thus convective heat transfer is negligible in this region.
(5) Air circulation through the cloth is neglected.
(6) All optical properties are assumed to be gray and diffuse.
(7) The skin and environment are assumed to be an ideal blackbody emitter and absorber.
(8) An average cloth temperature (e.g. mean of T_1 and T_2) is assumed for thermal emission by the cloth.
(9) All radiative view factors are equal to 1.
(10) Internal scattering and self-absorption effects are neglected within the cloth.
(11) It is assumed the absorption and emission profile is linear within the cloth. This is an approximation of the more rigorous exponential profile that governs absorption and emission when internal scattering is negligible. In the limit of either high cloth transmittance or reflectance, this is a reasonable assumption due to the linearity of the exponential decay. In the limit of high absorptance, this assumption will no longer be accurate. Despite this, the cooling power and the maximum ambient temperature can still be reasonable predicted since the difference between the inner and outer cloth temperatures is expected to be small.

The thermal conductivity of air is $k_a = 0.027$ W/mK and the thermal conductivity of the cloth fabric is assumed to be $k_y = 0.05$ W/mK.[208] Assuming a cloth porosity of 0.15, which is typical for

common clothing, the effective thermal conductivity of the cloth layer is $k_c = 0.047$ W/mK.[286] The thickness of the cloth is conservatively chosen to be $t_c = 0.5$ mm.

Additionally, the cloth is assumed to be partially reflective, transmissive, and absorptive with gray and diffuse optical properties. In conjunction with Kirchoff's law, the cloth's optical properties will adhere to the following relation,

$$\varepsilon_c = \alpha_c = 1 - \rho_c - \tau_c \tag{4.3}$$

where ε_c, α_c, ρ_c, and τ_c are the cloth's total hemispherical emittance, absorptance, reflectance, and transmittance, respectively.

Table 4.1 summarizes the input parameters used in this study. In order to determine the total cooling power through the cloth, the net heat flux in this analysis can be multiplied by the surface area of the human body, A.

Table 4.1: Input Parameters

Parameter Name	Value	Parameter Name	Value
Human body surface area, A	1.8 m^2	Cloth thickness, t_c	0.5 mm
Heat generation rate, q_{gen}	58.2 W/m^2	Total emittance of skin	1
Skin temperature, T_0	33.9°C (93°F)	Total emittance of environment	1
Thermal conductivity of air, k_a	0.027 $Wm^{-1}K^{-1}$	Conv. heat transfer coeff., h	3-5 $Wm^{-2}K^{-1}$
Thermal conductivity of yarn, k_y	0.05 $Wm^{-1}K^{-1}$	Air gap thickness, t_a	1.05-2.36 mm
Cloth porosity	0.15	Cloth reflectance, ρ_c	0-1
Thermal conductivity of cloth, k_c	0.047 $Wm^{-1}K^{-1}$	Cloth transmittance, τ_c	0-1

In this model, the overall goal is to determine the maximum ambient temperature that can be sustained without compromising a person's thermal comfort as a function of the cloth's optical properties. Although a minimum ambient temperature also exists, this is related to personal heating and is thus beyond the scope of this work. The criterion used to evaluate personal thermal comfort is based on the equivalence of the total cooling power with the total heat generation rate of 105 W from the human body. For a given set of material and environmental conditions, the ambient temperature is increased iteratively until the net cooling power can no longer dissipate the amount of heat generated by the human body. By fixing the skin temperature to be 33.9°C (93°F), the primary unknown variables in this model are the inner surface cloth temperature, T_1, the outer surface cloth temperature, T_2, and the ambient temperature, T_3.

Additionally, the air gap thickness, t_a, and the convective heat transfer coefficient, h, can also be varied to simulate different environmental conditions (i.e. tight-fitting vs. loose fitting cloth

on different areas of the human body, varying levels of air circulation within the ambient environment, etc.) independent of the environment temperature. In order to compare the impact of the cloth's optical properties on personal cooling for various environmental conditions, we constrain the air gap thickness and convective heat transfer coefficient to ensure a consistent baseline neutral temperature band is used regardless of the environmental conditions. To accomplish this, we adopt a reference case that assumes an ambient temperature of 23.9°C (75°F), corresponding to the upper limit of a typical neutral temperature band. The reflectance and transmittance of the cloth are also assumed to be $\rho_c = 0.3$ and $\tau_c = 0.03$, respectively, corresponding to measurements of conventional polyester and cotton fabrics. Under these conditions, we first choose the convective heat transfer coefficient and iterate the air gap thickness until the total cooling power exactly balances the total heat generation rate using the model equations as shown below. In this manner, the maximum ambient temperature for various environmental conditions and conventional clothing is always 23.9°C (75°F). Thus, any subsequent improvements can only be attributed to radiative cooling through the cloth. In this work, we assume an individual is cooled via natural convection, thus the convective heat transfer coefficient has a typical range of 3-5 W/m^2K with a corresponding air gap thickness of 1.05-2.36 mm.

4.4.3 Control Volume Analysis

The first component of the heat transfer model is to identify relevant control volumes (CV) and to apply an energy balance in order to obtain equations that connect the various heat transfer mechanisms included in this model. As shown in Fig. 4.3a, there are two control volumes that will be used in this study: CV1 is defined around only the human body and CV2 is defined around the entirety of the surrounding cloth. The expressions obtained when applying an energy balance around CV1 and CV2 are as follows,

$$\text{CV 1: } q_{gen} + q_{rad,c} + \tau_c \cdot q_{rad,e} - \left(1 - \rho_c\right) \cdot q_{rad,s} - q_{cond,a} = 0 \tag{4.4}$$

$$\text{CV 2: } \left(1 - \rho_c - \tau_c\right) \cdot q_{rad,s} + \left(1 - \rho_c - \tau_c\right) \cdot q_{rad,e} + q_{cond,a} - 2 \cdot q_{rad,c} - q_{conv} = 0 \tag{4.5}$$

where q_{gen} is the heat generation rate per unit area, $q_{cond,a}$ is the conductive heat flux between the skin and the cloth, q_{conv} is the convective heat flux from the cloth to the ambient environment, $q_{rad,s}$ is the radiative heat flux from the skin, $q_{rad,e}$ is the radiative heat flux from the ambient environment, and $q_{rad,c}$ is the radiative heat flux from the cloth. The conductive, convective, and

radiative heat flux terms are expressed using Fourier's law, Newton's law of cooling, and the Stefan-Boltzmann law as follows,

$$q_{cond,a} = k_a \cdot \frac{T_0 - T_1}{t_a} \tag{4.6}$$

$$q_{conv} = h \cdot \left(T_2 - T_3\right) \tag{4.7}$$

$$q_{rad,s} = \sigma T_0^4 \tag{4.8}$$

$$q_{rad,e} = \sigma T_3^4 \tag{4.9}$$

$$q_{rad,c} = \varepsilon_c \sigma \left(\frac{T_1 + T_2}{2}\right)^4 \tag{4.10}$$

where T_0 is the skin temperature, T_1 is the inner surface cloth temperature, T_2 is the outer surface cloth temperature, T_3 is the ambient temperature, k_a is the thermal conductivity of air, t_a is the air gap thickness, h is the convective heat transfer coefficient, σ is the Stefan-Boltzmann constant equal to $5.67 \cdot 10^{-8}$ $Wm^{-2}K^{-4}$. In Eq. (4.10), we assume a mean temperature of T_1 and T_2 to approximate radiative emission by the cloth. Additionally, in Eqs. (4.4), (4.5), (4.9), and (4.10), it was assumed the skin and environment behave like an ideal blackbody with an absorptance and emittance equal to 1.

Based on the control volume analysis, we obtain two fundamental Eqs. (4.4) and (4.5) that describe the various contributions to heat transfer in this system. Since there are three unknowns that must be solved for, an additional equation is required in order to complete this model. Equations (4.4) and (4.5) describe heat transfer around the human body and the cloth, respectively. By deduction, the remaining equation must describe the nature of heat transfer within the cloth itself. Specifically, by considering heat conduction, radiative absorption, and radiative emission, a temperature profile can be derived in order to link the unknown temperatures T_1 and T_2.

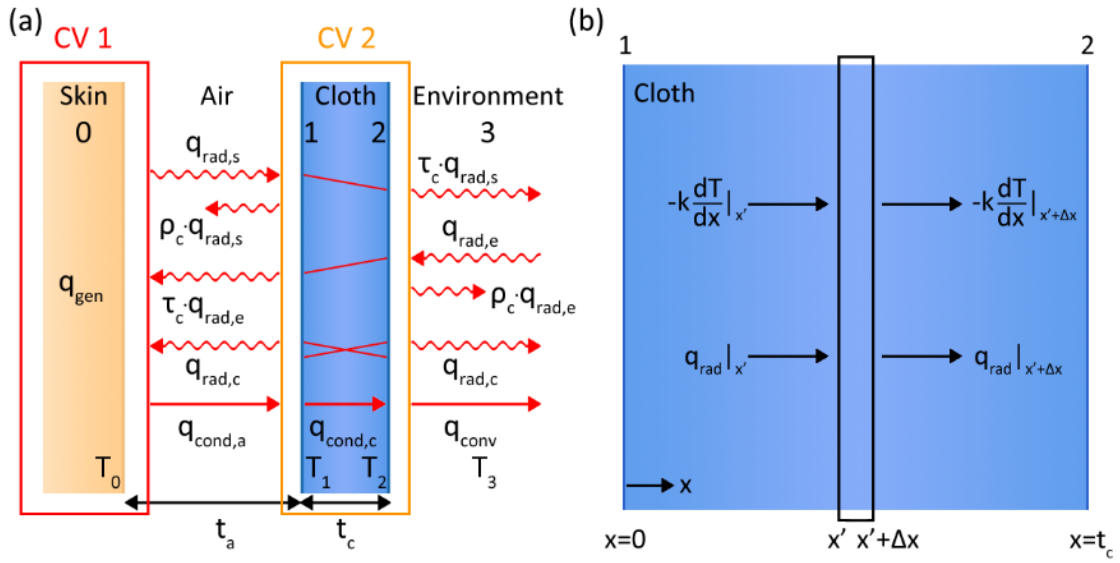

Figure 4.3: Illustrations depicting the control volume analysis and temperature profile formulation for the heat transfer model. (a) The control volumes chosen in this analysis consist of CV1 around the human body and CV2 around only the cloth. (b) A schematic illustrating the differential element and energy balance used to derive the temperature profile within the cloth. In addition to heat conduction, this analysis includes radiative absorption and emission.

4.4.4 Temperature Profile in Cloth

To determine the temperature profile within the cloth, heat conduction and radiative heat transfer must be included in the heat transfer analysis. If a differential volume element is taken within the cloth, as shown in Fig. 4.3b, the heat equation will take the following form,[287]

$$k_c \frac{\partial^2 T}{\partial x^2} - \frac{\partial}{\partial x}\left(q_{rad}\right) = 0 \tag{4.11}$$

where k_c is the cloth thermal conductivity and q_{rad} is the net radiative transfer within the cloth. In general, q_{rad} must be determined rigorously using the radiative heat transfer equation in order to account for all absorption, emission, and internal scattering processes. For simplicity, we assume internal scattering effects are negligible and only consider IR reflection at the boundaries of the cloth, as will be later shown when determining the expressions for each radiative heat flux. Additionally, self-absorption effects are also neglected. Therefore, the net radiative heat transfer will consist only of incident radiative absorption and outgoing radiative emission as follows,

$$k_c \frac{\partial^2 T}{\partial x^2} = \frac{\partial}{\partial x}\left(q_{rad,cL'}\right) + \frac{\partial}{\partial x}\left(q_{rad,cR'}\right) + \frac{\partial}{\partial x}\left(q_{rad,s'}\right) + \frac{\partial}{\partial x}\left(q_{rad,e'}\right) \tag{4.12}$$

where $q_{rad,cL'}$ is the radiative emission from the cloth to the skin, $q_{rad,cR'}$ is the radiative emission from the cloth to the ambient environment, $q_{rad,s'}$ is the absorption of radiation emitted from the skin, and $q_{rad,e'}$ is the absorption of radiation emitted from the ambient environment.

In general, the analytical form for radiative absorption and emission in the limit of negligible internal scattering will consist of an exponential decay in accordance to the Beer-Lambert law.[287] However, we again simplify the analysis by instead assuming the absorption and emission profile to be linear as follows,

$$q_{rad,i}(x) = A \cdot x + B \tag{4.13}$$

where A and B are unknown coefficients that will depend on the boundary conditions assumed for each radiative heat flux. In the limit of high absorption, the approximation of a linear absorption and emission profile will be inaccurate. Despite this limitation, it is nonetheless expected that this approximation will provide a reasonable estimation of heat transfer through the cloth since the difference in the inner and outer cloth temperature is not expected to be large, thus inherently making this analysis less sensitive to the absorption and emission profile used. Using Eq. (4.13) and appropriate boundary conditions for each radiative flux, we obtain the following,

1. Emission from cloth to skin:

$$\begin{aligned} &q_{rad,cL'}(x=0) = -q_{rad,c} \\ &q_{rad,cL'}(x=t_c) = 0 \end{aligned} \quad \rightarrow q_{rad,cL'}(x) = \frac{q_{rad,c}}{t_c} x - q_{rad,c} \tag{4.14}$$

2. Emission from cloth to ambient environment:

$$\begin{aligned} &q_{rad,cR'}(x=0) = 0 \\ &q_{rad,cR'}(x=t_c) = q_{rad,c} \end{aligned} \quad \rightarrow q_{rad,cR'}(x) = \frac{q_{rad,c}}{t_c} x \tag{4.15}$$

3. Absorption by cloth from skin:

$$\begin{aligned} &q_{rad,s'}(x=0) = (1-\rho_c) \cdot q_{rad,s} \\ &q_{rad,s'}(x=t_c) = \tau_c \cdot q_{rad,s} \end{aligned} \quad \rightarrow q_{rad,s'}(x) = -\frac{\alpha_c \cdot q_{rad,s}}{t_c} x + (1-\rho_c) \cdot q_{rad,s} \tag{4.16}$$

4. Absorption by cloth from ambient environment:

$$\begin{aligned} &q_{rad,e'}(x=0) = -\tau_c \cdot q_{rad,e} \\ &q_{rad,e'}(x=t_c) = -(1-\rho_c) \cdot q_{rad,e} \end{aligned} \quad \rightarrow q_{rad,e'}(x) = -\frac{\alpha_c \cdot q_{rad,e}}{t_c}(x-t_c) - (1-\rho_c) \cdot q_{rad,e} \tag{4.17}$$

Upon substituting Eqs. (4.14)-(4.17) into (4.12) and using the definition of heat fluxes defined by Eqs. (4.8)-(4.10), the heat equation will become,

$$\frac{\partial^2 T}{\partial x^2} = \frac{1}{k_c t_c}\left(2\varepsilon_c\sigma\left(\frac{T_1+T_2}{2}\right)^4 - \alpha_c\sigma T_0^4 - \alpha_c\sigma T_3^4\right) \tag{4.18}$$

where a mean temperature of T_1 and T_2 is again used to approximate radiative emission from the cloth. Although radiative emission from the cloth technically depends on the local temperature T as a function of position x, the use of a mean temperature is a reasonable approximation since T_1 and T_2 are not expected to be significantly different.

To determine the temperature profile, all that remains is to integrate Eq. (4.18) and apply appropriate boundary conditions,

$$\frac{\partial T}{\partial x} = \frac{1}{k_c t_c}\left(2\varepsilon_c\sigma\left(\frac{T_1+T_2}{2}\right)^4 - \alpha_c\sigma T_0^4 - \alpha_c\sigma T_3^4\right)x + C_1 \tag{4.19}$$

$$T = \frac{1}{2k_c t_c}\left(2\varepsilon_c\sigma\left(\frac{T_1+T_2}{2}\right)^4 - \alpha_c\sigma T_0^4 - \alpha_c\sigma T_3^4\right)x^2 + C_1 x + C_2 \tag{4.20}$$

The boundary conditions applied in this analysis includes temperature and heat flux continuity at surface 1 (x = 0) as follows,

$$T(x=0) = T_1 \tag{4.21}$$

$$-k\frac{\partial T}{\partial x}(x=0) = q_{cond,a} \tag{4.22}$$

Upon applying Eqs. (4.21) and (4.22) in Eqs. (4.19) and (4.20), we obtain the final expression for the temperature profile within the cloth,

$$T = \frac{1}{2k_c t_c}\left(2\varepsilon_c\sigma\left(\frac{T_1+T_2}{2}\right)^4 - \alpha_c\sigma T_0^4 - \alpha_c\sigma T_3^4\right)x^2 - \frac{k_a}{k_c}\frac{(T_0 - T_1)}{t_a}x + T_1 \tag{4.23}$$

By taking $x = t_c$ in Eq. (4.23), the following temperature relation is obtained,

$$T_2 = \frac{t_c}{2k_c}\left(2\varepsilon_c\sigma\left(\frac{T_1+T_2}{2}\right)^4 - \alpha_c\sigma T_0^4 - \alpha_c\sigma T_3^4\right) - \frac{k_a t_c}{k_c t_a}(T_0 - T_1) + T_1 \tag{4.24}$$

Therefore, with Eqs. (4.4), (4.5), and (4.24), we now have a complete set of equations to describe heat transfer from a human body covered by cloth to the ambient environment. These equations are used to first obtain the air gap thickness, t_a, for the previously described reference case with an assumed convective heat transfer coefficient. Following this calculation, we then use the same equations to solve for T_1, T_2, and T_3 as a function of the cloth's optical properties and the assumed

environmental conditions. From this analysis, we can find the maximum ambient temperature, T_3, which can be sustained without compromising personal thermal comfort.

4.4.5 Results and Analysis

Figures 4.4a and 4.4b show contour maps of the maximum ambient temperature as a function of the cloth's total reflectance and transmittance for different combinations of the air gap thickness, t_a, and the convective heat transfer coefficient, h, which represent a typical range of ambient environmental conditions where natural convection is dominant. In order to properly compare the impact of the cloth's optical properties on cooling for different environmental conditions, t_a and h are coupled such that at an ambient temperature of 23.9°C (75°F) and assuming typical optical properties for clothing ($\rho_c \sim 0.3$ and $\tau_c \sim 0.03$), the total cooling power is always equal to the total heat generation rate thus ensuring a consistent baseline neutral temperature band is used.[288]

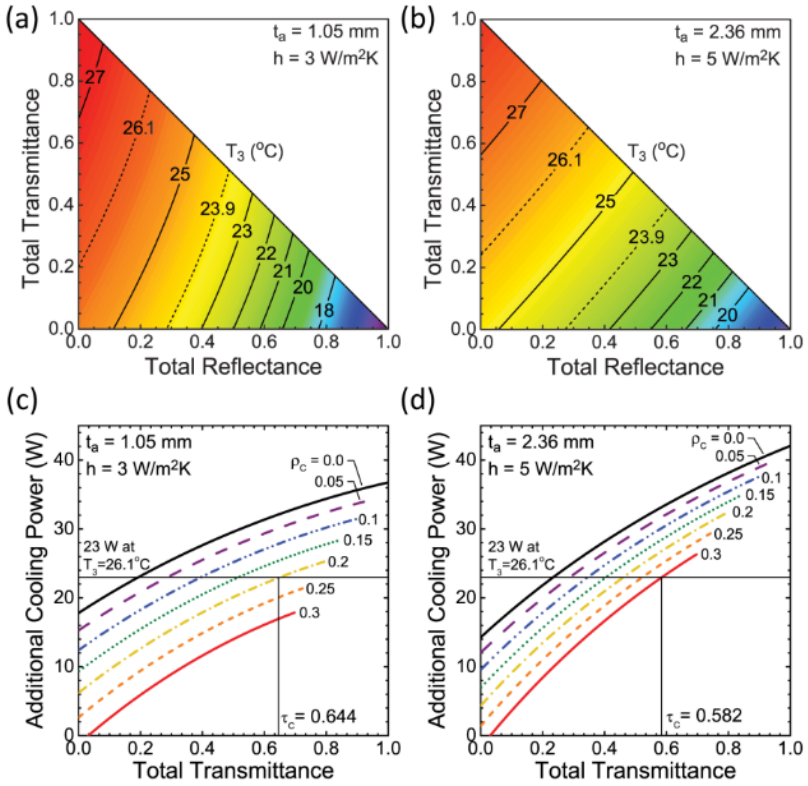

Figure 4.4: Evaluation of ITVOF mid- to far-IR optical requirements to maintain personal thermal comfort at elevated ambient temperatures. (a) A temperature map was computed showing the maximum ambient temperature attainable without compromising thermal comfort as a function of

the total reflectance and transmittance of the cloth. It is assumed the air gap is t_a = 1.05 mm and the convective heat transfer coefficient is h = 3 W/m^{2}K. (b) A corresponding temperature map assuming t_a = 2.36 mm and h = 5 W/m^{2}K. The range of h is typical for cooling via natural convection. (c) An additional cooling power curve showing quantitatively the effect of radiative cooling as a function of the total cloth transmittance and reflectance assuming t_a = 1.05 mm and h = 3 W/m^{2}K. (d) An additional cooling power curve assuming t_a = 2.36 mm and h = 5 W/m^{2}K. As shown, by decreasing the reflectance and increasing the transmittance, it is possible to achieve the necessary 23 W of cooling at an ambient temperature of 26.1 ºC using only thermal radiation.

In both cases, a reflective cloth is more detrimental to cooling performance than an absorptive cloth since a high absorptance implies a high emittance, which would allow clothing to radiate thermal radiation to the environment albeit at a lower temperature. It can also be observed in Fig. 4.4a that in the limit of high absorption, the maximum ambient temperature is higher for the case where the air gap between the skin and cloth is less insulating (t_a = 1.05 mm) despite the reduction in the convective heat transfer coefficient (h = 3 W/m^{2}K). This suggests heat conduction and thermal radiation are comparable in this limit, thus for conventional clothing it is crucial to minimize the thermal resistance to heat conduction. However, as the mid- to far-IR transparency of the cloth increases, radiative heat transfer becomes more dominant compared to heat conduction. As a result, the impact of the insulating air gap on cooling is mitigated, thus a higher maximum ambient temperature can be sustained, when the convective heat transfer coefficient is larger (h = 5 W/m^{2}K) even though the air gap is more insulating (t_a = 2.36 mm) as shown in Fig. 4.4b. These results show that by designing clothing to be transparent to mid- and far-IR radiation, it is possible to provide persistent cooling using thermal radiation even for loose fitting clothing where the trapped air normally acts as a thermally insulating barrier, which impedes heat transfer in conventional personal cooling technologies.

To determine quantitatively the optical properties required for the ITVOF to provide 23 W of additional cooling at an ambient temperature of T_3 = 26.1ºC (79ºF), additional cooling power curves were computed as a function of the cloth's total reflectance and transmittance in Figs. 4.4c and 4.4d. In the limit of an ideal opaque fabric (α_c = 1), it can be seen for both cases that it is not possible to reach 23 W of additional cooling. This indicates that unless convective cooling is improved, which is challenging to achieve for everyday use as described earlier, it is impossible

to maintain personal thermal comfort using opaque clothing; hence, the clothing must exhibit transparency to mid- and far-IR radiation.

For the case where t_a = 1.05 mm and h = 3 W/m^{2}K in Fig. 4.4c, if the cloth reflectance is larger than 0.2, it is also not possible to reach 23 W of additional cooling. This again shows that a higher cloth reflectance is more detrimental to the cooling performance of the cloth than absorption. Thus, when increasing the transmittance of the cloth, it is crucial that the reflectance is simultaneously reduced in order to maximize radiative cooling. Based on these results, the ITVOF must exhibit a maximum reflectance of 0.2 and a minimum transmittance of 0.644 in order to meet the personal thermal comfort criterion. For the case where t_a = 2.36 mm and h = 5 W/m^{2}K in Fig. 4.4d, the optical properties of the ITVOF become less stringent with a maximum reflectance of 0.3 and a minimum transmittance of 0.582. It should be emphasized that the reflectance and transmittance of the ITVOF are intrinsically coupled, thus a decrease in reflectance will lead to a corresponding decrease in the transmittance required to maintain thermal comfort as shown in Figs. 4.4c and 4.4d.

4.5 Spectral Properties of Common Textiles

In order to design the ITVOF, a baseline reference was first established by characterizing the optical properties of common clothing. Specifically, the optical properties of undyed cotton and polyester cloths, which comprise nearly 78% of all textile fiber production, were measured in both the visible and IR wavelength ranges.[289] Figures 4.5a and 4.5b show SEM images of the cotton and polyester cloths, respectively. The fabrics consist of fibers with a diameter of ~10 μm sewn into yarns that are 200 to 300 μm in size. Depending on the weave, the yarn can intertwine and overlap differently; however, the thickness of the cloth generally varies from one yarn to two overlapping yarns.

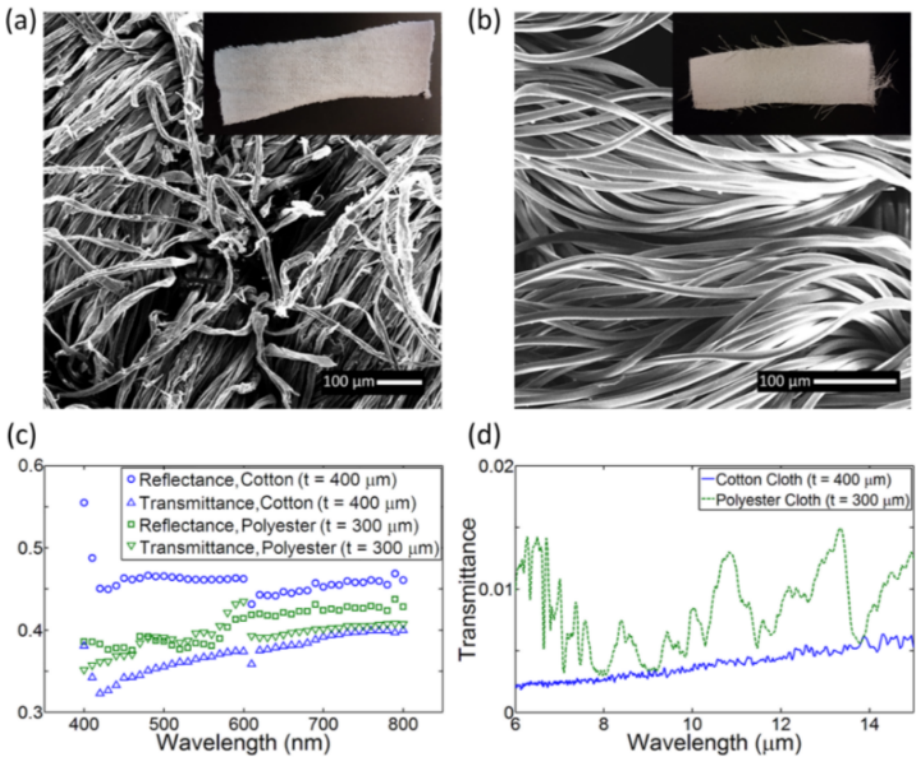

Figure 4.5: Optical properties of conventional clothing. SEM images of (a) undyed cotton cloth and (b) undyed polyester cloth which show the intrinsic fabric structure. The insets are optical images of the samples characterized. For both samples, the fiber diameter is on average 10 μm and the yarn diameter is greater than 200 μm. The scale bars both correspond to 100 μm. (c) Experimentally measured optical properties in the visible wavelength range. (d) Experimentally measured FTIR transmittance spectra of undyed cotton cloth (thickness, t = 400 μm) and undyed polyester cloth (t = 300 μm) showing the opaqueness of common fabrics in the IR.

The visible wavelength optical properties of both cloth samples were measured using a custom UV/visible spectrometer. This system consisted of a 500 W mercury xenon lamp source (Newport Oriel Instruments, 66902), a monochromator (Newport Oriel instruments, 74125), and a silicon photodiode (Newport Oriel instruments, 71675). To account for the diffuse scattering of light from the samples, an integrating sphere (Newport Oriel Product Line, 70672) was used to measure the hemispherical reflectance and transmittance of the cloth in the wavelength range of 400 nm to 800 nm. Total hemispherical reflectance measurements were performed by placing the cloth samples onto a diffuse black reference (Avian Technologies LLC, FGS-02-02c) to avoid reflection from the underlying substrate. Total hemispherical transmittance measurements were

performed by placing the cloth samples onto the input aperture of the integrating sphere. All measurements were calibrated using a diffuse white reference (Avian Technologies LLC, FWS-99-02c). The results are shown in Fig. 4.5c. As expected, the undyed cloth samples exhibit no distinct optical features in the reflectance and transmittance spectra. Both samples show similar optical properties with a reflectance ranging from 0.4 to 0.5 and a transmittance ranging from 0.3 to 0.4. The high transmittance is primarily due to the intrinsic properties of cotton and polyester which are weakly absorbing in the visible wavelength range.[146,290]

Although these cloth samples exhibit a high transmittance, their apparent opaqueness is due to a combination of the contrast sensitivity of the human eye and the diffuse scattering of light. The human eye is a remarkably sensitive optical sensor that can respond to a large range of light intensities.[291,292] However, past studies have shown that the human eye can only perceive variations in light intensity when the change in intensity relative to the background is sufficiently large.[293–296] This implies that for clothing to appear opaque, the fraction of light reflected by the skin and observed by the human eye must be sufficiently smaller than the fraction of light reflected by the fabric into the same direction. For these cloth samples, light will reflect and transmit diffusively. In addition, skin is also a diffuse surface with a reflectance that is as high as 0.6 at longer wavelengths.[297] Since the observation of skin requires light to be reflected from the skin and transmitted through the cloth twice, more light will be scattered into directions beyond what is observable by the human eye compared to light that is only reflected by the cloth thus ensuring the opaque appearance of the cloth. It is for these reasons that common clothing appears opaque to the human eye despite an inherently high transmittance. From these results, the criteria for opaqueness of the ITVOF design will be assessed by comparing the hemispherical reflectance and transmittance to measured data shown in Fig. 4.5c.

The IR transmittance spectra of the cloth samples were measured using a commercially available FTIR spectrometer (Thermo Fisher Scientific, Nicolet 6700) and an IR objective accessory (Thermo Fisher Scientific, Reflachromat 0045-402). The objective was placed 15 mm behind the samples, corresponding to the working distance of the objective, in order to capture infrared radiation transmitted through the samples. For the cloth samples, the total hemispherical transmittance will be underestimated since not all of the IR radiation that is diffusively transmitted through the cloth sample is captured. However, the objective used in this study was designed to capture IR radiation at a 35.5^{o} acceptance angle. Since it is expected that IR radiation will transmit

diffusively, the measured results are likely underestimated by a few percent, which is still in agreement with previous studies.

The IR transmittance spectra of the cotton and polyester samples, as shown in Fig. 4.5d, exhibit a low transmittance of 1% across the entire IR wavelength range in agreement with previous studies.[288,298–300] Therefore, both samples are opaque in the IR and thus cannot provide the necessary cooling to the wearer at higher ambient temperatures according to the heat transfer model.

The reasons for the low transmittances are two-fold. First, cotton and polyester are highly absorbing in the IR wavelength range. Figure 4.6a shows the FTIR transmittance spectra of a single strand of cotton yarn and a polyester thin film. Several absorption peaks can be observed which originate from the many vibrational modes supported in the complex molecular structure of these materials. Since fabrics are typically several hundreds of microns thick, which is much larger than the penetration depth, incident IR radiation is completely absorbed at these wavelengths. Second, the fibers in clothing are comparable in size to IR wavelengths, as shown in Figs. 4.5a and 4.5b, which enable the fibers to support optical resonances that can strongly scatter incident light. In this Mie regime, it is well known that particles can exhibit large scattering cross sections due to these resonances.[223,252,301–303] For an array of many fibers, the collective scattering by the fibers can result in a high reflectance. Therefore, the creation of an ITVOF must minimize these two contributions in order to maximize transparency to mid- and far-IR radiation.

4.6 Design Strategy for ITVOF

Based on the heat transfer modeling and the experimental results, the design strategy for an ITVOF is to use alternative synthetic polymers which are intrinsically less absorptive in the IR wavelength range and to structure the fibers to minimize the overall reflectance of the fabric in order to maximize radiative cooling. In general, synthetic polymers with simple chemical structures are ideal since fewer vibrational modes are supported thus resulting in less absorption. Additionally, these polymers must also be compatible with extrusion and drawing processes to ensure manufacturability for large scale production. Based on these criteria, polyethylene and polyacprolactam, more commonly known as nylon, were identified as potential candidate materials. It should be emphasized however that given the full gamut of synthetic polymers available, other synthetic polymers may also be suitable for an ITVOF.

Polyethylene is one of the simplest synthetic polymers available and the most widely used in industry today. The chemical structure of polyethylene consists of a repeating ethylene monomer with a total length that varies depending on the molecular weight. Because the chemical structure consists entirely of carbon-carbon and carbon-hydrogen bonds, few vibrational modes are supported. This is evidenced in Fig. 4.6b which shows measured FTIR transmittance spectra for an ultra-high molecular weight polyethylene (UHMWPE) thin-film (McMaster 85655K11). Absorption peaks can be observed at 6.8 μm corresponding to CH_2 bending modes, 7.3 μm and 7.6 μm to CH_2 wagging modes, and 13.7 μm and 13.9 μm to CH_2 rocking modes.[304] At longer wavelengths, additional rocking modes do exist, but are typically very weak. For textile applications, woven polyethylene fabrics are often used as geotextiles, tarpaulins, and tapes.[305] To assess the suitability of polyethylene for clothing applications, further studies are needed to evaluate mechanical comfort and durability.

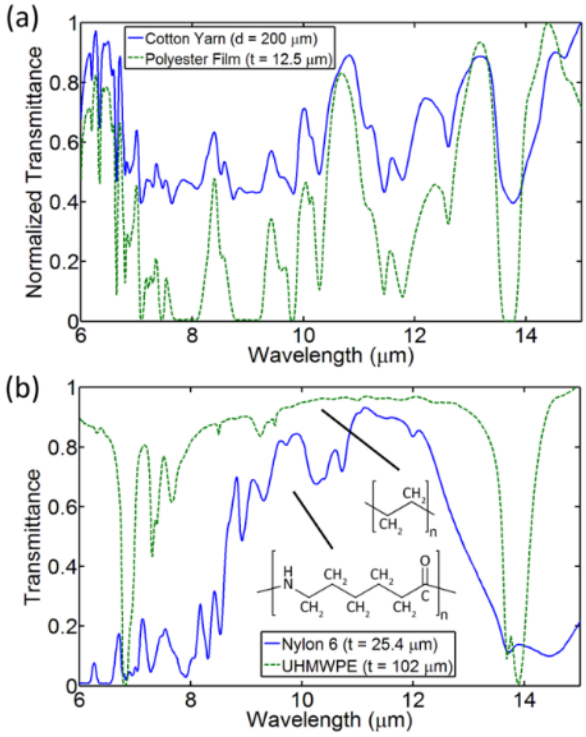

Figure 4.6: Intrinsic absorptive properties of various synthetic polymers. (a) The FTIR transmittance spectra for a single cotton yarn (diameter, d = 200 μm) and a polyester thin-film (thickness, t = 12.5 μm). The transmittance spectra is normalized to provide similar scaling due to the order of magnitude difference in sample size. (b) The FTIR transmittance spectra for two

candidate materials for the ITVOF. These materials include thin-films of nylon 6 (t = 25.4 μm) and UHMWPE (t = 102 μm).

Nylon (McMaster 8539K191) exhibits a similar structure to polyethylene with the key difference being the inclusion of an amide chemical group. As shown in Fig. 4.6b, this results in additional vibrational modes from 6 μm to 8 μm and 13 μm to 14 μm corresponding to the various vibrational modes from the amide group.[306] Although nylon is absorptive over a larger wavelength range compared to polyethylene, the advantage of nylon is that it is currently used in many textiles.

Compared to cotton and polyester, Fig. 4.6b shows that polyethylene and nylon exhibit fewer vibrational modes particularly in the mid-IR wavelength range near 10 μm where the human body thermally radiates the most energy. This indicates that polyethylene and nylon are intrinsically less absorptive and are therefore suitable for the creation of an ITVOF.

In order to further improve the IR transparency of an ITVOF constructed from these materials, structural photonic engineering can be introduced for both the fiber and yarn. Specifically, absorption by weaker vibrational modes can be minimized by reducing the material volume. This can be accomplished by simply decreasing the yarn diameter. To minimize backscattering of IR radiation, the fibers can also be reduced in size such that the diameter is small compared to IR wavelengths. In this manner, incident IR radiation will experience Rayleigh scattering where the scattering cross section of infinitely long cylinders in this regime decreases rapidly as a function of the diameter raised to the 4^{th} power.[223] By reducing the scattering cross section, back scattering of IR radiation will significantly decrease resulting in an overall lower IR reflectance.

Conversely, for the visible wavelength range the ITVOF must instead have a low transmittance to ensure ITVOF-based clothing is opaque to the human eye. Since polyethylene and nylon are not strongly absorptive in the visible wavelength range, reflection must be maximized. This can be achieved by using fibers that are comparable in size to visible wavelengths so that incident light experiences Mie scattering. In exactly the same manner that conventional clothing is opaque to IR radiation, fibers in this regime can support optical resonances that significantly increase the scattering cross section of each fiber thus increasing the overall backscattering of incident light.[223] Since the fabric is composed of an array of these fibers, not only will the total reflectance increase, but light scattering with the cloth will become more diffuse.

In conjunction with the contrast sensitivity of the human eye, this design approach can ensure the ITVOF is opaque to the human eye. Thus, the beauty of this structuring approach is that with an optimally chosen fiber diameter, two different regimes of light scattering are utilized in different spectral ranges in order to create a fabric which is simultaneously opaque in the visible wavelength range and transparent in the IR wavelength range.

In regards to the coloration of the ITVOF, polyethylene and nylon exhibit dispersionless optical properties in the visible wavelength range and with sufficient backscattering appear white in color. Despite the chemical inertness of polyethylene, it is possible to provide coloration through the introduction of pigments during fiber formation when polyethylene is in a molten state.[307] On the other hand, nylon fibers can be colored easily using conventional dyes.[308] Depending on the pigment or dye, additional vibrational modes may be introduced in the IR wavelength range reducing the overall transparency. However, for the sake of demonstrating the general concept of an ITVOF, this design aspect will be left for future studies.

4.7 Numerical Electromagnetics Modeling

To theoretically demonstrate the proposed strategy to create an ITVOF, numerical finite-element electromagnetic simulations were performed on a polyethylene fabric structure illustrated in Fig. 4.7a. In these simulations, circular arrays of parallel fibers are arranged into collective bundles in order to represent the formation of yarn. The yarn is then positioned in a periodic staggered configuration oriented 30^{o} relative to the horizontal plane to mimic the cross section of a woven fabric. For all simulations, it is assumed the fiber separation distance, D_s, is 1 μm and the yarn separation distance, D_p, is 5 μm, which is consistent with the cloth structures observed in Figs. 4.5a and 4.5b. Simulations in the IR wavelength range were conducted from 5.5 to 24 μm. Wavelengths shorter than 5.5 μm contribute only 2.7% to total blackbody thermal radiation and are thus considered negligible. Wavelengths longer than 24 μm contribute 17.2% to total blackbody thermal radiation; however, longer wavelengths are expected to yield an even higher transparency since polyethylene does not support vibrational modes beyond 24 μm. As a conservative estimate, the optical properties of the ITVOF design are spectrally integrated and normalized within only the 5.5 to 24 μm wavelength range, which will underestimate the transmittance and overestimate the reflectance and absorptance. Furthermore, the spectral integration is weighted by the Planck's distribution assuming a skin temperature of 33.9^{o}C (93^{o}F).

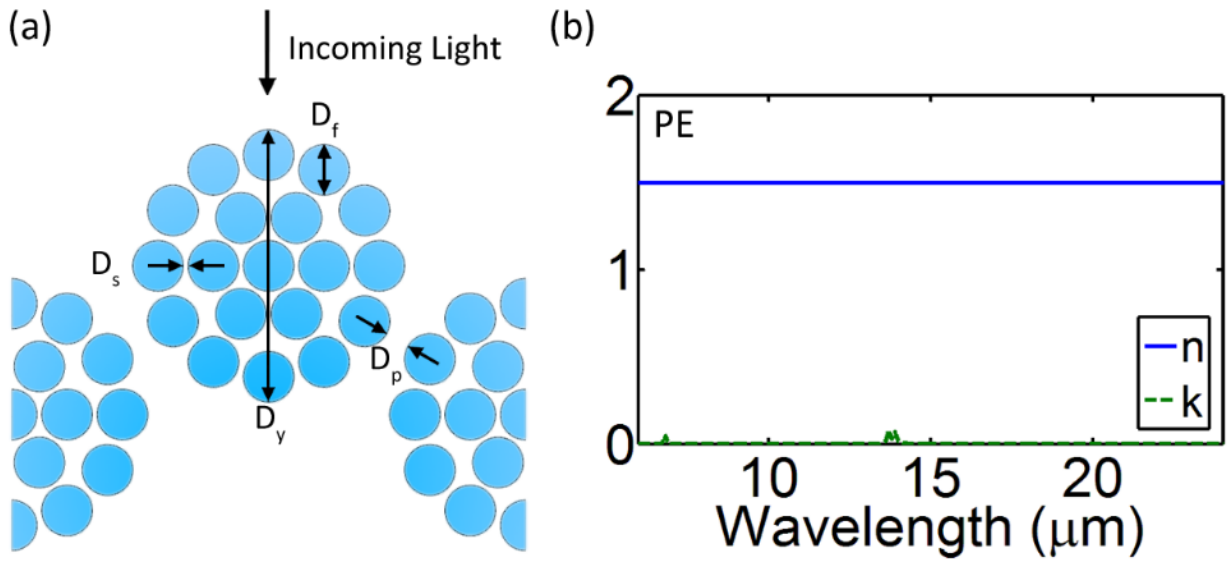

Figure 4.7: Simulation parameters. (a) A schematic of the numerical simulation model used to predict the optical properties of the ITVOF design. The parameters include: D_f – the fiber diameter, D_y – the yarn diameter, D_s – the fiber separation distance, and D_p – the yarn separation distance. For all simulations, the yarns were staggered 30° relative to the horizontal plane. In addition, incident light was assumed to be at normal incidence and the optical properties for unpolarized light were calculated by average light polarized parallel and perpendicular to the fiber axis. (b) The optical constants of polyethylene (PE) taken from the literature.[146] The refractive index, n, is extrapolated from shorter wavelength data. Based on the dispersion of the extinction coefficient, k, it is expected the refractive index will also exhibit some dispersion. However, this is assumed to be small and is thus neglected in this study.

Floquet periodic boundary conditions are used on the right and left boundaries to simulate an infinitely wide structure. Perfectly matched layers are used on the top and bottom boundaries to simulate an infinite free space. Simulations were conducted for incident light polarized parallel and perpendicular to the fiber axis at normal incidence. The optical properties for unpolarized light were determined by taking an average of the results for both polarizations. The optical constants of bulk polyethylene were taken from the literature and are shown in Fig. 4.7b.[146] Although the manufacture of polymer fibers and the subsequent stress imposed when woven into fabrics can introduce anisotropy in the dielectric permittivity, past studies have experimentally shown that the

optical properties of drawn UHMWPE exhibit minimal change when subjected to a high draw ratio and high stresses.[309,310] Therefore, anisotropic effects were neglected in this study.

4.8 Results and Discussion

To assess the impact of reducing the size of the fiber (D_f) and the yarn (D_y), the IR optical properties were computed by varying the yarn diameter (D_y = 30 μm, 50 μm, and 100 μm) assuming a fixed fiber diameter of D_f = 10 μm and by varying the fiber diameter (D_f = 1 μm, 5 μm, and 10 μm) assuming a fixed yarn diameter of D_y = 30 μm. The results are shown in Fig. 4.8 along with the total spectrally integrated IR transmittance (τ_c) and reflectance (ρ_c) weighted by the Planck's distribution assuming a skin temperature of 33.9°C (93°F). Based on these results, a reduction in the yarn diameter does yield a higher spectral transmittance in the IR wavelength range as evidenced by the increase in the total hemispherical IR transmittance from 0.48 for D_y = 100 μm to 0.76 for D_y = 30 μm. Simultaneously, the total hemispherical IR reflectance also decreases from 0.35 to 0.19. This can be explained by a reduction in the total material volume, which is defined in this study for a single yarn on a per unit depth basis with units of μm^2 corresponding to the cross section of the yarn. As the yarn diameter decreases from D_y = 100 μm to D_y = 30 μm, the material volume decreases from 4870 μm^2 to 550 μm^2, which results in less absorption. Additionally, a reduction in the yarn diameter will also decrease the number of fibers that can scatter incident IR radiation, which leads to less reflection. These results suggest that by decreasing only the yarn diameter to D_y = 30 μm, it is possible to create an ITVOF that already exceeds the minimum transmittance of 0.644 and maximum reflectance of 0.2 required to maintain thermal comfort at an ambient temperature of 26.1°C (79°F) in Fig. 4.4c.

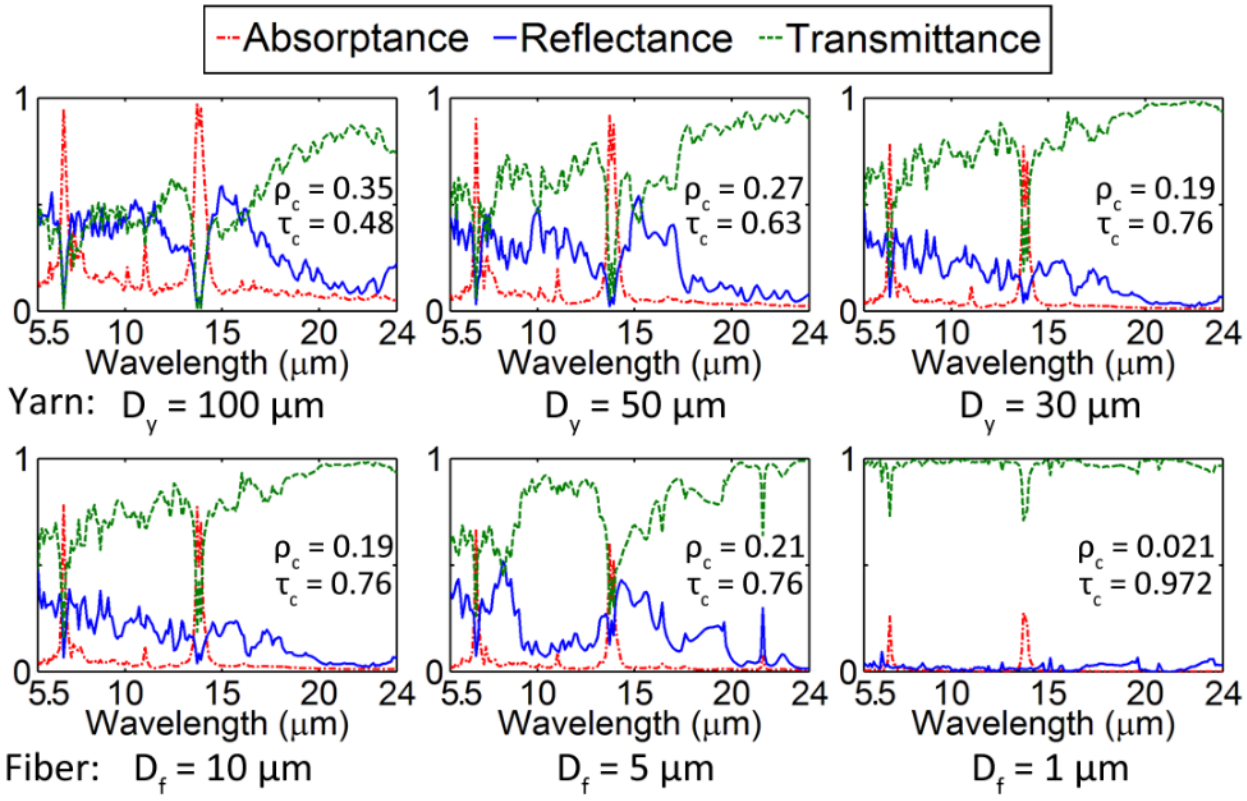

Figure 4.8: Numerical simulation results for the IR optical properties of a polyethylene-based ITVOF illustrating the effect of reducing the fiber and yarn size. Upper row: The yarn diameter is varied (D_y = 30 μm, 50 μm, and 100 μm) assuming a fixed fiber diameter of D_f = 10 μm. Lower row: The fiber diameter is varied (D_f = 1 μm, 5 μm, and 10 μm) assuming a fixed yarn diameter of D_y = 30 μm. For all simulations, the fiber separation distance is D_s = 1 μm and the yarn separation distance is D_p = 5 μm. The spectrally integrated transmittance (τ_c) and reflectance (ρ_c) is shown in each plot weighted by the Planck's distribution assuming a body temperature of 33.9°C (93°F). For D_f = 10 μm, the material volume per unit depth for a single yarn is 4870 μm^2 for D_y = 100 μm, 1492 μm^2 for D_y = 50 μm, and 550 μm^2 for D_y = 30 μm. For D_y = 30 μm, the material volume is 373 μm^2 for D_f = 5 μm and 136 μm^2 for D_f = 1 μm. The optical properties of the ITVOF are calculated for the wavelength range from 5.5 to 24 μm, which will provide a conservative estimate of the total transmittance and the reflectance.

However, the spectral optical properties in Fig. 4.8 indicate there is still room to further improve the transparency of the ITVOF as absorption and reflection are still substantial particularly at shorter wavelengths. In this wavelength range, the size of the fiber (D_f = 10 μm) is

comparable to the wavelength and is thus in the Mie regime where the fiber can support cavity resonances that can couple to and scatter incident IR radiation. Since the mode density of these resonances is higher at shorter wavelengths, the overall reflectance of the fabric structure will be higher as well. By reducing the size of the fiber, the number of supported cavity resonances will decrease resulting in a lower reflectance. The total material volume will also be reduced further from 550 μm^2 for D_f = 10 μm to 136 μm^2 for D_f = 1 μm thus decreasing the absorptance even further.

When the fiber diameter is reduced to 5 μm, the absorptance exhibits a marginal decrease. On the other hand, the reflectance actually increases compared to the case where D_f = 10 μm. This indicates that the fiber is still sufficiently large enough to support cavity resonant modes. Although there are fewer modes supported, as shown by the variation in reflectance, these modes become leakier for smaller size fibers thus resulting in a larger scattering cross section and a higher reflectance. As a result, there is little enhancement to the overall IR transmittance. Once the fiber diameter decreases to 1 μm, the reflectance dramatically decreases, which suggests the fiber is sufficiently small such that incident mid- to far-IR radiation will primarily experience Rayleigh scattering. In this Rayleigh regime, the fibers are too small to support cavity mode resonances thus reducing the reflection of IR radiation. Furthermore, the reduction in fiber size further reduces the total material volume again decreasing the absorptance. As a result, the total mid- to far-IR transmittance further increases from 0.76 for D_f = 10 μm to 0.972 for D_f = 1 μm, making the structure even more transparent to thermal radiation emitted by the human body. Simultaneously, the total mid- to far-IR reflectance decreases substantially from 0.19 to 0.021. By reducing the fiber diameter, the resulting improvements to the optical properties enable this ITVOF design to clearly surpass the requirements needed to provide 23 W of additional cooling at an ambient temperature of 26.1°C (79°F) based on Figs. 4.4c and 4.4d. It should again be noted that the calculated optical properties of the ITVOF only considered wavelengths from 5.5 to 24 μm. Since polyethylene is transparent at longer wavelengths, these results likely underestimate the total hemispherical transmittance and overestimate the total hemispherical reflectance and absorptance for mid- and far-IR radiation.

To assess the visible opaqueness, additional simulations were performed for the polyethylene-based ITVOF design assuming a constant refractive index of n = 1.5 and an extinction coefficient of $k = 5 \cdot 10^{-4}$ based on literature values for the visible wavelength range from

400 nm to 700 nm.[146] These simulations were performed for the optimal design where D_f = 1 μm, D_y = 30 μm, D_s = 1 μm, and D_p = 5 μm. The results are shown in Fig. 4.9 along with the experimentally measured optical properties of undyed cotton and polyester cloth for comparison.

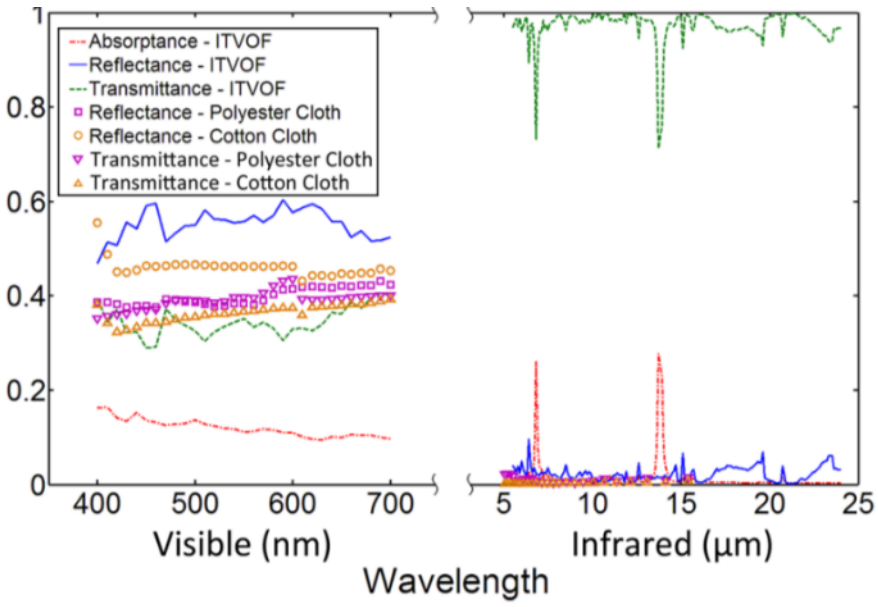

Figure 4.9: Theoretical results for the visible and IR wavelength range highlighting the contrast in optical properties needed for an ITVOF. These results correspond to the case of D_f = 1 μm, D_y = 30 μm, D_s = 1 μm, and D_p = 5 μm. For comparison, the experimentally measured reflectances and transmittances of cotton and polyester cloths are also shown.

The polyethylene-based ITVOF design exhibits a total hemispherical reflectance higher than 0.5 and a hemispherical transmittance less than 0.4 across the entire visible wavelength range, which is comparable to the optical properties of the experimentally characterized cotton and polyester cloth samples. The oscillatory behavior of the total hemispherical absorptance is indicative of whispering gallery and Fabry-Perot resonances supported in each fiber, as shown in Fig. 4.10, which confirms that light interaction is indeed in the Mie regime. As a result, these optical resonances provide strong backscattering to help ensure the fabric is opaque.

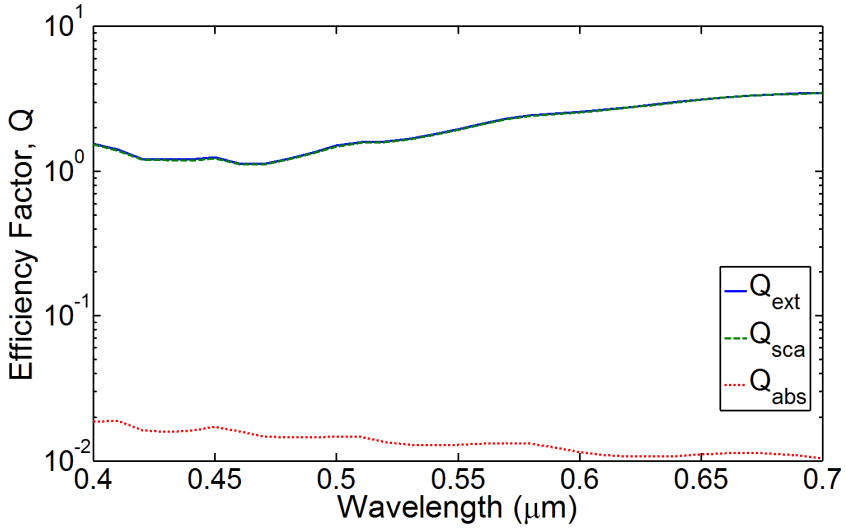

Figure 4.10: The visible wavelength extinction, scattering, and absorption efficiency of a single polyethylene fiber. The efficiency factor, Q, is defined as the ratio of the effective cross section normalized to the geometric cross section. The diameter of the fiber is D = 1 μm and the incident light is assumed to be unpolarized. For computation, the standard Mie theory solutions for an infinitely long cylinder were used.[223] As shown, the absorption efficiency exhibits a similar trend to the total hemispherical absorptance shown in Fig. 6 in the main text. The oscillatory behavior is indicative of whispering gallery modes supported by the fiber which are broadened due to material loss (n = 1.5, k = $5 \cdot 10^{-4}$). In addition, a broad Fabry-Perot resonance is also supported by the fiber as indicated by the scattering efficiency, which increases from 460 nm to 700 nm.

It can also be observed in Fig. 4.9 that the reflectance and transmittance do not follow the same trend as the absorptance. This can be attributed to the optical coupling of neighboring fibers in the fabric which collectively introduce additional optical resonances in the system due to the periodic nature of the assumed fabric structure. For a more realistic fabric structure where fiber and yarn spacing are non-uniform, long range optical coupling will be minimized resulting in a fabric which more diffusively scatters light. Due to the similarity to the experimentally characterized cloth samples, these results suggest the ITVOF design is optically opaque to the human eye. Furthermore, Fig. 4.9 clearly shows the contrast between the visible and IR properties of the ITVOF design which indicates that by optimally sizing the fiber, two vastly different regimes of light scattering can be simultaneously used.

Based on these results, it may appear that the creation of an ITVOF requires substantial reduction in material volume since the highest IR transmittance of 0.972 was predicted for the smallest yarn diameter (D_y = 30 μm) and fiber diameter (D_f = 1 μm). Although decreasing both of these parameters will certainly improve the overall transmittance in the IR wavelength range, additional simulations for various fiber diameters (D_f = 1 μm, 5 μm, and 10 μm) assuming a larger yarn diameter of D_y = 50 μm show a similar trend in the enhancement of transmittance, as shown in Fig. 4.11.

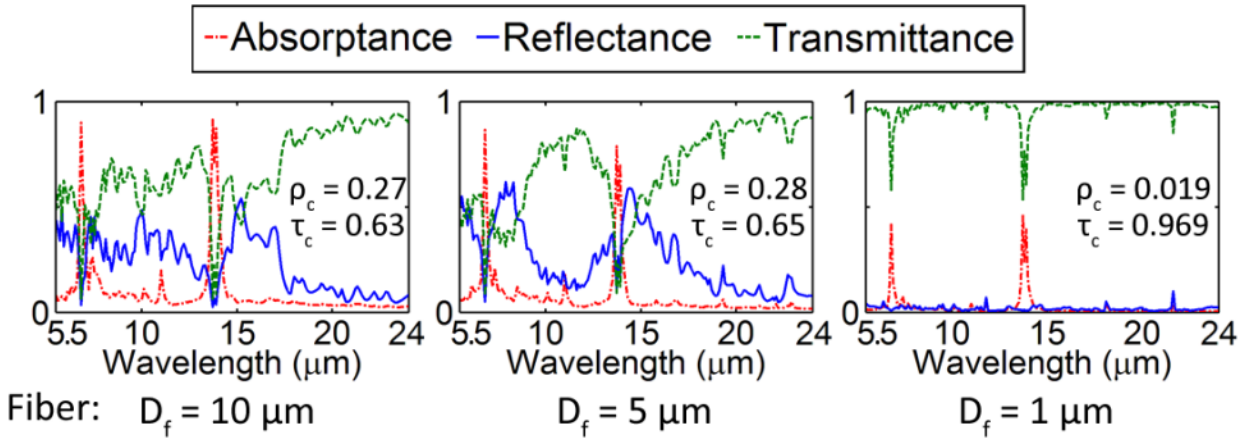

Figure 4.11: Numerical simulation results for the IR optical properties of a polyethylene-based ITVOF for the case of a varying fiber diameter (D_f = 1 μm, 5 μm, and 10 μm) assuming a fixed yarn diameter of D_y = 50 μm. As before, all simulations assume the fiber separation distance is D_s = 1 μm and the yarn separation distance is D_p = 5 μm. The spectrally integrated transmittance (τ_c) and reflectance (ρ_c) is shown in each plot weighted by the Planck's distribution assuming a body temperature of 33.9°C. Compared to the case where D_y = 30 μm, the overall transmittance is lower, as expected, due to the combination of a larger material volume that absorbs more incident IR radiation and a larger number of fibers available to scatter incident IR radiation thus increasing the reflectance. However, by reducing the size of the fiber to be D_f = 1 μm, which is far smaller than IR wavelengths, the total transmittance can again be significantly enhanced from 0.63 to 0.969 which is nearly equal to the case where D_y = 30 μm. Simultaneously, the reflectance of the ITVOF is reduced from 0.27 to 0.019 further improving radiative cooling. These results show that reducing the fiber size is far more important than reducing the yarn size. Therefore, this structuring methodology could potentially be applied to ITVOF that are comparable in size to conventional fabrics. The material volume per unit depth for a single yarn is 1492 μm^2 for D_f = 10 μm, 1217

μm^2 for D_f = 5 μm, and 445 μm^2 for D_f = 1 μm. The optical properties of the ITVOF are again calculated for the wavelength range from 5.5 to 24 μm, which will provide a conservative estimate of the total transmittance and the reflectance.

For a fiber diameter of D_f = 1 μm, the total hemispherical IR transmittance and reflectance was 0.969 and 0.019, respectively, which is similar to the case where D_y = 30 μm despite a material volume that is three times larger at 445 μm^2. This result shows that reducing the fiber diameter is far more crucial to improving transmittance compared to reducing the yarn diameter. Therefore, it may be suitable to create an ITVOF that is comparable in size to conventional fabrics so long as the fiber diameter is sufficiently small.

In addition, a polyethylene-based ITVOF may not exhibit sufficient fabric handedness due to the nature of the material used. To ensure the fabric is comfortable to the wearer, it may be necessary for the fabric to be composed of a mixture of different material fibers which will affect the transmittance of the fabric. To assess the potential extent in which the transmittance will be reduced, simulations were also performed for different volumetric concentrations of polyethylene and polyester (PET) again assuming D_f = 1 μm and D_y = 30 μm, as shown in Fig. 4.12a. The optical constants for PET were also taken from the literature, as shown in Fig. 4.12b.[290] For the most absorbing case of 25%PE/75%PET, the total hemispherical mid- to far-IR transmittance and reflectance was 0.728 and 0.038, respectively, which indicates that a fabric blend can still achieve a high transmittance and a low reflectance to provide sufficient cooling using thermal radiation.

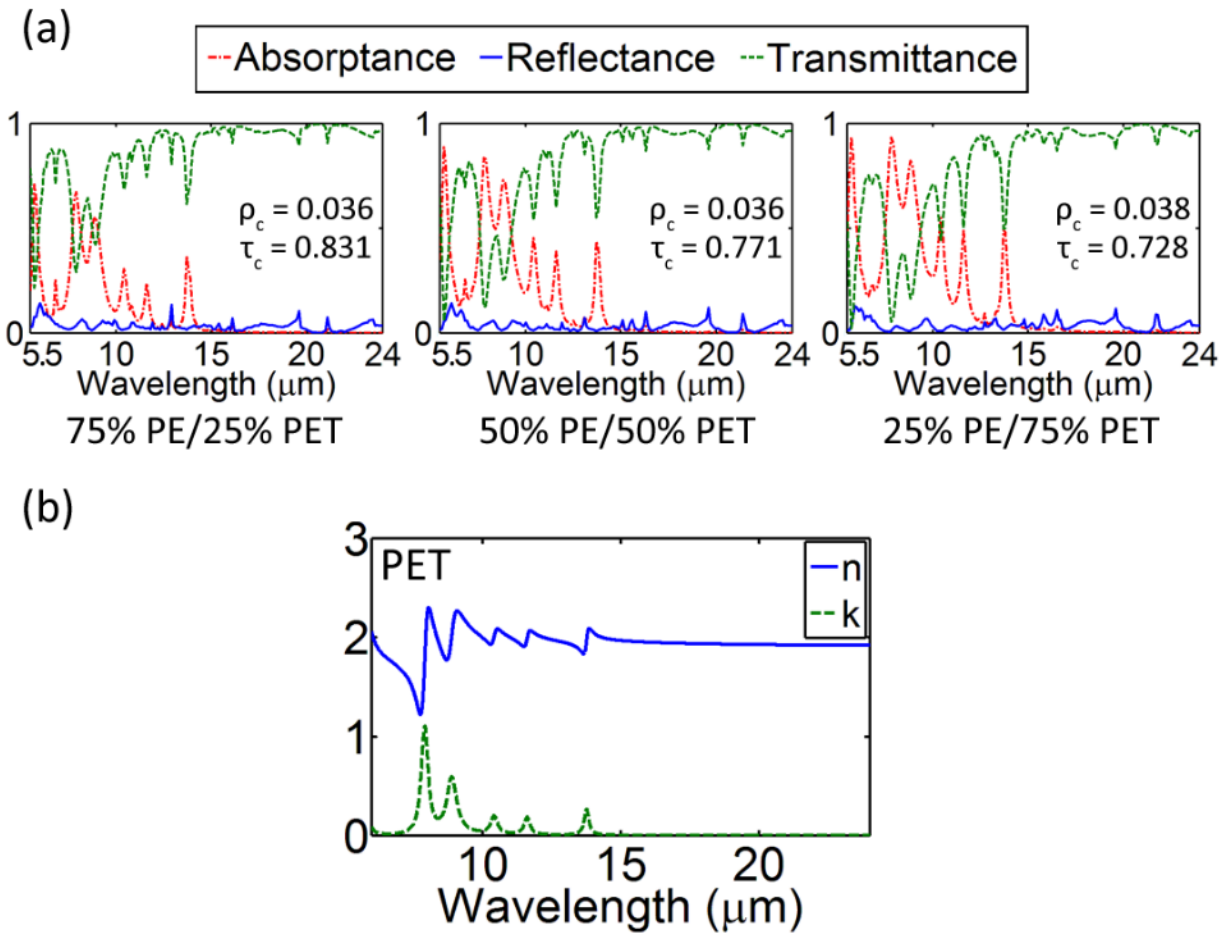

Figure 4.12: (a) Numerical simulation results for the IR optical properties of an ITVOF blend of polyethylene and polyester with varying volumetric concentrations. The PE and PET fibers were randomly distributed in the simulation. For all simulations it is assumed D_f = 1 μm, D_y = 30 μm, D_s = 1 μm, and D_p = 5 μm. Again, the spectrally integrated transmittance (τ_c) and reflectance (ρ_c) is shown in each plot weighted by the Planck's distribution assuming a body temperature of 33.9°C. As shown, a progressive increase in the volumetric concentration of PET results in an increase in the spectral absorptance thus decreasing the total transmittance. However, it can also be observed that the spectral reflectance is ~0.04 for all cases and exhibits no significant variation spectrally further reinforcing the point that so long as the fiber is sufficiently small compared to IR wavelengths, scattering will be minimal. Based on these results, even the highest volumetric concentration of PET fibers (25%PE/75% PET) can provide sufficient cooling to raise the ambient temperature to 26.1°C due to a combination of a high total transmittance of 0.728 and a low total reflectance of 0.038. The material volume per unit depth for a single yarn in all cases is equal to

135.9 μm^2. The optical properties of the ITVOF are again calculated for the wavelength range from 5.5 to 24 μm, which will provide a conservative estimate of the total transmittance and the reflectance. (b) The optical constants of polyethylene terephthalate (PET), more commonly known as polyester, taken from the literature. A Lorentzian model was used to fit experimental data from previous studies.[223]

4.9 Summary

In summary, we demonstrated a design for an infrared-transparent visible-opaque fabric (ITVOF) in order to provide personal cooling via thermal radiation from the human body to the ambient environment. We developed an ITVOF design made of polyethylene, which is an intrinsically low absorbing material, and structured the fibers to be sufficiently small in order to maximize the IR transparency and the visible opaqueness. For a 1 μm diameter fiber and a 30 μm diameter yarn, the total mid- and far-IR transmittance and reflectance are predicted to be 0.972 and 0.021, respectively, which exceed the minimum transmittance of 0.644 and maximum reflectance of 0.2 required to provide sufficient cooling at an elevated ambient temperature of 26.1ºC (79ºF). Simultaneously, the total hemispherical reflectance and transmittance in the visible wavelength range are comparable to existing textiles which indicates that the design is optically opaque to the human eye.

To practically realize an ITVOF, further studies are needed to experimentally evaluate the impact of radiative heat transfer on personal cooling. Although challenging, the fabrication of an ITVOF could be achieved using conventional manufacturing processes including drawing, extrusion, or electrospinning. Thermal and mechanical evaluation can be conducted using standardized testing methods as shown in previous studies including the use of thermal manikins, wash and dry cycling, and subject testing.[272,276,311–313] Additionally, vapor transport through the cloth, which is another key component for thermal comfort, must also be considered in future ITVOF designs. Although the porosity of the proposed ITVOF design is based on typical clothing, it would nonetheless be useful to quantitatively assess vapor transport to optimally design ITVOF-based clothing.[314] The inclusion of coloration for aesthetic quality is another important aspect that must be considered without compromising the effectiveness of radiative cooling. Alternative synthetic polymers, such as polypropylene or polymeric blends of UHMWPE and PET, should also be investigated for their suitability in an ITVOF design. Ultimately, ITVOF-based clothing

offers a simple, low-cost approach to provide cooling locally to the human body in a variety of indoor and outdoor environments without requiring additional energy consumption, compromising breathability, or requiring any lifestyle change. Therefore, ITVOF provides a simple solution to reduce the energy consumption of HVAC systems by enabling higher temperature set points during the summer.

Chapter 5

Summary & Future Outlook

5.1 Summary of Thesis

Radiative heat transfer is a ubiquitous phenomenon that is of key importance in the development of many technologies used to combat climate change, from renewable energy sources, such as photovoltaics or solar thermal receivers, to the thermal management of buildings and even individual people. A need thus exists to develop methods to engineer radiative heat transfer beyond what is currently capable. The goal of this thesis has been to explore approaches to spectrally shape, tune, and enhance radiative heat transfer from the near-field to the far-field regimes by using morphological effects to modify the photonic dispersion that governs radiative transport.

In chapter 2, thin-film morphological effects were applied to both semiconductors and plasmonic materials in the near-field regime. For semiconductors, it was theoretically shown that as the dimensionality of the film is reduced, thermal emission and absorption will become more spectrally selective due to trapped waveguide modes supported in these films. This effect was then applied to a theoretical TPV system using a realistic electrical model where it was shown that at relatively low emitter temperatures of 1000 K, it is theoretically possible to achieve energy conversion efficiencies as high as 46% in the near-field regime. For plasmonic materials, a thin-film morphology yields the opposite behavior where near-field radiative transfer is spectrally broadened due to the hybridization of surface polariton modes supported on both sides of the film. It was shown that when this effect is applied to AZO, the SPP resonance is broadened to such an extent that the total radiative heat flux in the near-filed regime can even exceed SiC at low temperatures.

In chapter 3, a measurement technique was developed to expand the capabilities of current methods used to empirically study near-field radiative heat transfer by enabling quantitative and gap-dependent spectral measurements of near-field thermal emission. The approach consisted of using a high index prism in an inverse Otto configuration. This prism acted as a bridge between the near- and far-field regimes by allowing evanescent modes to couple to the high momentum

states within the prism, which could then propagate from the prism to free-space. A conceptual demonstration of this method was shown using a custom-made experimental platform, which included a heated spherically convex N-BK7 lens as the thermal emitter, a ZnSe lens as the prism, and a FTIR spectrometer for spectral characterization. Following extensive analysis for various non-idealities in the experiment, preliminary results were presented that indicate quantitative, gap-dependent near-field enhancement spectra was observed.

In chapter 4, the focus shifted to the far-field regime where morphology effects were applied in the form of small cylindrical fibers. These fibers were designed to exploit different light scattering regimes in order to create an infrared transparent, visibly opaque fabric (ITVOF), which can enable passive cooling to the human body via direct radiative heat transfer from the human body to the surrounding environment. A theoretical design for an ITVOF was developed using polyethylene fibers, which is an intrinsically low absorbing material in the IR. Upon optimizing the fiber size, it was shown weak Rayleigh scattering can be used to maximize the transmittance of the fabric in the IR with a theoretical prediction of 0.972. For the same fiber size, it was also shown strong Mie scattering can occur in the visible wavelength range, resulting in a hemispherical reflectance and transmittance comparable to existing textiles, which indicates that the design is optically opaque to the human eye.

5.2 Future Outlook

The methodology of engineering radiative heat transfer using morphologically induced changes to the photonic dispersion is an area that is just beginning to be explored. As demonstrated in chapter 2, even a simple thin-film morphology can yield significant changes to the spectral radiative heat flux in the near-field regime. There are a variety of other morphologies that have yet to be investigated, which may result in even more profound effects. In particular, spherical particles that are comparable in size to the wavelength of light support whispering gallery mode (WGM) resonances, which are known to exhibit very high quality factor resonances despite the small form factor of the resonator.[97,98,224,315] Similarly, small sub-wavelength particles made of materials supporting surface polariton modes are well-known to exhibit large absorption cross sections due to the localization of the surface polariton mode.[223] Although the formalism to describe near-field radiative heat transfer from spherical particles has been known for several years, theoretical studies have primarily focused on large particles to compliment experimental studies where these effects

are suppressed. This presents an immediate opportunity to investigate the impact of WGM resonances and localized surface polariton resonances on near-field radiative heat transfer. Future studies may also consider core-shell geometries as well as ensembles of particles, which may provide additional degrees of freedom to spectrally shape and tune near-field thermal radiation.

To complement these theoretical studies, further advances must also be made to the empirical methods used to study near-field radiative heat transfer. Although experimental measurements in this field have primarily focused on measuring the total radiative heat flux in the near-field regime, extracting the spectral properties can provide a new level of insight to better understand the nature of near-field radiative heat transfer. As shown in chapter 3, one possible method was developed to quantitatively measure gap-dependent near-field enhancement spectra by using a high index prism to extract near-field thermal radiation to the far-field regime. If the improvements discussed at the end of chapter 3 are implemented, it may be possible to use this approach to investigate near-field radiative heat transfer for a variety of different geometrical configurations. However, one limitation with this prism-coupling approach is that near-field coupling will always be fundamentally limited by the refractive index of the prism. Further development is thus needed to create a measurement method capable of spectrally characterizing all of the high momentum near-field modes supported near a thermal emitter.

While further studies to elucidate the fundamental nature of radiative transfer are important, it is also crucial to apply this knowledge in the development of new technologies. Of particular importance is the ability to fabricate optical structures at low cost. To this end, the morphological tailoring of optical properties in the far-field regime is one area of study that exhibits a low barrier to transition from fundamental science to practical application. As shown in chapter 4, when a simple fiber morphology is applied to polyethylene, a fabric can be created that significantly improves cooling locally to the human body. This particular invention can be manufactured at an inherently low cost due to the material and morphology used. The same, however, cannot be said with near-field radiative heat transfer. While there are applications that are tailor-made to utilize near-field thermal radiation, such as heat-assisted magnetic recording, the primary barrier that has limited the application of near-field radiative heat transfer is developing a method to reliably align two macroscopic objects with a sub-micron gap separation. If a low cost method can be developed, this would pave the way for a new generation of technologies that can utilize radiative heat transport to an extent never before seen.

Bibliography

1. Cook, J. *et al.* Consensus on consensus: a synthesis of consensus estimates on human-caused global warming. *Environ. Res. Lett.* **11,** 048002 (2016).
2. Cohn, A. S., VanWey, L. K., Spera, S. A. & Mustard, J. F. Cropping frequency and area response to climate variability can exceed yield response. *Nat. Clim. Chang.* (2016).
3. Hansen, J. *et al.* Ice melt, sea level rise and superstorms: evidence from paleoclimate data, climate modeling, and modern observations that 2C global warming could be dangerous. *Atmos. Chem. Phys.* **16,** 3761–3812 (2016).
4. Ring, E. F. The historical development of thermometry and thermal imaging in medicine. *J. Med. Eng. Technol.* **30,** 192–198 (2006).
5. Putley, E. H. in *Recent Advances in Medical Thermology* (eds. Ring, E. F. J. & Phillips, B.) 151–166 (Springer New York, 1984).
6. Stewart, B. An account of some experiments on radiant heat. *Trans. R. Soc. Edinburgh* **22,** 1–20 (1858).
7. Kirchoff, G. R. Über die Fraunhofer'schen Linien. *Monatsberichte der Königlich Preuss. Akad. der Wissenschaften zu Berlin* 662–665 (1859).
8. Kirchoff, G. R. Über den Zusammenhang zwischen Emission und Absorption von Licht und Wärme. *Monatsberichte der Königlich Preuss. Akad. der Wissenschaften zu Berlin* 783–787 (1859).
9. Wien, W. Über die Energievertheilung im Emissionsspectrum eines schwarzen Körpers. *Ann. der Phys. und Chemie* **294,** 662–669 (1896).
10. Rayleigh, L. LIII. Remarks upon the law of complete radiation. *Philos. Mag.* **49,** 539 (1900).
11. Planck, M. Über eine Verbesserung der Wien'schen Spectralgleichung. *Verhandlungen der Dtsch. Phys. Gesellschaft* **2,** 202–204 (1900).
12. Planck, M. Zur Theorie des Gesetzes der Energieverteilung im Normalspectrum. *Verhandlungen der Dtsch. Phys. Gesellschaft* **2,** 237–245 (1900).
13. Planck, M. Entropie und Temperatur strahlender Wärme. *Ann. Phys.* **306,** 719–737 (1900).
14. Planck, M. Über irreversible Strahlungsvorgänge. *Ann. Phys.* **306,** 69–122 (1900).
15. Einstein, A. Über einen die Erzeugung und Verwandlung des Lichtes betreffenden heuristischen Gesichtspunkt. *Ann. Phys.* **17,** 132–148 (1905).
16. Viskanta, R. in *Advances in Heat Transfer, Volume 46* 49–80 (Academic Press, 2014).
17. Chen, G. *Nanoscale Energy Transport and Conversion: A Parallel Treatment of Electrons, Molecules, Phonons, and Photons*. (Oxford University Press, 2005).
18. Rupper, G., Kwong, N. H. & Binder, R. in *Optical Refrigeration: Science and Applications of Laser Cooling of Solids* 139–167 (WILEY-VCH Verlag GmbH & Co. KGaA, 2009).
19. Pendry, J. B. Radiative exchange of heat between nanostructures. *J. Phys. Condens. Matter* **11,** 6621–6633 (1999).
20. Boriskina, S. V., Ghasemi, H. & Chen, G. Plasmonic materials for energy: From physics to applications. *Mater. Today* **16,** 375–386 (2013).
21. Maier, S. A. *Plasmonics: Fundamentals and Applications*. (Springer-Verlag, 2007).

22. Song, B., Fiorino, A., Meyhofer, E. & Reddy, P. Near-field radiative thermal transport: From theory to experiment. *AIP Adv.* **5,** 053503 (2015).
23. Mulet, J.-P., Joulain, K., Carminati, R. & Greffet, J.-J. Enhanced Radiative Heat Transfer At Nanometric Distances. *Microscale Thermophys. Eng.* **6,** 209–222 (2002).
24. Rytov, S. M. *Theory of Electric Fluctuations and Thermal Radiation*. (Air Force Cambridge Research Center, 1959).
25. Cravalho, E. G., Domoto, G. A. & Tien, C. L. Measurements of Thermal Radiation of Solids at Liquid-Helium Temperatures. in *AIAA 3rd Thermophysics Conference* **No. 68-774,** (1968).
26. Domoto, G. A., Boehm, R. F. & Tien, C. L. Experimental Investigation of Radiative Transfer Between Metallic Surfaces at Cryogenic Temperatures. *J. Heat Transfer* **92,** 412–416 (1970).
27. Hargreaves, C. M. Anomalous Radiative Transfer between Closely-Spaced Bodies. *Phys. Lett.* **30A,** 491–492 (1969).
28. Polder, D. & Van Hove, M. Theory of Radiative Heat Transfer between Closely Spaced Bodies. *Phys. Rev. B* **4,** 3303 (1971).
29. Volokitin, A. I. & Persson, B. N. J. Radiative heat transfer between nanostructures. *Phys. Rev. B* **63,** 205404 (2001).
30. Mulet, J.-P., Joulain, K., Carminati, R. & Greffet, J.-J. Nanoscale radiative heat transfer between a small particle and a plane surface. *Appl. Phys. Lett.* **78,** 2931 (2001).
31. Narayanaswamy, A. 1D Metallo-Dielectric Photonic Crystals as Selective Emitters for Thermophotovoltaic Applications. in *AIP Conference Proceedings* **738,** 215–220 (AIP, 2004).
32. Chapuis, P.-O., Greffet, J.-J., Joulain, K. & Volz, S. Heat transfer between a nano-tip and a surface. *Nanotechnology* **17,** 2978–2981 (2006).
33. Lee, B. J., Park, K. & Zhang, Z. M. Energy pathways in nanoscale thermal radiation. *Appl. Phys. Lett.* **91,** 153101 (2007).
34. Francoeur, M. & Meguc, M. P. Role of fluctuational electrodynamics in near-field radiative heat transfer. *J. Quant. Spectrosc. Radiat. Transf.* **109,** 280–293 (2008).
35. Narayanaswamy, A. & Chen, G. Thermal near-field radiative transfer between two spheres. *Phys. Rev. B* **77,** 075125 (2008).
36. Ben-Abdallah, P., Joulain, K., Drevillon, J. & Domingues, G. Near-field heat transfer mediated by surface wave hybridization between two films. *J. Appl. Phys.* **106,** 044306 (2009).
37. Francoeur, M., Pinar Mengüç, M. & Vaillon, R. Solution of near-field thermal radiation in one-dimensional layered media using dyadic Green's functions and the scattering matrix method. *J. Quant. Spectrosc. Radiat. Transf.* **110,** 2002–2018 (2009).
38. Francoeur, M., Mengüç, M. P. & Vaillon, R. Spectral tuning of near-field radiative heat flux between two thin silicon carbide films. *J. Phys. D. Appl. Phys.* **43,** 075501 (2010).
39. Narayanaswamy, A. & Chen, G. Dyadic Green's functions and electromagnetic local density of states. *J. Quant. Spectrosc. Radiat. Transf.* **111,** 1877–1884 (2010).
40. Carrillo, L. Y. & Bayazitoglu, Y. Nanosphere Near-Field Radiative Heat-Exchange Analysis. *J. Thermophys. Heat Transf.* **24,** 309–315 (2010).
41. Carrillo, L. Y. & Bayazitoglu, Y. Nanorod near-field radiative heat exchange analysis. *J. Quant. Spectrosc. Radiat. Transf.* **112,** 412–419 (2011).
42. Kruger, M., Golyk, V. A., Bimonte, G. & Kardar, M. Interplay of roughness/modulation and curvature for surface interactions at proximity. *Europhys. Lett.* **104,** 41001 (2013).
43. Guo, Y., Molesky, S., Hu, H., Cortes, C. L. & Jacob, Z. Thermal excitation of plasmons for near-field thermophotovoltaics. *Appl. Phys. Lett.* **105,** 073903 (2014).
44. Datas, A., Hirashima, D. & Hanamura, K. FDTD Simulation of Near-Field Radiative Heat

Transfer between Thin Films Supporting Surface Phonon Polaritons: Lessons Learned. *J. Therm. Sci. Technol.* **8,** 91–105 (2013).
45. Didari, A. & Pinar Menguc, M. Analysis of near-field radiation transfer within nano-gaps using FDTD method. *J. Quant. Spectrosc. Radiat. Transf.* **146,** 214–226 (2014).
46. Luo, C., Narayanaswamy, A., Chen, G. & Joannopoulous, J. D. Thermal Radiation from Photonic Crystals: A Direct Calculation. *Phys. Rev. Lett.* **93,** 213905 (2004).
47. Rodriguez, A. W. *et al.* Frequency-Selective Near-Field Radiative Heat Transfer between Photonic Crystal Slabs: A Computational Approach for Arbitrary Geometries and Materials. *Phys. Rev. Lett.* **107,** 114302 (2011).
48. Kruger, M., Emig, T. & Kardar, M. Nonequilibrium Electromagnetic Fluctuations: Heat Transfer and Interactions. *Phys. Rev. Lett.* **106,** 210404 (2011).
49. Liu, X. & Zhang, Z. Near-Field Thermal Radiation between Metasurfaces. *ACS Photonics* **2,** 1320–1326 (2015).
50. Otey, C. & Fan, S. Numerically exact calculation of electromagnetic heat transfer between a dielectric sphere and plate. *Phys. Rev. B* **84,** 245431 (2011).
51. Rodriguez, A. W., Homer Reid, M. T. & Johnson, S. G. Fluctuating-surface-current formulation of radiative heat transfer for arbitrary geometries. *Phys. Rev. B* **86,** 220302(R) (2012).
52. Messina, R. & Anteza, M. Scattering-matrix approach to Casimir-Lifshitz force and heat transfer out of thermal equilibrium between arbitrary bodies. *Phys. Rev. A* **84,** 042102 (2011).
53. Kruger, M., Bimonte, G., Emig, T. & Kardar, M. Trace formulas for nonequilibrium Casimir interactions, heat radiation, and heat transfer for arbitrary objects. *Phys. Rev. B* **86,** 115423 (2012).
54. Lussange, J. *et al.* Radiative heat transfer between two dielectric nanogratings in the scattering approach. *Phys. Rev. B* **86,** 085432 (2012).
55. McCauley, A. P., Homer Reid, M. T., Kruger, M. & Johnson, S. G. odeling near-field radiative heat transfer from sharp objects using a general three-dimensional numerical scattering technique. *Phys. Rev. B* **85,** 165104 (2012).
56. Rodriguez, A. W. *et al.* Anomalous Near-Field Heat Transfer between a Cylinder and a Perforated Surface. *Phys. Rev. Lett.* **110,** 014301 (2013).
57. Rodriguez, A. W., Reid, M. T. H. & Johnson, S. G. Fluctuating-surface-current formulation of radiative heat transfer: Theory and applications. *Phys. Rev. B* **88,** 054305 (2013).
58. Edalatpour, S., Cuma, M., Trueax, T., Backman, R. & Francoeur, M. Convergence analysis of the thermal discrete dipole approximation. *Phys. Rev. E* **91,** 063307 (2015).
59. Edalatpour, S. & Francoeur, M. The Thermal Discrete Dipole Approximation(T-DDA) for near-field radiative heat transfer simulations in three-dimensional arbitrary geometries. *J. Quant. Spectrosc. Radiat. Transf.* **133,** 364–373 (2014).
60. Shen, S., Narayanaswamy, A. & Chen, G. Surface Phonon Polaritons Mediated Energy Transfer between Nanoscale Gaps. *Nano Lett.* **9,** 2909–2913 (2009).
61. Chiloyan, V., Garg, J., Esfarjani, K. & Chen, G. Transition from near-field thermal radiation to phonon heat conduction at sub-nanometre gaps. *Nat. Commun.* **6,** 6755 (2015).
62. Luo, Y., Fernandez-Dominguez, A. I., Wiener, A., Maier, S. A. & Pendry, J. B. Surface Plasmons and Nonlocality: A Simple Model. *Phys. Rev. Lett.* **111,** 093901 (2013).
63. Luo, Y., Zhao, R. & Pendry, J. B. van der Waals interactions at the nanoscale: The effects of nonlocality. *Proc. Natl. Acad. Sci.* **111,** 18422–18427 (2014).
64. Teperik, T. V., Nordlander, P., Aizpurua, J. & Borisov, A. G. Robust Subnanometric Plasmon

Ruler by Rescaling of the Nonlocal Optical Response. *Phys. Rev. Lett.* **110,** 263901 (2013).
65. Teperik, T. V., Nordlander, P., Aizpurua, J. & Borisov, A. G. Quantum effects and nonlocality in strongly coupled plasmonic nanowire dimers. *Opt. Express* **21,** 27306–27325 (2013).
66. Chapuis, P.-O., Volz, S., Henkel, C., Joulain, K. & Greffet, J.-J. Effects of spatial dispersion in near-field radiative heat transfer between two parallel metallic surfaces. *Phys. Rev. B* **77,** 035431 (2008).
67. Pan, J. L. Radiative transfer over small distances from a heated metal. *Opt. Lett.* **25,** 369 (2000).
68. Shen, S., Mavrokefalos, A., Sambegoro, P. & Chen, G. Nanoscale thermal radiation between two gold surfaces. *Appl. Phys. Lett.* **100,** 233114 (2012).
69. Bermel, P., Boriskina, S. V., Yu, Z. & Joulain, K. Control of radiative processes for energy conversion and harvesting. *Opt. Express* **23,** 1533–1540 (2015).
70. Bernardi, M. P. *et al.* Impacts of propagating, frustrated and surface modes on radiative, electrical and thermal losses in nanoscale-gap thermophotovoltaic power generators. *Sci. Rep.* **5,** 11626 (2015).
71. Lee, J.-H., Bargatin, I., Melosh, N. A. & Howe, R. T. Optimal emitter-collector gap for thermionic energy converters. *Appl. Phys. Lett.* **100,** 173904 (2012).
72. Messina, R. & Ben-Abdallah, P. Graphene-based photovoltaic cells for near-field thermal energy conversion. *Sci. Rep.* **3,** 1383 (2013).
73. Yang, R., Narayanaswamy, A. & Chen, G. Surface-Plasmon Coupled Nonequilibrium Thermoelectric Refrigerators and Power Generators. *J. Comput. Theor. Nanosci.* **2,** 75–87(13) (2005).
74. Laroche, M., Carminati, R. & Greffet, J.-J. Near-field thermophotovoltaic energy conversion. *J. Appl. Phys.* **100,** 063704 (2006).
75. Bermel, P., Luo, C., Zeng, L., Kimerling, L. C. & Joannopoulos, J. D. Improving thin-film crystalline silicon solar cell efficiencies with photonic crystals. *Opt. Express* **15,** 16986 (2007).
76. Bright, T. J., Wang, L. P. & Zhang, Z. M. Performance of Near-Field Thermophotovoltaic Cells Enhanced with a Backside Reflector. *J. Heat Transfer* **136,** 062701 (2014).
77. Francoeur, M., Vaillon, R. & Mengüç, M. P. Thermal Impacts on the Performance of Nanoscale-Gap Thermophotovoltaic Power Generators. *IEEE Trans. Energy Convers.* **26,** 686–698 (2011).
78. Zhou, N. *et al.* Plasmonic near-field transducer for heat-assisted magnetic recording. *Nanophotonics* **3,** 141–155 (2014).
79. Kryder, M. H. *et al.* Heat Assisted Magnetic Recording. *Proc. IEEE* **96,** 1810–1835 (2008).
80. Challener, W. A. *et al.* Heat-assisted magnetic recording by a near-field transducer with efficient optical energy transfer. *Nat. Photonics* **2,** 220–224 (2009).
81. Ilic, O., Jablan, M., Joannopoulos, J. D., Celanovic, I. & Soljačić, M. Overcoming the black body limit in plasmonic and graphene near-field thermophotovoltaic systems. *Opt. Express* **20,** A366 (2012).
82. Rousseau, E., Laroche, M. & Greffet, J.-J. Radiative heat transfer at nanoscale mediated by surface plasmons for highly doped silicon. *Appl. Phys. Lett.* **95,** 231913 (2009).
83. Shi, J., Li, P., Liu, B. & Shen, S. Tuning near field radiation by doped silicon. *Appl. Phys. Lett.* **102,** 183114 (2013).
84. Ding, D., Kim, T. & Minnich, A. J. Active thermal extraction of near-field thermal radiation. *Phys. Rev. B* **93,** 081402(R) (2016).
85. van Zwol, P. J., Joulain, K., Ben Abdallah, P., Greffet, J.-J. & Chevrier, J. Fast nanoscale

heat-flux modulation with phase-change materials. *Phys. Rev. B* **83,** 201404(R) (2011).
86. van Zwol, P. J., Joulain, K., Ben-Abdallah, P. & Chevrier, J. Phonon polaritons enhance near-field thermal transfer across the phase transition of VO2. *Phys. Rev. B* **84,** 161413(R) (2011).
87. Yang, Y., Basu, S. & Wang, L. Radiation-based near-field thermal rectification with phase transition materials. *Appl. Phys. Lett.* **103,** 163101 (2013).
88. Wang, L. P. & Zhang, Z. M. Phonon-mediated magnetic polaritons in the infrared region. *Opt. Express* **19,** A126–A135 (2011).
89. Bai, Y., Jiang, Y. & Liu, L. Enhanced near-field radiative heat transfer between a nanosphere and a hyperbolic metamaterial mediated by coupled surface phonon polaritons. *J. Quant. Spectrosc. Radiat. Transf.* **158,** 61–68 (2015).
90. Biehs, S.-A., Rosa, F. S. S. & Ben-Abdallah, P. Modulation of near-field heat transfer between two gratings. *Appl. Phys. Lett.* **98,** 243102 (2011).
91. Biehs, S.-A., Tschikin, M. & Ben-Abdallah, P. Hyperbolic Metamaterials as an Analog of a Blackbody in the Near Field. *Phys. Rev. Lett.* **109,** 104301 (2012).
92. Greffet, J.-J. *et al.* Coherent emission of light by thermal sources. *Nature* **416,** 61–64 (2002).
93. Guo, Y., Cortes, C. L., Molesky, S. & Jacob, Z. Broadband super-Planckian thermal emission from hyperbolic metamaterials. *Appl. Phys. Lett.* **101,** 131106 (2012).
94. Liu, B. & Shen, S. Broadband near-field radiative thermal emitter/absorber based on hyperbolic metamaterials: Direct numerical simulation by the Wiener chaos expansion method. *Phys. Rev. B* **87,** 115403 (2013).
95. Svetovoy, V. B., van Zwol, P. J. & Chevrier, J. Plasmon enhanced near-field radiative heat transfer for graphene covered dielectrics. *Phys. Rev. B* **85,** 155418 (2012).
96. Miller, O. D., Johnson, S. G. & Rodriguez, A. W. Effectiveness of thin films in lieu of hyperbolic metamaterials in the near field. *Phys. Rev. Lett.* **112,** 157402 (2014).
97. Ferrari, M. *et al.* Whispering gallery mode microresonators: Fundamentals and applications. *Riv. del Nuovo Cim.* **34,** 435–488 (2011).
98. Vahala, K. J. Optical Microcavities. *Nature* **424,** 839–846 (2003).
99. Ida, N. *Engineering Electromagnetics*. (Springer, 2015).
100. Rytov, S. M., Kravtsov, Y. A. & Tatarskii, V. I. *Principles of Statistical Radiophysics 3: Elements of Random Fields*. (Springer-Verlag Berlin Heidelberg, 1989).
101. Shen, S., Narayanaswamy, A. & Chen, G. Surface phonon polaritons mediated energy transfer between nanoscale gaps. *Nano Lett.* **9,** 2909–2913 (2009).
102. Dingle, R., Wiegmann, W. & Henry, C. Quantum States of Confined Carriers in Very Thin Al_{x}Ga_{1-x}As-GaAs-Al_{x}Ga_{1-x}As Heterostructures. *Phys. Rev. Lett.* **33,** 827–830 (1974).
103. Dupuis, R. D., Dapkus, P. D., Chin, R., Holonyak, N. & Kirchoefer, S. W. Continuous 300 °K laser operation of single-quantum-well AlxGa1−xAs-GaAs heterostructure diodes grown by metalorganic chemical vapor deposition. *Appl. Phys. Lett.* **34,** 265 (1979).
104. Kolm, H. H. Solar-battery power source. *Q. Prog. Rep. Solid State Res.* 13 (1956).
105. Aigrain, P. Thermophotovoltaic conversion of radiant energy; unpublished lecture series at MIT. (1956).
106. Swanson, R. M. Recent developments in Thermophotovoltaic Conversion. *Proc. Int. Electron. Devices Meet.* 186–189 (1980).
107. Wedlock, B. D. Thermo-photo-voltaic energy conversion. *Proceedings of the IEEE* **51,** 694–698 (1963).
108. Harder, N.-P. & W rfel, P. Theoretical limits of thermophotovoltaic solar energy conversion.

Semiconductor Science and Technology **18,** S151–S157 (2003).
109. Rephaeli, E. & Fan, S. Absorber and emitter for solar thermo-photovoltaic systems to achieve efficiency exceeding the Shockley-Queisser limit. *Opt. Express* **17,** 15145–59 (2009).
110. Datas, A. & Algora, C. Global optimization of solar thermophotovoltaic systems. *Prog. Photovolt Res. Appl.* 1040–1055 (2013). doi:10.1002/pip
111. Zenker, M., Heinzel, A., Stollwerck, G., Ferber, J. & Luther, J. Efficiency and power density potential of combustion-driven thermophotovoltaic systems using GaSb photovoltaic cells. *IEEE Trans. Electron Devices* **48,** 367–376 (2001).
112. Fraas, L. M., Avery, J. E., Huang, H. X. & Martinelli, R. U. Thermophotovoltaic system configurations and spectral control. *Semicond. Sci. Technol.* **18,** S165–S173 (2003).
113. Catalano, A. Thermophotovoltaics: A new paradigm for power generation? *Renew. Energy* **8,** 495–499 (1996).
114. Wurfel, P. & Ruppel, W. Upper limit of thermophotovoltaic solar-energy conversion. *IEEE Transactions on Electron Devices* **27,** 745–750 (1980).
115. Demichelis, F. & Minetti-Mezzetti, E. A solar thermophotovoltaic converter. *Solar Cells* **1,** 395–403 (1980).
116. Coutts, T. J. Thermophotovoltaic principles, potential, and problems. in *AIP Conference Proceedings* **404,** 217–234 (AIP, 1997).
117. Basu, S., Chen, Y.-B. & Zhang, Z. M. Microscale radiation in thermophotovoltaic devices—A review. *Int. J. Energy Res.* **31,** 689–716 (2007).
118. Celanovic, I., O'Sullivan, F., Jovanovic, N., Qi, M. & Kassakian, J. G. 1D and 2D Photonic Crystals for Thermophotovoltaic Applications. in *Photonics Europe* (eds. De La Rue, R. M., Viktorovitch, P., Sotomayor Torres, C. M. & Midrio, M.) 416–422 (International Society for Optics and Photonics, 2004). doi:10.1117/12.545539
119. Coutts, T. J. A review of progress in thermophotovoltaic generation of electricity. *Renew. Sustain. Energy Rev.* **3,** 77–184 (1999).
120. Coutts, T. J. & Ward, J. S. Thermophotovoltaic and photovoltaic conversion at high-flux densities. *IEEE Trans. Electron Devices* **46,** 2145–2153 (1999).
121. Durisch, W. & Bitnar, B. Novel thin film thermophotovoltaic system. *Sol. Energy Mater. Sol. Cells* **94,** 960–965 (2010).
122. Fraas, L. M. *et al.* Over 35-percent efficient GaAs/GaSb tandem solar cells. *IEEE Trans. Electron Devices* **37,** 443–449 (1990).
123. Nam, Y. *et al.* Solar thermophotovoltaic energy conversion systems with two-dimensional tantalum photonic crystal absorbers and emitters. *Sol. Energy Mater. Sol. Cells* **122,** 287–296 (2014).
124. Yeng, Y. X. *et al.* Performance analysis of experimentally viable photonic crystal enhanced thermophotovoltaic systems. *Opt. Express* **21 Suppl 6,** A1035–51 (2013).
125. Zhao, B., Wang, L., Shuai, Y. & Zhang, Z. M. Thermophotovoltaic emitters based on a two-dimensional grating/thin-film nanostructure. *Int. J. Heat Mass Transf.* **67,** 637–645 (2013).
126. Shen, Y. *et al.* Optical Broadband Angular Selectivity. *Sci.* **343 ,** 1499–1501 (2014).
127. Bermel, P. *et al.* Design and global optimization of high-efficiency thermophotovoltaic systems. *Opt. Express* **18 Suppl 3,** A314–34 (2010).
128. Chan, W. R. *et al.* Toward high-energy-density, high-efficiency, and moderate-temperature chip-scale thermophotovoltaics. *Proc. Natl. Acad. Sci. U. S. A.* **110,** 5309–14 (2013).
129. Datas, A. & Algora, C. Development and experimental evaluation of a complete solar thermophotovoltaic system. *Prog. Photovolt Res. Appl.* 1025–1039 (2013). doi:10.1002/pip

130. Lenert, A. *et al.* A nanophotonic solar thermophotovoltaic device. *Nat. Nanotechnol.* **9,** 126–30 (2014).
131. Wernsman, B. *et al.* Greater than 20% radiant heat conversion efficiency of a thermophotovoltaic radiator/module system using reflective spectral control. *IEEE Trans. Electron Devices* **51,** 512–515 (2004).
132. Colangelo, G., de Risi, A. & Laforgia, D. Experimental study of a burner with high temperature heat recovery system for TPV applications. *Energy Convers. Manag.* **47,** 1192–1206 (2006).
133. Crowley, C. J. Thermophotovoltaic Converter Performance for Radioisotope Power Systems. in *AIP Conference Proceedings* **746,** 601–614 (AIP, 2005).
134. Ferrari, C., Melino, F., Pinelli, M. & Spina, P. R. Thermophotovoltaic energy conversion: Analytical aspects, prototypes and experiences. *Appl. Energy* **113,** 1717–1730 (2014).
135. DiMatteo, R. S. Micron-gap ThermoPhotoVoltaics (MTPV). in *AIP Conference Proceedings* **653,** 232–240 (AIP, 2003).
136. DiMatteo, R. S. *et al.* Enhanced photogeneration of carriers in a semiconductor via coupling across a nonisothermal nanoscale vacuum gap. *Appl. Phys. Lett.* **79,** 1894 (2001).
137. Narayanaswamy, A. & Chen, G. Surface modes for near field thermophotovoltaics. *Appl. Phys. Lett.* **82,** 3544 (2003).
138. Niv, A., Gharghi, M., Gladden, C., Miller, O. D. & Zhang, X. Near-Field Electromagnetic Theory for Thin Solar Cells. *Phys. Rev. Lett.* **109,** 138701 (2012).
139. Pan, J. L., Choy, H. K. H. & Fonstad, C. G. Very large radiative transfer over small distances from a black body for thermophotovoltaic applications. *IEEE Trans. Electron Devices* **47,** 241–249 (2000).
140. Whale, M. D. & Cravalho, E. G. Modeling and performance of microscale thermophotovoltaic energy conversion devices. *IEEE Trans. Energy Convers.* **17,** 130–142 (2002).
141. Bett, A. W. & Sulima, O. V. GaSb photovoltaic cells for applications in TPV generators. *Semiconductor Science and Technology* **18,** S184–S190 (2003).
142. Sulima, O. . & Bett, a. . Fabrication and simulation of GaSb thermophotovoltaic cells. *Sol. Energy Mater. Sol. Cells* **66,** 533–540 (2001).
143. Algora, C. Modelling And Manufacturing GaSb TPV Converters. *AIP Conf. Proc.* **653,** 452–461 (2003).
144. Fraas, L. M. *et al.* Fundamental characterization studies of GaSb solar cells. *Conf. Rec. Twenty-Second IEEE Photovolt. Spec. Conf. - 1991* **1,** 80–84 (1991).
145. Stelmakh, V. *et al.* Evolution of sputtered tungsten coatings at high temperature. *J. Vac. Sci. Technol. A Vacuum, Surfaces, Film.* **31,** 061505 (2013).
146. Palik, E. D. *Handbook of optical constants of solids*. (Academic Press, 1997).
147. Popovic, Z. & Popovic, B. D. *Introductory Electromagnetics*. (Prentice Hall, 1999).
148. Boriskina, S. V., Benson, T. M., Sewell, P. & Nosich, A. I. Highly efficient full-vectorial integral equation solution for the bound, leaky, and complex modes of dielectric waveguides. *IEEE J. Sel. Top. Quantum Electron.* **8,** 1225–1232 (2002).
149. Boriskina, S. V. & Nosich, A. I. Radiation and absorption losses of the whispering-gallery-mode dielectric resonators excited by a dielectric waveguide. *IEEE Trans. Microw. Theory Tech.* **47,** 224–231 (1999).
150. Shockley, W. & Queisser, H. J. Detailed Balance Limit of Efficiency of p-n Junction Solar Cells. *J. Appl. Phys.* **32,** 510 (1961).

151. McKelvey, J. P. *Solid state and semiconductor physics*. (Harper & Row, 1966).
152. Park, K., Basu, S., King, W. P. & Zhang, Z. M. Performance analysis of near-field thermophotovoltaic devices considering absorption distribution. *J. Quant. Spectrosc. Radiat. Transf.* **109,** 305–316 (2008).
153. Williams, B. W. *Power Electronics: Devices, Drivers, Applications and Passive Components*. (McGraw-Hill, 1992).
154. Rosencher, E., Vinter, B. & Piva, P. G. *Optoelectronics*. (Cambridge University Press, 2002).
155. Fraas, L. M., Avery, J. E. & Huang, H. X. Thermophotovoltaic furnace–generator for the home using low bandgap GaSb cells. *Semicond. Sci. Technol.* **18,** S247–S253 (2003).
156. Brudieu, B. *et al.* Sol-Gel Route Toward Efficient and Robust Distributed Bragg Reflectors for Light Management Applications. *Adv. Opt. Mater.* n/a–n/a (2014). doi:10.1002/adom.201400292
157. Lin, A., Zhong, Y.-K., Fu, S.-M., Tseng, C. W. & Yan, S. L. Aperiodic and randomized dielectric mirrors: alternatives to metallic back reflectors for solar cells. *Opt. Express* **22 Suppl 3,** A880–94 (2014).
158. Sheng, X. *et al.* Integration of Self-Assembled Porous Alumina and Distributed Bragg Reflector for Light Trapping in Si Photovoltaic Devices. *IEEE Photonics Technol. Lett.* **22,** 1394–1396 (2010).
159. Isabella, O., Dobrovolskiy, S., Kroon, G. & Zeman, M. Design and application of dielectric distributed Bragg back reflector in thin-film silicon solar cells. *J. Non. Cryst. Solids* **358,** 2295–2298 (2012).
160. Chang, Y.-A. *et al.* Fabrication and characterization of back-side illuminated InGaN/GaN solar cells with periodic via-holes etching and Bragg mirror processes. *Opt. Express* **22,** (2014).
161. Mutitu, J. G., Shi, S., Barnett, A. & Prather, D. W. Hybrid Dielectric-Metallic Back Reflector for Amorphous Silicon Solar Cells. *Energies* **3,** 1914–1933 (2010).
162. Ivanov, I. I., Nychyporuk, T. V., Skryshevsky, V. A. & Lemiti, M. Thin silicon solar cells with SiOx/SiNx Bragg mirror rear surface reflector. *Semicond. Physics, Quantum Electron. Optoelectron.* **12,** 406–411 (2009).
163. Jeong, S., McGehee, M. D. & Cui, Y. All-back-contact ultra-thin silicon nanocone solar cells with 13.7% power conversion efficiency. *Nat. Commun.* **4,** (2013).
164. Hitchcock, C. . *et al.* Ternary and quaternary antimonide devices for thermophotovoltaic applications. *J. Cryst. Growth* **195,** 363–372 (1998).
165. Mauk, M. G. & Andreev, V. M. GaSb-related materials for TPV cells. *Semicond. Sci. Technol.* **18,** S191–S201 (2003).
166. Gonzalez-Cuevas, J. A., Refaat, T. F., Abedin, M. N. & Elsayed-Ali, H. E. Modeling of the temperature-dependent spectral response of In(1-x)Ga(x)Sb infrared photodetectors. *Opt. Eng.* **45,** 044001 (2006).
167. Hicks, L. & Dresselhaus, M. Effect of quantum-well structures on the thermoelectric figure of merit. *Phys. Rev. B* **47,** 12727–12731 (1993).
168. Kim, J., Naik, G. V., Emani, N. K., Guler, U. & Boltasseva, A. Plasmonic resonances in nanostructured transparent conducting oxide films. *IEEE J. Sel. Top. Quantum Electron.* **19,** 4601907 (2013).
169. Williams, C. C. & Wickramasinghe, H. K. Scanning thermal profiler. *Appl. Phys. Lett.* **49,** 1587 (1986).
170. Dransfeld, K. & Xu, J. The heat transfer between a heated tip and a substrate: fast thermal

microscopy. *J. Microsc.* **152,** 35–42 (1988).
171. Xu, J. B., Lauger, K., Dransfeld, K. & Wilson, I. H. Thermal sensors for investigation of heat transfer in scanning probe microscopy. *Rev. Sci. Instrum.* **65,** 2262 (1994).
172. Xu, J.-B., Läuger, K., Moller, R., Dransfeld, K. & Wilson, I. H. Heat transfer between two metallic surfaces at small distances. *J. Appl. Phys.* **76,** 7209 (1994).
173. Muller-Hirsch, W., Kraft, A., Hirsch, M. T., Parisi, J. & Kittel, A. Heat transfer in ultrahigh vacuum scanning thermal microscopy. *J. Vac. Sci. Technol. A* **17,** 1205 (1999).
174. Kittel, A. *et al.* Near-Field Heat Transfer in a Scanning Thermal Microscope. *Phys. Rev. Lett.* **95,** 224301 (2005).
175. Worbes, L., Hellmann, D. & Kittel, A. Enhanced Near-Field Heat Flow of a Monolayer Dielectric Island. *Phys. Rev. Lett.* **110,** 134302 (2013).
176. Guha, B., Otey, C., Poitras, C. B., Fan, S. & Lipson, M. Near-Field Radiative Cooling of Nanostructures. *Nano Lett.* **12,** 4546–4550 (2012).
177. Kim, K. *et al.* Radiative heat transfer in the extreme near field. *Nature* **528,** 387–391 (2015).
178. Narayanaswamy, A., Shen, S. & Chen, G. Near-field radiative heat transfer between a sphere and a substrate. *Phys. Rev. B* **78,** 115303 (2008).
179. Rousseau, E. *et al.* Radiative heat transfer at the nanoscale. *Nat. Photonics* **3,** 514–517 (2009).
180. Song, B. *et al.* Enhancement of near-field radiative heat transfer using polar dielectric thin films. *Nat. Nanotechnol.* **10,** 253–258 (2015).
181. van Zwol, P. J., Ranno, L. & Chevrier, J. Tuning Near Field Radiative Heat Flux through Surface Excitations with a Metal Insulator Transition. *Phys. Rev. Lett.* **108,** 234301 (2012).
182. van Zwol, P. J., Thiele, S., Berger, C., de Heer, W. A. & Chevrier, J. Nanoscale Radiative Heat Flow due to Surface Plasmons in Graphene and Doped Silicon. *Phys. Rev. Lett.* **109,** 264301 (2012).
183. Hu, L., Narayanaswamy, A., Chen, X. & Chen, G. Near-field thermal radiation between two closely spaced glass plates exceeding Planck's blackbody radiation law. *Appl. Phys. Lett.* **92,** 133106 (2008).
184. Kralik, T., Hanzelka, P., Musilova, V., Srnka, A. & Zobac, M. Cryogenic apparatus for study of near-field heat transfer. *Rev. Sci. Instrum.* **82,** 055106 (2011).
185. Kralik, T. *et al.* Strong Near-Field Enhancement of Radiative Heat Transfer between Metallic Surfaces. *Phys. Rev. Lett.* **109,** 224302 (2012).
186. Ottens, R. S. *et al.* Near-Field Radiative Heat Transfer between Macroscopic Planar Surfaces. *Phys. Rev. Lett.* **107,** 014301 (2011).
187. St-Gelais, R., Guha, B., Zhu, L., Fan, S. & Lipson, M. Demonstration of Strong Near-Field Radiative Heat Transfer between Integrated Nanostructures. *Nano Lett.* **14,** 6971–6975 (2014).
188. Feng, C., Tang, Z., Yu, J. & Sun, C. A MEMS Device Capable of Measuring Near-Field Thermal Radiation between Membranes. *Sensors* **13,** 1998–2010 (2013).
189. Song, B. *et al.* Radiative heat conductances between dielectric and metallic parallel plates with nanoscale gaps. *Nat. Nanotechnol.* (2016).
190. De Wilde, Y. *et al.* Thermal radiation scanning tunnelling microscopy. *Nature* **444,** 740–743 (2006).
191. Zhang, L. M. *et al.* Near-field spectroscopy of silicon dioxide thin films. *Phys. Rev. B* **85,** 075419 (2012).
192. Jones, A. C. & Raschke, M. B. Thermal Infrared Near-Field Spectroscopy. *Nano Lett.* **12,** 1475–1481 (2012).
193. Babuty, A., Joulain, K., Chapuis, P.-O., Greffet, J.-J. & De Wilde, Y. Blackbody Spectrum

Revisited in the Near Field. *Phys. Rev. Lett.* **110,** 146103 (2013).
194. Joulain, K. *et al.* Strongtip–sample couplinginthermalradiationscanning tunnelingmicroscopy. *J. Quant. Spectrosc. Radiat. Transf.* **136,** 1–15 (2014).
195. Peragut, F., Brubach, J.-B., Roy, P. & De Wilde, Y. Infrared near-field imaging and spectroscopy based on thermal or synchrotron radiation. *Appl. Phys. Lett.* **104,** 251118 (2014).
196. O'Callahan, B. T., Lewis, W. E., Jones, A. C. & Raschke, M. B. Spectral frustration and spatial coherence in thermal near-field spectroscopy. *Phys. Rev. B* **89,** 245446 (2014).
197. Centrone, A. Infrared Imaging and Spectroscopy Beyond the Diffraction Limit. *Annu. Rev. Anal. Chem.* **8,** 101–126 (2015).
198. Otto, A. Excitation of Nonradiative Surface Plasma Waves in Silver by the Method of Frustrated Total Reflection. *Zeitschrift für Phys.* **216,** 398–410 (1968).
199. Kretschmann, E. Die Bestimmung optischer Konstanten von Metallen durch Anregung von Oberfliichenplasmaschwingungen. *Zeitschrift für Phys.* **241,** 313–324 (1971).
200. Yu, Z. *et al.* Enhancing far-field thermal emission with thermal extraction. *Nat. Commun.* **4,** 1730 (2013).
201. Shen, S., Narayanaswamy, A., Goh, S. & Chen, G. Thermal conductance of bimaterial microcantilevers. *Appl. Phys. Lett.* **92,** 063509 (2008).
202. Barnes, J. R., Stephenson, R. J., Welland, M. E., Gerber, C. & Gimzewski, J. K. Photothermal spectroscopy with femtojoule sensitivity using a micromechanical device. *Nature* **372,** 79–81 (1994).
203. Sadat, S. *et al.* Room temperature picowatt-resolution calorimetry. *Appl. Phys. Lett.* **99,** 043106 (2011).
204. Canetta, C. & Naryanaswamy, A. Sub-picowatt resolution calorimetry with a bi-material microcantilever sensor. *Appl. Phys. Lett.* **102,** 103112 (2013).
205. SAS, C. Macor - Datasheet. at <www.corning.com/specialtymaterials/macor>
206. Adachi, S. *Properties of Group-IV, III-V and II-VI Semiconductors*. (John Wiley & Sons, Ltd., 2005).
207. Sasihithlu, K. & Narayanaswamy, A. Proximity effects in radiative heat transfer. *Phys. Rev. B* **83,** 161406(R) (2011).
208. Mills, A. F. *Heat Transfer*. (Prentice Hall: Upper Saddle River, 1998).
209. Adachi, S. *Handbook on Physical Properties of Semiconductors*. (Springer, 2007).
210. Ltd., C. *Optical Glass (N-BK7 and B270 types) Datasheet*. at <http://www.crystran.co.uk/optical-materials/optical-glass-n-bk7-and-others>
211. Mishchik, K. *et al.* Photoinscription domains for ultrafast laser writing of refractive index changes in BK7 borosilicate crown optical glass. *Opt. Mater. Express* **3,** 67–85 (2013).
212. Gautam, C., Yadav, A. K. & Singh, A. K. A Review on Infrared Spectroscopy of Borate Glasses with Effects of Different Additives. *ISRN Ceram.* **2012,** 428497 (2012).
213. Maxwell, J. *Atreatiseonelectricityandmagnetism*. (Oxford: Clarendon Press, 1873).
214. Rayleigh, L. On the light from the sky, its polarization and colour. *Philos. Mag.* **41,** 107–120 (1871).
215. Rayleigh, L. On the scattering of light by small particles. *Philos. Mag.* **41,** 447–454 (1871).
216. Mie, G. Beiträge zur Optik trüber Medien, speziell kolloidaler Metallösungen. *Ann. Phys.* **330,** 377–445 (1908).
217. Debye, P. Der Lichtdruck auf Kugeln von beliebigem Material. *Ann. Phys.* **30,** 57–136 (1909).
218. Lorenz, L. Lysbevaegelsen i og uden for en af plane Lysbolger belyst Kugle. *K. Danske Vidensk. Selsk. Skr.* **6,** 1–62 (1890).

219. *The Mie Theory: Basics and Applications*. (Springer-Verlag Berlin Heidelberg, 2012).
220. Horvath, H. Gustav Mie and the scattering and absorption of light by particles: Historic devlopments and basics. *J. Quant. Spectrosc. Radiat. Transf.* **110,** 787–799 (2009).
221. Mishchenko, M. I. & Travis, L. D. Gustav Mie and the Evolving Discipline of Electromagnetic Scattering by Particles. *Bull. Am. Meteorol. Soc.* **89,** (2008).
222. Zsigmondy, R. & Alexander, J. *Colloids and the ultramicroscope*. (J. Wiley & sons, 1909, 1909).
223. Bohren, C. F. & Huffman, D. R. *Absorption and Scattering of Light by Small Particles*. (WILEY-VCH Verlag GmbH & Co. KGaA, 2007). at <http://onlinelibrary.wiley.com/book/10.1002/9783527618156>
224. Matsko, A. B. & Ilchenko, V. S. Optical resonators with whispering-gallery modes part I: basics. *IEEE J. Sel. Top. Quantum Electron.* **12,** 3–14 (2006).
225. Calzetti, D., Kinney, A. L. & Storchi-Bergmann, T. Dust Extinction of the Stellar Continua in Starburst Galaxies: The Ultraviolet and Optical Extinction Law. *Astrophys. J.* **429,** 582–601 (1994).
226. Draine, B. T. Interstellar Dust Grains. *Annu. Rev. Astron. Astrophys.* **41,** 241–289 (2003).
227. Li, A. & Greenberg, J. M. A unified model of interstellar dust. *Astron. Astrophys.* **323,** 566–584 (1997).
228. Pei, Y. C. Interstellar Dust from the Milky Way to the Magellanic Clouds. *Astrophys. J.* **395,** 130–139 (1992).
229. Wang, S., Li, A. & Jiang, B. W. Modeling the infrared interstellar extinction. *Planet. Space Sci.* **100,** 32–39 (2014).
230. Weingartner, J. C. & Draine, B. T. Dust Grain-Size Distributions and Extinction in the Milky Way, Large Magellanic Cloud, and Small Magellanic Cloud. *Astrophys. J.* **548,** 296–309 (2001).
231. Bond, T. C. & Bergstrom, R. W. Light Absorption by Carbonaceous Particles: An Investigative Review. *Aerosol Sci. Technol.* **40,** 27–67 (2006).
232. Christina Hsu, N., Tsay, S.-C., King, M. D. & Herman, J. R. Aerosol Properties Over Bright-Reflecting Source Regions. *IEEE Trans. Geosci. Remote Sens.* **42,** 557–569 (2004).
233. Collis, R. T. H. & Uthe, E. E. Mie scattering techniques for air pollution measurement with lasers. *Opto-electronics* **4,** 87–99 (1972).
234. Horvath, H. Atmospheric Light Absorption - A Review. *Atmos. Environ.* **27A,** 293–317 (1993).
235. Levy, R. C., Remer, L. A. & Dubovik, O. Global aerosol optical properties and application to Moderate Resolution Imaging Spectroradiometer aerosol retrieval over land. *J. Geophys. Res.* **112,** 3210 (2007).
236. Malm, W. C., Sisler, J. F., Huffman, D., Eldred, R. A. & Cahill, T. A. Spatial and seasonal trends in particle concentration and optical extinction in the United States. *J. Geophys. Res.* **99,** 1347–1370 (1994).
237. McMurry, P. H. A review of atmospheric aerosol measurements. *Atmos. Environ.* **34,** 1959–1999 (2000).
238. Moosmuller, H., Chakrabarty, R. K. & Arnott, W. P. Aerosol light absorption and its measurement: A review. *J. Quant. Spectrosc. Radiat. Transf.* **110,** 844–878 (2009).
239. Sorensen, C. M. Light Scattering by Fractal Aggregates: A Review. *Aerosol Sci. Technol.* **35,** 648–687 (2001).
240. De, M., Ghosh, P. S. & Rotello, V. M. Applications of Nanoparticles in Biology. *Adv. Mater.*

20, 4225–4241 (2008).
241. Dreaden, E. C., Alkilany, A. M., Huang, X., Murphy, C. J. & El-Sayed, M. A. The golden age: gold nanoparticles for biomedicine. *Chem. Soc. Rev.* **41,** 2740–2779 (2012).
242. Dykman, L. & Khlebtsov, N. Gold nanoparticles in biomedical applications: recent advances and perspectives. *Chem. Soc. Rev.* **41,** 2256–2282 (2012).
243. Huang, X., Neretina, S. & El-Sayed, M. A. Gold Nanorods: From Synthesis and Properties to Biological and Biomedical Applications. *Adv. Mater.* **21,** 4880–4910 (2009).
244. Jain, P. K., Huang, X., El-Sayed, I. H. & El-Sayed, M. A. Review of Some Interesting Surface Plasmon Resonance-enhanced Properties of Noble Metal Nanoparticles and Their Applications to Biosystems. *Plasmonics* **2,** 107–118 (2007).
245. Jain, P. K., Huang, X., El-Sayed, I. H. & El-Sayed, M. A. Noble Metals on the Nanoscale: Optical and Photothermal Properties and Some Applications in Imaging, Sensing, Biology, and Medicine. *Acc. Chem. Res.* **41,** 1578–1586 (2008).
246. Jain, P. K., Lee, K. S., El-Sayed, I. H. & El-Sayed, M. A. Calculated Absorption and Scattering Properties of Gold Nanoparticles of Different Size, Shape, and Composition: Applications in Biological Imaging and Biomedicine. *J. Phys. Chem. B* **110,** 7238–7248 (2006).
247. Kelkar, S. S. & Reineke, T. M. Theranostics: Combining Imaging and Therapy. *Bioconjug. Chem.* **22,** 1879–1903 (2011).
248. Saha, K., Agasti, S. S., Kim, C., Li, X. & Rotello, V. M. Gold Nanoparticles in Chemical and Biological Sensing. *Chem. Rev.* **112,** 2739–2779 (2012).
249. Awazu, K. *et al.* A Plasmonic Photocatalyst Consisting of Silver Nanoparticles Embedded in Titanium Dioxide. *J. Am. Chem. Soc.* **130,** 1676–1680 (2008).
250. Baxter, J. B. & Aydil, E. S. Nanowire-based dye-sensitized solar cells. *Appl. Phys. Lett.* **86,** 053114–3 (2005).
251. Cao, L., Fan, P., Barnard, E. S., Brown, A. M. & Brongersma, M. L. Tuning the Color of Silicon Nanostructures. *Nano Lett.* **10,** 2649–2654 (2010).
252. Cao, L. *et al.* Engineering light absorption in semiconductor nanowire devices. *Nat. Mater.* **8,** 643–647 (2009).
253. Garnett, E. C. & Yang, P. Silicon Nanowire Radial p−n Junction Solar Cells. *J. Am. Chem. Soc.* **130,** 9224–9225 (2008).
254. Hu, L. & Chen, G. Analysis of Optical Absorption in Silicon Nanowire Arrays for Photovoltaic Applications. *Nano Lett.* **7,** 3249–3252 (2007).
255. Linic, S., Christopher, P. & Ingram, D. B. Plasmonic-metal nanostructures for efficient conversion of solar to chemical energy. *Nat. Mater.* **10,** 911–921 (2011).
256. Ningfeng, H., Chenxi, L. & Povinelli, M. L. Broadband absorption of semiconductor nanowire arrays for photovoltaic applications. *J. Opt.* **14,** 024004 (2012).
257. Tachibana, Y., Vayssieres, L. & Durrant, J. R. Artificial photosynthesis for solar water-splitting. *Nat. Photonics* **6,** 511–518 (2012).
258. Tian, B. *et al.* Coaxial silicon nanowires as solar cells and nanoelectronic power sources. *Nature* **449,** 885–889 (2007).
259. Vj, L. *et al.* A Perspective on Nanowire Photodetectors: Current Status, Future Challenges, and Opportunities. *Sel. Top. Quantum Electron. IEEE J.* **17,** 1002–1032 (2011).
260. Jiang, R., Li, B., Fang, C. & Wang, J. Metal/Semiconductor Hybrid Nanostructures for Plasmon- Enhanced Applications. *Adv. Mater.* **26,** 5274–5309 (2014).
261. Mayer, K. M. & Hafner, J. H. Localized Surface Plasmon Resonance Sensors. *Chem. Rev.*

111, 3828–3857 (2011).
262. Yazdi, M. & Sheikhzadeh, M. Personal cooling garments: a review. *J. Text. Insititute* **105,** 1231–1250 (2014).
263. Pérez-Lombard, L., Ortiz, J. & Pout, C. A review on buildings energy consumption information. *Energy Build.* **40,** 394–398 (2008).
264. Energy, U. S. D. of. *2011 Buildings Energy Data Book*. (2011).
265. Sadineni, S. B., Madala, S. & Boehm, R. F. Passive building energy savings: A review of building envelope components. *Renew. Sustain. Energy Rev.* **15,** 3617–3631 (2011).
266. Wang, S. & Ma, Z. Supervisory and Optimal Control of building HVAC Systems: A Review. *HVAC&R Res.* **14,** 3–32 (2008).
267. Memon, S. A. Phase change materials integrated in building walls: A state of the art review. *Renew. Sustain. Energy Rev.* **31,** 870–906 (2014).
268. Hong, C. J. & Kim, J. B. A study of comfort performance in cotton and polyester blended fabrics. I. Vertical wicking behavior. *Fibers Polym.* **8,** 218–224 (2007).
269. Kaplan, S. & Okur, A. Thermal comfort performance of sports garments with objective and subjective measurements. *Indian J. Fibre Text. Res.* **37,** 46–54 (2012).
270. Das, B., Das, A., Kothari, V. K., Fanguiero, R. & de Araújo, M. Effect of fibre diameter and cross-sectional shape on moisture transmission through fabrics. *Fibers Polym.* **9,** 225–231 (2008).
271. McCullough, E. A. & Eckels, S. Evaluation of personal cooling systems for soldiers. in *13th Int. Environmental Ergonomics Conf.* 200–204 (2009).
272. Gao, C., Kuklane, K., Wang, F. & Holmér, I. Personal cooling with phase change materials to improve thermal comfort from a heat wave perspective. *Indoor Ai* **22,** 523–530 (2012).
273. Muir, I. H., Bishop, P. A. & Ray, P. Effects of a Novel Ice-Cooling Technique on Work in Protective Clothing at 28C, 23C, and 18C WBGTs. *Am. Ind. Hyg. Assoc. J.* **60,** 96–104 (1999).
274. Rothmaier, M., Weder, M., Meyer-Heim, A. & Kesselring, J. Design and performance cooling garments based on three-layer laminates. *Med. Biol. Eng. Comput.* **46,** 825–832 (2008).
275. Elbel, S., Bowers, C. D., Zhao, H., Park, S. & Hrnjak, P. S. Development of Microclimate Cooling Systems for Increased Thermal Comfort of Individuals. in *International Refrigeration and Air Conditioning Conference* 1183 (2012).
276. Kayacan, O. & Kurbak, A. Effect of Garment Design on Liquid Cooling Garments. *Text. Res. J.* **80,** 1442–1455 (2010).
277. Yang, J.-H., Kato, S. & Seok, H.-T. Measurement of Airflow around the Human Body with Wide-cover Type Personal Air-conditioning with PIV. *Indoor Built Environ.* **18,** 301–312 (2009).
278. Yang, Y.-F., Stapleton, J., Diagne, B. T., Kenny, G. P. & Lan, C. Q. Man-portable personal cooling garment based on vacuum desiccant cooling. *Appl. Therm. Eng.* **47,** 18–24 (2012).
279. Nag, P. K., Pradhan, C. K., Nag, A., Ashetekar, S. P. & Desai, H. Efficacy of a water-cooled garment for auxiliary body cooling in heat. *Ergonomics* **41,** 179–187 (1998).
280. Steketee, J. Spectral emissivity of skin and pericardium. *Phys. Med. Biol.* **18,** 686–694 (1973).
281. Sanchez-Marin, F. J., Calixto-Carrera, S. & Villasenor-Mora, C. Novel approach to assess the emissivity of the human skin. *J. Biomed. Opt.* **14,** 024006 (2009).
282. Incropera, F. P., Dewitt, D. P., Bergman, T. L. & Lavine, A. S. *Fundamentals of Heat and Mass Transfer*. (John Wiley & Sons, Inc., 2007).
283. Hoyt, T., Lee, K. H., Zhang, H., Arens, E. & Webster, T. Energy savings from extended air temperature setpoints and reductions in room air mixing. *Int. Conf. Environ. Ergon. 2009*

(2005). at <https://escholarship.org/uc/item/28x9d7xj>
284. Federspiel, C. Predicting the frequency and cost of hot and cold complaints in buildlings. *Cent. Built Environ.* (2000). at <https://escholarship.org/uc/item/8m6814qd>
285. ASHRAE. ASHRAE Handbook-Fundamentals. *ASHRAE Handbook-Fundamentals* (2005).
286. Jakšić, D. & Jakšić, N. in *Woven Fabric Engineering* 255–272 (Sciyo, 2010).
287. Modest, M. F. *Radiative Heat Transfer*. (Academic Press, 2003).
288. Lee, T.-W. *Thermal and Flow Measurements*. (CRC Press, 2008).
289. Oerlikon Leybold Group. The Fiber Year 2006/07 - A World Survey on Textile and Nonwovens Industry. (2007).
290. Laskarakis, A. & Logothetidis, S. Study of the electronic and vibrational properties of poly(ethylene terephthalate) and poly(ethylene naphthalate) films. *J. Appl. Phys.* **101,** 053503 (2007).
291. Ferwada, J. Elements of early vision for computer graphics. *IEEE Comput. Graph. Appl.* **21,** 21–23 (2001).
292. Wandell, B. A. *Foundations of Vision*. (Sinauer Associates, 1995).
293. Stevens, S. S. On the psychophysical law. *Psychol. Rev.* **64,** 153–181 (1957).
294. Fechner, G. T. *Elemente der psychophysik*. (Breitkopf und Hartel, 1860).
295. Stevens, S. S. To Honor Fechner and the Repeal of His Law. *Science (80-.).* **133,** 80–86 (1961).
296. Steinhardt, J. Intensity Discrimination in the Human Eye: I. The Relation of DetlaI/I to Intensity. *J. Gen. Physiol.* **20,** 185–209 (1936).
297. Norvang, L. T., Milner, T. E., Nelson, J. S., Berns, M. W. & Svaasand, L. O. Skin pigmentation characterized by visible reflectance measurements. *Lasers Med. Sci.* **12,** 99–112 (1997).
298. Zhang, H., Hu, T. & Zhang, J. Transmittance of Infrared Radiation Through Fabric in the Range 8-14 μm. *Text. Res. J.* **80,** 1516–1521 (2010).
299. Carr, W. W. *et al.* Infrared Absorption Studies of Fabrics. *Text. Res. J.* **67,** 725–738 (1997).
300. Xu, W., Shyr, T. & Yao, M. Textiles' Properties in the Infrared Irradiation. *Text. Res. J.* **77,** 513–519 (2007).
301. Brönstrup, G. *et al.* Optical Properties of Individual Silicon Nanowires for Photonic Devices. *ACS Nano* **4,** 7113–7122 (2010).
302. Tong, J. K. *et al.* Direct and quantitative photothermal absorption spectroscopy of individual particulates. *Appl. Phys. Lett.* **103,** (2013).
303. Boriskina, S. V., Sewell, P., Benson, T. M. & Nosich, A. I. Accurate Simulation of 2D Optical Microcavities with Uniquely Solvable Boundary Integral Equations and Trigonometric-Galerkin Discretization. *J. Opt. Soc. Am. A* **21,** 393–402 (2004).
304. Krimm, S., Liang, C. Y. & Sutherland, G. B. B. M. Infrared Spectra of High Polymers. II. Polyethylene. *J. Chem. Phys.* **25,** 549 (1956).
305. Crangle, A. in *Polyolefin Fibres: Industrial and Medical Applications* (ed. Ugbolue, S.) 3–34 (Woodhead Publishing in Textiles, 2009).
306. *Infrared and Raman Spectroscopy: Methods and Applications*. (VCH, 2007).
307. Charvat, R. A. *Coloring of Plastics: Fundamentals*. (John Wiley & Sons, Ltd., 2005).
308. *Colorants and auxiliaries: Organic Chemistry and Application Properties*. (Society of Dyers and Colourists, 2002).
309. Schael, G. w. Determination of Polyolefin Film Properties from Refractive Index Measurements. II. Birefringence. *J. Appl. Polym. Sci.* **12,** 903–914 (1968).

310. Wool, R. P. & Bretzlaff, R. S. Infrared and Raman Spectroscopy of Stressed Polyethylene. *J. Polym. Sci. Part B Polym. Phys.* **24,** 1039–1066 (1986).
311. ASTM D3995-14, Standard Performance Specification for Men's and Women's Knitted Career Apparel Fabrics: Dress and Vocational.
312. ASTM Standard F1868, Standard Test Method for Thermal and Evaporative Resistance of Clothing Materials Using a Sweating Hot Plate. doi:10.1520/F1868
313. ISO 11092 Textiles - Physiological Effects - Measurement of thermal and water-vapour resistance under steady-state conditions (sweating guarded-hotplate test).
314. ASTM Standard E96/ E96M, 2013, Standard Test Methods for Water Vapor Transmission of Materials. (2013). doi:10.1520/E0096_E0096M
315. Benson, T. M. *et al.* in *Frontiers in Planar Lightwave Circuit Technology. NATO Science Series II: Mathematics, Physics and Chemistry Volume 21* 39–70 (Springer, 2006).